Chemomechanics of Attached and Suspended Cells

by

John Mapes Maloney

B.S. Mechanical Engineering, University of Maryland, 1999
M.S. Mechanical Engineering, University of Maryland, 2001
M.Eng. Materials Science and Engineering, Massachusetts Institute of Technology, 2006

Submitted to the Department of Materials Science and Engineering
in partial fulfillment of the requirements for the degree of

Doctor of Philosophy in Materials Science and Engineering

at the

MASSACHUSETTS INSTITUTE OF TECHNOLOGY

February 2012

Author .....
Department of Materials Science and Engineering
December 12, 2011

Certified by .....
Krystyn J. Van Vliet
Paul M. Cook Career Development
Associate Professor of Materials Science and Engineering
Thesis Supervisor

Certified by .....
Robert Langer
David H. Koch Institute Professor
Thesis Supervisor

Accepted by .....
Gerbrand Ceder
Richard P. Simmons Professor of Materials Science and Engineering
Chair, Departmental Committee on Graduate Students

Chemomechanics of Attached and Suspended Cells
by
John Mapes Maloney

Submitted to the Department of Materials Science and Engineering
on December 12, 2011, in partial fulfillment of the
requirements for the degree of
Doctor of Philosophy in Materials Science and Engineering

Abstract

Chemomechanical coupling in single eukaryotic animal cells is investigated in the context of the attached (substratum-adhered) and the suspended (free-floating) states. These dichotomous configurations determine behavioral differences and commonalities relevant to therapeutic reimplantation of stem cells and to our general understanding of the cell as an animate material. Analytical, simulation, and experimental techniques are applied to key questions including: (1) How deep can mechanosensitive attached cells "feel" into the adjacent environment? (2) In what manner do suspended cells deform, absent the prominent actomyosin stress fibers that arise upon attachment to a rigid substratum? (3) What explains the remarkable mechanical heterogeneity among single cells within a population? (4) Can we leverage putative mechanical markers of useful stem cells to sort them before reimplantation in tissue generation therapies?

Attached cells are found to barely detect an underlying rigid base more than 10 micrometers below the surface of a compliant coating. This conclusion, based on extensions to the Boussinesq problem of elasticity theory, is validated by observations of cell morphology on compliant polyacrylamide coatings in a range of thicknesses. Analytical equations are developed for estimating the effective stiffness sensed by a cell atop a compliant layer. We also identify and consider conceptualizations of a "critical thickness," representing the minimum suitable thickness for a specific application. This parameter depends on the cell behavior of interest; the particular case of stem cell culture for paracrine extraction is presented as a case study.

Suspended cells are found to exhibit no single characteristic time scale during deformation; rather, they behave as power-law (or "soft glassy") materials. Here, optical stretching is used as a non-contact technique to show that stress fibers and probe-cell contact are not critical in enabling power-law rheological behavior of cells. Furthermore, suspended cell fluidity, as characterized by both the hysteresivity of complex modulus and the power-law exponent of creep compliance, is found to be unaffected by adenosine triphosphate (ATP) depletion, showing that ATP hydrolysis is not the origin of fluidity in cells during deformation. However, ATP depletion does reduce the natural variation in hysteresivity values among cells. This finding, and the finding that changes in the power-law exponent and stiffness of single cells are correlated upon repeated loading, motivates study of how and why these parameters are coupled.

To further explore this coupling, chemomechanical cues are applied to cell populations to elucidate the origin of the wide, right-skewed distribution of stiffness values that is consistently observed. The distribution and width are found to be not detectably dependent on cell-probe contact, cell lineage, cell cycle, mechanical perturbation, or fixation by chemical crosslinking. However, ATP depletion again reduces heterogeneity, now in the case of cell stiffness values. It is further found analytically that a postulated Gaussian distribution of power-law exponent values leads naturally to the log-normal distribution of cell stiffness values that is widely observed. Based on these connections, a framework is presented to improve our understanding of the appearance of mechanical heterogeneity in successively more complex assemblies of cell components. Two

case studies are described to explore the implications of unavoidable intrinsic variation of cell stiffness in diagnostic and therapeutic applications.

Finally, all the single-cell mechanical parameters studied so far (stiffness during creep and recovery, stiffness heterogeneity among cells, and power-law exponents in creep and recovery) are characterized in mesenchymal stem cells during twenty population doublings with the aim of developing a high-throughput sorting tool. However, mechanical and structural changes that are observed in the attached state during this culture time are not observed after cell detachment from the substratum. The absence in the suspended state of these alterations indicates that they manifest themselves through stress fiber arrangement rather than cortical network arrangement. While optical stretching under the present approach does not detect mechanical markers of extended passaging that are correlated with decreased differentiation propensity, the technique is nevertheless found capable of investigating another structural transition: mechanical stiffening over tens of minutes after adherent cells are suspended. This previously unquantified transition is correlated with membrane resorption and reattachment to the cortex as the cell "remodels" after substratum detachment.

Together, these quantitative studies and models of attached and suspended cells define the extremes of the extracellular environment while probing mechanisms that contribute to cellular chemomechanical response. An integration of the results described above shows that no one existing model can describe cell chemomechanics. However, the cell can be usefully described as a material—one in which animate mechanisms such as active contraction will generally, but not invariably, need to be considered as augmenting existing viscoelastic theories of inanimate matter.

Thesis Supervisor: Krystyn J. Van Vliet
Title: Paul M. Cook Career Development
Associate Professor of Materials Science and Engineering

Thesis Supervisor: Robert Langer
Title: David H. Koch Institute Professor

Acknowledgments

I am tremendously grateful to my co-advisors, Professor Krystyn Van Vliet and Professor Robert Langer, for encouragement and guidance. Krystyn provided a welcome environment of research freedom. Bob's unflagging support was the perfect complement to Krystyn's critical (but always considerate) eye, and both gave courage and clarity to my attempts to communicate ideas. I have been lucky to work with both of them.

I have also been lucky to work with fine coauthors that dependably contributed honest and top-notch data and ideas: Christopher Bruce and Emily Walton (MIT), Franziska Lautenschläger and Jochen Guck (University of Cambridge), Dessy Nikova (MIT), Emer Clarke (ReachBio, Inc.), Eric Lehnhardt (Arizona State University), and the Okajima Group (Hokkaido University). My undergraduate collaborators, Kyle Bryson (Pennsylvania State University), Martha Gross (MIT), and Jennifer DeBerardinis (Smith College), greatly impressed me with their creativity and determination.

My thesis committee members—Professor Chris Schuh, Professor Matt Lang, and Professor Scott Manalis—asked damn tough questions, but I never doubted their confidence in me; for this I thank them.

Of all the Van Vliet Group members who brightened my days, I am especially happy to acknowledge my friend Ranjani Krishnan Paradise, whose support and good sense made an enormous difference.

I am deeply indebted to Professor Michael Cima (MIT), Professor Don DeVoe (University of Maryland), and Dr. John Santini (MicroCHIPS, Inc.) for their support of my graduate career. I will always be thankful to Al Myers (Prometheus Inc.), manager extraordinaire, for his patience, trust, and guidance. I gratefully acknowledge funding from NIH (Molecular, Cellular, Tissue and Biomechanics Training Grant EB006348) and the Arnold and Mabel Beckman Foundation. Portions of this work have been published previously [1–4], and are reprinted with the permission of the American Physical Society, Landes Bioscience, the Institute of Physics Publishing, and Elsevier.

I appreciate gracious responses to my communications from Prof. Nathan Sniadecki, Prof. Rudolf Merkel, Dr. Guillaume Lenormand, Prof. Jeffrey Fredberg, Dr. Philip Kollmannsberger, Prof. Ben Fabry, Dr. Jens Glaser, and Prof. Klaus Kroy. Their papers, helpful comments, and contributions to the field of biophysics have been inspiring.

Finally, it is a pleasure to recognize my parents, John Martin and Rosemary Mapes Maloney and Henry and Barbara Casey, whose support I cherish, and my wife, Mary Kathleen (Katie) Casey Maloney, who has brought peace to my life. I have often claimed that my passions are limited to engineering, beer, and Katie—and that the true ordering is as elusive as an understanding of cell chemomechanics. After careful thought, I reaffirm this list, and am proud to present a thesis produced in a rapture of all three.

Contents

List of Figures

List of Tables

Chapter 1

Introduction

1.1 Context and themes

The living cell is the preeminent material to be understood. Every physical action we take depends on the structural stability of our cells. Every object and phenomenon we experience through touch is mediated by our cells' chemomechanical[1] nature. No other material is so intimate to our existence.

But how should we think of the cell as a material? Where would we start? With its complex animate nature—internal molecular motors, dynamic and heterogeneous physical structure, and near-fluidic deformation behavior—the living eukaryotic animal cell differs considerably from the idealized elastic solid presented in introductory Mechanics of Materials texts. Yet we must confront this complexity as we attempt to improve our understanding of Nature, first by generating and testing hypotheses, and ultimately by developing and reconciling different viewpoints of cell chemomechanics that are useful to engineers, physicists, biologists, and physicians.

Thus, this thesis begins by delineating the unique challenges in studying cell chemomechanics.

1.1.1 What are the unique attributes of cells?

Because the living cell lies outside the context of more conventional engineering materials (metals, ceramics, and polymers, for example), it seems appropriate to start by reviewing some of the unique attributes of cells. Let us consider three prominent and relevant attributes, reviewed below and schematized in Figure 1-1.

Active contractility and mechanosensing. Adherent[2] cells are sticky, anchoring to adjacent substrata[3] at discrete sites of noncovalent interactions (Fig. 1-1(a), Fig. 1-2(a)) [8–10]. At these sites, patches of transmembrane molecules—the class of integrins, for example—mechanically link the cell to the external environment, typically a natural or synthetic extracellular matrix (ECM). These adhesion sites are sometimes

[1] **Chemomechanics** herein means chemical-mechanical coupling in a material [5–7], in the present context the responses (chemical and mechanical) of cells to chemical and mechanical signals. Examples addressed in this thesis include, for example, molecular unbinding in the cytoskeleton induced by a mechanical load and whole-cell mechanical heterogeneity regulated by metabolic chemical reactions.

[2] **Adherent** herein means having a tendency to attach, but not necessarily attached at all times. Most eukaryotic cells are adherent, though they may be brought from the attached to the suspended state through mechanical or chemical induction (e.g., detachment via chemical cleaving of molecular attachments).

[3] **Substratum** (pl. substrata) herein means the material directly adjacent to and contacted by the cell (cf. substrate, an underlying base upon which layers are fabricated).

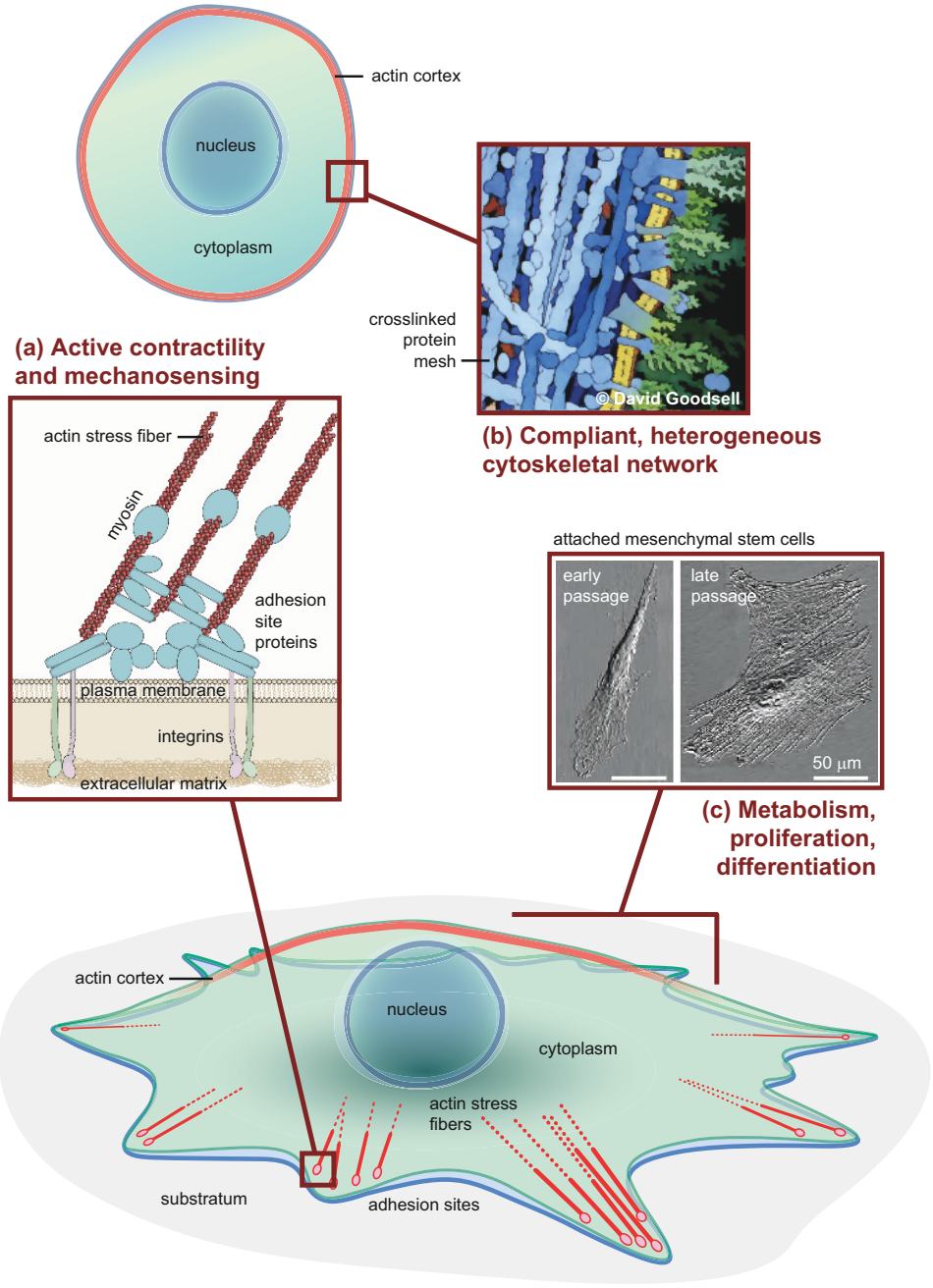

Figure 1-1: **In comparison to typical engineering solids, living cells are distinguished by their animate nature, including the following unique attributes: the ability to probe and respond to the chemomechanical properties of their surrounding environment; an extremely compliant cytoskeletal network of crosslinked macromolecules; and the ability to divide repeatedly and (for stem cells) differentiate down lineages of therapeutic value for tissue regeneration.** (a) Attached cells use stress fibers (bundles of actin filaments tensioned by myosin motors) to deform the extracellular matrix via transmembrane integrin molecules. (b) A compliant cytoskeletal mesh with a disperse collection of characteristic length scales deforms by local rearrangement of gel-like protein networks, including an actin cortex. (c) A collection of primary mesenchymal stem cells contains subpopulations that predominate at different stages of *in vitro* culture, leading to transitions in typical morphology over population lifetime. (Inset images adapted from [11], [12], and [13], respectively.)

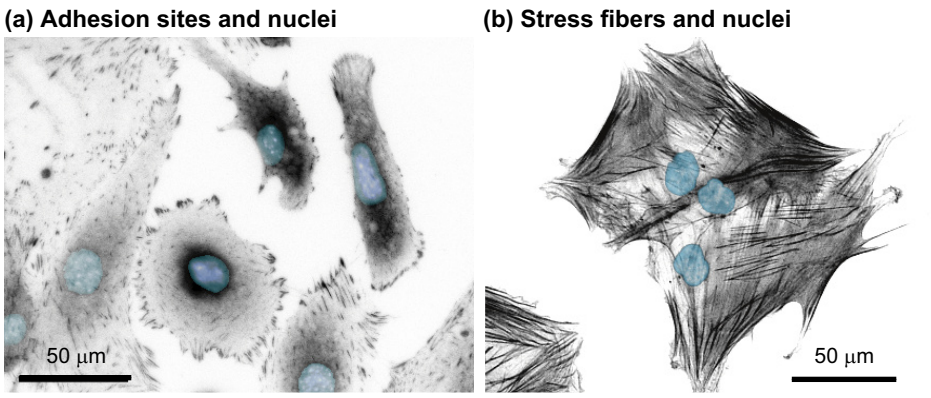

Figure 1-2: **Epifluorescent micrographs of fixed and stained cells display mechanical components of attached cells on stiff substrata.** (a) In fibroblasts stained for the adhesion site protein vinculin, discrete features—often appearing at the periphery of the cells—correspond to adhesion sites between the cell and the adjacent surface (black: anti-vinculin antibody; blue: DAPI stain for DNA). (b) In mesenchymal stem cells stained for filamentous actin, stress fibers spanning each cell connect adhesion sites and enable the cell to probe the surrounding environment (black: rhodamine phalloidin stain for actin; blue: DAPI stain for DNA). (Images prepared via protocols in App. C.3.)

further classified as initial focal complexes or mature focal adhesions depending on their size, state of development, and characteristic participating proteins [14].[4]

Adhesion sites are connected via adaptor proteins to crucial structures in the attached cell cytoskeleton called stress fibers (Fig. 1-2(b)), bundles of filamentous actin (F-actin) pulled into uniaxial tension by myosin molecular motors powered by adenosine triphosphate (ATP) hydrolysis. At adhesion sites, this internal actomyosin contraction exerts O(1 kPa)[5] stress parallel to the substratum [15]. In turn, the substratum supplies an equal and opposite stress. The cell and substratum each deform to some degree from these stresses (though the deformation of a near-rigid substratum such as glass would be difficult to detect).

The amount of substratum deformation influences cell behavior in a process, not completely understood, known as mechanosensitivity [16–19]. Cells receive information about the stiffness[6] of their mechanical environment from the coupling between stress applied by the cell at adhesion sites and the resulting deformation at these sites. This information strongly modulates such widespread types of cell behavior as adhesion site size, spread area, proliferation rate, and gene expression [20–24]. Loss of anchorage for a prolonged duration (several days, for example) can trigger programmed cell death in adherent cells [25].

In summary, adherent cells mechanically load their surroundings and react to the resulting deformation. This active, responsive behavior is an attribute of cells that generally distinguishes them from inert materials; accordingly, the first major focus of this thesis is the nature of the load-deformation coupling.

Compliant, heterogeneous cytoskeletal network. Cells are extremely compliant, with typical stiffness between 0.01–10 kPa [26–30] (at time and strain scales of O(1 s) and O(1%), respectively). Broadly viewed, the cell resembles a gel, a dilute crosslinked biopolymer network [31]. Current understanding is that cell stiffness is generally correlated with greater F-actin content and organization in both attached and recently

[4] **Adhesion sites** herein generically refers to initial adhesions/complexes, focal adhesions/complexes, and all such terms referring to patches of transmembrane integrin-RGD (arginine-glycine-aspartic acid) linkages.

[5] Read "on the order of 1 kPa."

[6] **Compliant/stiff** herein means the ease/difficulty of achieving *elastic* or *reversible* deformation (cf. the soft/hard dichotomy for *plastic* or *permanent* deformation).

suspended cells [32–35]. (Contributions from other cytoskeletal structures such as microtubules and intermediate filaments are not altogether absent, but the influence of these components has been reported as relatively small [33, 36–39].) The prominent crosslinked F-actin structures in attached cells are stress fibers (as discussed earlier, contractile actomyosin bundles that tightly link pairs of cell-substratum adhesion sites) and a $\lesssim$1 μm-thick cortex (a contractile actomyosin mesh just inside, and connected to, the outer plasma membrane). While stress fibers disappear upon cell suspension, the actin cortex remains and provides continued structural support (Fig. 1-1(b)) [34].

Two empirical rheological findings are especially relevant in this overview; the first involves the rheological behavior of a single cell or average behavior of a group of cells, and the second involves the population distribution of individual cell stiffness measurements. First, on physiologically relevant time scales (at least three orders of magnitude centered on 1 s), and in experiments at multiple length scales (Fig. 1-3(a)), attached cells regularly exhibit so-called power-law rheology (PLR, Fig. 1-3(b)) [40,41]. For example, the complex modulus $G^\star(\omega)$ scales with frequency ω as $G^\star(\omega) \propto (i\omega)^a$ [26,42–44], and creep compliance $J(t)$ [29, 42] and stress relaxation modulus $G(t)$ [45, 46] scale with time t as $J(t), 1/G(t) \propto t^a$.[7] (The mathematical connection between these frequency and time regimes has also been explored [29, 47, 48].) Furthermore, the hysteresivity or loss tangent $G''/G' = \tan(\pi a/2)$. The power-law exponent a in these experiments has consistently been found to lie in the approximate range 0.1–0.5 and is Gaussian-distributed. This rheological behavior is attributed to the varied possible arrangements in cytoskeletal networks, each with its own relaxation time, that integrate to form a material with no single characteristic time scale [49].

The second common rheological finding involves the distribution of individual cell stiffness values around a population average. A growing array of experiments have revealed that cell stiffness is distributed log-normally—again, largely independent of experimental technique and length scale [26, 29, 50, 51], metabolic state [52], and cytoskeletal perturbation [42, 43, 48] (Fig. 1-3(c)). The geometric standard deviation $\mathrm{SD}_{\mathrm{geo}}$ of this distribution typically lies in the range 1.2–5.4. (An intrinsic $\mathrm{SD}_{\mathrm{geo}}$ of 2, for example, implies that 16% of cells are $<1/2\times$, and another 16% $>2\times$, the median of the observations.)

The cell therefore behaves as a mechanical material intermediate between an elastic solid and a viscous fluid, two materials that exhibit power-law rheology with $a = 0$ and $a = 1$, respectively. Nevertheless, cells deform quite differently from elastic solids such as metals and elastomers, which deform elastically via stretching of atomic bonds and uncoiling of polymer chains, respectively. Rather, cell deformation appears best described by agitation-driven local yielding and rearrangement, though a clear path leading from individual molecular events to emergent rheological parameters does not yet exist [41, 49, 53].

In summary, cell populations—obtained from various sources and measured by various techniques—exhibit some striking commonalities in chemomechanical response, though the common element is not fully understood. This overall characteristic behavior, particularly the combination of power-law and log-normally distributed rheological behavior, is a second unique attribute of cells, and the origin and extent of these hallmarks is the second major focus of this thesis.

Metabolism, proliferation, and differentiation. The idea that a material sample could transform over time or in response to external stimuli is not unusual. However, cells—and stem cells in particular—take this dynamic sensitivity and potential usefulness to an extreme. The example of interest in this thesis is a primary cell for which

[7] The complex modulus ($G^\star(\omega) = G' + iG''$ where G' is the storage modulus and G'' is the loss modulus) is the ratio of complex stress to complex strain, $\sigma^\star/\varepsilon^\star$, where these two parameters are generally out of phase in viscoelastic materials. The creep compliance $J(t)$ is the time-dependent strain following a step increase in stress, and the relaxation modulus $G(t)$ is the time-dependent stress following a step increase in strain.

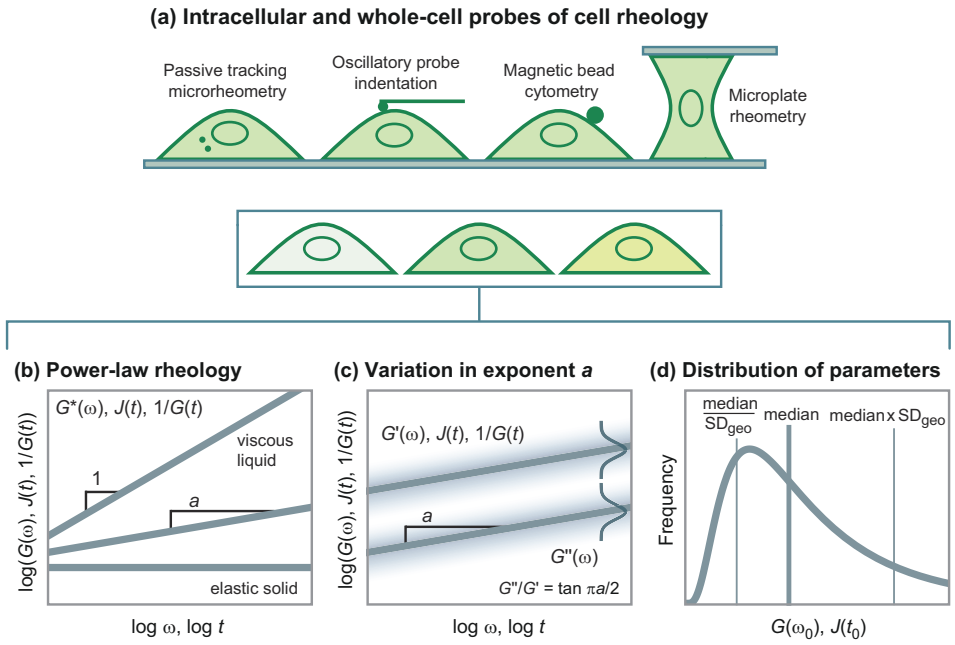

Figure 1-3: **Universal mechanical behavior of living cells can be described by general rheological response and by the population distribution of individual measurements.** (a,b) It has been widely observed, through multiple experimental techniques, that the stiffness (specifically, the complex modulus G^*) of individual cells increases as a power law with frequency ω, where the power-law exponent a is typically found to be 0.1–0.5 by experiment. The same power law also describes the dependence of creep compliance $J(t)$ and reciprocal stress relaxation modulus $1/G(t)$ on time t. (c) The exponent a is Gaussian distributed and further modulates the hysteresivity (the ratio of the loss modulus G'' to the storage modulus G') as $G''/G' = \tan(\pi a/2)$. (d) Individual measurements of stiffness (or compliance) are distributed log-normally with a typical geometric standard deviation $\mathrm{SD}_{\mathrm{geo}}$ of 1.2–5.4.

potential therapeutic applications abound: a minor cell subpopulation of adult human bone marrow stroma often termed mesenchymal stem cells (MSCs; the mesenchyme is a class of embryonic tissue that develops into bone and cartilage, among other tissues) [54]. These cells have been explanted, expanded (i.e., cultured for maximum population size), and deployed in clinical trials for conditions including osteogenesis *imperfecta* [55], myocardial infarction [56], joint repair [57], and other pathologies that would benefit from mesenchymal tissue (re)growth (Fig. 1-4).

Standardized MSC purification protocols have been developed. Generally, MSCs are first separated from other cells within the bone marrow stroma by density centrifugation and then seeded upon tissue culture polystyrene (TCPS) [58]; indeed, attachment and rapid proliferation on a near-rigid substratum partially define MSCs [59]. Human MSCs are also defined by expression or lack thereof of certain surface epitopes, which are usually characterized by fluorophore-conjugated antibody tagging, and finally by their ability to differentiate into several downstream lineages such as adipocytes, chrondrocytes, and osteoblasts via chemical induction [54].

After identification of MSCs, continued culture maintenance is required; cells continue to proliferate, dividing approximately twice a week for approximately twenty population doublings until entering senescence [58]. A crucial part of *in vitro* culture is repeated detachment and transfer to larger culture areas. (Were the cells not routinely detached and diluted, a confluent layer would develop and suppress further division via a cell response known as contact growth inhibition.) Detachment is typically achieved by cleaving cell adhesive bonds with the enzyme trypsin and by simultaneously sequestering adhesion-required calcium with the chelator ethylenediaminetetraacetic acid (EDTA). The cell suspension is then diluted and seeded into new

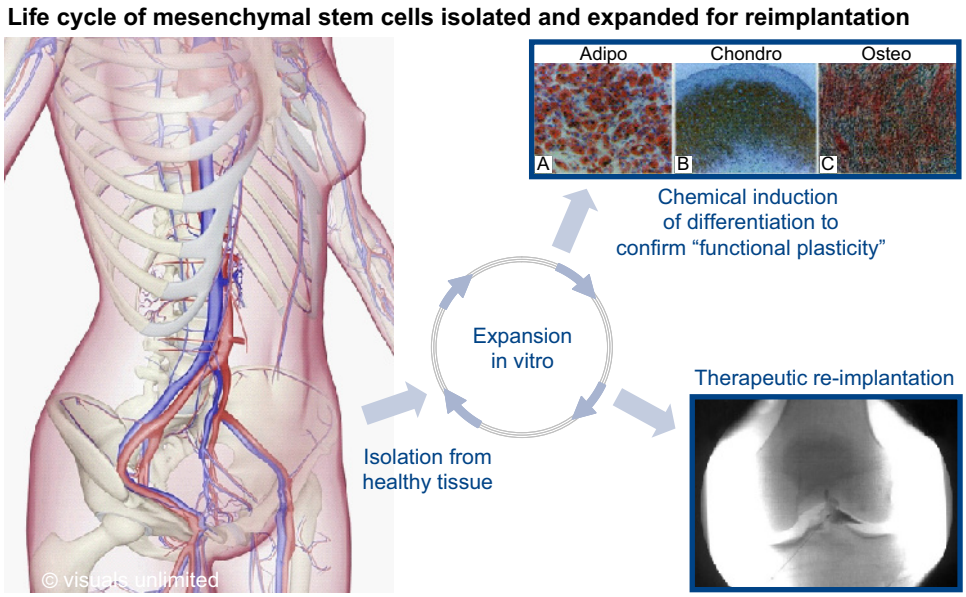

Figure 1-4: Mesenchymal stem cell (MSC)-enabled therapeutic tissue regeneration is exemplified by a process in which bone marrow is removed from the iliac crest of the hip, then processed and purified to separate the (adherent and rapidly proliferating) MSCs. The multipotent capability, or “functional plasticity,” of these cells may be confirmed by chemically inducing differentiation toward one of several terminal lineages (e.g., adipogenic, chondrogenic, osteogenic). MSCs are expanded—cultured—over multiple passages *in vitro* to increase population size, then re-implanted in an area where new mesenchymal tissue repair is desired, such as an area of damaged cartilage in the knee [57]. (Images from [54, 57].)

vessels, where the cells subsequently sink to the bottom and attach over several hours.

Recent work has advanced our knowledge considerably about the influence of external mechanical cues on population phenotype [22, 60]. MSCs generally require mechanical anchorage to survive and proliferate; however, long-term culturing even on stiff substrata leads inevitably to decreased growth rate and eventual senescence, attendant with decreased differentiation propensity and telomere length [58, 61–63] (Fig. 1-1(c)). Thus, expansion involves a trade-off where more cells are made available at the cost of possible reduction of overall differentiation capability. The optimal approach for MSC expansion is still unknown.

In summary, MSCs undergo morphological and structural changes during the process of *in vitro* expansion for therapeutic purposes. These changes and their relationship with stem cell proliferation and differentiation is a third unique attribute of cells, and exploration of this process is the third and final major focus of this thesis.

1.1.2 Why examine the attached and suspended states?

It should be clear from the last section that cultured adherent cells are frequently exposed to the disparate mechanical environments of attachment and suspension. The dichotomy of these two mechanical settings is a central theme of this thesis, which relies on the assumption that it is appropriate and worthwhile to compare and contrast cell chemomechanics in the attached and the recently suspended states. But how can this claim be justified, given that both attachment to a near-rigid substratum (adjacent stiffness $E \to \infty$) and complete suspension (surrounding stiffness $E \approx 0$) are arguably unphysiological environments for adherent cells and for MSCs in particular?

The attached vs. suspended testing strategy is selected for several reasons. First,the attached and suspended states represent extremes that bound *in vivo* mechanical environments. For cells in general, changes in the surrounding mechanical environment

modulate a phenotypic continuum. For example, adhesion site size, stress fiber prominence, cell stiffness, and proliferation rate all increase with ECM stiffness [17, 64, 65]. Because the mechanical nature of the MSC *in vivo* niche is still underdefined and could vary considerably [66], it is useful to define the limits of possible cell behavior.

Second, cell suspension eliminates stress fibers without pharmacological intervention. A longstanding strategy in studying the cell as a material is to disable various components, often pharmacologically, and look at the effects. For example, 10 μM cytochalasin is known to inhibit actin polymerization and disrupt stress fibers, and this chemical has therefore been applied to elucidate the importance of stress fibers [33, 67]. In contrast, mechanical probing of the fully suspended cell, in the absence of cell-substratum contact, offers an alternative technique to decouple the effects of stress fibers without exposing the cells to additional chemicals. A common finding under both pharmacological intervention and cell suspension is less likely to be artifactual, and it is therefore appealing to use the attached-to-suspended transition specifically to study the role of actin stress fibers in cell structure and mechanics.

Third, the attached-to-suspended transition is an important event in therapeutic implantation of stem cells that have been expanded *in vitro*. In the process of MSC expansion, culture on near-rigid TCPS is the conventional approach and may in fact be necessary for rapid proliferation and minimal turnaround between explantation and re-implantation. In contrast, MSCs are necessarily suspended during passaging and are also often re-implanted in the suspended state, from which they are expected to extravasate from the patient's bloodstream into tissue. Additionally, this suspended state offers the possibility of high-speed cell sorting by mechanical properties in a manner analogous to fluorescence cell sorting, FACS, of cells based on molecular properties. An understanding of the mechanics of this transition is therefore highly relevant both for understanding and for optimizing MSC therapy.

In summary, the opposite settings of attachment to near-rigid substrata vs. complete suspension, while arguably both artifacts of current *in vitro* culture practice, are still eminently worthy of study. The remainder of this introductory chapter identifies open questions in the field that need attention to improve our understanding of cell chemomechanics; it also summarizes the benefits that new studies will bring.

1.2 Motivation for new studies

Let us now consider key questions that arise when considering cell mechanics in the attached and suspended states. For each of the unique cell attributes discussed in §1.1.1, questions emerge regarding each of the attached and suspended states (Table 1.1).

Table 1.1: **Thesis framework: leading questions that arise when describing the cell as a chemomechanical material.**

Unique cell attribute(s)	Attached state	Suspended state
Contractility, mechanosensing	**How deep can cells feel?**	**What part does contractility play in the recently suspended state?**
Compliant, heterogeneous cytoskeletal network	**What are the origins and extent of cell-to-cell mechanical variation?**	**How does a suspended cell deform?**
Metabolism, proliferation, differentiation	**Do stem cells have useful mechanical markers?**	**Can we leverage putative mechanical markers for high-throughput suspended stem cell sorting?**

1.2.1 How deep can cells feel?

Cell behavior studies are frequently performed on various two-dimensional (2-D) substrata to explore mechanosensitivity, quantify cell-induced traction,[8] or mimic *in vivo* ECM. Often, the substratum consists of a compliant coating attached to a stiffer support for structural stability [17, 20, 68]. Layers of more than 1 μm in thickness may be unavailable based on processing limitations (e.g., layer-by-layer deposition of polyelectrolyte multilayers [69, 70]) or may be undesirable because of a need for optical transparency (e.g., cell traction studies that employ the motion of substratum-embedded beads or surface features for displaying cell-exerted stresses [15, 71–73]).

Given these limitations, what is the minimum coating thickness to avoid the scenario in which the cells can mechanically sense, or "feel," the underlying base? Confusingly, a range of estimates exists in the literature concerning the minimum suitable coating thickness in 2-D cell culture experiments (Table 1.2). Reported estimates of this parameter—let us call it the "critical thickness"—have in fact varied by one to two orders of magnitude both theoretically and experimentally. Thus, the question posed above—essentially, **How deep can cells feel?**—remains open.

Table 1.2: Definitions of critical thickness in the literature, as identified from other groups' proposals of associated length scales. **Estimates of the depth that cells "feel" differ by up to two orders of magnitude; why has it been difficult to narrow this range?**

Length scale to be compared	Value	Group
Magnitude of substratum surface displacements	1 μm	Dembo and Wang (1999) [71]
Lateral dimensions of the cell	50–100 μm	Butler et al. (2002) [74]
Adhesion site size or adhesion cluster size	several μm	Schwartz et al. (2002) [73]
Cell height	<5 μm	Engler et al. (2004) [75]
Observation distance from adhesion site	1–100 μm	Merkel et al. (2004) [68]
Depth of 0.1% strain	<3 μm	Oommen et al. (2006) [2, 76]

There are several reasons to conduct a new study to address this question. First, it is desirable to predict whether the mechanical properties of a film and a base are being conflated via cell sensing. Second, a more quantitative, predictive study would let us test theories about the mechanism of mechanosensation, which is poorly understood. Third, such a study could be applied to *in vivo* environments; even a study limited to 2-D configurations could be applied to planar tissue environments such as the basement membrane of blood vessels [77]. These possibilities justify a new look at the problem.

1.2.2 What part does contractility play in the recently suspended state?

In the process of cell expansion, cells are routinely detached from the surface to be passaged to more or larger culture vessels. Additionally, when MSCs are re-implanted for therapeutic purposes, the first step is to detach them into the suspended state via chemical treatment such as trypsin/EDTA. When adhesive bonds are cleaved, stress fibers are disassembled following loss of mechanosensory indication from the adhesion sites. Cortical contraction and surface energy minimization then pull the cell into a spherical morphology that is easily dislodged from the substratum.

[8] **Traction** herein means any surface stress, tangential or perpendicular, applied to the substratum.

This transition represents an extraordinary change to cell mechanics; after all, stress fibers disappear and the cortex is totally reshaped as cell morphology changes from spread to spherical. During this process, **What part does contractility play in the recently suspended state?** There are clear benefits studying the dynamics of cell deformability in this state. The first is specific to MSCs, the focus cell of this thesis. It is difficult to mechanically probe the suspended state without arousing cell response, but mechanics are expected to influence flow and extravasation of injected MSCs. The expected benefit here is better prediction of how MSCs behave during the implantation process.

A second benefit is more general. The recently suspended state was characterized morphologically several decades ago [78–80] but has remained largely uninvestigated since then despite featuring fascinating cellular mechanisms such as non-apoptotic dynamic blebbing (cortex-membrane detachment and subsequent membrane herniation [81, 82]). Phase contrast photographs and scanning electron micrographs show that excess plasma membrane exists after suspension, as indicated by topographic features such as blebs and microvilli, and that this excess membrane is ultimately resorbed into the cell. However, the mechanical transition has never been measured, because any physical contact from a probe would activate cell attachment mechanisms, prompt the re-formation of stress fibers, and thus confuse interpretation of the response. It would be useful to find a way around this limitation by demonstrating a cell mechanics probe that avoids such confusion.

1.2.3 How does a suspended cell deform?

Let us now consider existing models of suspended cell deformability with the aim of developing a thorough understanding of cell mechanics. As reviewed §1.1.1, it is well established that attached cells exhibit power-law rheology (PLR). Described in this section are the data that have justified this conclusion and the uncertainties that remain.

PLR implies that a broad spectrum of relaxation times exist, or equivalently that no single characteristic time scale characterizes the material. (Consider, in contrast, simple lumped-component viscoelastic models containing several springs and dashpots that combine to form assemblies with characteristic time scales. For example, the Kelvin-Voigt model contains an elastic spring with stiffness E in parallel with a fluid dashpot with viscosity η; the resulting creep response is $J(t) \propto (1 - e^{-t/\tau})$ where the time constant of the assembly is $\tau = \eta/E$.) Multiple groups have reported a good fit of $G'(\omega)$, $G''(\omega) \propto \omega^a$ or $J(t) \propto t^a$ over multiple decades of frequency or time, respectively, which precludes a single characteristic time scale [29, 48]. Fabry et al. concluded that the best model for cells at physiological time scales is the structural damping model, which implies power-law rheology and a physical picture in which elastic and viscous components cannot be decoupled into a finite number of springs and dashpots. They further warned that power-law and lumped-component responses are easily confused when only one or two frequency or time decades are examined [48].

It is still possible to test model fitting when only one or two decades are available, however, by comparing fitting metrics such as adjusted r^2 or Akaike Information Criterion, for example, or by comparing plots of residuals—unexplained deviations from the fit. Another approach is to interrogate the cell in both the time and frequency domains. Most studies using one or more of these approaches have concluded that attached cells exhibit PLR, explicitly rejecting lumped-component models (Table 1.3).

However, the deformation behavior of suspended cells is not as clear. A previous investigation by Wottawah et al. rejected the PLR model for fully suspended cells in favor of a spring-dashpot model with a characteristic relaxation time [38, 86], and this conclusion has been taken as evidence for a fundamental mechanical difference between adherent cells in the attached and suspended states [41, 88]. Subsequently, it has been implied that stress fibers are necessary to create the cytoskeletal conditions

Table 1.3: Comparisons of power-law ($\varepsilon(t) = At^a$) vs. lumped-component viscoelasticity (one or two time scales) on (A)ttached/adhered and fully (S)uspended cells in the literature. Most studies of attached cells concluded that they exhibited power-law rheology (equivalently, they exhibited no characteristic relaxation time at physiological timescales). However, a study of fully suspended cells concluded that they did exhibit a single relaxation time (albeit by testing one or several cells only). **Are suspended cells indeed different in terms of general rheological behavior, displaying just one or several characteristic time scales?**

Tool and data set size	Regime	State	Better fit	Reference
Magnetic bead cytometry ($n = 903$)	Creep	A	Power law ($a = 0.20$)	Lenormand et al. (2004) [42]
Micropipette aspiration ($n = 81$)	Creep	A	Power law ($a = 0.30$)	Zhou et al. (2010) [83]
Atomic force microscopy ($n = 120$)	Relaxation	A	Power law ($a = 0.10$)	Hemmer et al. (2009) [45]
Atomic force microscopy ($n = 24$)	Frequency	A	Power law ($a = 0.18$)	Roca-Cusachs et al. (2006) [84]
Magnetic bead cytometry ($n = 25$)	Creep	A	3 components ($\tau = 7.2\,\mathrm{s}$)	McDowell et al. (2007) [85]
Optical stretching ($n \sim O(1)$)	Creep	S	3 components ($\tau = 2.5\,\mathrm{s}$)	Wottawah et al. (2005) [86]
Electrodeformation ($n = 10$)	Creep	S	Equally good ($a = 0.36$, $\tau = 6.2\,\mathrm{s}$)	MacQueen et al. (2010) [87]

that produce PLR [53]. However, Wottawah et al.'s sample size was small—one or several cells—and the better fit of the lumped-component model may have been caused by chance.

Therefore, the question **How does a suspended cell deform?** can be considered still open. With stress fibers absent, does a broad spectrum of relaxation times still exist, or is cortical deformation characterized by just one or two characteristic time scales? To be sure, both lumped-component and power-law models are abstractions, and one might ask whether a better fit to one or the other has any relevance. It is argued here that a well-reasoned conclusion to the question is extremely relevant. Considerable mystery remains in the field of soft matter physics, especially the biophysics of the animate cell. The nature of the "glassy" state is considered among the most important areas of study in physics today [89], and the disordered, far-from-equilibrium structure of the cell exemplifies this state [90]. More data are needed to compare competing models—for example, the soft glassy rheology [49, 91, 92] and glassy wormlike chain [93, 94] models—that predict PLR. An experimental study that eliminates stress fibers, a key cytoskeletal component, could provide biophysical insight into the mechanics of cells and other soft and compliant states of matter.

1.2.4 What are the origins and extent of cell-to-cell mechanical variation?

It is a common finding that cell stiffness exhibits a pronounced right-skewed distribution (Fig. 1-3(c)) that is typically fit to a log-normal model and characterized by the geometric standard deviation. In contrast to the existence of multiple models of PLR, the observed log-normal distribution has remained largely uninvestigated and especially lacks any predictive explanation.

Until recently, in fact, this variation was assumed to be an artifact of the measurement process. When cell stiffness had only been characterized by magnetic bead cytometry or phagocytosed tracers, the large variation was attributed to variations in bead-cell contact area [95] or to variations in tracer-network contact points [96], re-

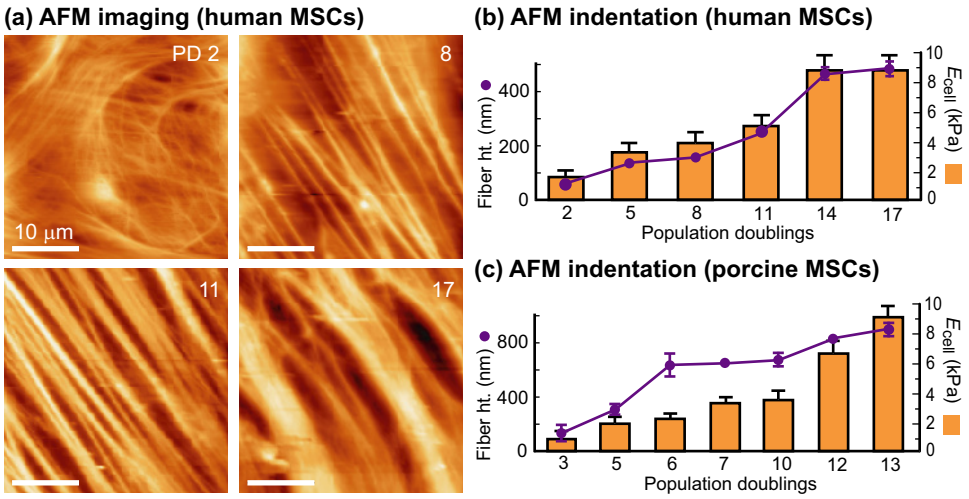

Figure 1-5: **Attached MSC cytoskeletal structure and mechanics vary over multiple PDs *in vitro*.** (a) Images of MSC topography acquired by atomic force microscopy (AFM) show cytoskeletal coarsening with increasing culture time *in vitro* (PD = population doubling number). (b,c) For both human and porcine MSCs, cytoskeletal fiber height (representing fiber radius) and cell effective Young's modulus E_{cell} as measured from topography and by AFM-enabled indentation, respectively, are well correlated and increase significantly with passaging. (All data shown as mean ± standard error.) Adapted from [4]; measurements performed by D. Nikova and K. J. Van Vliet.

spectively. Further studies with different tools and at different length scales identified the same variation [50], however, and current consensus is that cell stiffness is intrinsically log-normally distributed.

What factors could cause a population of cells—all progeny of a single ancestor—to exhibit mechanical heterogeneity? As we develop a better understanding of the cell as a mechanical material, natural questions are whether power-law rheology implies a log-normal distribution (and if so, under what necessary postulates), and whether fluctuations in cytoskeletal networks can be linked to mechanical variation among cells. In summary, we ask **What are the origins and extent of cell-to-cell mechanical variation?** A well-supported resolution to these questions would illuminate the influence of stochastic events on measurements of cell deformability within populations.

1.2.5 How should we interpret mechanical markers of adult stem cells, and can we leverage these markers?

Characteristic mechanical and structural markers of attached MSCs exist that change during *in vitro* expansion on TCPS (Fig. 1-5) [4]. Multiple mechanical and structural alterations occur over 17 population doublings (PDs), including coarsening of the cytoskeleton, increased stress fiber radius, and increased stiffness. Atomic force microscopy (AFM) images of living MSCs indicate that cytoskeletal actin fibers, initially concentrated around the nucleus, coarsen via increased bundling over 17 PDs *in vitro*, and appreciable increases in fiber radius are also readily apparent (Fig. 1-5(a)). A five-fold increase in local cytoskeletal stiffness is correlated with increased volume fraction of bundled cytoskeletal actin, as nominal fiber radius increases from 100 to 500 nm; the same trends have been observed in porcine MSCs expanded for 13 PDs on TCPS (Fig. 1-5(b,c)). These cells thus exhibit mechanical markers correlated with extended passaging and with loss of differentiation propensity [4]. **How should we interpret these mechanical markers?**

For those interested in MSC therapy, the natural question in response to seeing Fig. 1-5 is **Can we leverage these markers for useful purposes?** Such mechanical differences could be used in a high-throughput mechanical sorting device to separate

certain groups of suspended MSCs into groups of higher and lower therapeutic potential. The first step in realizing this goal is to characterize these differences in the suspended state.

This work is necessary because it is still mysterious how MSCs behave *in vivo*. In fact, it is unknown whether MSCs actually form new connective tissue by differentiation and proliferation, or whether MSCs merely secrete signaling agents to encourage nearby cell growth. It is also unknown whether MSCs therapy can be improved by delivering only a subset of MSCs. Insight in these areas would improve our ability to harness MSCs for therapeutic purposes and ultimately to enable regeneration of connective tissue.

1.3 Thesis strategy and organization

Now established are the six leading questions that motivate the research described in the remainder of this thesis. The overarching objective is to (1) advance hypotheses designed to answer these six questions; (2) develop and apply analytical, simulation, and experimental methods as appropriate to test these hypotheses; and (3) summarize and interpret the results and their implications. To that end, four cell (chemo)mechanics studies have been performed on cell configurations from the attached to the suspended state. Each study includes novel approaches to advance our knowledge of cell chemomechanics, and each has generated answers to one or more of the leading questions discussed above. These studies are described in four chapters, organized as follows, with an additional chapter discussing the conclusions and implications of this work:

- **Chapter 2 ("Active contractility and mechanosensing")** addresses the adherent cell in the attached state. The question **How deep can cells feel?** is treated by (1) extending elasticity theory to calculate the surface deformation of finite areas of traction applied to a relatively compliant film atop a rigid base, and by (2) extending experimental study of cell response to compliant substrata of >2 thickness values. These combined analytical and experimental approaches enable a reconciliation of wide-ranging reports of the "critical thickness" needed by a natural or synthetic ECM film to avoid substantial mechanical influence from an underlying rigid base.
- **Chapter 3 ("Compliant cytoskeletal networks I")** targets the deformation of suspended cells. Optical stretching, a photonic and fully noncontact technique, is used to probe thousands of recently suspended cells to resolve discrepancies in (1) reports of the existence of weak power-law rheology (PLR) in suspended cells and (2) interpretations of the role of ATP hydrolysis in enabling PLR in all cells. Compared to previous studies, a much larger data set (>2,000 individually measured cells) acquired in the present study is used to resolve the question **How does a suspended cell deform?** in a statistically rigorous way.
- **Chapter 4 ("Compliant cytoskeletal networks II")** addresses the distribution of stiffness values in attached and suspended cells. Primary and immortalized cell lines are exposed to a collection of chemomechanical cues to elucidate the origins of mechanical heterogeneity in cells. It is proposed that intrinsic, Gaussian-distributed variation in cytoskeletal "agitation" partially answers the question **What is the origin of cell-to-cell mechanical variation?**, as it is shown that an analytical framework based on this postulate explains multiple empirical findings in a quantitative way. Mechanical heterogeneity in animate and inanimate materials is compared, and two case studies on the implications of intrinsic cellular mechanical variation are presented, to place this chapter's experimental findings in context and to inform further study.

- **Chapter 5 (“Metabolism, proliferation, and differentiation”)** targets the mechanical changes in attached and suspended mesenchymal cells during multiple population doublings and following chemically induced differentiation. It is demonstrated that the structural and mechanical changes of attached MSCs during *in vitro* culture are concomitant with a decrease in osteodifferentiation potential, and these findings are interpreted with the aim of answering the question **How should we interpret mechanical markers of adult stem cells?** Further, suspended MSCs from multiple passages are characterized to pursue an answer to the question **Can we leverage putative mechanical markers in the suspended state?** and specifically to determine whether a high-throughput sorting technique could be used to separate useful subpopulations. This chapter also focuses on the transition from the attached to the suspended state. A key structural transformation that occurs during this process is quantified and interpreted to determine **What part does contractility play in the recently suspended state?**
- **Chapter 6 (“Conclusions and implications”)** summarizes the findings. Key contributions of the thesis are reviewed to justify the claim that we can now better investigate, understand, and predict cell mechanics in both the attached and suspended states. Finally, our improved understanding the cell as a chemomechanical material is discussed, and the thesis is concluded with a look back at the state of this understanding in 1950, as described by pioneers in the field.

Chapter 2

Active contractility and mechanosensing

Synopsis

Equations of elasticity theory are extended and used to predict how much the presence of an underlying rigid base will affect cell-induced deformation at the surface of a compliant coating. The coating thickness that attenuates the surface deformation by 10% (compared to the case of a very thick coating) serves as a useful "critical thickness" at which an adherent cell barely feels the rigid base. The predicted critical thickness is found to be several times the magnitude of (O(1 μm)) individual adhesion site radii, assuming that the deformation from neighboring adhesion sites is small. This estimate is independent of coating stiffness. Experimental results presented here confirm that cell morphology—specifically spread-cell area, a reporter of cell mechanosensation—changes abruptly as coating thickness is decreased below 10 μm. New expressions allow the effective stiffness sensed by an attached cell to be predicted from known values of coating stiffness and thickness, given a certain mechanosensory mechanism. Widely disparate reports of critical thickness in the literature are resolved by showing that (1) different definitions of critical thickness exist depending on what type of deformation is being attenuated and to what degree, (2) these definitions correspond to different experiment types, and (3) the relevant experiments generally agree with predictions of the present framework. A case study is presented to demonstrate application of the tools developed here.

2.1 Study background, hypothesis, and design

The first study in this thesis addresses our limited understanding of how the cell obtains mechanical information from its environment. To review and expand on the relevant material in §1.2.1: cells are actively contractile, pulling at the adjacent extracellular matrix (ECM) at adhesion sites and reacting to the resulting deformation [14, 18]. Each site consists of a dense aggregate of transmembrane integrin receptors linked to the termini of parallel actin filaments through a multimolecular collection of adaptor proteins (Fig. 1-1(a)). Scenarios often arise, especially through *in vitro* cell culture, in which the cell is attached to and probes a compliant coating, or film, atop a relatively rigid base [17, 65, 71, 102–105]. However, a thin compliant coating attached to a comparably stiff base may present a very different mechanical environment to the cell than the bulk properties of the coating material would suggest. Can the cell detect the base? If so, how much thicker must the coating be to remove this mechanical conflation?

Table 2.1: **Reports of how deep cells can feel, referred to herein as a "critical thickness," the characteristic or minimum thickness of a compliant coating to prevent cells from detecting a rigid underlying base.** Even though a spectrum of techniques—scaling arguments, finite element numerical simulations, and live cell experiments—have been applied, the estimated value and interpretation are still in dispute.

Type of evidence	Critical thickness	Group	Notes
Scaling	1 μm	Dembo and Wang (1999) [71]	Related to maximum marker displacement in cell traction microscopy (CTM).
Scaling	O(1 μm)	Balaban and Schwartz et al. (2001) [15]	Maximum marker displacement in CTM.
Scaling	several μm	Schwartz and Balaban et al. (2002) [73]	Thickness should be greater than both maximum marker displacement and adhesion site size (or size of adhesion site cluster).
Scaling	50 μm to 100 μm	Butler et al. (2002) [74]	Size of cell, assuming traction occurs around periphery.
Numerical	>70 μm	Yang et al. (2006) [97]	For a 70-μm-thick coating, predicted displacement was attenuated 90% at 70 μm away from adhesion site (though absolute error was only O(10 nm)).
Numerical	O(1 μm)	Oommen and Van Vliet (2006) [2, 76]	Depth of 0.1% principal strain magnitude.
Experimental	<5 μm	Engler and Discher et al. (2004) [75]	Spread-cell projected areas on 5-μm- and 70-μm-thick polyacrylamide gels were identical within error.
Experimental	O(1 μm)	Engler and Discher et al. (2006) [22]	Cell spreading differed on 0.5-μm- and 70-μm-thick polyacrylamide gels. "MSCs feel into matrices on the length scales of their adhesions and not much deeper."
Experimental	26 μm	del Álamo et al. (2007) [98]	Based on peak of spectral energy density of cell-induced displacements on gelatin coatings.
Experimental*	3.4 μm	Buxboim and Discher et al. (2010) [99]	Function fit to spread-cell areas of mesenchymal stem cells atop polyacrylamide.
Experimental*	50 μm to 100 μm	Lin and Butler et al. (2010) [100]	Cell spreading increased with decreasing thickness of polyacrylamide gels (coatings were >50 μm thick).
Experimental*	>130 μm	Leong et al. (2010) [101]	Mesenchymal stem cell spreading differed on 130-μm- and 1440-μm-thick collagen gels.
Experimental and analytical	1.6a or 3.4a	**This work**	For mechanosensory mechanisms that detect attenuation of adhesion site distortion or displacement, respectively, where a is the adhesion site radius, assuming that the influence of neighboring sites is small. (See §2.3.4 for adapting the model if this assumption does not hold.)

*Cites the study described in this chapter, which was published in part in 2008 [1].

A considerable discrepancy exists in how these questions have been answered in the literature. Previously reported values of the minimum sufficient thickness, referred to in this thesis as the critical thickness h_{crit}, are listed in Table 2.1. Reported values have varied by one to two orders of magnitude both theoretically and experimentally, and thus it is worth reviewing how other researchers generated such disparate estimates.

Let us begin with scaling arguments, which have been used to support critical thickness estimates from several μm to tens of μm. In the context of avoiding interference from a rigid base when performing cell traction microscopy (CTM), Dembo and Wang [71] and Balaban et al. [15] connected the minimum suitable thickness to the magnitude of surface displacements, arguing that the minimum coating thickness should at least be large compared to the (O(1 μm)) displacements of substratum-embedded beads. Schwartz et al. added the additional condition that the coating should be larger than the size of adhesion sites, or possibly adhesion site clusters if the sites' resolved force vectors point in similar directions [73]. This condition would suggest that $h_{\text{crit}} \approx 1\,\mu\text{m}$ to 10 μm. In contrast, Butler et al. estimated the minimum suitable thickness to be similar to the cell size (i.e., tens of μm), idealizing the cell as a circular region and adhesion sites as points of centripetal force around the region's periphery [74].

Finite element simulation serves as another tool available to groups investigating cell-induced substratum deformation. In agreement with Butler et al.'s conclusion, Yang et al. reported numerical results that suggest that a 70-μm-thick coating may not be sufficiently thick to prevent a fibroblast of 50 μm length from being affected by an underlying rigid base [97]. The reasoning was that the presence of the base almost completely attenuated surface deformation at this distance. Oommen et al. also simulated substratum displacements, but pursued an alternate approach by assigning the critical thickness to the depth of an arbitrary principal strain (0.1%) to examine how this depth changed with substratum stiffness [2, 76]. This depth was O(1μm), many times smaller than Yang et al.'s value of 70 μm or more. Much the same as scaling arguments, therefore, numerical studies have thus far produced equivocal results.

Finally, even experimental reports of critical thickness have varied. For example, del Álamo et al. concluded from spectral energy density data that critical thickness is dependent on cell size and is in the tens of μm [98]. However, Engler et al. found no detectable difference in smooth muscle cell morphology on 5-μm- and 70-μm-thick polyacrylamide gel coatings on glass and concluded that cells cannot feel as deep as 5 μm [75]. A subsequent study of mesenchymal stem cells on 500-nm- and 70-μm-thick coatings led them to conclude that cells do feel deeper than 500 nm, however, as the average spread-cell area (which is strongly modulated by substratum effective stiffness) was different in these two cases [22]. They first compared the sensing depth to cell height [75], but later compared it to adhesion site size [22]. A follow-up study by the same group yielded a specific characteristic depth of $h_{\text{crit}} = 3.4\,\mu\text{m}$ [99]. In contrast, two other studies recommended much larger values: an experimental follow-up to Butler et al.'s earlier report was confirmatory in that it found that coating thickness influenced cell behavior even at thicknesses >50 μm [100], and Leong et al. presented evidence of cell behavior on collagen gels that indicated that $h_{\text{crit}} > 130\,\mu\text{m}$ [101], although this group attributed their large value to the nonlinear elastic nature of collagen gels compared to polyacrylamide's linear elastic response for typical cell-induced forces.

As a result of these differing estimates of h_{crit}, and considering that a resolution would benefit both synthetic ECM design principles and a fuller understanding of cell mechanosensitivity, the question remains open and worthy of systematic study. This study's hypothesis is:

A well-reasoned analytical[1] study of idealized focal adhesions, comple-

[1] **Analytical** herein means (1) expressed in terms of the problem's variables (cf. finite element simulations that output a numerical value or set of values) and (2) giving an exact answer within the scope of its domain

mented by an experimental study of cell response to substrata of multiple thicknesses, will provide more general and rigorous answers to the question **How deep do cells feel?** than scaling arguments and will provide more insight than finite element simulation of specific systems.

An analytical approach is pursued here because scaling arguments and finite element solutions may not be capable of providing a complete understanding of mechanosensitivity. The limitation of scaling arguments is that multiple length scales exist in the problem—cell length, adhesion site size, and adhesion cluster size, among others—and each of these has been associated with the critical thickness [22, 73, 74]. The resulting ambiguity makes it doubtful that these arguments alone will resolve the discrepancy. Finite element simulations have also been pursued to complement these scaling arguments, but these results are typically applicable to one particular geometry and boundary condition only and thus provide less insight into the questions above for the general case. Simulations of strain vs. depth [2, 76], for example, are difficult to apply to the present problem, as cells do not respond to strain below the surface; moreover, it is not clear how an arbitrary strain threshold should be chosen.

A joint analytical and experimental study offers a chance to reconcile conflicting reports found in the literature. The analytical strategy is to calculate directly, via elasticity theory, adhesion site deformation as a function of the site's own traction, the traction of neighboring sites, and the coating thickness. The driving insight for this approach is that the cell can sense only surface deformation; therefore, the focus is on deformation *attenuation* from an underlying base. To illustrate this idea, consider two substratum arrangements (Fig. 2-1): (a) a semi-infinite region (sometimes called a half space), and (b) a compliant coating bonded to a rigid underlying base. Observe that an area of cell-induced traction—arising from actomyosin contraction transmitted through the adhesion site—results in deformation at and around the traction area. If the surface deformation matches between these two cases, then the cell cannot sense the rigid base by any mechanosensitive means. If, however, the surface deformation is attenuated by the constraint of the base, the cell will sense a higher effective stiffness. The goal of the present study's analytical side is to quantify this relationship in the form of predictive equations.

It is always desirable to validate quantitative predictions with experimental results. It is especially favorable to work with a variety of coating thicknesses (i.e., more than one or two) to elucidate trends in a relationship that has been interpreted in such different ways in previous studies. The strategy for the experimental side of this study is to use controlled-thickness polyacrylamide gels as the substrata for adherent mechanosensing cells. This system is schematized in Fig. 2-2. Consider a polyacrylamide hydrogel material that is fabricated into multiple coatings with identical stiffness values but different thickness values. Cells react prominently to the larger effective stiffness detected on the thinner coatings by increasing their spread-cell projected area, which can be quantified by phase contrast microscopy and subsequent image analysis. Cell morphology is thus used a surrogate for the effective stiffness sensed by attached cells.

Existing methods

The methods used in this study build on the following standard techniques and assumptions:

Deformation solutions in elasticity theory for point loads on single- and multilayer semi-infinite regions. The starting point is the so-called Boussinesq solution (sometimes called Cerruti's solution in the case of a tangential load) [106–109], which relates the deformation of a half space to a surface point load. For example, a tangential

(cf. scaling arguments that provide a proportional relationship only).

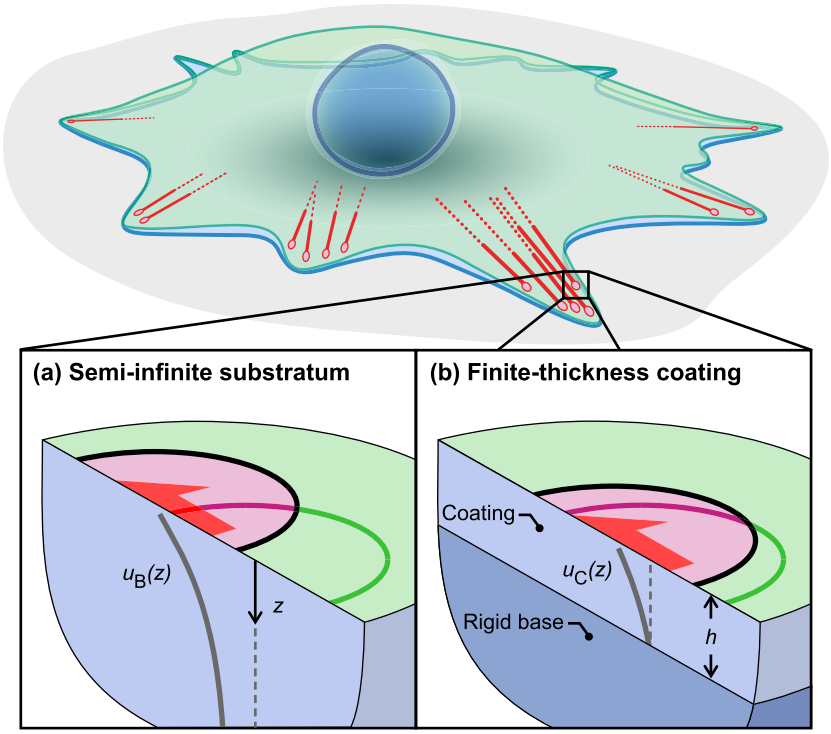

Figure 2-1: **Schematic of an adherent cell attached to (a) a semi-infinite substratum and (b) a coating of thickness h of the same material grafted to a rigid base.** Adherent cells are contractile, exerting surface traction at adhesion sites, here idealized as circular areas. The circular surface outlines indicate the undeformed and deformed position and boundary of the adhesion sites. Traction-induced deformation is attenuated by the presence of the rigid base; the displacements u_B and u_C, respectively, correspond to the *B*oussinesq, or semi-infinite substratum, solution and the finite *C*oating solution, as discussed in the text. An understanding of this attenuation, which corresponds to an increase in effective stiffness sensed by the cell, could reconcile conflicting theories of cell-substratum interaction.

x-direction point force F at the origin is coupled to a surface displacement u in the same direction by

$$u = \frac{F}{2\pi\mu}\left(\frac{2-\nu}{2r} + \frac{\nu(x^2-y^2)}{2r^3}\right), \tag{2.1}$$

where ν is Poisson's ratio, μ is the shear modulus, and $r = \sqrt{x^2+y^2}$. Thus, the displacement varies linearly with force and inversely with stiffness; note also that this equation diverges when $x = y = 0$, so the displacement at the origin is not available. (A more general coupling between displacement and force is used as a starting point for extending this theory in App. A.1.)

Multilayer solutions of surface traction have been developed previously that accommodate bonded layers with different values of E and ν [110,111]. The most convenient approach may be Yue's solution [110], which relies on integral transformation into the Fourier domain for solution, and which was applied to point adhesion sites by Merkel et al. [68]. All existing multi-layer solutions also diverge at the point of load application, however, and therefore require adaptation to apply to finite-size adhesion sites.

Idealization of adhesion sites as circular areas of constant tangential traction. The frequent idealization of adhesion sites as approximately circular [73, 112, 113] is based on the visualization of these sites via immunofluorescent staining of actin-binding adaptor proteins. The resulting micrographs show punctate features on very compliant materials ($E < 5$ kPa) [17,105,114], transitioning to more irregular or elon-

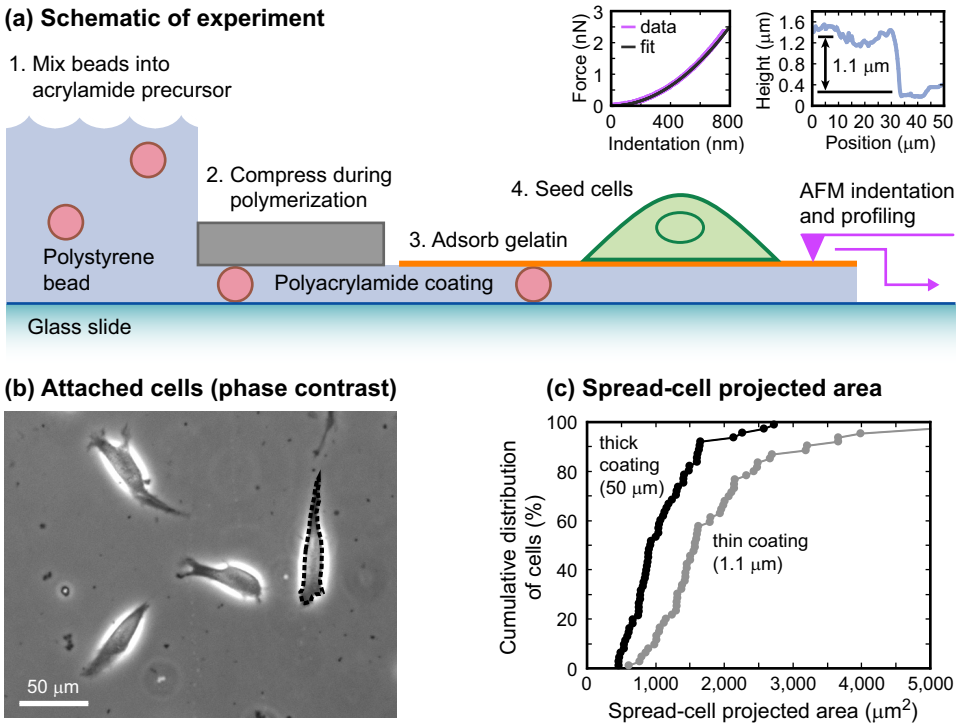

Figure 2-2: **The critical thickness for a compliant coating to resemble a semi-infinite region can be identified by seeding cells on coatings of different thicknesses and quantifying morphological presentation.** (a) Compliant polyacrylamide gels with calibrated thickness are fabricated by mixing acrylamide precursor solution with polystyrene spacer beads and compressing during curing to provide thickness control. Fibroblasts are then seeded atop an adsorbed gelatin film of negligible thickness. The projected spread-cell area of the fibroblasts serves as a reporter for effective substratum stiffness. Insets, atomic force microscopy (AFM) characterizes gel coating stiffness and thickness by indentation and surface profiling, respectively. (b) Cell population morphology is characterized by phase contrast microscopy and image analysis; the projected spread area is determined by tracing single cells via software (shown on the rightmost cell). (c) The cumulative distribution of projected area values for relatively thick and thin coatings displays an increase in spread-cell area resulting from the increased effective stiffness "felt" by cells on thinner coatings.

gated features on stiffer substrata (Fig. 1-2).

Many discrete ECM ligand-integrin receptor pairs within the adhesion site transmit a mechanical load that is often assumed to be tangential and uniform [74, 112]. While the tangential traction within an adhesion site may not actually be constant, data are not yet available to suggest a more accurate traction distribution. Additionally, it should be noted that some component of surface load is known to act perpendicularly to the substratum [115]; thus, the assumption of uniform and fully tangential traction is also a simplification, though one with precedent.

Cell culture on thin polyacrylamide gels. Polyacrylamide (PAAm) is frequently used as a compliant, non-toxic substratum for cell culture [17, 71, 102, 103], with several appealing qualities. For example, PAAm can be approximated as incompressible ($\nu \approx 0.5$) [116] and linear elastic for cell-induced displacements not exceeding 1 μm to 2 μm [105, 117]. PAAm stiffness characterization by atomic force microscope (AFM) indentation is well established [20, 65, 75, 114]. PAAm can be assumed to act as an isotropic continuum because the characteristic length scale of material inhomogeneity is small compared to the adhesion site radius; the mesh size (i.e., effective pore radius) of similar gel formulations to that used in this work is approximately 100 nm [118], approximately an order of magnitude smaller than adhesion sites [14]. Finally, cell attachment and spreading atop PAAm is readily promoted by adsorbing collagen [22, 119],

gelatin [120], or fibronectin [65, 72]; these materials present the arginine-glycine-aspartic acid (RGD) tripeptide sequence to which integrins attach.

Fibroblast projected cell area as a marker for cell mechanosensitivity. NIH 3T3 fibroblasts are an immortalized cell line that advertises the cell-sensed effective stiffness of an adjacent substratum by substantial changes in spread-cell projected area [17, 65, 104]. This behavior is typical for adherent cells; a similar response is seen in primary fibroblasts [100], adult human mesenchymal stem cells [22], kidney epithelial cells [17], endothelial cells [104], and smooth muscle cells [75, 105].

Novel methods

To complete this study, it has also been necessary to develop novel methods that augment the standard methods described above.

Integration of Green's tensor over an area of traction. Cells can only sense deformation where they are attached. However, existing solutions such as Eq. 2.1 diverge at the point of load application [68]. Therefore, it is necessary to integrate infinitesimal point forces, spread over a finite area of traction, analytically to obtain a finite deformation at the area of direct molecular mechanical transfer. (Previous investigations have performed this step numerically [73, 112, 121].) A circular area of uniform tangential traction is assumed here based on adhesion site observations and ease of calculation, but the model can be adapted to accommodate more complex geometry and stress distributions.

Identification of different deformation modes. Considering the surface deformation of the substratum as two separate modes, displacement and distortion, may help clarify models of adhesion site growth and stability. Let us look ahead slightly to gain an intuitive sense of these two modes. Shown in Fig. 2-3 is the deformation of a circular area of traction on the surface of a half space, as determined from expressions developed in the course of the present study. Clearly, the center and other parts of the circle translate, or displace, to a degree that increases with increasing traction or decreasing substratum stiffness. Besides this displacement, however, other modes of deformation also exist. For example, the leading side of the circular area contracts substantially, while the trailing side elongates.

This latter mode of contraction and elongation is relevant when considering possible information that an attached cell integrates, as the mechanisms of mechanosensitivity are not precisely known [122, 123]. While displacement has long been regarded as an important parameter in models of adhesion site behavior on elastic substrata [124,125], some researchers have conjectured that the spacing of bound integrin molecules correlates with their binding affinity and lifetime, thereby influencing adhesion site growth and stability [126–128]. Distortion of the substratum adjacent to the adhesion area may affect this spacing. Consequently, the present study investigates both modes, and further modes could also be defined and quantified by adapting the expressions presented here.

Quantitatively calculating effective stiffness by considering deformation attenuation. A consequence of finite substratum thickness is that cell traction-induced deformation may be reduced by mechanical contribution of the rigid support, anthropomorphized as the cell "feeling" a stiffer substratum than would be expected from the known elastic properties of the substratum material and consequently adopting new cell morphologies or behaviors consistent with a stiffer external environment. With this paradigm in mind, consider that an effective shear modulus μ_{eff} can be calculated by

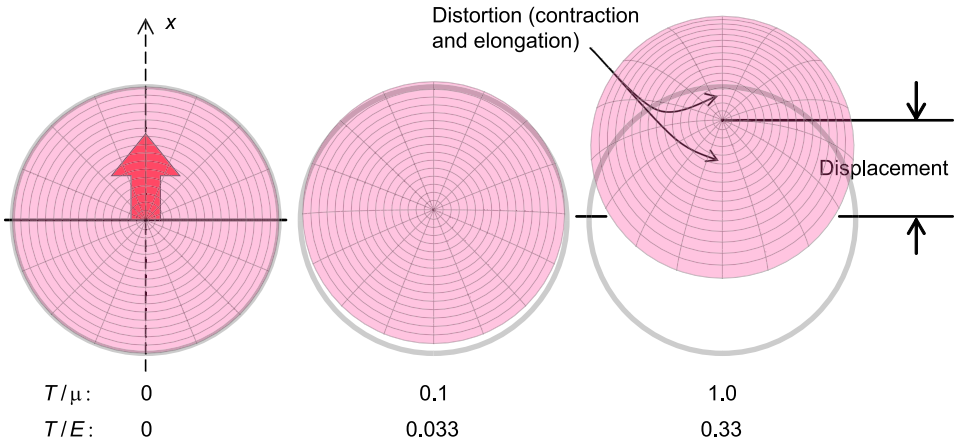

Figure 2-3: **Multiple ways exist for characterizing the deformation of substratum adhesion sites.** Displacement and distortion of a circular area of applied tangential traction are shown with increasing shear-stress-to-substratum-stiffness ratio; substratum Poisson's ratio $\nu = 0.5$. The deformation is calculated for a tangential traction T and substratum shear modulus μ or Young's elastic modulus E by using equations derived in App. A.1.

dividing the coating shear modulus μ by a (yet-to-be-calculated) thickness-dependent normalized function U_i that ranges between zero (deformation completely attenuated) and one (deformation identical to the semi-infinite case):

$$\mu_{\text{eff}} = \frac{\mu}{U_i}, \tag{2.2}$$

where μ can be replaced with $E = 2\mu(1+\nu)$ because the Poisson's ratio ν is assumed to be constant (and equal to 0.5 for compliant coatings[2]):

$$E_{\text{eff}} = \frac{E}{U_i}. \tag{2.3}$$

An effective stiffness for a given compliant coating is thus acquired by dividing its actual Young's elastic modulus E by a normalized deformation factor U_i that varies from zero to one. The calculation and manipulation of this factor is the primary analytical goal of this study.

The use of a range of thin compliant coatings to characterize mechanosensitivity. Thin PAAm coatings have previously been made with spacer beads [75], but a systematic study with a range of thickness values has not been reported.[3] Such a range, as performed in this work, allows identification of a trend of reporter parameter (here, cell area) and is therefore well suited for characterizing the continuous relationship of cell detection of—and response to—effective substratum stiffness. The observation and analysis of this relationship is the primary experimental goal of this study.

[2]The justification for assuming $\nu = 0.5$ comes from the relationship $\mu = 3K(1-2\nu)/(2+2\nu)$ (where K is the bulk modulus) and the fact that compliant solids are much more easily sheared than compressed; thus, $\mu \ll K$.

[3]Since this work was published [1], other groups have taken up the use of a range of coating thicknesses for investigating mechanosensitivity [99, 100].

2.2 Materials and methods

Integration and normalization of surface deformation

Surface deformation at a finite adhesion site was determined by analytically integrating the Green's tensor that relates deformation to a point force (App. A.1). Equations governing the deformation (displacement and distortion) of a semi-infinite region representing a bulk material or very thick coating were derived, and these values served as baselines for expressing the effects of incorporating an underlying rigid base.

The model for conversion of stiffness data to thickness data and vice versa (Eq. 2.3) was applied to the experimental data collected here and also to published experimental data reported by Engler et al. that consists of area measurements of mesenchymal stem cells on compliant polyacrylamide coatings of thickness $h = 500\,\text{nm}$ and $70\,\mu\text{m}$ bonded to a rigid underlying base [22].

Preparation and characterization of polyacrylamide gels

Cell behavior was investigated on coatings of various thicknesses. Polyacrylamide gel coatings were used as model elastic substrata; these gels were prepared atop glass cover slips by polymerizing acrylamide solutions (App. C.2). Coating thickness h was controlled via two methods. Gels of thickness $h > 5\,\mu\text{m}$ were prepared by sandwiching a known volume of precursor solution between two glass cover slips [119]. Gels of thickness $h < 5\,\mu\text{m}$ were prepared with a precursor solution containing polystyrene beads of diameters of $0.3\,\mu\text{m}$, $0.6\,\mu\text{m}$, $1.1\,\mu\text{m}$, $3\,\mu\text{m}$, or $6\,\mu\text{m}$, sandwiching between two glass cover slips, and clamping until polymerization was complete [75] (Fig. 2-2(a)). Polymerized gels were functionalized for cell attachment by room temperature incubation for two hours in a gelatin solution ($1\,\text{mg}\,\text{mL}^{-1}$ in phosphate buffered saline), followed by rinsing in purified water.

Gel stiffness was measured via AFM-enabled indentation (Molecular Imaging, now Agilent) by using cantilevers of user-calibrated stiffness $k = 0.03\,\text{N}\,\text{m}^{-1}$ (Veeco). Force-distance indentation responses were analyzed to determine stiffness E by using a previously described model [70] (Fig. 2-2(a, left inset)). The mean and standard deviation of stiffness for the polyacrylamide gels was $E = 5.6 \pm 1.1\,\text{kPa}$ for gels of thickness $h = 60\,\mu\text{m}$ indented to a maximum indentation depth of 800 nm; this measurement is expected to be unaffected by the underlying substrate [129]. Gel thickness values were verified by AFM profiling over through-thickness scratches (Fig. 2-2(a, right inset)) or, for the thicker gels ($h > 20\,\mu\text{m}$), calibrated optical microscopy. Gelatin adsorption did not detectably alter coating thickness as measured by AFM (Fig. C-1).

Cell culture, observation, and analysis

NIH-3T3 fibroblasts were cultured according to protocols described in App. C.1. Experiments were performed in duplicate. The cells were seeded at a surface density of 5,000 cells cm^{-2} onto gelatin-coated gels atop glass cover slips. After 24 hours, the culture medium was exchanged and the adherent cells were imaged with an optical microscope in phase contrast (Olympus IX-81, see Fig. 2-2(b)).

Cell areas were analyzed by using the software ImageJ (NIH); one researcher used this software to trace the cell areas on images randomly labeled by a colleague (Fig. 2-2(b)). Only the areas of free (noncontiguous) cells were measured because of the possibility of contact growth inhibition and its resulting influence on spread-cell area.

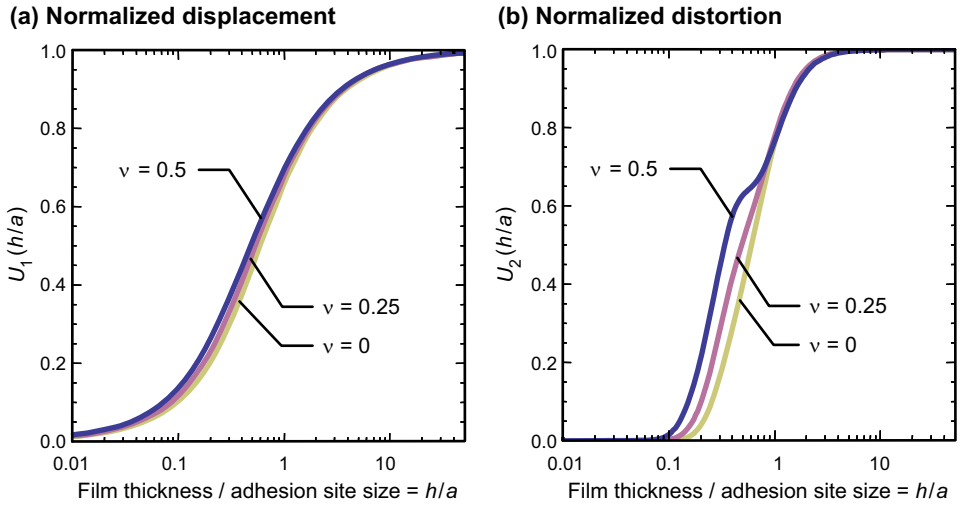

Figure 2-4: **Surface deformation is attenuated as coating thickness h decreases.** (a) Normalized coefficient $U_1(h/a)$ (associated with the *displacement* of a circular adhesion site of radius a caused by the presence of an underlying rigid base at depth h) for three values of substratum Poisson's ratio ν (0, 0.25, 0.5). (b) Normalized coefficient $U_2(h/a)$ (associated with the *distortion* of the same circular adhesion site). As the coating thickness $h \to \infty$, U_1 and U_2 approach one and the displacement and distortion approach that of the half-space solution. As h approaches zero, the displacement and distortion approach zero, representing complete attenuation of deformation caused by the constraint of the rigid base.

2.3 Results

2.3.1 Analytical solutions predict the surface deformation of tangential traction circles

The strategy of analytically obtaining deformation values from a finite area of traction, with and without an underlying rigid base, was successful. Based on equations derived in App. A.1, the shape of a deformed area of traction, representing a single adhesion site, is shown in Fig. 2-3. The x-direction displacement at the center of the circle is $u_B(0,0) = Ta(2-\nu)/2\mu$ (Eq. A.8). The y and z displacements v_B and w_B, respectively, are zero at the center of the circle and average to zero over the area circumscribed by the circle. The distortion—or strain gradient, a measure of leading edge contraction and trailing edge elongation—at the center of the adhesion site is $a(\partial^2 u_B(0,0)/\partial x^2) = -T(4-3\nu)/8\mu$ (Eq. A.13).

When a rigid base is present at depth h, the normalized center displacement of the adhesion site is predicted to be (Eq. A.25):

$$U_1(h/a) = 1 - \frac{2}{2-\nu}\int_0^\infty \frac{1}{\rho}\left[\mu\Phi_1\left(\frac{\rho h}{a}\right) + \frac{2-\nu}{2}\right] J_1(\rho)\, d\rho, \tag{2.4}$$

where Φ_1 is defined in Eq. A.16 and J_1 is the first-order Bessel function.

The dependence of U_1 on the ratio h/a is shown for three values of Poisson's ratio in Figure 2-4(a). As h/a becomes large, U_1 approaches one (100%) and the adhesion site center displacement is unattenuated and nearly equivalent for a compliant coating of thickness h to what it would be on a semi-infinite substratum of the same material. As h/a becomes small, U_1 approaches zero and the adhesion site center displaces as it would on a rigid substratum; that is, it does not displace at all. A consequence of this smooth transition is the need to specify a practical percentage when considering how deep a cell can "feel" (that is, the coating thickness that corresponds to a detectable change in cell behavior). Let us choose key values of $U_1(h/a)$ to be {10%, 50%, 90%}, which correspond to $h/a = \{0.075, 0.485, 3.42\}$ for $\nu = 0.5$. The 90% value, which is

equivalent to 10% attenuation, serves as a reasonable definition of critical thickness h_{crit}.

The normalized distortion of an adhesion site on a coating of thickness h atop a rigid base is predicted to be (Eq. A.34):

$$U_2(h/a) = 1 - \frac{4}{4-3\nu}\int_0^\infty \left\{ \rho \left[\mu\Phi_1\left(\frac{\rho h}{a}\right) + \frac{2-\nu}{2} \right] J_1(\rho) + \left[\mu\Phi_2\left(\frac{\rho h}{a}\right) - \frac{\nu}{2} \right] J_A(\rho) \right\} d\rho, \quad (2.5)$$

where Φ_1 and Φ_2 are defined in Eq. A.16, $J_A = (\rho/4)J_1(\rho) + J_2(\rho) - (\rho/4)J_3(\rho)$, and J_m is the Bessel function of order m.

The dependence of U_2 on the ratio h/a is shown for three values of Poisson's ratio in Figure 2-4(b). The coefficient U_2, like U_1, asymptotically approaches zero and one for small and large values of h/a, respectively. Key values of $U_2(h/a)$ for $\nu = 0.5$ are $\{10\%, 50\%, 90\%\}$ at $h/a = \{0.156, 0.341, 1.58\}$. Therefore, calculations involving both deformation modes predict that an underlying rigid base under a normalized coating thickness $h/a > 1.6$ to $h/a > 3.4$ is nearly undetectable by adherent cells that respond primarily to one or both of these modes.

The following closed-form approximate solution for U_1 is derived from the geometry, fits to within 10%, and like the true solution, converges to $4h/3a$ for small h/a:

$$U_1(h/a) \approx 1 - \frac{1}{2a(2-\nu)}\left[\frac{h^2}{\sqrt{a^2+h^2}} + (4-2\nu)\sqrt{a^2+h^2} - (5-2\nu)h \right]. \quad (2.6)$$

This and additional approximations for U_1 and U_2 are developed in App. A.1.

It is useful to consider an effective spring constant for substratum surface displacement,

$$k_{\text{eff}} = \frac{F}{u_B(0,0)} = \frac{2\pi\mu a}{2-\nu} = \frac{\pi E a}{(1+\nu)(2-\nu)}, \quad (2.7)$$

to link this model with the spring constant calculations made by researchers working with cells adhered to compliant posts or pillars [130–132]. Micropillars are typically designed to have a spring constant of approximately $1\,\text{nN}\,\mu\text{m}^{-1}$ to $20\,\text{nN}\,\mu\text{m}^{-1}$. By using Eq. 2.7, this range translates to a Young's elastic modulus of 0.7 kPa to 14 kPa on a flat, semi-infinite compliant substratum undergoing tangential traction at a circular adhesion site with radius 1 μm.

The key analytical results of this work are Eqs. A.25 and A.34, reprinted here as Eqs. 2.4 and 2.5, which describe how surface deformation is attenuated. These relationships are used in conjunction with the experimental results in the next section to obtain predictions of cell behavior as a function of coating thickness.

2.3.2 Cells respond strongly to thickness changes from 1 μm to 10 μm

As shown in Fig. 2-2, polyacrylamide thickness changes were successfully found to modulate cell behavior on a configuration of cells attached to polyacrylamide gel coatings atop glass. Measurements of fibroblast spread-cell area for different coating thickness values are shown in Figure 2-5(a). This spread-cell area A is most sensitive to changes in coating thickness around thicknesses of several μm. Above this thickness, cell area values decrease at a progressively smaller rate with increasing thickness, indicating that the underlying glass base has become nearly undetectable by cell mechanosensory mechanisms.

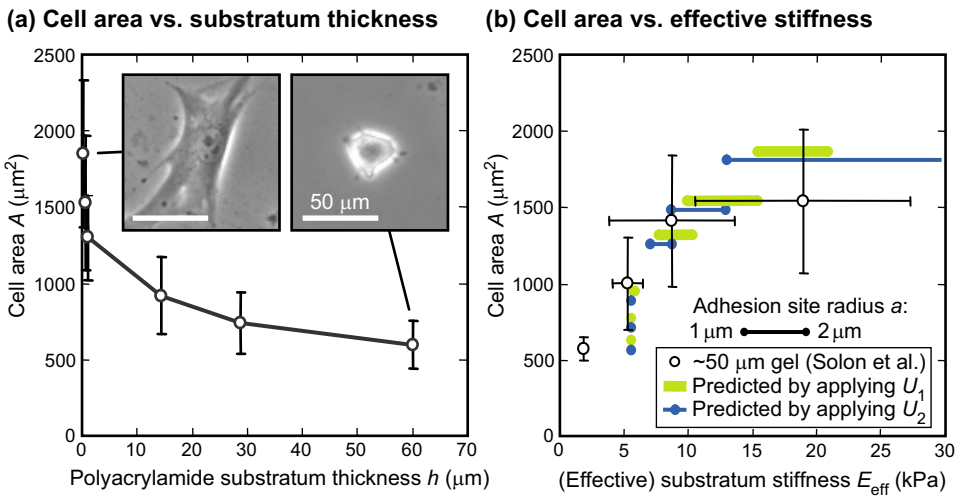

Figure 2-5: **Cell area is strongly dependent on coating thickness in the range of 1 μm to 10 μm.** (a) Cell area A for 3T3 fibroblasts adhered to polyacrylamide gels with Young's elastic modulus $E = 5.6$ kPa and a range of thicknesses fabricated atop glass. The reduction in thickness of a compliant coating on an underlying rigid base results in increased effective stiffness and an increase in spread-cell area. Error bars represent standard error ($n \geq 47$). Inset, phase contrast photographs of cells adhered to relatively thin and thick coatings of the same formulation of polyacrylamide. (b) The same data plotted as a function of *effective* Young's elastic modulus (calculated by dividing the actual Young's elastic modulus by the deformation function U_1 or U_2) for two assumed adhesion site radii, 1 μm and 2 μm, show good agreement with Solon et al.'s measurements of fibroblast area on relatively thick polyacrylamide gels [65]. In (b), cell area error bars are omitted and the predictions from U_1 and U_2 are slightly offset vertically for clarity.

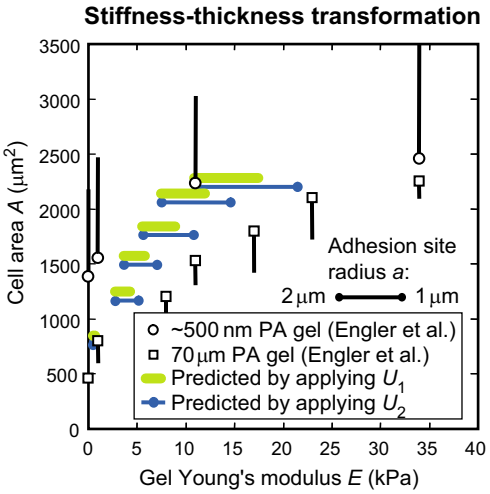

Figure 2-6: **Thick-coating cell behavior can be predicted from thin-coating behavior and vice versa.** Open symbols are cell area measurements on 70 μm (square) and 500 nm (circle) compliant polyacrylamide hydrogel coatings as reported by Engler et al. [22]; data and vertical error bars are as published in [22]. Closed symbols are the result of applying the model's functions U_1 and U_2 to the 70 μm data to predict cell area on a 500 nm coating. The predictions from U_1 and U_2 are slightly offset vertically for clarity, and the horizontal range of U_1 and U_2 arises from the range of assumed adhesion site radii a from 1 to 2 μm.

2.3.3 Finite thickness can be analytically transformed into effective stiffness

Cell area as a function of substratum thickness (A–h data) can be transformed into cell area as a function of effective stiffness (A–E_{eff} data) by using Eq. 2.3. In applying this transformation to the present data, U_i is evaluated by using the measured polyacry-

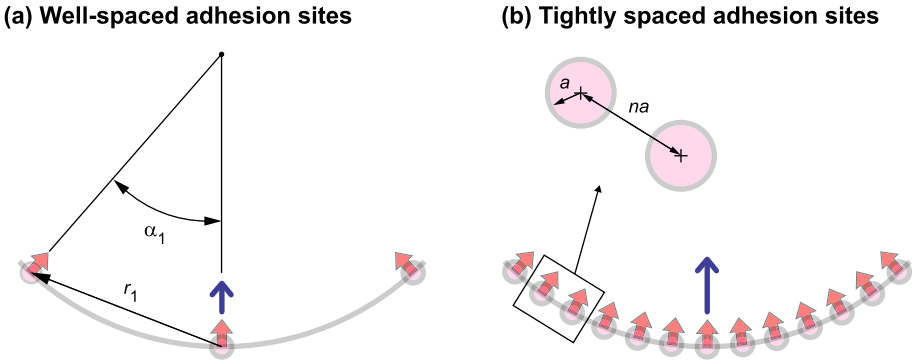

Figure 2-7: **Deformation superposes from multiple adhesion sites, resulting in increased deformation sensed by any one adhesion site.** (a) Angular spacing α and distance from force location r illustrated on an arrangement of relatively large spacing between sites. (b) Linear spacing n and adhesion site radius a illustrated on an arrangement of relatively small spacing.

lamide bulk Young's elastic modulus E, the Poisson's ratio $\nu = 0.5$, and an assumption of adhesion site radius $a = 1\,\mu\text{m}$ or $2\,\mu\text{m}$. The transformed relationship is shown in Fig. 2-5(b); note the corresponding cell area values in Figs. 2-5(a) and (b). The predictions are in good agreement with a previously reported relationship for 3T3 fibroblasts on thick ($50\,\mu\text{m}$) polyacrylamide coatings [65].

The model can also operate on thickness and stiffness specifications in such a way as to predict thick-coating behavior from thin-coating behavior and vice versa. In application to the data reported by Engler et al. [22], the model can predict thin-coating ($500\,\text{nm}$) cell behavior based on the reported thick-coating ($70\,\mu\text{m}$) behavior by multiplying the measured stiffness values of the thick coating by $U_1(h/a)$ and $U_2(h/a)$ for adhesion site radii $a = 1\,\mu\text{m}$ and $2\,\mu\text{m}$. Both Engler et al.'s experimental data and the model's predictions of cell area on a 500-nm-thick coating are shown in Fig. 2-6. Note that the only input to the model was the substratum stiffness in the semi-infinite-region case (taken to be the stiffness reported for the thick-coating case) and the assumed adhesion site radii a. The model is a good predictor of the change in cell behavior (here, spread-cell projected area A) resulting from the use of a thinner vs. a thicker coating of the same material.

2.3.4 The proximity of other adhesion sites is predicted to influence the critical thickness

So far, only the deformation of a single adhesion site has been considered. However, every cell contains multiple adhesion sites, each of which generates a deformation field that is conceivably detectable by mechanosensory mechanisms at neighboring sites. Thus, it is reasonable to ask: How does the presence of other adhesion sites affect the results obtained so far?

The influence of neighboring adhesion sites can be explored by considering a line of equally spaced (i.e., centers separated by na, as shown in Fig. 2-7) adhesion sites of radius a as an idealization of the arrangement found at the periphery of an attached cell (Fig. 1-2(a)). The line is perpendicular to the x-direction tangential traction and extends along the y-axis. At the center of any particular site, the displacement from the two nearest neighbor sites is

$$2 \times \pi a^2 \times \frac{T}{2\pi\mu}\left(\frac{2-\nu}{2r} + \frac{\nu(x^2-y^2)}{2r^3}\right) = \frac{Ta}{n\mu}, \tag{2.8}$$

where the other sites can be approximated as point forces when $n \geq 4$ [73, 112] and

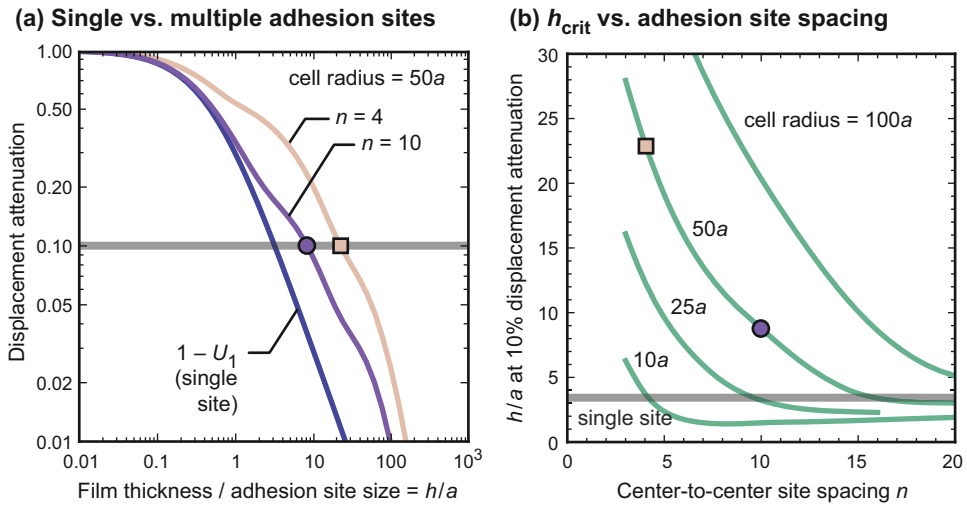

Figure 2-8: **The model of finite traction area and finite coating thickness, derived in App. A.1, is extended to multiple adhesion sites.** (a) $U_1(h/a)$ is replotted from Fig. 2-4 as $1 - U_1(h/a)$ to emphasize percent attenuation of displacement, along with simulated cases incorporating neighboring adhesion sites evenly spaced around a circular cell with radius $50a$. The addition of neighboring sites increases the critical thickness h_{crit} from $3.4a$ to $>20a$. Horizontal line, 10% attentuation criterion for labeling h_{crit}. (b) Critical thickness (represented by h_{crit}/a, or h/a at 10% displacement attenuation) as a function of site spacing for various cell sizes. Filled circles and squares in (a) and (b) link equivalent configurations. Neighboring adhesions sites represent a perturbative presence that may increase or decrease critical thickness h_{crit}.

where $r = x = na$ and $\nu = 0.5$. This displacement can be compared to the displacement caused by the tangential traction of the central adhesion site, which is $3Ta/4\mu$. For a relatively close spacing of $n = 4$, the contribution from the two nearest neighbors alone is predicted to be one-third of the self-displacement (defined as the displacement at the central site and solely caused by the central site). This is not a negligible amount, and thus it is worth exploring more fully how these other adhesion sites quantitatively affect predictions of h_{crit}.

Let us now perform a more complete calculation of the total displacement from adhesion sites all around the periphery of the cell, employing the finite-thickness expressions developed in this thesis (for finite-area sites) and by Merkel et al. (for point sites) [68]. Consider a typical cell with a radius of 50 μm and evenly spaced adhesion sites around the periphery. The total displacement for any one adhesion site is the sum of the self-displacement and the displacement field contributions from all other sites. For a compliant half space ($h \to \infty$), this multiple-site value is found by combining Eqs. A.8 and A.1 to obtain

$$u_{B,mult} = \frac{Ta(2-\nu)}{2\mu} + T\pi a^2 \sum_i \left[G_{B,11}(r_i)\cos\alpha_i + G_{B,12}(r_i)\sin\alpha_i \right], \tag{2.9}$$

where r_i is the distance to, and α_i the angular position of, each neighboring site i (with $\alpha = 0$ for the site of interest), as shown in Fig. 2-7. For the case of a finite-thickness coating, the displacement $u_{C,mult}$ is calculated in an analogous way by using the expressions developed in App. A.1 (for self-displacement) and by Merkel et al. (for neighboring-site displacement) [68]. Furthermore, a new normalized function $U_{1,mult} = u_{C,mult}/u_{B,mult}$ can be defined that represents the normalized displacement inclusive of the influence of other adhesion sites. (The normalized *distortion* inclusive of other sites, $U_{2,mult}$, can be developed in the same way, but is not examined here.)

The parameter $U_{1,mult}$ as a function of h/a is shown in Fig. 2-8(a) for $n = 4$ and 10, assuming a circular cell with a radius of $50a$, adhesion sites evenly spaced around the periphery, and substratum $\nu = 0.5$. While related to Fig. 2-4(a), which also displayed

normalized displacement, this figure extends the relationship to include neighboring-site displacement and also is plotted in terms of *attenuation* ($1-U$ vice U) to emphasize when displacement is attenuated by key values such as 1% and 10%. Shown as a reference is the single-site case $1-U_1(h/a)$ where, as discussed previously, $h_{\text{crit}} = 3.42a$. The presence of nearby sites is predicted to increase the critical thickness h_{crit} by up to an order of magnitude depending on the cell spread-cell area and the site spacing.

Shown in Fig. 2-7(b) is the predicted critical thickness as a function of cell radius and adhesion site periphery spacing; two equivalent configurations are marked by a square and circle in both Fig. 2-7(a) and (b) for clarity. Note that neighboring adhesion sites do not always increase h_{crit}; they can sometimes decrease it. A decrease occurs when the deformation field arising from other sites counteracts the self-deformation; in these cases, attenuation of this field at smaller coating thicknesses results in the adhesion displacing *farther* and the cell sensing a *lower* effective stiffness. In most cases, though, the presence of neighboring adhesion sites increases h_{crit}. In general, the perturbative effect of neighboring adhesion sites modulates the $h_{\text{crit}} \approx a$ connection derived earlier in a way unique to each cell's attachment to the substratum. Based on Fig. 2-7(a) and (b), this modulation is predicted to affect h_{crit} by a factor of less than 10.

2.4 Discussion

2.4.1 How deep do cells feel?

It is desirable to predict cell mechanosensory inputs for arbitrary values of substratum stiffness and thickness, to inform the design of synthetic substrata intended to produce a particular cell behavior. Previous considerations of substratum thickness have typically been limited to the extreme cases of very thin and very thick coatings (e.g., [128]). The effective-stiffness model presented here goes further, providing a quantitative link from very thin coatings to semi-infinite regions in the form of the normalized deformation functions U_i. The calculations are not dependent on any particular theory of adhesion site formation and growth. In its calculation of an effective stiffness, the model is in agreement with Nicolas et al.'s general predictions that a thin, compliant extracellular matrix (ECM) should lead to a similar behavior as a thick, stiffer ECM [128], and these predictions in turn are in agreement with observations of spread-cell area, a reporter of cell-sensed effective stiffness, as a function of coating thickness [22, 75].

The two normalized deformation functions U_1 (quantifying attenuation of center displacement) and U_2 (quantifying attenuation of distortion) represent possible ways of characterizing the influence of an underlying rigid base. Both are functions of the dimensionless ratio h/a, and both therefore describe the coupling between the two primary length scales of the model (coating thickness and adhesion site radius). To enable an estimate of critical thickness h_{crit} for cell mechanosensory mechanisms, key 10% attenuation[4] values are $3.42a$ for $U_1(h/a)$ and $1.58a$ for $U_2(h/a)$. (The typical radii a of adhesion sites such as focal adhesions is O(1 μm) [14].) The U_i functions therefore predict that the adhesion site deformation is barely attenuated for h values of several μm or more. (Interestingly, this estimate is independent of the coating material stiffness E.) An interpretation of this result is that—for substratum thicknesses exceeding several μm—an underlying rigid base is undetectable via cell mechanosensory mechanisms that respond primarily to either adhesion site displacement or distortion, assuming that the influence of other sites is negligible.

It should be noted that the model does not inform the user of which function U_i to use. In both examples of calculating effective stiffness (fibroblasts and mesenchy-

[4] At this attenuation percentage, one could say that the surface deformation has been *decimated*—in the original sense of the word.

mal stem cells), the predictions from using functions U_1 and U_2 are similar enough to prevent drawing any conclusions on whether the cells used either displacement- or distortion-related feedback to sense substratum stiffness. Furthermore, while adhesion site models in the literature appear to ascribe a mechanosensory mechanism to adhesion site displacement and/or distortion, there is nevertheless no assurance that mechanosensation is affected by these parameters. Feedback of substratum stiffness employed by the cell may incorporate one or the other parameter, both parameters, or additional information not yet defined. It seems clear, however, that the feedback must incorporate some aspect of surface deformation of the 2-D substratum on which the cell is attached. As physical models of adhesion site growth and stability emerge, additional modes of deformation may be found to be important. The model presented here provides a method for calculating the attenuation caused by finite coating thickness for any mode of deformation, by returning to the Green's tensors given in Eqs. A.1 and A.15 and calculating $\mathbf{u}_B$ and $\mathbf{u}_C$.

Similar to previous analytical models, reported experiments of mechanosensation have focused on only two values of coating thickness per study (e.g., [22, 75]). The present study extends this work by using six different coating thicknesses to allow discernment of a trend in the spread-cell area vs. thickness relationship. Cell area changes considerably for thickness changes under 10 μm, indicating a considerable change in the effective stiffness that these cells sense. However, the trend of decreasing mean cell area with increasing thickness is still observed when coating thickness is >10 μm. It is therefore concluded that the transition is gradual (and monotonic), and that it is necessary to define carefully what one means by a critical thickness. This study has focused on the thickness at which surface deformation is attenuated by 10%, and other possible definitions are developed in the next section to interpret literature reports.

The incorporation of neighboring adhesion sites can modulate the critical thickness in a manner dependent on the site-to-site spacing and on the radius of the cell. For close spacing (adhesion sites separated by equally sized spaces) and large cells, the critical thickness is predicted to increase by as much as an order of magnitude. It is plausible that this perturbative effect explains the continued trend of decreasing cell area for coating thicknesses of 10 μm or more, a trend apparent in Fig. 2-5(a) and in Butler and Lin et al.'s findings for fibroblasts atop collagen-coated PAAm (Table 2.1) [100]. However, this neighboring-site effect is secondary, and both the analytical and experimental findings generally agree that the most prominent length scale in this problem is that of the (O(1 μm)) adhesion site radius.

2.4.2 Multiple definitions of critical thickness exist in the literature

In the process of considering literature reports of a minimum suitable coating thickness to reasonably assume half-space behavior, different possible definitions have been identified of a critical thickness h_{crit} of compliant coatings used in cell biophysical studies (Table 2.2). A critical thickness could be said to correspond to the depth that a cell can feel, or, more specifically, the minimum coating depth to avoid any meaningful interference from an underlying rigid base. It is important to identify and compare definitions to avoid misunderstandings and to clarify data on cell traction-induced substratum deformation. The definitions in Table 2.2 can be divided into: (1) consideration of the depth at which a certain principal strain magnitude is predicted; (2) consideration of the minimum coating thickness to assume that the half-space solution is reasonable in cell traction microscopy (CTM); and (3) considerations of the minimum coating thickness such that a cell cannot detect a rigid base.

The definitions in Table 2.2 are ordered according to proposed relevance in the design of finite-thickness coatings intended to elicit a predicted response of adherent cells. The first two items are less relevant in this ordering. As discussed earlier, the arbitrary nature of a chosen strain magnitude (definition (1)) is of limited usefulness, and cells

Table 2.2: **Collection of definitions of critical cell-sensing depth or coating thickness for cells attached to 2-D substrata, delineated to clarify previous conflicting reports.**

Description of critical depth or thickness	Effect of increasing coating stiffness
(1) Depth at which a certain primary strain exists [2, 76]	Decreases $\left(\propto \sqrt{T/\mu}\right)$
(2) Coating thickness that attenuates cell traction microscopy (CTM) measurements at a distance r by a certain percentage [68]	Independent ($\propto r$)
(3a) Coating thickness that attenuates adhesion site displacement by a certain percentage (characterized by U_1) (**this work**)	Independent ($\propto a$)
(3b) Coating thickness that attenuates adhesion site distortion by a certain percentage (characterized by U_2) (**this work**)	Independent ($\propto a$)
(3c) Coating thickness that maintains a certain traction-induced surface displacement or distortion	Increases $\left(f(a,\mu)\right)$

furthermore do not detect strain at depth but rather on the coating surface (i.e., the adhesion site location) only. The key length scale of definition (2), the critical thickness for cell traction microscopy (CTM), is controlled by the distance from adhesion site to bead, a measurement of no significance in cell mechanosensitivity.

The metrics of attenuation defined in the present study (the group of definitions (3a, b, c)) are arguably more useful. It seems clear, for example, that a cell cannot feel an underlying base that is too far away to attenuate traction-induced surface deformation at an adhesion site; this is the reasoning behind definitions (3a) and (3b), which differ only by the deformation mode of interest. Finally, the last item in Table 2.2 (definition (3c)) may be the most relevant to cell behavior: a coating thickness that would produce a certain surface deformation. However, it is difficult to theorize further about this last definition of critical thickness without knowing more about the cell mechanosensory mechanism and about which modes of substratum deformation provide primary feedback to an adherent cell. Future experiments that consider the effects of finite coating thickness may help resolve this issue.

Of particular interest are the different ways that the characteristic depths in Table 2.2 depend on a material property such as coating stiffness. Depending on one's criterion (strain cutoff, attenuation of remote bead displacement, maintenance of adhesion site deformation), the depth may increase, decrease, or remain unchanged as a result of increasing stiffness. Such disparate relationships further confuse discussions of critical thickness and cell mechanosensation when definitions are not precisely stated and applied. Based on the successes described in this chapter, the framework developed and applied here (i.e., definitions (3a, b) and the associated class of U_i functions) is concluded to be well-suited for analyzing cell attachment to and mechanosensation of compliant coatings and tissues atop comparatively rigid materials.

2.4.3 Reconciling disparate literature reports

The previous reports tabulated in Table 2.1 are now reviewed in light of the multiple definitions of h_{crit} delineated in Table 2.2 and the present analytical and experimental results. First, definition (1) represents the work of Oommen et al. [2, 76], as discussed above. Second, the cell traction microscopy (CTM) context of definition (2) has produced critical thickness estimates from 1 μm to >70 μm [15,71,73,97,98]. Importantly, Merkel et al.'s investigation of deformation fields on coating thicknesses produces a characteristic dimensionless ratio of h/r, the ratio between coating thickness and distance to the adhesion site [68]. Based on these reports, the minimum coating thickness to perform CTM appears to be the distance from the farthest adhesion site of interest. This conclusion agrees with Yang et al.'s simulations, Merkel et al.'s calculations, and del Álamo et al.'s observations, as this distance corresponds to the length of a cell that

one is observing. Dembo and Wang's scaling argument that the coating thickness need only exceed O(1 μm) marker displacement is necessary but not sufficient, based on the more quantitative analyses performed by later researchers.

(How, then, can one explain successful CTM on <40-μm-thick coatings [73] when the imaged markers are farther than 40 μm from some adhesion sites? Let us consider the nature of the error from idealizing the coating as a half-space. As the distance from the adhesion site increases, the relative error increases while the traction-induced displacement decreases. Consequently, at a distance large enough to result in a considerable relative error (e.g., 100% or more), the surface displacement value is likely near or below the noise floor. Thus, the data that are most susceptable to error from the half-space assumption probably contribute only minimally to cell traction measurements. This conclusion is supported by Yang et al.'s prediction of a relatively large but nevertheless unmeasurable error (Table 2.1). Dembo and Wang's more lenient requirement appears to be incorrect in theory, but evidently valid in practice, at least for CTM experiments.)

Third, the group of definitions (3) in Table 2.2 is of greatest relevance for cell mechanosensitivity. The model presented here predicts that the most prominent length scale is that of the adhesion site radius (O(1 μm)); it also provides a quantitative relationship in terms of $U_i(h/a)$. This model is compatible with findings from the Discher group (Engler et al. [22, 75] and Buxboim et al. [99]) that spread-cell projected area is affected by switching coating thickness to 500 nm but not 5 μm. Butler and Lin et al.'s finding that cells still react observably to thickness changes around the vicinity of 50 μm [74, 100] can plausibly be attributed to the influence of neighboring adhesion sites on h_{crit}, as discussed in §2.3.4. However, this effect is concluded to be secondary in magnitude and importance. Lin et al. did not look at coating thicknesses smaller than 50 μm, but it is at thicknesses below this value that cells are expected to be most prominently affected, based on Fig. 2-5(a), Fig. 2-8(a), and the experimental results of the present study.

A final consideration is Leong et al.'s finding of $h_{\text{crit}} > 130\,\mu\text{m}$ for cell cultured on collagen gels; recall that the authors attributed this unusually large value to the use of strain-stiffening collagen rather than polyacrylamide. An investigation of the critical thickness on nonlinear elastic materials is outside the scope of the present study, but would be an interesting approach to pursue in the future, as the transmission of mechanical forces through ECM could involve nonlinear effects. The present assumption of linear elasticity is based both on the reported behavior of polyacrylamide for the displacements of interest and on the motivation to keep the equations as simple as possible. Possibly the current model could be usefully extended to accommodate nonlinear, poroelastic, or biphasic constitutive behavior.

2.4.4 Case study: Substratum design to enable near-quiescence of mesenchymal stem cells for paracrine agent extraction

A case study is presented to demonstrate the analytical tools developed in this study. The context is human mesenchymal stem cells (MSCs), which, as discussed in §1.1.1, are currently being explored as a way to regrow connective tissue upon injection or infusion. An intriguing alternate hypothesis, studied by Yarmush et al., is that only selected chemical signals from MSCs are needed, and not the actual cells [133, 134]. Under this approach, MSCs could be maintained in culture *ex vivo* and the secreted chemicals delivered continually *in vivo*, perhaps in a process similar to dialysis. Let us pursue the design of a proof-of-concept device for evaluating this hypothesis.

Assume, as suggested by Yarmush, that the prototype device used to culture MSCs is based on an off-the-shelf dialysis filter, which consists of parallel hollow capillaries that normally enable molecular exchange and blood purification [135]. For this application, assume the capillary wall material is polysulfone, which has a Young's modulus of

2.7 GPa, and that the inner diameter of the capillaries is 100 μm and the wall thickness is 20 μm [135].

It is desired to keep the cells in a near-quiescent state to avoid proliferation, monolayer formation, and the resulting inhibition of cell activity. We will maintain this state by reducing the effective substratum stiffness sensed by the cell; assume that a stiffness (as quantified by the Young's elastic modulus) of >10 kPa prompts cell proliferation with a division time of 4 days. At the other extreme, however, a substrate that is too compliant triggers anoikis, or programmed cell death from the lack of physical attachment to a substratum [25]. The quiescent state has been reported to be maintainable at 250 Pa [24]; for this application, assume that 1 kPa provides a suitable substrate stiffness to maintain paracrine agent secretion without inducing excessive proliferation.

The polysulfone capillaries, as fabricated, are too stiff; to mollify or alleviate their rigidity, a compliant layer or coating is needed between the polysulfone and the cells. However, the coating's thickness is constrained: the cross-sectional area of the capillaries should not be greatly reduced, and very thick coatings are subject to delamination. Most importantly, the coating deposition will be accomplished through a layer-by-layer process, and this technique will be arduous if the desired thickness is too great. Let us assume that the design thickness is 3 μm. At this thickness, can the cell detect, through mechanosensory mechanisms, the relatively rigid polysulfone capillary? If so, can the coating be designed to present an effective stiffness of 1 kPa?

Assume that at the intended effective stiffness of 1 kPa, MSCs have a radius of 25 μm and adhesion sites that are punctate with a typical diameter of 1 μm and a center-to-center spacing of 5 μm. Also assume that the critical mode for mechanosensing is displacement of the adhesion site. With these parameters, it is now possible to analyze the problem. Note that $a = 0.5\,\mu\text{m}$, the nondimensional thickness $h/a = 6$, and the spacing parameter $n = 10$. It follows that approximately 30 adhesion sites are spaced around the periphery of each cell. Consider first the attenuation of displacement of a single site as a result of the relatively rigid base 3 μm underneath. By using the approximation given for $U_1(h/a)$ in Eq. A.44, we predict that deformation is reduced to $U_1(6) \approx 94.6\%$; the exact value from numerically solving Eq. 2.4 (derived at Eq. A.25) is $U_1(6) = 94.2\%$. Thus, the displacement is predicted to be attenuated roughly 5% by the presence of the rigid base, given that each adhesion site detects only its own displacement.

Now consider the case where the influence of neighboring sites is considered. The traction exerted by these sites increases the displacement of the adhesion site of interest (for neighboring sites on the same side of the cell). This displacement is also attenuated by the rigid base, of course. By applying the analysis given in §2.3.4, the displacement is found to be $U_{1,\text{mult}} = 87.2\%$ of the value expected from a semi-infinite substratum. (This value can also be estimated by examining Fig. 2-7.) Consequently, a naive design selection of 1 kPa stiffness for the coating is too high by 15%. To enable an effective stiffness of 1 kPa sensed by the cells, the 3 μm compliant coating material should be manufactured with a Young's modulus of 872 Pa. This case study thus illustrates both the influence of a rigid base for a single adhesion site, and also how this influence is affected by neighboring adhesion sites.

2.5 Outcome

Conclusions

The results support the study's hypothesis. The approach of (1) extending elasticity theory to predict adhesion site self-deformation on a coating surface, along with (2) performing experiments to obtain cell response on a range of compliant substratum thicknesses, does provide new insight toward a resolution to the central question—how deep

do cells feel—of this chapter. This resolution has not been available from finite element numerical solutions or from experiments of only one or two coating thickness values, because these approaches arguably cannot provide sufficient insight or information to obtain and interpret trends occurring over multiple relevant length scales.

It is important to understand the extent to which finite substrata thickness affects the mechanical resistance encountered via cellular traction at discrete adhesion sites. The continuum elasticity model and its distinction between adhesion site displacement (U_1) and distortion (U_2) was applied to calculate the effective stiffness of finite-thickness coatings deformed via traction at adhesion sites. The goal was to rationalize the wide range of estimates for critical thickness that has been advanced in the present literature, from the diameter of molecular complexes to the diameter of entire cells. It was verified through experiment that this thickness-defined effective stiffness rationalizes comparable cell areas observed for thick, stiff gels and thin, compliant gels both in previously reported experiments and in new results for fibroblasts on polyacrylamide gels.

It is concluded that several distinct and valid definitions of critical thickness h_{crit} exist depending on whether the deformation location of interest occurs at the adhesion site (as is the case with cell mechanosensitivity) or at a distance from multiple adhesion sites (as is the case with cell traction microscopy). The existence of different suitable definitions for different applications explains some disparity in literature reports. It is further shown that these definitions depend in different ways on the mechanical stiffness of the coating material. The model quantitatively connects the critical thickness definition most relevant in considerations of mechanosensitivity to the characteristic size of adhesion sites, a connection that has been observed in experiments and intuited through scaling arguments but not previously derived rigorously.

The present study and its results present implications both for applied studies of coatings synthesized to recapitulate tissue environments and for fundamental studies of mechanosensitivity. Herein are provided the means to describe and predict cell-level responses for substrata of varying stiffness and thickness in terms of effective substratum thickness; this framework should facilitate quantitative comparison among disparate experimental conditions as well as effective design of coatings intended to represent a predefined mechanical environment to adhered cells. Practical applications of this model still require careful consideration of the purposes for which mechanically defined substrata are employed, and a crucial consideration is whether one's goal is to match *in vivo* degrees of adhesion site displacement, of cell morphology, of substratum contraction, of maximal cell traction, and/or metabolic activity. For applications in which the substratum is intended to provide a well-defined mechanical environment that maintains a specified surface deformation, for example, the model provides researchers with expressions for calculating self-deformation at finite adhesion sites as a function of coating thickness.

Of greatest general interest, likely, are the mechanisms by which this mechanical environment is converted to biochemical processes that alter cellular functions, and the extent to which these mechanisms depend separately (if at all) on the displacement and distortion of the multimolecular adhesion sites at which stress is transferred from the intra- to extracellular environments. The present model cannot entirely resolve this important question based on available experimental data. However, the results presented here provide insight to design and interpret future experiments that seek to define and leverage these primary feedback mechanisms.

Possibilities for continued research

There are many appealing directions available for continuing this research. Four are described here, ordered from straightforward model refinement to broader approaches for understanding cell behavior.

First, incorporation of traction *perpendicular* to the surface would expand the analytical framework to accommodate the vertical component of adhesion site loads that have very recently become measurable by CTM [115, 136–138]. This work would require an investigation of the $G_{C,i3}$ components of the finite-coating Green's tensor given in Eq. A.15.

Second, the model could be extended to incorporate changes in adhesion site size as a function of stiffness. Adhesion sites are known to be larger on stiffer substrata [114], and the present work predicts that sensing depth should increase with adhesion site radius a. Therefore, it is conceivable that the resulting positive feedback loop is detectable and relevant to cell mechanosensory response. At some certain depth, the detection of a rigid base might "snap on" from this positive feedback. Such a rapid increase may be observable in experimental results such as those shown in Fig. 2-5.

Third, the model could be applied to cell-to-cell communication. Current understanding is that cells communicate in part by generating deformation fields in the adjacent substratum [124, 139–141]. The equations developed here allow the deformation from nearby cells to be compared to the self-deformation of a single adhesion site to explore this phenomenon. This approach may be capable of resolving remaining questions about the relative importance of adhesion site displacement or distortion in mechanisms of substratum stiffness sensing by cells.

Fourth, the model could be applied to a suitable *in vivo* environment such as the basement membrane of blood vessels, essentially a 2-D, or planar, substratum for adherent epithelial cells that consists of a meshwork of collagen fibers with branch points spaced at 45 nm [142]. The use of continuum theory is a reasonable assumption for such materials. Possibly other *in vivo* environments exist in which modulation of the thickness of the adjacent or surrounding matrix is interpreted by cells as a change in effective stiffness, and consequently plays a part in normal or abnormal physiological processes in a way that could be elucidated by applying the techniques developed in this study. For example, the present method of calculating an effective stiffness could be applied to areolar connective tissue that may be sufficiently thin to produce a multilayer mechanical response to adherent, epithelial-type cells [143].

Online material

A 9-minute video overview of this research can be accessed at one of the following locations:

`http://vimeo.com/7197516`
`http://www.scivee.tv/node/14949`
`http://www.youtube.com/watch?v=HSi0ykvUXpc`

Acknowledgments

Christopher Bruce fabricated polyacrylamide gels, characterized their thickness and stiffness via atomic force microscopy, cultured cells on these substrata, and produced and analyzed phase contrast photographs of cell spread area as part of his MIT senior thesis [144]. Emily Walton contributed to planning the research and interpreting and expressing the results. Portions of this chapter and associated appendices have been published previously [1–3], and are reprinted with the permission of the American Physical Society, Landes Bioscience, and the Institute of Physics Publishing.

Chapter 3

Compliant cytoskeletal networks I

Synopsis

Optical stretching, a noncontact technique for deforming fully suspended cells, is used to investigate the creep compliance and complex modulus of single cells immediately after they are brought from the attached to the suspended state. Measurements of >2,000 human mesenchymal stem cells and murine fibroblasts in both the time and frequency domains reveal that the suspended adherent whole cell deforms as a linear power-law material in both stretching and recovery; that is, the creep compliance $J(t)$ scales with time t as $J(t) \propto t^{\alpha}$ and the hysteresivity or loss tangent is $G''/G' = \tan(\pi\alpha/2)$, where the power-law exponent, a measure of material fluidity, is $\alpha = 0.3$–0.4. Equivalently, no characteristic time scales appear that would correspond to a viscoelastic model of one or several springs and dashpots. This finding corrects the conclusion of a previous study with a much smaller data set, and moreover marks a step forward in understanding how cells fit into the class of so-called soft glassy materials, which exhibit power-law rheological behavior. It is concluded that cytoskeletal stress fibers and adhesion sites, prominent in attached cells but absent in suspended cells, are not necessary for such behavior. Furthermore, insensitivity of the average exponent value $\overline{\alpha}$ to intracellular adenosine triphosphate (ATP) depletion shows that ATP, while unquestionably a power source for cellular contractile machinery, does not provide the essential non-thermal agitation energy that enables fluidity during deformation. However, ATP is found to contribute to cellular mechanical heterogeneity, as quantified by the standard deviation in measured values of α. These findings address a controversial point in the literature on enabling factors of cytoskeletal deformation and the relationship between live cells and inanimate soft glassy matter.

3.1 Study background, hypothesis, and design

The second study in this thesis focuses on the deformability of single suspended cells. As discussed in §1.2.3, cells—attached cells, at least—are known to exhibit so-called weak power-law rheology (PLR, reviewed in [40, 41]). The PLR response is characterized by a straight line with slope α (with $0 < \alpha < 1$) over many decades on log-log plots of creep compliance $J(t)$ vs. time t, or of complex modulus $G^*(\omega) = G'(\omega) + iG''(\omega)$ vs. frequency ω (Fig. 1-3, Table 3.1). PLR is found at time scales spanning several decades around 1 s and at length scales from sub-μm atomic force microscopy (AFM) indentation depths [46, 51, 84, 149, 150] to micrometer-scale beads moving with sub-μm amplitudes [26, 42, 43, 48, 52, 53] to whole-cell deformation [29, 50].The power-

Table 3.1: **Relevant studies when investigating whether suspended eukaryotic cells exhibit characteristic viscoelastic time scales.** Recent studies of attached cells have provided strong evidence that *attached cells*, at least, exhibit power-law rheology and a lack of characteristic time scales.

Attached cells

Sample type and size	Technique	Constitutive model	Group
Attached ($n > 10,000$)	Magnetic bead cytometry	Power-law rheology ($a \approx 0.2$)	Fabry and Fredberg et al. (2001–2005) [26, 42, 43, 48]
Attached ($n > 100$)	Uniaxial stretching	Power-law rheology ($a \approx 0.2$)	Desprat and Balland et al. (2005–2006) [29, 50]
Attached ($n \approx 300$)	Scanning probe indentation	Power-law rheology ($a \approx 0.2$)	Hiratsuka et al. (2009) [51]

Table 3.2: **Relevant studies when investigating whether suspended eukaryotic cells exhibit characteristic viscoelastic time scales.** In comparison to attached cell studies, few and smaller studies have investigated suspended cells, which lack stress fibers and therefore may be governed by a different constitutive behavior. (Methods: AFM = atomic force microscopy.)

Near- or fully suspended cells and possible suspended-cell analogues

Sample type and #	Technique	Constitutive model	Group	Notes
Lipid vesicle	Optical tweezers	2-element lumped component ($\tau = 1.1\,\mathrm{s}$)	Zhou et al. (2011) [145]	
Actin solution	Parallel-plate rheometry	Power-law rheology ($a \approx 0.17$)	Gardel et al. (2006) [146]	Required applied stress to exhibit PLR.
Red blood cell	Optical tweezers	Unclear	Puig-de-Morales-Marinkovic et al. (2007) [147]	Neither full power-law behavior nor characteristic relaxation times were identified.
Nucleus	Optical tweezers	Power-law rheology ($a \approx 0.3$)	Dahl et al. (2005) [148]	PLR observed over >4 time decades for stretching and recovery.
Eukaryotic nonadherent ($n = 24$)	AFM	Power-law rheology ($a = 0.18$)	Roca-Cusachs et al. (2006) [84]	Rejected lumped-component models by comparing fits of $G^\star$ vs. ω.
Eukaryotic adherent ($n \approx 1$)	Optical stretching	3-element lumped component ($\tau = 2.5\,\mathrm{s}$)	Wottawah et al. (2005) [86]	Rejected power-law rheology by comparing r^2 values.
Eukaryotic adherent ($n = 81$)	Micropipette aspiration	Power-law rheology ($a = 0.30$)	Zhou et al. (2010) [83]	
Eukaryotic adherent ($n = 10$)	Electrodeformation	Power-law rheology ($a = 0.36$), lumped component ($\tau = 6.2\,\mathrm{s}$)	MacQueen et al. (2010) [87]	Unclear; both models fit well.
Eukaryotic adherent ($n > 2,000$)	Optical stretching	Power-law rheology ($a \approx 0.37$)	**This work**	Lumped-component viscoelastic models and characteristic time scales are rejected by comparing adjusted r^2 and AIC values and by observing constant-phase behavior in the frequency domain.

law exponent a is additionally found to modulate the hysteresivity or loss tangent $\eta = G''/G' = \tan(\pi a/2) \sim \mathrm{O}(0.1)$. Because $a = 0$ would correspond to an elastic solid and $a = 1$ to a fluid, findings of $a \approx 0.1$–0.5 have led to a view of the cell as a viscoelastic material, or one with behavior intermediate between that of a solid and a fluid [151].

Power-law rheology differs from what one would expect from a relatively simple lumped-component viscoelastic model—that is, an assembly of several[1] springs and dashpots. Lumped-component models were long the standard for analyzing time-dependent cell deformation [152–156]. However, Fabry and Fredberg et al. have unequivocally rejected these models and their associated discrete time scales [26, 48]. They argue that small portions of a power law can be fit with apparent success by assemblies of several springs and dashpots, but that the extracted time constants simply reflect the experiment duration and do not represent any meaningful relaxation times that elucidate material structure. They further conclude that in the cytoskeleton, elastic and viscous components cannot be decoupled as is possible with spring-dashpot assemblies. How, then, should the rheological mechanism in cells be visualized?

The experimental findings described above, along with evidence of shear-induced fluidization and resolidification[2] in cells [151, 157, 158], led Fabry and Fredberg et al. to propose that cells may be a type of "soft glassy material," a class of disordered and metastable materials such as foams, emulsions, and pastes that flow homogeneously at a time scale of $\mathrm{O}(1\,\mathrm{s})$ [26, 48, 49, 159]. Broadly, these materials tend to yield by local rearrangement of structural regions, such that deformation and other kinetic processes in soft glassy materials are dominated not by thermal energy but by a larger "noise temperature," or agitation energy, that represents the jostling among these regions (App. B.2). Rheological constitutive equations that link these concepts to predictions of deformability have been developed by Sollich et al. [91, 92, 160]; these equations constitute the soft glassy rheology (SGR) model.[3] A fundamental part of the model's framework is the parameterization of the noise temperature $x = a+1$ as the ratio of the material's intrinsic agitation energy to a threshold energy (interpreted as a glass transition temperature) below which a bulk yield stress exists and above which flow will occur at any stress level. In this context, one could interpret the cell as self-regulating its noise temperature to provide an appropriate degree of fluidity in response to chemomechanical cues [49].

A reductionist strategy has motivated investigations of dilute actin solutions as simple cytoskeletal models to see if cell-like behavior appears. Notably, Gardel et al. found that crosslinked actin does exhibit power-law rheology as long as the network is placed under sufficient load [146, 161] (the networks act as solids otherwise [162]). Attention consequently turned to the actomyosin contraction that loads the cytoskeleton in live cells (and as examined in the previous chapter, acts via stress fibers in attached cells to apply traction to the adjacent substratum) [40, 53]. The view that contractility modulates power-law rheology was reinforced by findings that pharmacological perturbation of cytoskeletal stress (e.g., the use of cytochalasin, an inhibitor of actin polymerization) strongly affects the value of the exponent a [28, 163]; attached cell populations with larger internal tension exhibit lower power-law exponent a, and vice

[1] Emphasis on *several*. A large number of spring-dashpot pairs can produce a response indistinguishable from power-law rheological behavior, and in fact such an arrangement can be used to simulate power-law rheology (§4.3.3, App. B.2).

[2] Fluidization (shear thinning) and subsequent resolidification are characteristic behaviors of soft glassy materials exposed to relatively large loads; these behaviors are reviewed in this work in App. B.2.

[3] In keeping with the literature (e.g., [29, 49, 91, 92, 148]), **power-law rheology (PLR)** herein means the *experimental* findings described above that involve mechanical parameters such as creep compliance and complex modulus. The **soft glassy rheology (SGR)** model means Sollich et al.'s coarse-grained *abstraction* of structural configurations visualized as "elements" trapped in energy wells (representing the metastability of particular mesoscopic regions) that are subject to agitation leading to rearrangement—yielding—and corresponding exchange for a new well.

versa [42, 43, 48, 164].

It is not obvious, however, how the suspended cell should be expected to deform. Stress fibers are absent in the suspended state, but some degree of contractility is still known to occur via actomyosin motors in the cortex [165], the crosslinked structural shell of actin that lies just inside the plasma membrane. Previous experiments have not demonstrated conclusively whether the PLR behavior that characterizes soft glassy materials is or is not present in the suspended state (Table 3.1). In fact, relatively few studies have investigated suspended cells, and data sets are smaller because suspended cells are generally probed serially and with a relatively low throughput (e.g., 1 cell min^{-1} or less).

On the one hand, studies investigating the rheological behavior of cells and related structures [145–148] suggest that suspended cells (adherent and nonadherent) do possibly exhibit power-law rheology (as do cell nuclei, along with actin solutions under certain circumstances) while simple vesicles do not (Table 3.1). One could argue, however, that the studies on so-called suspended cells mostly involved some degree of cell-probe contact that might have triggered an attachment response of adhesion site and stress fiber formation.

On the other hand, previous studies by Wottawah et al. that did not involve probe-cell contact explicitly rejected power-law rheology and concluded that suspended cells exhibit a single relaxation time constant [38, 86]. That conclusion led others to consider suspended-cell rheology as being fundamentally different from attached-cell rheology [41, 88]. Because that data set consisted of one or several cells only, however, the body of evidence is relatively small compared to the case of attached cells. How, then, do suspended cells deform—more like vesicles, or more like attached cells? A new study of suspended cells is necessary to determine their rheological behavior conclusively.

Another unclear area involves the origin of agitation within the living cell. Sollich et al. developed SGR theory in the context of inanimate materials, and they speculated that the noise temperature represents an effective mean-field energy ($\gg kT$) that describes jostling from the yielding of neighboring regions. Fredburg et al. in turn noted that adenosine triphosphate (ATP) is an effective energy carrier that the cell employs for actomyosin contraction—ATP powers the so-called myosin "power stroke" that tensions stress fibers—and they proposed that ATP hydrolysis provides the agitation needed to enable power-law rheology in cells [40, 166–168]. It seems reasonable that in this proposed model, removal of ATP should be expected to decrease or eliminate cell fluidity (equivalently, cause the power-law exponent a to fall toward zero). In contrast to this idea, however, consider the finding that contraction-generated (and thus ATP-enabled) internal tension *decreases* the power-law exponent [28, 163]. One could therefore argue that ATP depletion should actually shift the power-law exponent to larger values because internal tension can no longer be maintained. Finally, on the experimental side others have reported that cells exhibit power-law rheology even when ATP is depleted [52, 151, 157, 169]. In conclusion, multiple contradictory conjectures and indications exist in the literature on the precise connection between ATP, internal tension, and cell rheological behavior.

In light of these uncertainties in our understanding of cell rheology, the present study's hypothesis is:

> High-throughput optical stretching, as a tool for studying cell mechanics that requires no cell-probe or cell-substratum contact, can address the question **How do suspended cells deform?** by decoupling the influence of stress fibers and adhesion sites, by probing cells in both the time and frequency domains, and by testing cells exposed to pharmacological perturbation such as depletion of intracellular ATP.

The technique of optical stretching (OS) offers a way to address the challenges described above. Optical stretching evaluates whole-cell mechanics in the suspended

state as measured by creep compliance, or deformation under a constant applied load (Fig. 3-1) [34, 170]. Dual counterpropagating laser beams attract and center a single suspended cell, which deforms by outward photon-induced surface stress caused by the change in refractive index at the cell edge. The cell response is typically characterized by its deformation along the laser axis as a function of time (Fig. 3-1(c,d)). Cells can also be exposed to various chemical environments by media exchange either before or after detachment from the substratum.

"High-throughput" optical stretching is specified to distinguish this study from previous studies. Serial techniques for interrogating single cells are notorious for low throughput, usually producing data sets of <100 cells per experimental condition (Table 3.1). In contrast, experiments on attached cells via bead cytometry, for example, routinely include hundreds or thousands of cells. It is undoubtedly more difficult to draw conclusions from a limited sample size; conclusions of rheological behavior, for example, could be caused by chance. Efforts to augment existing methods to allow hundreds or thousands of cells to be interrogated, along with the use of statistical tools to classify results that are more or less likely to be caused by chance, offer considerable return in improved confidence when attempting to answer the important questions raised above.

In the present work, an optical stretcher augmented with syringe rotation for improved throughput was used to examine >10,000 cells and to generate creep compliance and complex modulus measurements in stretching and recovery of >2,000 cells. Two model cell types were used: (1) the adult human bone-marrow-derived mesenchymal stem or stromal cell (MSC), which undergoes the attached-to-suspended transition repeatedly during passaging, most notably at the last detachment immediately before re-implantation for therapeutic purposes; and (2) the transformed—or immortalized—murine fibroblast, which is relatively easy to culture due to rapid proliferation, does not enter senescence, and is commonly used as a model cell in rheology studies [46, 83, 171, 172]. Together, the use of disparate cell types supports generalization of results across the scope of connective tissue cells. Testing in both the time and frequency domains allows estimation of the fluidity or power-law exponent a by two methods—the slope of the creep compliance response on a log-log scale and the phase lag under an oscillatory load—to reduce the role of chance and experimental artifacts. Finally, the statistical tool of bootstrapping is applied for the first time in this context to estimate variance in key parameters and therefore to enable hypothesis testing even when the assumptions required by parametric tests might not be met.

Existing methods

The methods used in this study build on the following demonstrated techniques:

MSC isolation and expansion. MSCs are mononuclear adherent tissue cells that are multipotent; that is, they can be taken down various differentiation pathways toward terminal cell types [54, 173]. MSCs are found in many connective tissues and are most commonly obtained via bone marrow aspiration. The cells are separated from non-adherent cells and from non-MSCs by density centrifugation and seeding atop tissue culture polystyrene, on which MSCs are triggered to rapidly proliferate by mechanosensing of a stiff substratum [59]. The cells divide several times per week and must be passaged upon near-confluence; that is, they must be detached, diluted, and re-seeded onto new surfaces [58]. MSCs are routinely expanded in the attached state and can be detached by methods such as trypsinization for study in the suspended state.

Optical stretching in the time domain. This technique, introduced by Guck and Käs et al. [34], measures the deformability of single whole cells in suspension by applying

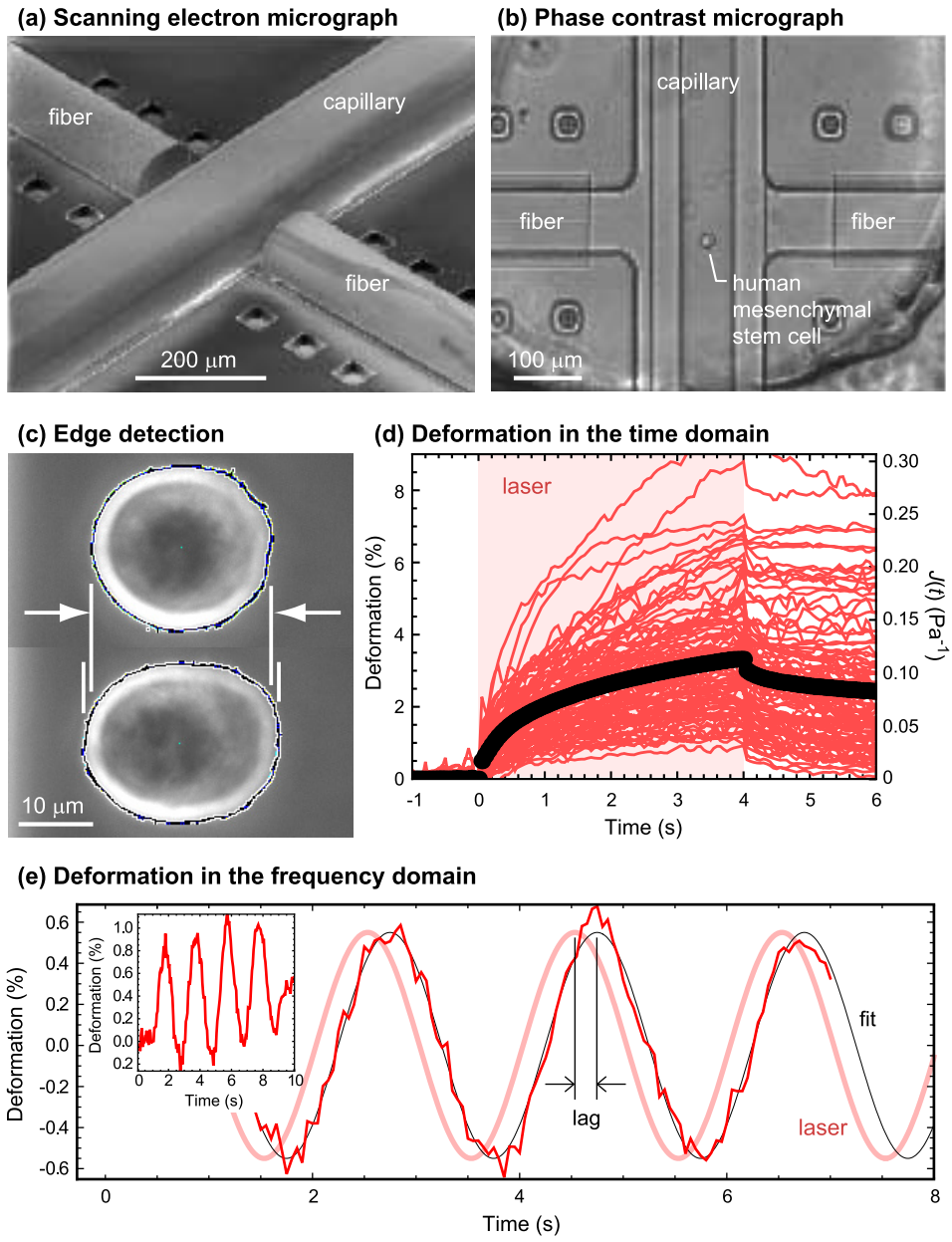

Figure 3-1: **Optical stretching (OS) measures the stiffness of adherent cells in suspension, absent physical contact and direct influence of substratum chemomechanical properties.** (a) Scanning electron and (b) phase contrast micrographs of opposing optical fibers that are positioned to face a hollow glass capillary filled with cell suspension during operation. Under the fibers and capillary lie microfabricated grooves to ensure correct orthogonal alignment and fiber elevation; adjacent $50 \times 50\,\mu m^2$ holes with $100\,\mu m$ spacing serve as calibration marks to indicate fiber position. (c) Edge detection of cell shape with machine vision before (top) and during (bottom) irradiation; the percent elongation of the cell diameter along the laser beam axis is used to quantify cell deformability over time, or creep compliance when normalized by the applied photonic stress. (d) From one passage of human mesenchymal stem cells (MSCs, $n = 98$ cells), gray lines show individual cell deformation and creep compliance in response to a step increase and decrease in laser power. Black markers show deformation geometric mean for 1,288 cells. (e) Oscillatory deformation (minus baseline) of a single cell in response to sinusoidal loading. Inset, edge-detected deformation before baseline removal. The total phase lag includes both experimental lag (which is subtracted in analysis) and the viscoelastic lag of the cell, a measure of cell fluidity.

photonic pressure. The experimental setup consists of two well-aligned coaxial optical fibers that issue divergent counter-propagating laser beams into a suspension of cells (Fig. 3-1(a,b)) [34]. Light that passes into a cell moves from a region of lower to higher dielectric index, and the resulting change in photon momentum produces an outward force normal to the cell membrane. This optical effect automatically centers any cell proximate to the intersection of the beams and enables trapping of single cells. The resultant body force is zero when a cell is trapped, leaving only second-order surface forces that induce stretching (Fig. 3-1(c)). Time-dependent images of the deforming cell are recorded during the process for later analysis [174]. A white ring visible in phase contrast microscopy is fit by a radial function decomposed into Fourier components [174] and the extension of the cell along the laser axis is used to quantify cell deformation.

The optical stretcher offers the possibility of large-scale cell sampling in a flow configuration similar to that used in fluorescence flow cytometry, with higher throughput than is possible from AFM or micropipette aspiration. The technique has previously been used to detect differences in the whole-cell deformability of normal and diseased cells [35].

Whole-cell rheological characterization. The cell is undoubtedly heterogeneous, containing a variety of molecules that individually display nonlinear elasticity in the form of single polymer chains; however, an effective whole-cell stiffness can be usefully defined and measured [29, 34, 50, 87]. Linear viscoelasticity has been reported to hold via other experimental techniques at sufficiently small deformations [48, 50, 83, 175], though this finding has not yet been confirmed via optical stretching. One motivation for probing the whole cell is that complex networks can, under certain circumstances, exhibit an emergent behavior that differs from the constituent individual components (as is the case with soft glassy materials) [49]. Additionally, whole-cell mechanical measurements offer the possibility to sort cells for therapeutic purposes or to characterize disease states that manifest themselves as changes in mechanical properties [35, 176].

Cytochemical perturbation by ATP depletion and confirmation by luciferase assay. A standard technique for depleting the cell's power source uses deoxyglucose and sodium azide [52, 96, 157, 177] to eliminate ATP stores within the cell and inhibit further production. Depletion is confirmed by lysing the cells and performing on the lysate a luciferase-based luminometry assay (i.e., a light-producing chemical reaction that relies on ATP).

Model fitting and parameter estimation. The twin goals that always accompany model fitting are to match the data as well as possible and to work with the simplest suitable model. These goals are simultaneously evaluated with fitting metrics that not only score fitting success but also penalize model complexity. Two examples of such metrics are the Akaike Information Criterion [178] and the adjusted r^2 metric [179]. Though standard tools, they have had only a rare presence so far in comparing constitutive equations of cell deformability [85].

Parameter estimation is achieved by nonlinear fitting to a model of interest, or by applying established estimation techniques (such as by estimating the phase lag ϕ in the deformation model $F\sin(\omega t - \phi)$ (when the frequency ω is known) by decoupling that expression to $F_1\sin(\omega t) + F_2\cos(\omega t)$ and $\phi = \tan^{-1}(F_2/F_1)$, which constitutes a simpler linear regression problem).

Novel methods

To complete this study, it has also been necessary to develop new techniques and to integrate techniques that have not previously been applied in this context.

Optical stretching in the frequency domain. Wottawah et al. previously simulated frequency response based on an assumed lumped-component model [38]. Because the validity of this lumped-component model is being tested in the present work, it is important to perform actual frequency-domain testing to measure complex modulus. The optical stretching software was adapted to increase frame rates from 10–20 frames s^{-1} to 50 frames s^{-1} (by cropping the image recorded from the camera before frames are transmitted) and to estimate phase lag accurately (by triggering the beginning of frame recording with a return signal from the DAQ card that confirms the stretching profile is being transmitted to the laser, and by measuring the delay with visible laser pulses, see Fig. C-2). Background deformation is also removed either by subtracting a moving average or by fitting non-sinusoidal information to a quadratic function, which is then subtracted.

Wafer-scale microfabrication of alignment structures for optical stretcher fixturing. The optical stretcher developed by Guck et al. [34, 170] and augmented by Lincoln et al. [174, 180] uses alignment structures of photocurable epoxy to position fiber height and maintain perpendicular alignment between the fibers and the capillary [174] (Fig. 3-1(a,b)). The substrate was previously a glass slide, and the structures were produced serially and with a single design, which limited consistency and opportunity to test different structures (F. Lautenschläger, personal communication). For the present study, wafer-scale microfabrication tools were used to produce dozens of structures simultaneously on 4-inch glass wafers in a cleanroom, improving consistency and providing several options of groove size and arrangement (App. C.2, Fig. C-6). These devices and protocol have been shared with the Guck group for wider implementation in future optical stretching studies.

Syringe rotation during optical stretching to keep heavy adherent cells suspended. Adherent cells tend to sink in media, as part of their characteristic behavior of settling onto and attaching to a suitable surface. During optical stretching experiments on suspended adherent cells, consequently, the challenge arises of how to keep these cells in the suspended state. As described in App. C.2, a syringe rotator was developed that rotates the cell suspension syringe through nearly a complete circle at 6 rpm for the duration of the stretching experiment (Fig. C-7). Inside the syringe, cell movement is described by small circles in suspension, preventing sinking to the bottom of the syringe or attachment to the sides of the syringe. As long as cell density is sufficiently low (to prevent circular paths of multiple cells from intersecting, which would result in adhesion and clumping), this tool provides a steady supply of single cells.

Interpolation to combine multiple deformation profiles with precise timing. Guck et al.'s optical stretching technique records camera frames of phase contrast images as they are received from a camera. A complication is that these frames do not arrive at evenly spaced times for a single cell or between groups of cells; rather, the frame rate can vary (from 10–15 frames s^{-1}, for example). Consequently, it is difficult to compare the averaged response of all cells at precise times such as 0.50 s after the start of laser initiation. This factor does not represent any important disadvantage when comparing creep compliance between populations of cells [39], but it is undesirable when identifying the best-fitting constitutive relation for creep compliance vs. time, or for estimating phase lag in the frequency domain. The use of 20 frames s^{-1} or 50 frames s^{-1} interpolation during the analysis process, as described in App. C.2 (Fig. C-5), allows comparison

of average cell deformability or creep compliance at precise times and allows accurate extraction of phase lag.

Bootstrapping to extract the variance of rheological parameters. After model fitting, it is always desirable to know the error in fitted parameters, as well as how likely the choice of a constitutive model could be caused by chance alone. Ideally, an experiment or set of experiments would be repeated over and over to provide this information. Another possibility is to use the existing data to identify the uncertainty in one's conclusions. A statistical technique called bootstrapping, or resampling with replacement, exists that provides this information without having to repeat entire studies and without requiring assumptions needed to justify parametric methods of estimating variance [181–186].

An overview of bootstrapping is provided in App. B.1. Briefly, the key concept is that existing data are the best estimate for any possible future data. For example, out of a set of measurements from n different samples, a new set (also of size n) is created by resampling with replacement, and the candidate constitutive equation(s) are fit to, and parameters estimated from, the new set. This process (sampling with replacement and fitting) is repeated many times—perhaps thousands or tens of thousands of times. The standard deviation of the resulting distribution of fitted parameters, multiplied by a factor close to one, estimates the standard error of that same parameter fitted to the original set. Furthermore, if one picks the better model for each bootstrapped set, the fraction of successes for each model effectively constitutes a statistical p-value that can be used to reject hypotheses with the rigor of statistical significance. The bootstrapping technique has not previously been applied to cell rheology investigations.

3.2 Materials and methods

Cell culture and ATP depletion

Immortalized murine NIH 3T3 fibroblasts and primary adult human mesenchymal stem cells (MSCs) were cultured *in vitro* as model cells to characterize cell deformability in response to chemomechanical cues. Fibroblasts were cultured as described in Chap. 2 by using the protocol in App. C.1. MSCs were obtained from the bone marrow of three adult donors (via Stem Cell Technologies or ReachBio LLC), isolated and expanded by density gradient centrifugation and plating on tissue culture polystyrene [58], and cultured according to protocols described in App. C.1. Because all parameters were constant within error vs. MSC passage number (discussed in §5.4.1), data from all passages were pooled.

ATP was depleted by exposing fibroblasts to 0.05% sodium azide (which inhibits ATPase and thus ATP synthesis) and 50 mM 2-deoxyglucose (which depletes intracellular ATP stores), as described in App. C.1. The degree of ATP depletion was assayed by the luciferase assay as described in App. C.3 and was found to be {95%, 96%, 96%, 98%} in four replicate experiments. Initial ATP depletion experiments were performed both before and after trypsinization. When performed before trypsinization, the suspended cells were not spherical (Fig. 3-2(a)), indicating that cell remodeling processes initiated by trypsinization and detachment could not be completed, and confirming that active cytoskeletal processes were interrupted by ATP depletion. All stretching experiments were thus performed by depleting ATP after the cells were detached, which resulted in spherical cells (Fig. 3-2(b)). The remodeling process that occurs during and after detachment and the influence of this transformation on effective cell deformability is discussed in §5.3.2.

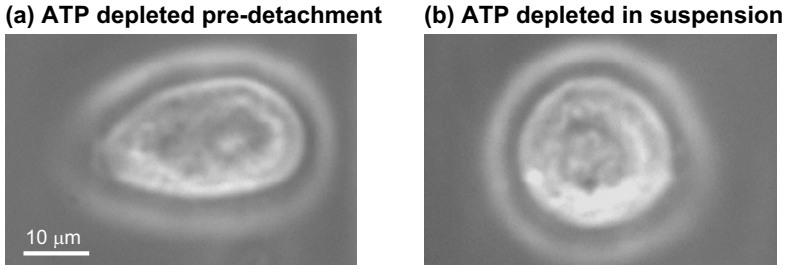

Figure 3-2: **ATP depletion hinders the ability of adherent cells to remodel into a spherical shape following substratum detachment.** (a) Cells exposed to an ATP depletion cocktail before trypsinization generally appear non-spherical when later examined in suspension. (b) Cells exposed to an ATP depletion cocktail tens of minutes after suspension appear spherical, having remodeled through actomyosin-enabled processes further investigated in §5.3.2.

Microfluidic optical stretching

Cell responses to chemomechanical cues were obtained via optical stretching, which evaluates whole-cell deformability in the suspended state as measured by creep compliance or complex modulus. As described in App. C.2, cells at 50–80% confluence in T-25 (25 cm^2 culture area) flasks were treated with 0.05% trypsin / 1 mM EDTA until the cells detached with gentle tapping (approximately 5–10 min). The detachment process was halted by adding complete media, and the suspension was then centrifuged and resuspended in complete media to a cell density of 100–500 $K\,mL^{-1}$. A syringe containing the cell suspension was attached to a customized syringe rotator. The cells were injected into a hollow square glass capillary (80 μm ID, 160 μm OD) that was positioned between two single-mode optical fibers split from a 1064 nm fiber laser (YLR-3X2-1064, IPG Photonics) [174]. The laser was controlled by using a customized LabView program and a National Instruments data acquisition card (USB-6229).

After injection of the cell suspension into the capillary, a microfluidic valve (Upchurch) was used to connect the capillary to adjustable-height reservoirs capable of controlling the flow to bring a single cell to a motionless position between the fibers. Cells were stretched only when the flow was stopped, as any residual flow tends to rotate the cell during stretching.

In the time-domain experiments, trapping power (0.2 W for 2 s), stretching power (0.9 W for 4 s), and trapping power (0.2 W for 2 s) per fiber were applied to bring the cell to an equilibrium position, deform the cell, and allow recovery, respectively. Simultaneously, cell images were recorded by phase contrast microscopy at 10–15 frames s^{-1}. In the frequency-domain experiments, cells were interrogated in the frequency domain by irradiating them with a sinusoidal laser profile (frequency 0.25 Hz to 5 Hz) for 8 s with a mean power of 1 W per fiber and a peak-to-peak value of 1 W per fiber, with a 1 s trapping period at 0.2 W before and after. Images were recorded at approximately 50 frames s^{-1}. Laser power values were chosen to ensure measurable cell deformation while minimizing cell heating. Laser impingement at this wavelength results in a temperature increase on the order of $10^{\circ}C\,W^{-1}$ [187–189]; 1 W stretching power per beam is therefore estimated to increase the cell temperature temporarily from room temperature to 35–50°C.

Photonic stress on the cell was calculated by using the method described by Guck et al. [170, 180] (App. C.2). Briefly, beam widening after exiting the single-mode fiber core was calculated from the position of the fibers, the geometry of the chamber, and the refractive indices of index-matching gel, glass, and cell suspension media. A refractive index value of 1.372 for eukaryotic cells [86] was confirmed by suspending cells in different concentrations of bovine serum albumin [190, 191], to see when index matching (equal brightness inside and outside the cell) occurred. The estimate of photonic stress was not calibrated to a verifiable standard, however, and therefore val-

ues of creep compliance and complex modulus should be considered as effective values suitable for identifying relative trends for this optical stretching assembly only.

Data analysis

A customized LabView program was used to detect the edge of each stretched cell by its brightness gradient and then to calculate deformation (quantified as the normalized change in diameter along the laser axis) over time [174]. All cells that rotated perceptibly were ruled out, as were cells for which the deformation changed by a value of >1% during trapping and cells for which the responses suggested rotation (e.g., sudden discontinuities in deformation or negative deformation), as advised by Lincoln [180]. Data were interpolated to exactly 20 frames s^{-1} (creep compliance) or 50 frames s^{-1} (complex modulus).

In time-domain experiments, reported maximum deformation values correspond to the deformation at the end of the 4 s stretching period. Various phenomenological constitutive equations were considered for the average time-dependent stretching and recovery of cells by OS. Candidates included lumped-component viscoelastic models such as a four-element model (a series-spring-dashpot unit in series with a parallel-spring-dashpot unit):

$$\varepsilon(t) = \begin{cases} \dfrac{1}{E_1}\left(1 - e^{-tE_1/\eta_1}\right) + \dfrac{t}{\eta_2} + \dfrac{1}{E_2} & (0.5 \le t \le 4\,\mathrm{s}), \\ \dfrac{1}{E_1}\left(1 - e^{-tE_1/\eta_1}\right) e^{-(t-4\,\mathrm{s})E_1/\eta_1} + \dfrac{4\,\mathrm{s}}{\eta_2} & (4 < t \le 6\,\mathrm{s}); \end{cases} \tag{3.1}$$

a three-element model (a series-spring-dashpot unit in series with a spring) with a stretched exponential of power β [192]:

$$\varepsilon(t) = \begin{cases} \dfrac{1}{E_1}\left(1 - e^{-(tE_1/\eta_1)^{\beta}}\right) + \dfrac{1}{E_2} & (0.5 \le t \le 4\,\mathrm{s}), \\ \dfrac{1}{E_1}\left(1 - e^{-(tE_1/\eta_1)^{\beta}}\right) e^{-[(t-4\,\mathrm{s})E_1/\eta_1]^{\beta}} & (4 < t \le 6\,\mathrm{s}); \end{cases} \tag{3.2}$$

and power-law models of the form At^a and $At^a + B$ (i.e., pure and offset power laws). Lumped-component constitutive equations can be found most easily by combining Laplace-domain compliances ($1/E$ for springs and $1/(\eta s)$ for dashpots) in series or in parallel, multiplying by the Laplace-domain term $\sigma_0(1 - e^{-4s})/s$ to represent the laser excitation profile described above, and taking the inverse Laplace transform to determine the time-dependent deformation $\varepsilon(t)$.

Model equations were fit to the data by nonlinear regression (Mathematica) with $1/y^2$ weighting applied to squared residuals. The fitting period began at 0.5 s because the creep compliance measurements were obtained with an earlier software version, not yet optimized for synchronicity, and were not synchronized to better than 0.1 s. Fits were compared by the Akaike Information Criterion (AIC) value [178] or by the adjusted r^2 value to accommodate models with different numbers of fitting variables [179]. AIC is calculated as

$$\mathrm{AIC} = n \ln \sum_i [y_i - f(x_i)]^2 + 2k + \frac{2k(k+1)}{n-k-1}, \tag{3.3}$$

where n is the sample size, f is the fitting function, and k is the number of fitting parameters. The first term, effectively $n\ln(\mathrm{RSS})$ where RSS is the residual sum of squares,

is a penalty term for poor fitting. The second term is a penalty term for excess parameters, and the third term is a finite-sample-size correction term, shown for completeness, that is negligible for large n. The most likely model is the one with the smallest AIC value.

The adjusted r^2 parameter is calculated as

$$r^2_{\text{adj}} = 1 - \frac{\sum_i [y_i - f(x_i)]^2}{\sum_i (y_i - \overline{y})^2} \left(\frac{n-1}{n-k-1} \right). \tag{3.4}$$

The presence of k in the second term penalizes models with more fitting parameters. The model with the largest adjusted r^2 value is the best at reducing error without adding excessive model complexity.

In frequency-domain experiments, amplitudes and phase angles were extracted by one of two methods, which were found to give equivalent results (Fig. C-3). In the first method, a moving average with a width of a single period was subtracted from the deformation to center the deformation around zero. Then, parameters from the equation $\varepsilon(t) = F \sin[2\pi f(t - t_0 - t_1) - \phi]$ were fit by nonlinear regression (Mathematica) where F is the amplitude, f is the applied frequency, $t_0 = 41$ ms is the measured lag of the tool (processing time and transmission of laser data and image frames) as determined by timed laser pulses (Fig. C-2) and optimization of the software to ensure synchronicity to better than 10 ms, $t_1 = 10$ ms is half the inverse frame rate to accommodate the finite collection time of each image [193], and ϕ is the phase angle, or loss angle, of the cell. In the second method, linear regression (LabView) was used to fit parameters from the equation $\varepsilon(t) = F_1 \sin[2\pi f(t - t_0 - t_1)] + F_2 \cos[2\pi f(t - t_0 - t_1)] + F_3 t^2 + F_4 t + F_5$. The last three terms constitute a quadratic fit to the underlying baseline signal, which is subtracted. It can be verified that $F = (F_1^2 + F_2^2)^{1/2}$ and $\phi = \tan^{-1}(F_2/F_1)$. Complex modulus magnitude $|G^*|$ was calculated as σ_0/ε_0, where σ_0 is the amplitude of the photonic stress and ε_0 is the amplitude of a sinusoid fitted to cell deformation. The power-law exponent a was calculated as $a = 2\phi/\pi$, where ϕ is the phase lag of cell deformation.

All values are expressed as mean ± standard error unless otherwise noted. The standard error of fitted constitutive law parameters was determined by using the bootstrapping technique (App. B.1). All values converged suitably within 1,000 iterations (Fig. 3-7).

In experiments of repeated stretching, stretches were performed with intermediate pauses of several seconds at most, so that ten 10 s stretches were generally completed within 2 min. Following observation of increased stiffness and decreased power-law exponent with repeated stretching, experiments were performed to see if this effect could be caused by accumulated debris (e.g., proteins or lipid) trapped in line with the laser axis. In these experiments, a small flow was induced after several stretches to flush the capillary, and this flow was increased until the cell was pulled out of a trapping configuration. The cell was then brought back to the laser axis, trapped again, and stretched. The last stretch was still consistent with increased stiffness and decreased power-law exponent, and these parameters did not return to their original values seen at the first stretch, which would have been consistent with the hypothesis of beam attenuation or scattering caused by trapped debris. Therefore, it is concluded that alterations in these parameters were indeed attributable to intrinsic behavior of cells exposed to repeated mechanical loading.

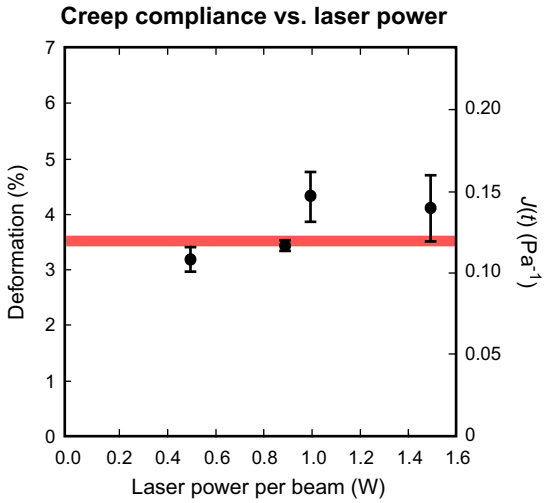

Figure 3-3: **MSC deformation vs. laser power indicates linear viscoelasticity.** Creep compliance measurements that are independent of laser power (within error for per-beam powers up to 1.3 W above trapping power after 4 s stretching) indicate that MSCs are deformed in the linear regime at and below this power level. (All data shown as mean ± standard error, $n \geq 35$.)

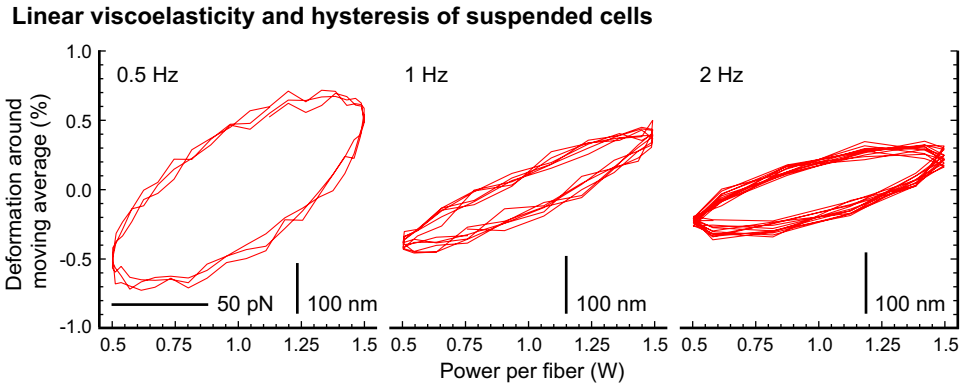

Figure 3-4: **Elliptical Lissajous figures support MSC linear viscoelasticity.** Elliptical paths of MSC deformation vs. power (for three different cells, scale bars shown) indicate that cells are deformed in the linear regime for powers up to at least 1.5 W.

3.3 Results

3.3.1 OS can measure whole cells in the linear regime

As shown in Fig. 3-3, creep compliance is not detectably altered by laser power up to at least 1.5 W per beam. A linear response (i.e., constant deformability with changing load magnitude) is also indicated by elliptical Lissajous figures of deformation vs. load in Fig. 3-4. (The elliptical nature of these figures also exemplifies the viscoelastic nature of the cell; an elastic solid would be represented by a straight line.) Additionally, a near-constant moving average of creep compliance vs. cell diameter, as shown in Fig. 3-5, indicates that whole-cell stiffness is not detectably dependent on suspended cell major diameter.

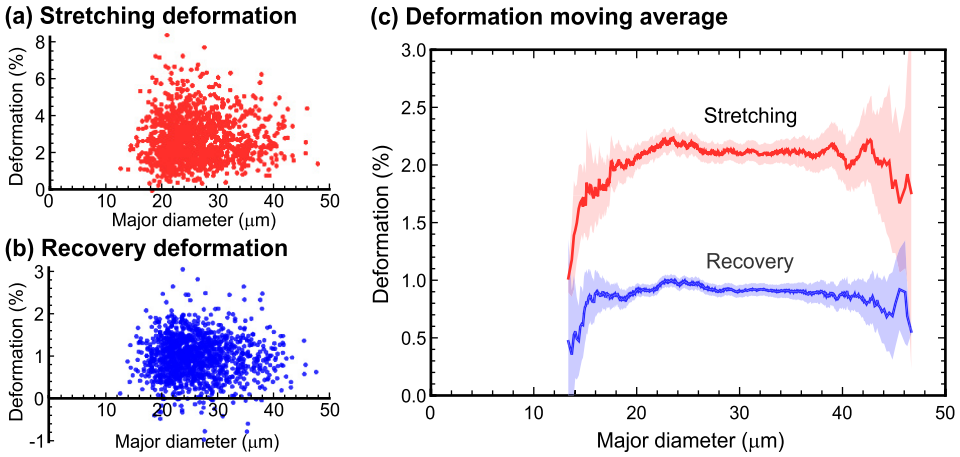

Figure 3-5: **MSC stretching and recovery deformation are essentially independent of suspended cell diameter.** (a) Individual stretching and (b) recovery deformation values after 2 s as a function of cell major diameter; (c) 400-cell moving average (mean ± 95% confidence interval) reveals no dependence, within error, of cell deformation on suspended cell major diameter.

3.3.2 Suspended cells exhibit power-law rheology in the time and frequency domains, and in stretching and recovery

Of the constitutive models fitted to creep compliance data and compared by adjusted r^2 or Akaike Information Criterion (AIC) value, the best fits were acquired with offset and pure power laws (Table 3.3). These fits generally scored better than the lumped-component models.

In the frequency domain, the MSC power-law exponent—as calculated from the phase lag—was insensitive to driving frequency and had an average value of $\overline{a} = 0.38 \pm 0.01$ ($n = 183$). This result rules out the offset power law in Table 3.3, instead

Table 3.3: **Estimated MSC creep compliance models (power-law rheology and lumped-component) scored with adjusted r^2 and AIC metrics** ($n = 1,288$). Larger adjusted r^2 values and smaller AIC values indicate better fits. The combination of model scoring and the finding of $a = 0.38$ in the frequency domain leads to the selection of the pure power law with separate stretching and recovery exponents (shown in bold) as the best model.

Viscoelastic model	Fitted parameters	Adjusted r^2	AIC
Parallel-spring-dashpot (E_1, η_1) in series with dashpot (η_2)	$E_1 = 21\,\text{Pa}$, $\eta_1 = 4\,\text{Pa s}$, $\eta_2 = 46\,\text{Pa s}$	0.997	−324
Parallel-spring-dashpot (E_1, η_1) in series with series-spring-dashpot (E_2, η_2)	$E_1 = 36\,\text{Pa}$, $\eta_1 = 11\,\text{Pa s}$, $E_2 = 50\,\text{Pa}$, $\eta_2 = 46\,\text{Pa s}$	0.998	−348
Power law with one exponent (At^a stretching, Ct^a recovery)	$A = 0.072\,\text{Pa}^{-1}$, $a = 0.36$, $C = 0.027\,\text{Pa}^{-1}$	0.9998	−626
Parallel-spring-dashpot (E_1, η_1) in series with spring (E_2) , with stretched exponential factor β	$E_1 = 2.8\,\text{Pa}$, $\eta_1 = 89\,\text{Pa s}$, $E_2 = 132\,\text{Pa}$, $\beta = 0.4646$	0.99993	−733
Power law with separate exponents (At^{a_S} stretching, Ct^{a_R} recovery)	$A = 0.072\,\text{Pa}^{-1}$, $a_S = 0.37$, $C = 0.029\,\text{Pa}^{-1}$, $a_R = 0.25$	0.99995	−780
Power law with separate exponents and offsets ($At^{a_S} + B$ stretching, $Ct^{a_R} + D$ recovery)	$A = 0.12\,\text{Pa}^{-1}$, $a_S = 0.24$, $B = -0.048\,\text{Pa}^{-1}$, $C = 0.027\,\text{Pa}^{-1}$, $a_R = 0.27$, $D \approx 0$	0.999996	−1,064

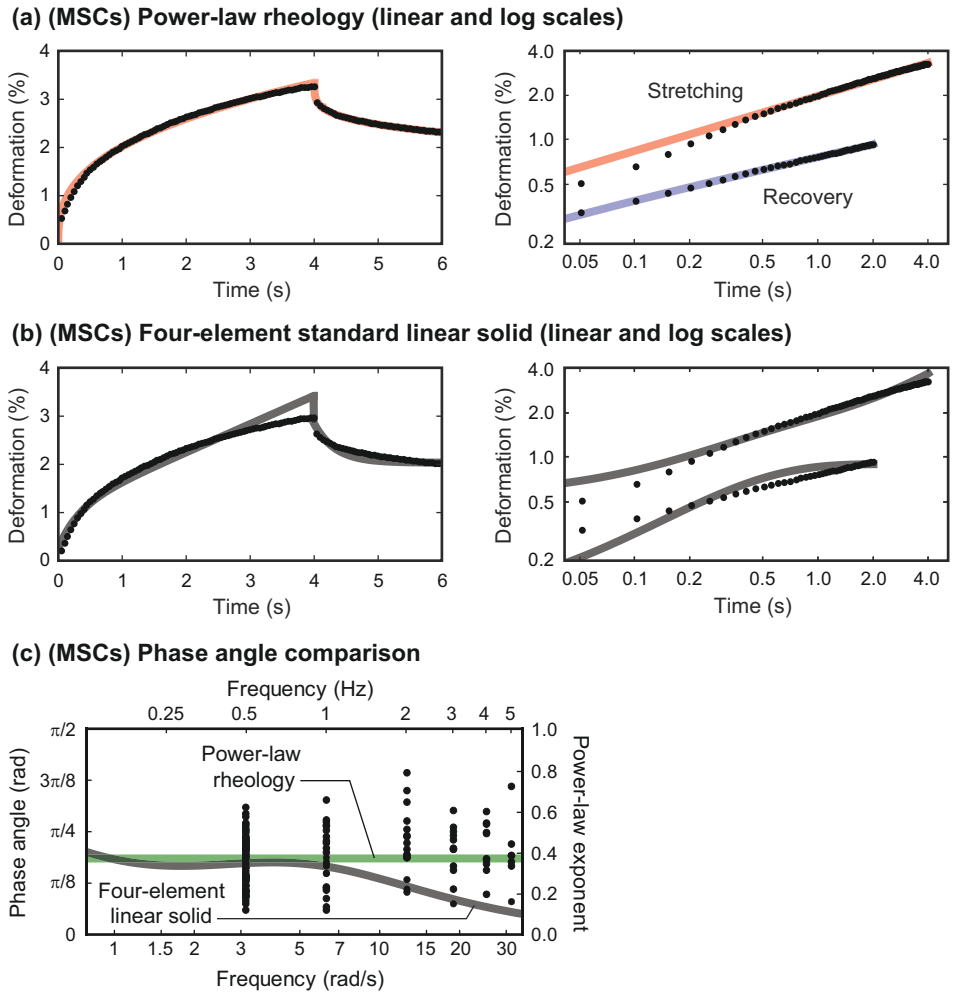

Figure 3-6: **Suspended MSCs exhibit power-law rheology, as measured by optical stretching.** Comparison of (a) power-law rheology vs. (b) 4-element lumped-component viscoelasticity (shown on linear and log-log scales) as a constitutive relation for whole-cell deformability over time. (c) Constant phase lag corresponding to $\overline{\alpha} = 0.38$ at different frequencies confirms power-law rheology.

supporting the second-best-scoring model of a pure power law with distinct exponents for stretching and recovery. The combined time- and frequency-domain measurements are shown in Fig. 3-6. To check whether the better fit of the power-law model was possibly caused by chance, the fitting comparison was performed 1,000 times while resampling the data with the bootstrap technique (Fig. 3-7). The power-law model had a higher adjusted r^2 value and lower AIC than the four-element lumped-component model each time, indicating that the better fit of the power-law model is unlikely to be caused by chance ($p < 0.001$). Bootstrapping was also used to identify the uncertainty in the estimated parameters (Fig. 3-7), leading to a parameterization of

$$\varepsilon(t) = \begin{cases} At^{\alpha_S} & (0.5 \le t \le 4\,\mathrm{s}) \\ \varepsilon(4\,\mathrm{s}) - C(t - 4\,\mathrm{s})^{\alpha_R} & (4 < t \le 6\,\mathrm{s}), \end{cases} \tag{3.5}$$

where $A = 2.11 \pm 0.03$, $\alpha_S = 0.37 \pm 0.01$, $C = 0.86 \pm 0.01$, and $\alpha_R = 0.25 \pm 0.01$, where A and C are expressed in terms of percent deformation. The bootstrap means were essentially the same as the original fitted parameters; equivalently, the distributions were symmetric around the means, indicating negligible estimator bias.

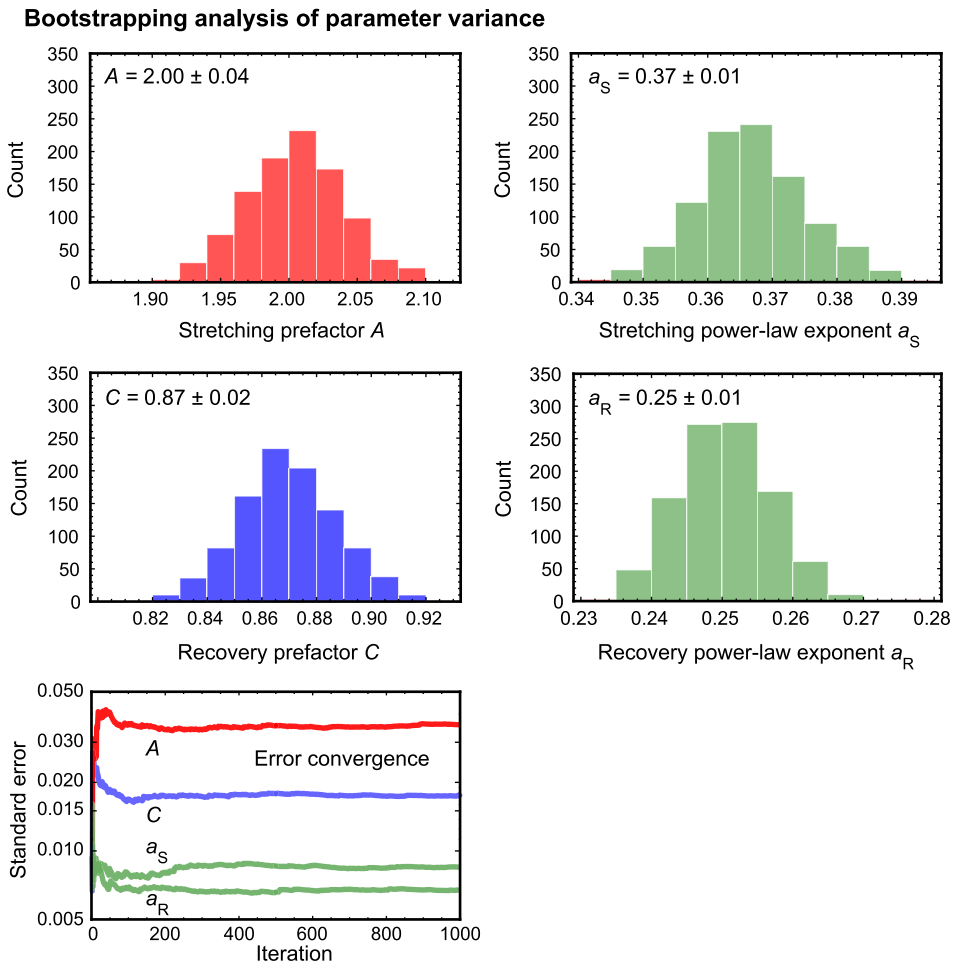

Figure 3-7: **The standard error of fitted parameters and their possible bias was determined by using the bootstrapping technique.** Bootstrapping distribution, distribution mean and standard deviation (equivalent to parameter standard error as $n \to \infty$), and convergence are shown for each parameter. All estimates of variance suitably converged and all bootstrapped distributions were essentially symmetric, indicating negligible estimator bias.

The finding of power-law rheology in MSCs was replicated with fibroblasts (Fig. 3-8): in creep compliance, the parameterization yielded $A = 1.55 \pm 0.05$, $a_S = 0.34 \pm 0.01$, $C = 0.80 \pm 0.03$, and $a_R = 0.23 \pm 0.01$ ($n = 249$). In the frequency domain, the phase lag of fibroblasts corresponded to an average power-law exponent of $\overline{\alpha} = 0.39 \pm 0.01$ ($n = 161$).

3.3.3 ATP depletion does not detectably alter power-law exponent

The fluidity of ATP-depleted fibroblasts (as quantified by the average power-law exponent $\overline{\alpha}$) was 0.39 ± 0.02 in the time domain (creep compliance measurements, vs 0.34 ± 0.01 for controls) and 0.36 ± 0.01 in the frequency domain (complex modulus measurements, vs 0.39 ± 0.01 for controls). Cumulative distributions and histograms of single-cell power-law exponents are compared in Fig. 3-9.

The pooled values from time- and frequency-domain testing of fibroblasts are $\overline{\alpha} = 0.368 \pm 0.008$ ($n = 258$) for ATP depletion vs. $\overline{\alpha} = 0.358 \pm 0.010$ ($n = 410$) for no treatment. In light of the standard errors of the parameters, these values are not detectably different and could have arisen by chance. Put another way, the influence of

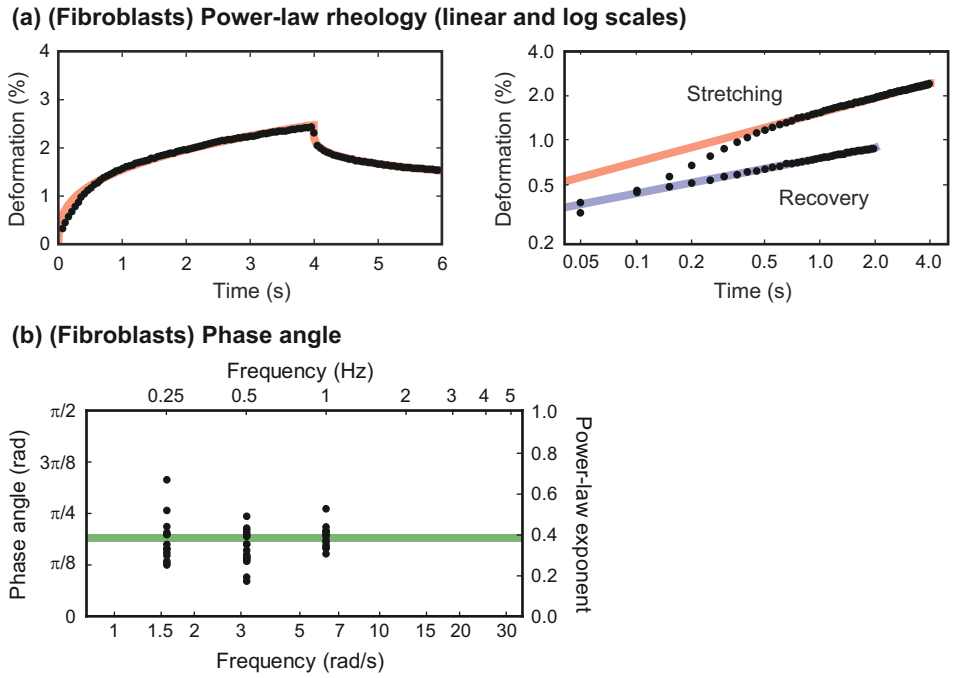

Figure 3-8: **As with MSCs, fibroblasts exhibit power-law rheology in both the time and frequency domains.** This finding is illustrated by (a) a good fit of Eq. 3.5 to creep compliance data and (b) a phase angle not detectably dependent on frequency.

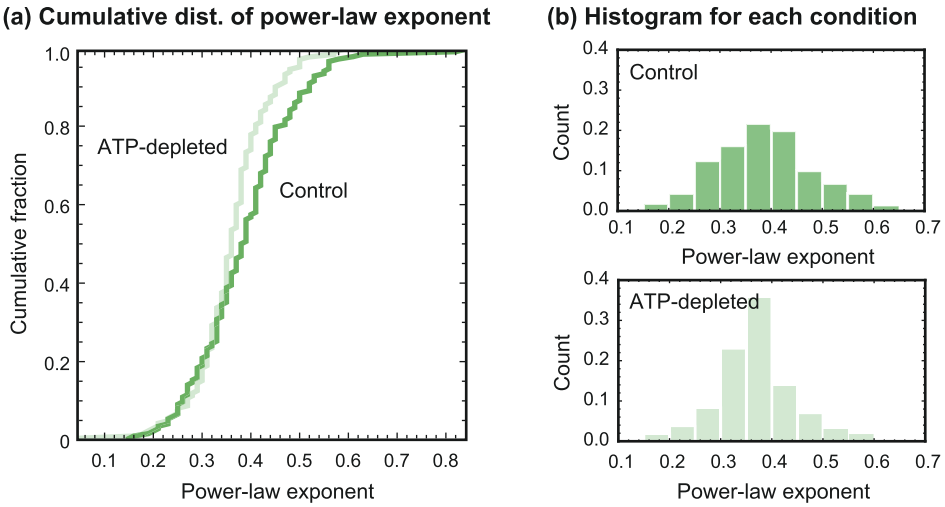

Figure 3-9: **Depletion of 95% of the ATP in cells does not detectably influence the measured phase lag or hysteresivity, linked to the average power-law exponent or noise temperature in suspended fibroblasts.** (a) Cumulative distributions and (b) histograms of exponent values. The width of the distribution, as quantified by standard deviation σ_a, is significantly less for the ATP-depleted cells (0.0776 vs. 0.1059, $p = 0.0177$ as determined by bootstrapping).

ATP presence or absence during the deformation process is not detectable.

However, the standard deviation σ_a of the power-law exponent was lower for the ATP-depleted population (0.0776 vs. 0.1059), and bootstrapping showed that this difference was unlikely to be caused by chance ($p = 0.0177$). This finding indicates that ATP depletion reduces the heterogeneity of cell populations, as discussed in §3.4.2 and more fully pursued in Chapter 4.

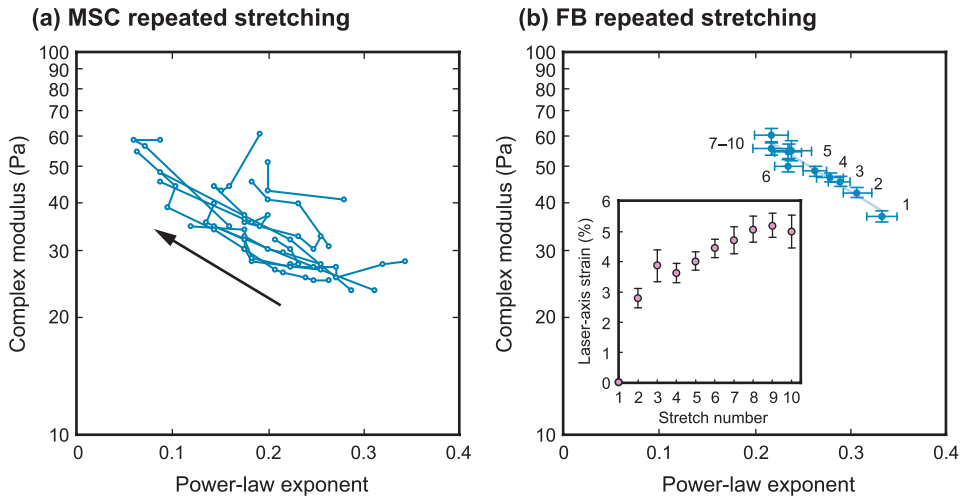

Figure 3-10: **Repeated stretching of single cells reveals a correlation between larger stiffness and smaller power-law exponent as the cell is stretched taut.** (a) Repeated stretching of single MSCs at 0.5 Hz generally results in increased stiffness $|G^*|$ and decreased power-law exponent α. (b) Repeated stretching of fibroblasts at 1 Hz reveals the same trend, shown as an average for each stretch number (inset, increasing cell diameter normalized to initial value along the laser axis with repeated stretching).

3.3.4 Stiffness and power-law exponent are correlated at the single-cell level

When 10 s oscillatory loads were applied repeatedly to single cells, their deformation amplitude F and phase angle ϕ tended to decrease; equivalently, repeated loading increased their stiffness $|G^*|$ and decreased their fluidity α. This trend can be seen for single MSCs in Fig. 3-10(a). The larger number of fibroblasts tested under these conditions makes the trend more difficult to discern for single cells (data not shown) but easier to discern when average stiffness and fluidity values are plotted for each successive loading event (Fig. 3-10(b)). Cell diameter along the laser axis also generally increased during repeated stretching (Fig. 3-10(b, inset)).

3.4 Discussion

3.4.1 Linear power-law rheology characterizes suspended cells

The topic of this chapter is how suspended cells deform, and deformation data from two rheological domains, collected from two disparate eukaryotic cell populations—along with the results of chemical inhibition of metabolic processes—provides considerable new information with which to examine this subject.

The first focus is the finding of power-law behavior in suspended cells by a non-contact technique, which extends and is compatible with many studies in the literature that have explored the dependency of PLR on the presence of certain cytoskeletal components. Other groups have applied cytoskeletal inhibitors to reduce stress fibers and inhibit actomyosin contraction [157], decoupled attachment mechanisms by attaching probes with various molecular linkers to engage an assortment of transmembrane receptors [29, 43], and minimized adhesion to reduce the formation of features such as focal adhesions and stress fibers by testing cells on relatively inert poly(HEMA) coatings [84] and with micropipette aspiration [83]. Cells under all of these conditions have exhibited power-law behavior. The present study takes the avoidance of contact effects, stress concentrations, and focal adhesions to its limit; during OS the MSCs are totally suspended and engaged with a photonic load only.

Both a pure power law and an offset power law scored better as constitutive law fits compared to lumped-component models that included groups of one or several springs and dashpots. The frequency-domain finding of an average power-law exponent of $\overline{a} = 0.38 \pm 0.01$ justifies rejecting the best-scoring creep compliance model (with its $a_S = 0.24$) in favor of the second-best model (with $a_S = 0.37 \pm 0.01$). It may be that the detected offset represents an intrinsic or experimental transient at the time of load applications; such a transient would be ignored during frequency domain analysis, in which deformation models are fit over repeated periods of oscillation after subtracting transients and background drift.

These results serve to correct an earlier report that adherent cells do not exhibit PLR in the suspended state, as measured by optical stretching [38,86], which has since been interpreted as an indication of a fundamental rheological difference between cells in the suspended and attached states [41,88]. That study compared r^2 values between a power-law and a lumped-component fit and found that the lumped-component model scored better. Three possible reasons for the discrepancy can be identified. First, the earlier study was restricted to the time domain only, while the present study explores the frequency domain as well. A characteristic of power-law rheology is a frequency-independent hysteresivity or phase lag G''/G' (in fact, the model is sometimes called the "constant-phase" model [194]), and this characteristic was observed for both MSCs and fibroblasts. The phase angles were not compatible with any viscoelastic model of several springs and dashpots, as these models exhibit not plateaus but strong changes of phase angle ϕ in the vicinity of characteristic times.

Second, the earlier comparison was performed for a relatively small collection of cells or possibly a single cell only [86]; thus, the better fit to a lumped-component viscoelastic model could have been caused by chance. The larger present data set, along with bootstrap resampling, leads to the conclusion that the better fit of the power law here is not a result of chance alone.

Third, the former viscoelastic model featured three fitted parameters (representing a dashpot in series with a spring-dashpot parallel unit), while the power law featured just two (i.e., $\varepsilon(t) = At^a$). In general, more parameters will produce a better fit, and so this comparison does not fairly evaluate the models based on the desirable metric of combined good fit and simplicity. In the present study, models have been compared by using adjusted r^2 and AIC as criteria, as these metrics penalize additional terms and therefore enable a fairer comparison between models with different numbers of fitted parameters.

The second focus is the finding of a power-law exponent of $a > 0.30$. Earlier it was reviewed (and tabulated in Table 1.3) that previous large-scale studies of attached cells have yielded $a \approx 0.2$. However, the present findings (e.g., $\overline{a} = 0.34 \pm 0.01$ for fibroblasts tested in the frequency domain) are significantly different. What explains this discrepancy?

A plausible reason for large a in suspended cells is that this parameter (related to the putative noise temperature x of the cell as a soft glassy material through $x = a+1$) is known to be inversely correlated with intracellular tension [28, 163]. The origin of this relationship is not understood, though it may be caused by stress stiffening in tensioned networks, which would in turn increase the degree of "caging," increase SGR well depths, and lower the relative amount of mean-field agitation in comparison [195]. Nevertheless, the correlation has been repeatedly observed, by applying cytoskeletal relaxation and contractile agents to attached cells to modulate stress fiber presentation and internal tension [42, 43, 48, 164]. Stamenović et al. proposed an empirical fit in which the power-law exponent increased beyond 0.35 for negligible prestress in cells, and Kollmannberger has corroborated that model's predictions with additional data [172]. Rheological behavior has not been as commonly reported for suspended cells (which lack stress fibers), though experiments with relatively little cell-probe attachment such as micropipette aspiration have indicated relatively high

power-law exponent values (Table 1.3). In the present study, it has been possible to test sufficient cells to obtain an exponent standard error $\sigma_a/\sqrt{n} \sim \mathrm{O}(0.01)$, bringing relative confidence to the higher value of a. Cells in optical stretching are free of physical probe contact, and the only remaining tension is produced by actomyosin contraction in the cortex. This prestress may well be negligible compared to the stress-fiber-regulated tension in attached and fully spread cells, and so a larger a would follow according to existing empirical relationships. Quantitative studies comparing the network tension in the attached and suspended states would be valuable in testing this hypothesis.

Another model of power-law exponent expression considers the whole-cell rheological response to represent the superposition of two PLR systems: the untensioned and more fluidic cytosol and the tensioned and less fluidic cortex [41, 52]. For example, Hoffman et al. found different power-law exponents via internal and external passive microrheology [52], and the values ($a = 0.26$ internally, $a = 0.17$ at the cortex) reflected a correlation between higher internal stress and lower fluidity. Wilhelm recently found an exponent of >0.5 from a microrheological study of driven bead movement within the cytoplasm [194]. The whole-cell measurements acquired in the present study are in general agreement with such a decoupled model, in that tensioned actin bundles may play a smaller role in suspended cells where stress fibers are absent (though again, the cortical actomyosin network remains), and thus whole-cell measurements may feature a larger contribution from relatively fluidic cytoplasm. This interpretation qualitatively agrees with Stamenović et al.'s relationship described above.

In summary, the present finding of $a > 0.30$ is supported by estimates of the standard error of this parameter, is compatible with two existing models of expressed a and its plausible alteration in the relatively unexplored case of suspended whole cells, and is expected to be useful as experimental validation for refining such models. While it is not possible to decouple intracellular responses with the optical stretcher to compare models quantitatively, the present whole-cell measurements remain relevant in considerations of natural cell behavior *in vivo* and of engineered cell sorting or diagnosis by mechanical properties *ex vivo*, as well as an understanding of how different complex regions superpose to provide the whole-cell rheological response.

The third focus is the finding of linear PLR under the loading conditions used in this study. It is not obvious that such linear behavior would be seen for cells probed by optical stretching in the present configuration and power levels. Linear elasticity is expected from stable materials in equilibrium for sufficiently small deformations, as energy minimums are approximately parabolic and therefore Hookean for small perturbations. However, the cell is not usually thought of as being in equilibrium, and furthermore the cell consists of a heterogeneous collection of internal components (among them the cortex, organelles, and the nucleus), including proteins that individually exhibit nonlinear elastic behavior over the full range of extension. Nevertheless, linear elastic cell deformation has been observed with other mechanical probe techniques such as bead cytometry [48, 175], microplate rheometry [50], and micropipette aspiration [83]. Optical stretching of suspended cells can be added to this list, based on observation of load-independence and linear elasticity in Figs. 3-3 and 3-4. Importantly, this linear behavior, independent of cell diameter within error, justifies the assumptions that the change in geometry during a single stretching event is negligible and that the precise variation of photonic stress over the membrane [34, 196, 197] can be replaced with a generic load. It appears, however, that the effective stiffness changes after each successive stretch, possibly approaching a constant after many stretches, as shown in Fig. 3-10 and discussed in §3.4.3. Thus, the crossover into nonlinear behavior is just outside the parameters of a single stretching cycle.

The fourth focus is the finding of PLR in creep recovery, as such reports are rare in comparison to reports of PLR in creep stretching. Power-law recovery has been previously observed for isolated nuclei that were mechanically deformed, then released, by

micropipette aspiration [148] and also for attached cells probed by magnetic bead cytometry [172]. However, the present results appear to be the first such observations to be reported for suspended whole cells. As expositions on soft glassy rheology have not previously considered recovery after creep deformation, this area is certainly worthy of further study. For example, it seems clear that power-law behavior must transition to another regime at some point during recovery, for the cell is unlikely to contract to less than its original diameter (ignoring active effects occurring on longer time scales).

3.4.2 ATP is not the origin of crucial non-thermal agitation in the context of soft glassy rheology models of power-law rheology in cells

ATP hydrolysis is the means by which the living eukaryotic cell effects active contraction, and this chemical reaction further represents a source of non-thermal mechanical fluctuations in the cytoskeleton. Trepat and Fredberg et al. found that ATP depletion reduces the progress of resolidification after fluidization [151].[4] Because resolidification is interpreted to result from agitation-driven yielding of regions of soft matter, Fredberg et al. have argued that ATP specifically is the source of mechanical agitation in cells [49, 90, 151, 157, 164, 166, 167].

However, the same protocol of ATP depletion appears to have no detectable effect on the power-law exponent linked to fluidity in cells. One example is Hoffman and Crocker et al.'s measurements of Brownian bead motion that necessitated ATP-depleted cells [52, 96].[5] Hoffman et al. observed typical values of $\alpha \approx 0.2$ (though without comparison to untreated cells), and Crocker et al. have since emphasized ATP independence of soft glassy material fluidity during deformation, based on these results [41, 198]. Another example is Chowdhury et al.'s report that ATP depletion did not detectably alter α in airway smooth muscle cells, though this group did not report confirmation of depletion by chemical assay [169]. Finally, in Fredberg et al.'s experiments on resolidification of attached cells, the power-law exponent did not appear to be suppressed by ATP depletion [151, 157] (and here depletion was confirmed by assay and control experiments were performed). In the present study it is shown that in suspended cells as well, ATP depletion does not detectably alter the average power-law exponent $\overline{\alpha}$ (Fig. 3-9). Furthermore, data are now presented with more detail on the distribution of obtained values of α, particularly the mean and standard deviation, to enable examination of the variation of α among cells (Chap. 4).

(Could the O(1%) ATP that remains in the cell after depletion (as quantified by luciferase assay) be enough to maintain fluidity? In this interpretation (J. Fredberg, personal communication), a surplus of ATP exists over that needed to enable contractility and—putatively—PLR. However, this hypothesis seems unlikely, based on the images compared in Fig. 3-2. ATP depletion before detachment (Fig. 3-2(a)) decouples active and inactive (i.e., metabolic vs. physical) processes of rounding. It is clearly seen that the remaining fraction of ATP is not sufficient to remodel the cell into a spherical shape after detachment. It is therefore concluded that the current depletion protocol is sufficient in reducing intracellular ATP below the level at which the whole cell can effect contractility as usual. Note also that a comparison of these morphologies gives a partial

[4] In the SGR theory (reviewed in App. B.2), solidification is a transient process occurring in soft glassy materials in which regions relax into successively more stable structural configurations (equivalently, a process in which abstracted structural arrangements—elements—transition into deeper energy wells) with time. A fluidizing event is one in which a relatively large load causes widespread yielding and reselection of new and typically more shallow wells that correspond to greater compliance and an interruption of solidification.

[5] Briefly, ATP enables active transport processes that influence bead motion in the cytoskeleton that would otherwise be Brownian and thus offer information about the viscoelasticity of the network through the Stokes-Einstein relationship. Active transport violates the fluctuation-dissipation theorem and produces so-called superdiffusive motion. ATP depletion eliminates this complicating factor, restores Brownian motion, and allows use of the same interpretative framework as used in rheological studies of inanimate samples.

answer to one of the leading questions of this thesis, on the role of contractility in the suspended state. The transformation that occurs upon cell-substratum detachment is further investigated in §5.3.2.)

Why would cell fluidity a be unaltered upon ATP depletion, as is shown in Fig. 3-9? As described in §3.1, one could make plausible arguments for decreasing or increasing a. If Fredberg et al. are correct, ATP reactions in the cell provide the non-thermal agitation that is quantified as the noise or agitation temperature $x = a + 1$ in the soft glassy rheology model. Thus, without ATP the cell should exhibit a lower value of a or, equivalently, should more closely resemble an elastic solid. (Note, though, that ATP hydrolysis clearly cannot universally be the origin of PLR in matter, for PLR is exhibited by the inanimate soft matter about which the SGR theory was originally formulated [91, 92].) Conversely, the actomyosin contraction enabled by ATP is known to increase internal tension in the cell. Therefore, ATP depletion should reduce tension and should increase a based on the relationship between these parameters described earlier.[6]

Setting aside the possibility of counteracting mechanisms that coincidentally cancel exactly, a possible clue arises from the nature of chemical binding between actin and myosin. Left alone, these molecules bind strongly; the crucial role of ATP in cell contractility is to modulate this attachment and to provide the reaction product (phosphate) that changes the configuration of myosin upon the product's departure. (This is the so-called "power stroke"). Without ATP, the myosin remains attached in a rigor state—the origin of rigor mortis in corpses—that holds the network in molecular stasis. Consequently, the absence of ATP actually leaves the cytoskeleton in a state that does not immediately relax, instead continuing to exhibit power-law rheology from non-thermal but also non-ATP-related origins. This factor explains why a might not increase upon ATP depletion, but does not explain the role of ATP in resolidification concurrent with its apparent lack of role in deformation.

ATP could be crucial for resolidification in an unknown way that does not involve non-thermal agitation. One notable difference between Trepat et al.'s resolidification experiment and the present study is the former's use of a relatively large fluidizing load. In the SGR model, fluidization occurs when the strain energy is no longer negligible compared to the agitation energy (App. B.2). As a result, yielding is promoted (exponentially as a function of strain), elements hop out of even the deepest traps, the average yielding rate increases by a factor of as much as $x^2/(x^2-1) \approx 3$ [151], and the material flows like a viscous fluid. It may be that fluidization (i.e., strain-induced yielding) disturbs the cytoskeletal network sufficiently to necessitate ATP hydrolysis in the subsequent resolidification, but that ATP plays a negligible role in noise-induced yielding and linear power-law rheology that is more often the domain of cell deformation in experimental studies. Supporting this hypothesis are e Silva et al.'s recent finding that actomyosin contraction acts to organize actin networks [201]. and Chen et al.'s conclusion that resolidification after fluidization involves the reformation of networks that were disrupted with a large stretch [202].

Finally, it is notable that ATP is here found to be partially responsible for heterogeneity in cell populations, as quantified by the standard deviation (essentially, the distribution width) of power-law exponent values acquired in the frequency domain. A discussion of this finding is postponed until the following chapter, however, which focuses exclusively on origins and models of mechanical heterogeneity in cell populations.

[6] Results from studies of inanimate protein solutions have also been somewhat at odds. ATP is known to enable considerable fluidization in solutions of actin and myosin alone; however, this effect is attributed to contraction in non-crosslinked solutions; in solutions crosslinked by actin-binding proteins, which more closely resemble cells, ATP enables stiffening [177, 195, 199, 200].

3.4.3 Repeated stretching recapitulates pharmacologically driven contraction

Let us turn now to the chemomechanical response of a cell that has been repeatedly loaded. What changes are likely to appear in the cell's rheological behavior, and how do plausible changes compare with what is actually seen?

The first mechanism to examine is the strain stiffening that is generally expected to appear in polymer networks under increasing load. The simplest example is illustrated with a single molecule undergoing thermal undulations; as the endpoints are moved apart via an applied uniaxial load, eventually approaching the contour length in separation, the mechanism of elastic deformation transitions from the uncoiling of thermally induced chain curvature (an entropic stiffness) to stretching of atomic bonds (a much larger enthalpic stiffness). For full networks, additional effects such as bending and chain alignment are also expected to occur, but the relative contributions of these effects in cells are still unknown [53,203]. This stiffening is verified to occur with cells, and can be decoupled from any active response by chemically crosslinking (and killing) the cell [204,205].

The second mechanism is a general inverse coupling between stiffness (as quantified by complex modulus magnitude $|G^*|$) and fluidity (as quantified by power-law exponent a) that is commonly reproduced *in vitro* in cell populations by pharmacological intervention [42,43,48,164]. Cytoskeletal contractile agents such as histamine and serotonin tend to increase internal tension, decrease fluidity, and increase stiffness, while relaxing agents such as blebbistatin and cytochalasin tend to do the opposite. This relationship is not as readily recapitulated by mechanical means, however. One reported example is the mechanical stretching of attached cells as modulated by substratum strain, which did reproduce the above trends [206]. In another experiment, Bursac et al. loaded the cell with a relatively large oscillatory motion (applied by magnetic bead cytometry), then used smaller oscillations to track cell stiffness over time afterward. Bursac saw stiffening beginning after six creep compliance stretches of 10 s each, but did not discuss the finding, as the focus of that work was on resolidification of the cell after a large fluidizing load (the resolidification effect disappeared after these six stretches, spaced over 1,200 s) [157]. Finally, Mierke et al. found stiffening but no change in the power-law exponent of attached cells repeatedly stretched via microplate rheometry [207].

The third mechanism is much different from the first two. It involves active cell stiffening, an animate response, following loading. For example, Thoumine et al. stretched cells between microplates, and saw stress relaxation give way to active contraction approximately ten minutes after the load was applied [208]. Icard et al. loaded cells by optical tweezers applied to attached beads and monitored stiffness [209]. They connected increasing stiffness to F-actin recruitment. Actin-binding protein (ABP) recruitment may also play a role, as the addition of these crosslinkers promotes strain stiffening in actin gels [210]. However, this active response did not occur until several minutes after the first load application, and the response was attributed to a mechanosensitive response linked to stress applied to focal adhesions. Additionally, the transition did not appear to affect the power-law exponent [209]. It is not yet clear whether this behavior could even be caused by optical stretching of suspended cells or whether substratum attachment and adhesion site machinery are needed to provide the necessary signaling.

In the present study, oscillatory measurements are found to couple decreasing stiffness G with increasing power-law exponent a for single cells (Fig. 3-10). By stretching the cell an extent of 1% to 10% of its diameter (Fig. 3-10(b,inset)), the cell is being pulled taut, increasing internal tension possibly to the level of that existing in the attached state. The reduction in power-law exponent presumably represents this increase in internal tension. However, some amount of generic stress stiffening (that would oc-

cur in any polymeric system, and which is not described by SGR theory) may also contribute, and it is not even clear whether these two effects (the first two mechanisms discussed in this section) might possibly be intimately connected. Further experimentation is needed in this area. It does seem clear, however, that active response is not involved in the transition found here, as all ten stretches were completed within approximately two minutes. This duration is too short to involve any considerable actin or crosslinker recruitment, according to Thoumine et al. and Icard et al.'s reports [208, 209].

The coupled relationship shown in Fig. 3-10 is qualitatively predicted by SGR theory (because a larger agitation energy implies relatively more deformation for a given load [91]). Such a prediction has not been demonstrated previously for a single experimental condition, however. (The conflation of probe attachment that occurs with bead cytometry, for example, has been reported to introduce the opposite correlation [43, 48, 95].) Confirmation of the relationship, therefore, is notable, especially because the findings immediately prompt new questions: If stiffness and fluidity are now *measurably* coupled (not just coupled in SGR theory), could experiments also link the population heterogeneity in these parameters? Should not the smaller distribution width of fluidity measurements in ATP-depleted cells (Fig. 3-9) imply that their stiffness is also more narrowly distributed? Could the large variation in stiffness values commonly measured in cell populations be attributed to cell-to-cell variation of intracellular agitation—abstracted as a noise temperature x and quantified through the power-law exponent $a = x - 1$ in creep compliance measurements and as the hysteresivity $\tan(\pi a/2)$ in complex modulus measurements? These questions are addressed in the next study and the next chapter of this thesis.

3.5 Outcome

Conclusions

The results support this study's hypothesis. Optical stretching, augmented with new high-throughput capability for this study, is capable of characterizing single, whole-cell rheological behavior without complications from cell-probe or cell-substratum physical contact. This work's contribution to the field has been to explore the time- and frequency-dependent deformation of suspended cells in the seconds after a photonic load is applied. A data set size of >2,000 cells was used to correct a previous conclusion of suspended-cell rheology that was based on a much smaller data set of one or several cells. The new conclusion, that suspended cells exhibit power-law rheology, was statistically analyzed and found unlikely to be caused by chance alone. Additionally, it is found that the cell can be described as a material with an effective stiffness (e.g., a time-dependent creep compliance or a frequency-dependent complex modulus) that is independent of single cell diameter and independent of load (under the conditions employed here), but with a history dependence that becomes apparent with repeated loading.

The finding that suspended cells exhibit PLR is compatible with a view of these cells as soft glassy materials. However, the role of internal stresses is still not precisely known, as contraction in the cortex maintains hydrostatic internal pressure even in the suspended cell. Nevertheless, the key finding—that power-law creep compliance does not depend critically on *stress-fiber-generated* internal stresses—is expected to be valuable in the refinement of constitutive models of whole-cell deformation that both predict the emergence of power-law rheology and also can be related directly to molecular mechanisms.

It is also emphasized that the contemporary exchange of paradigms of cell mechanics from lumped-component viscoelastic models to power-law rheological models not only better describes reality, but also provides a more satisfying framework for inter-

pretation. Little meaning can usefully be given, for example, to a second dashpot or third elastic spring in a lumped-component viscoelastic model that is fit to cell creep compliance. In contrast, the power-law exponent represents a single parameter that governs deformability over many decades of time or frequency measurements, that is coupled to other rheological parameters such as the hysteresivity, that can be modulated predictably by pharmacological perturbation of the cytoskeleton, and that can be interpreted in a simple—albeit abstract—way as an agitation energy, much larger than thermal energy, that underlies mechanical deformation.

Importantly, ATP in the cell and the resulting actomyosin contraction does not constitute the non-thermal agitation referenced in the soft glassy rheology theory. It is emphasized that this conclusion needs to be expressed precisely, as ATP likely plays some part in assembling the network that exhibits PLR, according to another group's cytoskeletal resolidification experiments. It is thus too vague to say that ATP hydrolysis is or is not responsible for power-law rheology. The present study's findings are specifically that ATP hydrolysis plays no detectable part in the average fluidity (as quantified by hysteresivity or phase lag) during oscillatory measurements in the linear regime of power-law rheology. Further investigation is needed to determine conclusively why resolidification (which follows large nonlinear deformations) is reported to be affected by ATP depletion but that behavior in the linear regime is not affected. Plausibly, ATP hydrolysis is crucial for cytoskeletal network formation and maintenance, but is relatively unimportant during brief (O(10 s)) deformation periods resulting from loads below the fluidization threshold. Because myosin binds strongly to actin in the absence of ATP, ATP depletion causes the network to be held in place, exhibiting PLR possibly through filament untangling and crosslinking unbinding and unfolding—the molecular origins of PLR are themselves not understood. This hypothesis reconciles the statements by Fredberg et al. and Crocker et al., but awaits further validation with additional experimental results.

It is important to understand how materials, even relatively complex materials such as living cells, might be classified as types of matter, even if multiple possible classifications exist. The class of soft glassy materials, addressed by the soft glassy rheology model, is remarkably—and frustratingly—broad; because the framework can be applied to a collection of materials such as emulsions, pastes, slurries, semi-flexible polymer networks, and possibly live cells, the framework requires no set of particular molecular mechanisms. Therefore, it is not immediately clear how best to integrate into the SGR theory basic polymer network behavior such as strain stiffening and basic cell behavior such as ATP-enabled active contraction. The present study's findings are presented with the aim of validating candidate models to address this limitation.

Possibilities for continued research

The capabilities and results demonstrated in this chapter suggest several future research topics.

First, it would be desirable to test further the present conclusion that the relatively large average power-law exponent $\overline{\alpha} \approx 0.37$ arises because of relatively low internal-tension manifested in the suspended cell. Is it possible to affect this parameter with the pharmacological approaches that are well-established for cells in the attached state? One option to be considered is the use of a contractile agent (e.g., histamine or serotonin) to increase actomyosin-related tension in the actin cortex, and consequently possibly reduce the power-law exponent. Such an experiment would also be a useful way of determining the degree to which the cortex dominates viscoelastic behavior in the suspended cell.

Second, it may be possible to relate the suspended state (which is relatively poorly studied, though occurring upon every passaging event and relevant for implantation of stem cells for therapeutic purposes) to other physiological cell states. In particular,

the attached cell is observed, upon mitosis, to partially detach from the surface and become rounded. Is the mitotically rounded state similar in any way to the suspended state? That is, do stress fibers disappear while the cell remodels to reattach the plasma membrane and suppress blebbing, as in the recently suspended cell? What conclusions of common or differing rheological behaviors can be drawn? Such conclusions could provide insight into one or both cell configurations.

Third, it should be possible to investigate nuclear deformation within the suspended cell by optical stretching. For example, a live-cell (i.e., lipid-permeable and nontoxic) DNA-binding fluorescent dye could be used to characterize deformation by fluorescence microscopy during stretching (with the caution that intracellular dyes are known to alter cell mechanics [211]). Furthermore, it may be possible to adjust the cell suspension media to match the refractive index of the cytoplasm but not the nucleus, the refractive index of which can differ from the rest of the cell [212]. Impinging laser light under this condition could deform the nucleus alone, allowing chemomechanical characterization without extraction from its natural environment within the cell.

Acknowledgments

Prof. Jochen Guck and Franziska Lautenschläger (Cavendish Laboratory, University of Cambridge) provided manufacturing design documents, customized software, and guidance for performing and interpreting optical stretching experiments. Eric Lehnhardt (Arizona State University & MIT REU program) cultured fibroblasts, performed optical stretching on them in normal and ATP-depleted states, assayed them for successful ATP depletion, and contributed interpretations of experimental results. Emer Clarke (StemCell Technologies and ReachBio) provided guidance in techniques for MSC isolation, culture, and differentiation. Portions of this chapter and associated appendices have been previously published [4], and are reprinted with the permission of Elsevier.

Chapter 4

Compliant cytoskeletal networks II

Synopsis

The population distribution of cell stiffness values is characterized for different cell lineages and multiple chemomechanical environments to explore the origin and extent of mechanical differences between single cells. Independent of cell lineage, cell cycle, mechanical perturbation or chemical crosslinking, cell stiffness values among cells exhibit a right-skewed distribution with a width corresponding to a geometric standard deviation $SD_{geo} \approx 1.6$. This finding, obtained by optical stretching, suggests that a minimum intrinsic variation exists in mechanical properties of cell populations independent of cell-probe or cell-substratum contact. It is postulated that this mechanical variation predominantly arises from Gaussian fluctuations in power-law exponent, interpreted as the emergent agitation energy in the energy landscape of soft glassy materials. This postulate leads naturally to an approximately log-normal distribution of complex modulus and creep compliance, and also explains frequency- and parameter-dependent values of distribution widths that have previously been reported as empirical findings lacking interpretation. Two case studies are presented to explore the implications of a minimum variation in cell mechanics in applications where mechanical properties are used for disease diagnosis and single-cell sorting.

4.1 Study background, hypothesis, and design

The third study in this thesis addresses cell-to-cell mechanical heterogeneity within a population, as quantified by the distribution width of mechanical measurements obtained from cells from any single population. High-throughput studies of hundreds or thousands of cells have revealed that attached cell stiffness is distributed as a strongly right-skewed variable that is generally fit by a log-normal distribution [26, 50–52], the width of which can be quantified by the geometric standard deviation SD_{geo}.[1] Sufficient literature reports are now available to extract distribution widths from published figures to pursue the origin of this distribution (Table 4.1), and several conclusions can be drawn from this tabulated data.

[1] The **geometric standard deviation** is e raised to the power of the standard deviation of the log-transformed data. A geometric standard deviation of 2 indicates that 68% of the samples lie between $1/2\times$ and $2\times$ the sample median; furthermore, it implies that fully 16% of cells exhibit more than four times the stiffness of the 16% most compliant cells and that the 2% stiffest cells are more than *eight* times stiffer than the 2% most compliant cells. SD_{geo} is not the only way to characterize heterogeneity, however, and another approach is compared in §4.4.5.

Table 4.1: **Findings of cell-to-cell mechanical variation.** This variation is generally found to be log-normally distributed across multiple tools. How much do cells intrinsically differ from each other mechanically? Variation is quantified by the geometric standard deviation SD_{geo}, or the exponential function applied to the standard deviation of log-transformed data. (Techniques: AFM = atomic force microscopy, LTM = laser tracking microrheology, MBC = microbead cytometry, MPA = micropipette aspiration, MPR = microplate rheometry, OT = optical tweezers, OS = optical stretching, TPM = two-point microrheology. Connections: RGD = arginine-glycine-aspartic acid, CAD = cadherin, FN = fibronectin, NF = nonfunctionalized. Cytoskeletal contractile agent: DBcAMP = dibutyryl cyclic adenosine monophosphate.)

Findings of a log-normal distribution of stiffness and compliance						
Cell type and number	Technique	Connection	Time scale	SD_{geo}	Group	Notes
Embryonic carcinoma ($n = 202$)	MBC	RGD	5 s	4.1*	Alenghat et al. (2000) [213]	
Muscle ($n = 500$–$1{,}700$)	MBC	RGD	O(1 s)	2.5–2.6*	Fabry et al. (2001) [95]	Histamine and DBcAMP increased and decreased stiffness, respectively, but did not alter SD_{geo}.
Muscle ($n > 658$)	MBC	RGD	0.005–10 s	1.2–1.5	Bursac et al. (2005) [157]	
Myoblast ($n = 7$–43)	MBC, MPR, OT	CAD, GLUT, FN, RGD, ICAM-1	0.02–100 s	1.3–5.4*	Balland et al. (2006) [29]	Showed that variation does not arise solely from bead attachment via RGD.
Epithelial ($n = 7$–103)	MBC, TPM, LTM	RGD	0.001–10 s	1.4–4.0*	Hoffman and Massiera et al. (2006–2007) [44, 52]	ATP-depleted cells used exclusively to avoid superdiffusive motion. Passive techniques showed that variation does not arise solely from external load.
Fibroblast ($n = 300$)	AFM	NF	N/A	1.9–2.2*	Mizutani et al. (2008) [171]	Showed that variation does not arise solely from cytoskeletal anchoring.
Fibroblast ($n = 130$)	AFM	NF	0.005–0.2 s	1.2–1.8*	Hiratsuka et al. (2009) [46]	Includes histograms of G' and G'' at three different frequencies.
Fibroblast ($n = 81$)	MPA	NF	100 s	1.4*	Zhou et al. (2010) [83]	
MSC, fibroblast ($n > 2{,}000$)	OS	No physical connection	0.05–4 s	1.6	**This work**	Includes confidence intervals (95% CI: [1.5,1.7]), no physical probe-cell contact, comparison after exposure to a variety of chemomechanical influences.
Finding of a Gaussian distribution of stiffness						
Cell type and number	Technique	Connection	Time scale	SD_{geo}	Group	Notes
Epithelial cancer ($n = 40$)	AFM	NF	1 s	N/A	Cross et al. (2007) [214]	Results are re-examined in §4.4.4.

*Extracted from plots in published reports.

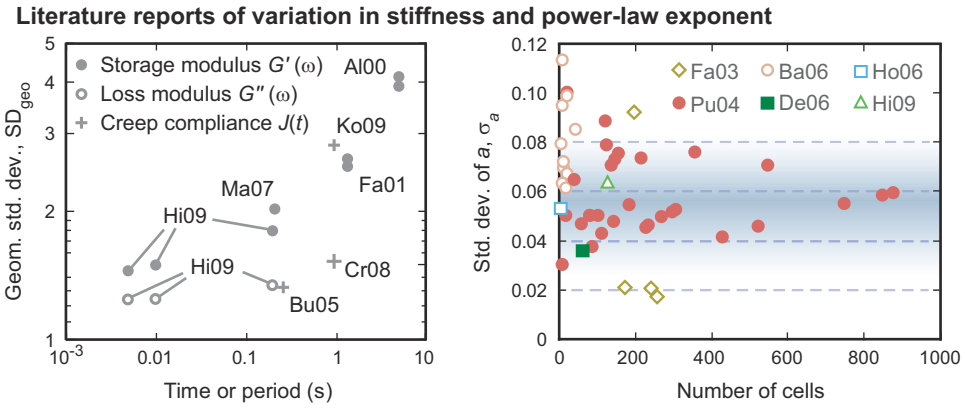

Figure 4-1: **Findings of variation in stiffness and power-law exponent within cell populations.** (a) The observed variation in cell stiffness, as quantified by geometric standard deviation SD_{geo} of a log-normal fit to creep compliance or complex modulus, as a function of experimental time scale, for studies of >100 cells. Note the general trend of increasing SD_{geo} with experiment time or period. (b) Existing estimates of standard deviation σ_a of power-law exponent a as a function of data set size suggest that an inherent uncertainty in a exists and may converge to $\sigma_a \lesssim 0.02$–0.10. Data referenced by study author and year [26, 29, 42–44, 48, 50–52, 157, 158, 213–216].

First, the variation does not depend crucially on any particular attachment mechanism or loading method. Once thought to arise solely from the vagaries of probe attachment area [95], the characteristic distribution has now been observed via different flavors of probe-cell molecular attachment [43]; nonfunctionalized engagement of the cytoskeleton via atomic force microscopy (AFM) indentation [51]; and passive (non-driven) motion of internal organelles [52]. Second, the strongly right-skewed distributions are not exclusive to cells from a single tissue type, but are seen with cells from connective, epithelial, and muscle tissue—thus, the feature can be generalized to appear with adherent eukaryotic cells, at least. Third, the variation is seen at multiple length scales corresponding to intracellular granules ($L \sim$ O(0.5 μm)), attached beads ($L \sim$ O(5 μm)), and stretching of whole cells ($L \sim$ O(50 μm)), and because of the last factor cannot be attributed solely to spatial mechanical heterogeneity within the cell. Fourth, it is not inevitable that soft or compliant materials are mechanically heterogeneous; lipid vesicles [217], dilute actin solutions [218, 219], and cartilage [220] exhibit relatively narrow and Gaussian distributions of stiffness, in contrast. Up to this point, these common findings have not been interpreted to explain mechanical variation among cells.

Why would one cell be mechanically different from another? In contrast to the theoretical exploration of power-law rheology (PLR, reviewed in [40, 41]), the wide variation in cell mechanical properties has remained largely uninvestigated, with some exceptions [29, 216]. Nevertheless, dedicated exploration of the origin and extent of mechanical variation is valuable in both scientific and engineering contexts. From a *scientific* perspective, heterogeneity that arises from correlations at particular length and time scales currently prompts investigation. Certain configurations of soft matter may imply large variation in mechanical measurements; could there be something about the soft glassy nature that produces large mechanical variation? Can the variation be attributed to the animate nature of cells? Can the effect be understood—or at least replicated—through stochastic models? An understanding of intrinsic[2] heterogeneity would improve our familiarity with the viscoelastic materials that lie in an intermediate position between elastic solids and viscous fluids.

[2]**Intrinsic** noise or heterogeneity is defined here as the true mechanical variation between cells under standard conditions of an assay. **Extrinsic** noise includes variations in sample preparation and error in measurement, which in theory could be reduced to a negligible level. Intrinsic noise, as a property of the cell population, cannot be reduced—except possibly by changing cell preparation techniques.

An analogy from the elasticity of polycrystalline materials may be useful here. For measurement locations within a single grain, we expect that elastic stiffness of the crystal structure in a particular direction is location-independent (ignoring the effects of defects such as vacancies, and impurities). For example, the Young's modulus of a gold crystal in the (100) direction has been measured to be $E_{100} = 43\,\text{GPa}$ [221]. Such a single grain, elastically, is expected to be relatively homogeneous. Now consider a group of grains in which a particular laboratory measurement orientation lines up with the (100) direction in some grains and the (111) direction in other grains. With a Young's modulus of gold of $E_{111} = 117\,\text{GPa}$ in the (111) direction [221], the polycrystalline sample is generally heterogeneous when measured in different locations (different grains) at the same orientation. (In this example, the ratio of measured stiffness values can be as large as $E_{111}/E_{100} = 2.7$.) At a still larger length scale, assuming that elasticity measurements take place across many randomly oriented grains, the central limit theorem tells us that a superposition of many Young's modulus values produces a Gaussian-distributed average value. Thus, stiffness measurements now return the Young's modulus $E = 79\,\text{GPa}$ for bulk polycrystalline gold, and these measurements are again location independent and relatively homogeneous.

The gold example emphasizes how length scales can influence the observed heterogeneity of mechanical measurements. These transitions are relatively well understood for metal crystals. In contrast, the emergence of heterogeneity and the importance of length scales (whether caused by anisotropy, composition, preparation method, or a combination of these) is not at all well understood for complex fluids—including the cytoskeleton of a live cell. The previous chapter of this thesis showed that even suspended cells from a single population exhibit considerable mechanical variation (Fig. 3-1(d)), though uncommented upon at the time. Let us now explore this behavior and, if possible, isolate its origin(s).

From an *engineering* perspective, it is beneficial to understand the minimum intrinsic noise level of single cells during mechanical measurements, as large intrinsic variation could hinder practical applications such as cancer diagnosis [35] and mechanical cell sorting [176]. The wider the distributions of mechanical properties in any cell populations, the harder it is to distinguish one subpopulation from another. It is thus desirable to understand the nature and extent of intrinsic noise or variation in cell mechanics.

What experimental questions remain to be considered? The role of probe-material engagement has not been determined. Variation from different techniques (e.g., time domain vs. frequency domain) has not been considered. The possibility that cell orientation (to match the grain orientation analogy above), cell cycle position, and/or cell diameter influence mechanical heterogeneity has not been tested. Few origins of heterogeneity have been postulated, and predictive models of variation have not yet been reported. Finally, small sample sizes bring into question the uncertainty in SD_{geo} reported values; in essence, the variation in variation has never been reported, and this limitation prevents us from saying with confidence—even with Table 4.1 at our disposal—whether any one population or experimental condition induces more or less mechanical heterogeneity than another.

With these unexplored questions in mind, the present study's hypothesis is:

> A comprehensive experimental study of cell-to-cell mechanical variation under chemomechanical cues, combined with analytical modeling of cell mechanical variation and simulation of deformation kinetics, will extend conclusions drawn from existing literature and address the question **What are the origins and extent of cell-to-cell mechanical variation?**

The tools applied in the last chapter—particularly optical stretching, bootstrapping, and soft glassy rheology (SGR) theory—are eminently suitable to apply to this challenge. Why? First, optical stretching can interrogate cell stiffness in the time and

frequency domains, offers relatively high throughput for a single-cell technique, can simultaneously record cell diameter (a surrogate for cell cycle position), and avoids physical contact. Optical stretching measures single whole cells without variation from probe-cell attachment and and conflation of internal cell mechanical heterogeneity. Second, bootstrapping can be used to estimate the variance in any estimated parameter. This variance can be used in hypothesis testing to conclude that stiffness variation can be altered with statistical significance. Third, SGR constitutive equations can be applied to the problem, now with confidence based on confirmatory results from Chap. 3; with this framework, it is possible to connect postulated variations in one parameter with the resulting distribution of values in another parameter.

This chapter addresses multiple possible origins of the large mechanical variation and right-skewed stiffness distribution observed in cell populations. The first component is experimental. Primary vs. immortal lines are compared to consider the role of subpopulations, and creep compliance and complex modulus measurements are obtained to compare time- and frequency-domain measurements. A group of chemomechanical cues are also applied; compared here are live and chemically crosslinked cells, cells that have been recently exposed to mechanical perturbation, and cells for which the active metabolic processes have been blocked. Finally, variation connected to the cell cycle is also investigated. The second component involves an analytical model, the predictions of which are compared with experiment and simulation, that explores the relationship between the power-law exponent α and cell stiffness $|G^\star|$ that was empirically observed in §3.3.4. Based on experimental evidence and reasoning from leading models of PLR, the exponent α is postulated to vary *intrinsically* among cells approximately as a Gaussian-distributed variable. This approach is found to be successful in explaining a variety of experimental findings from the present study and from existing literature reports. The third component is an examination of others' reports of heterogeneity, from single cells as tabulated in Table 4.1 to simpler inanimate structures.

Novel methods

This study applies existing technologies in new ways, in each case to extend our understanding of the origin and extent of mechanical variation among cells:

Comparison of mechanical heterogeneity in primary and immortalized cell lines. Primary mesenchymal stem cells (MSCs) are known to exhibit subpopulations [58,222, 223]; that is, multiple groups exist and are distinguished by morphological and proliferative differences during the limited lifetime of the population. (This topic arises again in §5.4.1.) In contrast, immortalized cell lines such as the NIH 3T3 fibroblasts continue proliferating without the constraint of eventual senescence, and thus represent a genetically homogeneous group that has predominated over slower-dividing and non-immortalized subpopulations in the original culture [224–226]. It follows that such a line might exhibit relative homogeneity in mechanical properties as well. No previous study has compared primary vs. immortalized cell lines in this way, however.

Light crosslinking of cells in suspension. Cytoskeletal covalent crosslinking by formaldehyde or glutaraldehyde immobilizes the protein network, killing cells and increasing stiffness. Crosslinking occurs in a dose-dependent manner with fixative chemical concentration [227]. In this study, relatively dilute solutions are used to kill cells without substantial crosslinking, and thus without reducing deformation below the noise floor of the optical stretcher tool. Though the technique is well demonstrated on attached cells [169, 205, 227–229], deformation has not previously been measured on cells fixed in the suspended state.

Statistical approaches: Change-of-variables and bootstrapping A statistical change-of-variable technique is used to propagate uncertainty through parameters in postulated physical models of deformability. Bootstrapping, introduced in Chap. 3 and described in App. B.1, is here used to determine the uncertainty of the geometric standard deviation parameter (essentially, the variation of the variation in cell mechanical properties) to allow comparison of cell populations and experimental conditions.

Monte Carlo simulation of soft glassy materials by Gillespie algorithm. The Gillespie algorithm is a method for simulating stochastic events [230–233] that has not yet been applied to cell deformation or the SGR model. Briefly, the Gillespie algorithm simulates kinetic events by generating a random number for each possible event; each number is chosen from an exponential distribution $P(t_i) \propto e^{-r_i t_i}$ where r_i corresponds to the rate of event i. The event with the smallest t_i value is chosen to occur at time t_i, the time is reset, and the process is repeated. In the SGR context, the yielding of a particular region constitutes a single event, as described in App. B.2.

4.2 Materials and methods

Cell culture, optical stretching, and data analysis

The deformation of single cells in suspension under various chemomechanical influences was used to build a collection of observations about cell-to-cell mechanical variation. Fibroblasts and mesenchymal stem cells were cultured as described in Chap. 2 and 3, respectively, by using protocols in App. C.1. Optical stretching was performed as described in Chap. 3 by using the protocol in App. C.2. ATP depletion and confirmation by ATP assay was performed as described in Chap. 3 by using protocols in App. C.1 and App. C.3, respectively.

Fixation by light chemical crosslinking was accomplished by incubating suspended cells in 0.01% glutaraldehyde in complete media for 10 min at 37°C (App. C.1). The effectiveness of fixation in destroying normal cell processes was validated by seeding cells upon TCPS and confirming that they failed to attach.

Log-normal parameters such as $\mathrm{SD}_{\mathrm{geo}}$ were estimated by nonlinear fitting (Mathematica). Standard estimation techniques such as maximum likelihood estimation and the method of moments were also explored and gave similar results (Fig. C-4).

Bootstrapping was used to determine standard errors and confidence intervals by using the protocol in App. B.1.

Analytical transformation of probability distributions from one parameter to another

For examining correlations of SGR model parameters, the change-of-variables equation $P(y) = |dz/dy|P(z)$ was used to transform one probability distribution into another (App. A.2), and Taylor series expansion was used to simplify analytical expressions. Bootstrapping was used to examine whether a better fit of one distribution or another was likely to be caused by chance (App. B.1).

Monte Carlo simulation of cell deformation kinetics

Creep in the SGR model is equivalent to an infinite configuration of springs in parallel (with infinitesimal stiffness) with lifetimes chosen from the appropriate distribution [160] (App. B.2). As each spring yields at time t, the deformation increase can be numerically calculated from the difference in equilibrium positions at constant load

with and without the yielding element. Because the total restoring force is identical before and after element j yields, it can be seen that

$$\frac{1}{N}\sum_{i}^{N} l_i = \Delta\varepsilon + \frac{1}{N}\sum_{i\neq j}^{N} l_i \tag{4.1a}$$

$$\Delta\varepsilon = \frac{l_j}{N} \tag{4.1b}$$

where N is the number of simulated elements, l_i is the length of element i, and $\Delta\varepsilon$ is the deformation increase (Fig. B-2),

Simulations were performed in which 200–500 elements were assigned lifetimes of $\tau = e^{E/(a+1)}$ based on the equilibrium energy distribution $P_0(E) \propto e^{-E}e^{E/(a+1)}$ [92,160]. Upon element yielding, a new energy was selected from the distribution $\rho(E) = e^{-E}$ and a new relaxation time calculated from this energy.

4.3 Results

4.3.1 The population of creep compliance values is well fit by a log-normal distribution for primary and immortalized cells

To determine whether the mechanical heterogeneity observed in MSCs (Fig. 3-1(d)) could be attributed to the primary nature of these cells—which were explanted from live tissue fewer than 20 generations ago—the study included 3T3 fibroblasts as an example of an immortalized, repeatedly passaged, and relatively homogeneous population. Upon optical stretching in the time domain, the creep compliance of both cell lines was found to be distributed approximately log-normally around a power-law mean (Fig. 4-2). The width of the distributions is quantified by the geometric standard deviation $\mathrm{SD}_{\mathrm{geo}}$, which was approximately 1.6 for each cell line (Fig. 4-3(a,b), Table 4.2).

4.3.2 Relationships between mechanical variation and cell lineage, chemomechanical cues, and the cell cycle

The value of $\mathrm{SD}_{\mathrm{geo}}$ was not significantly changed by repeated stretching or by holding each cell in place for one minute to pause after the process of moving through the microfluidics and capillary (Fig. 4-3(c,d), Table 4.2). Interestingly, the variation was also not altered by light fixation (Fig. 4-3(e)), though the power-law exponent was significantly decreased compared to all other conditions ($p = 0.033$, Fig. 4-4(a)).

ATP depletion of fibroblasts significantly narrowed the distribution of creep compliance values compared to untreated fibroblasts ($p = 2 \times 10^{-5}$, Fig. 4-3(f), Fig. 4-4(b)), qualitatively matching the decrease in σ_a previously observed upon ATP depletion (Fig. 3-9).

Finally, as shown in Fig. 4-5, the creep compliance and distribution width $\mathrm{SD}_{\mathrm{geo}}$were not detectably correlated with cell diameter, used here as a surrogate for cell cycle position.

4.3.3 Gaussian power-law exponent implies log-normal mechanical variation

Based on the correlation between stiffness $|G^*|$ and power-law exponent a found in the previous study (§3.3.4) it is plausible to posit that the noise temperature $x = a+1$ could vary intrinsically among cells and that this variation in agitation energy influences

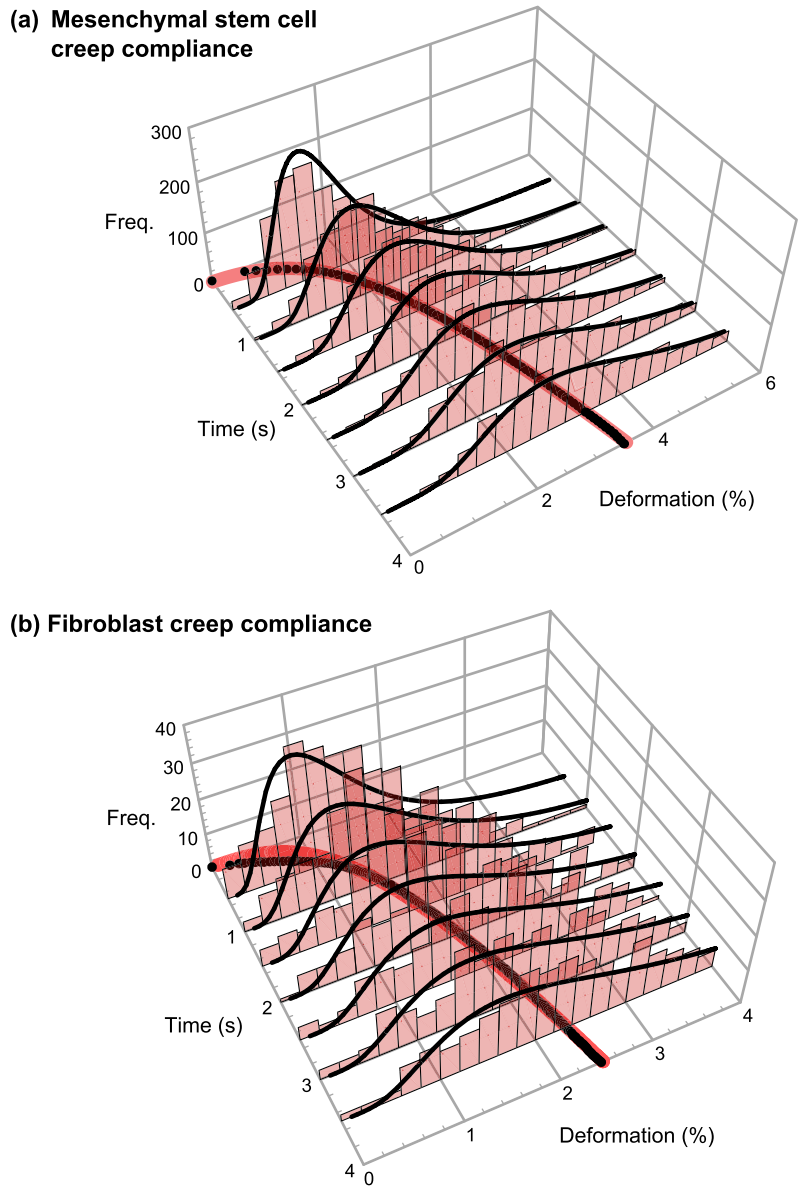

Figure 4-2: **Cell-to-cell variation in creep compliance around a power-law average.** Histograms of experimentally observed optical stretching deformation over time for (a) 1,288 mesenchymal stem cells from three donors, passages 1–9, and (b) 249 fibroblasts. Black markers in time-deformation plane are mean response, fit by a power law response (red line in time-deformation plane). Black lines in deformation-frequency plane slices are probability distribution functions (pdfs) of log-normal distributions at each 0.5 s timepoint with $\mathrm{SD}_{\mathrm{geo}} = 1.6$, to compare with the experimental histograms. There is no detectable difference in mechanical heterogeneity between these primary and immortalized cell lines.

measurements of cell mechanical behavior. It is simplest to assume that a is Gaussian distributed, and in fact this assumption is compatible with the interpretation of a as the sum of many independent energies. The connection between Gaussian a and its standard deviation σ_a and rheological parameters such as the storage and loss moduli, both of which are predicted to be approximately log-normally distributed, is developed in App. A.2 and summarized in Table A.1. Most importantly for the current study, this derivation predicts the heterogeneity of complex modulus $G^*(\omega) = G'(\omega) + iG''(\omega)$ to be $\mathrm{SD}_{\mathrm{geo}} \propto (\omega/Y_0)^{\sigma_a}$ for the storage modulus G' and $\mathrm{SD}_{\mathrm{geo}} \propto e^{-\sigma_a/\overline{a}}(\omega/Y_0)^{\sigma_a}$ for the

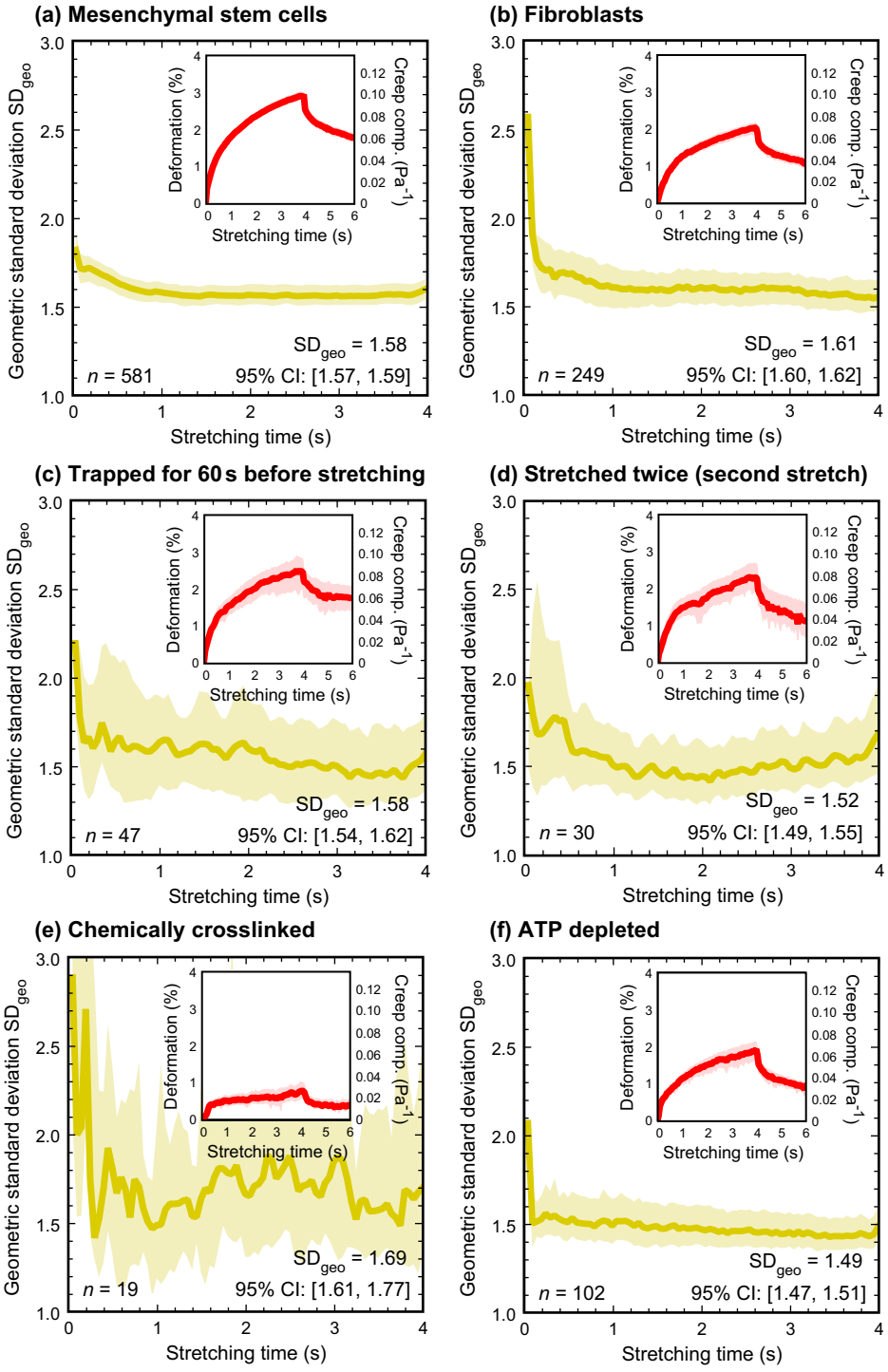

Figure 4-3: **Mechanical variation across cell populations as a function of lineage, previous mechanical perturbation, or active metabolic processes.** Insets, creep compliance as a function of time. (a,b) Comparison of primary human mesenchymal stem cells and immortalized murine fibroblasts. (c,d) Cells exposed to mechanical perturbation (held at low trapping laser power for one minute after movement through microfluidics, stretched a second time after one minute at trapping power). (e,f) Cells exposed to chemical perturbation (lightly crosslinked by glutaraldehyde, depleted of ATP). 95% confidence intervals are determined by bootstrapping. See also Table 4.2 for tabulated values. (Note that relatively jaggedness of some SD_{geo} profiles can arise from lower data set size, not necessarily from experimental condition; compare (e) and (f) where $n = 19$ and $n = 102$, for example.)

Table 4.2: **Findings of stiffness and power-law exponent (mean and standard error) and geometric standard deviation for a primary and an immortalized cell line in response to a variety of chemomechanical cues. (Standard error identified from 2,000 bootstrapping runs.)**

Human mesenchymal stem cells (MSCs)					
Treatment and data set size	Stiffness* (Pa)	$\overline{a}$	$\sigma_a/\sqrt{n}$	SD_{geo}	95% CI
Control ($n = 581$)	16.5 ± 0.4	0.37	0.01	1.58	[1.57,1.59]
Rest 60 s ($n = 47$)	18.8 ± 1.5	0.37	0.02	1.58	[1.54,1.62]
Second stretch ($n = 30$)	19.3 ± 1.7	0.35	0.04	1.52	[1.49,1.55]
Lightly fixed ($n = 19$)	58.9 ± 8.4	0.22	0.07	1.70	[1.61,1.77]
(Murine) NIH 3T3 fibroblasts (FBs)					
Treatment and data set size	Stiffness* (Pa)	$\overline{a}$	$\sigma_a/\sqrt{n}$	SD_{geo}	95% CI
Control ($n \geq 249$)	22.3 ± 1.0	0.36**	0.01**	1.61	[1.60,1.62]
ATP-depleted ($n \geq 102$)	26.0 ± 1.7	0.37**	0.01**	1.49	[1.47,1.51]

*Geometric mean of reciprocal creep compliance at 1 s, $1/J(1\,s)$, $\pm$ standard error.
**Pooled from creep compliance and complex modulus measurements; see §3.3.3.

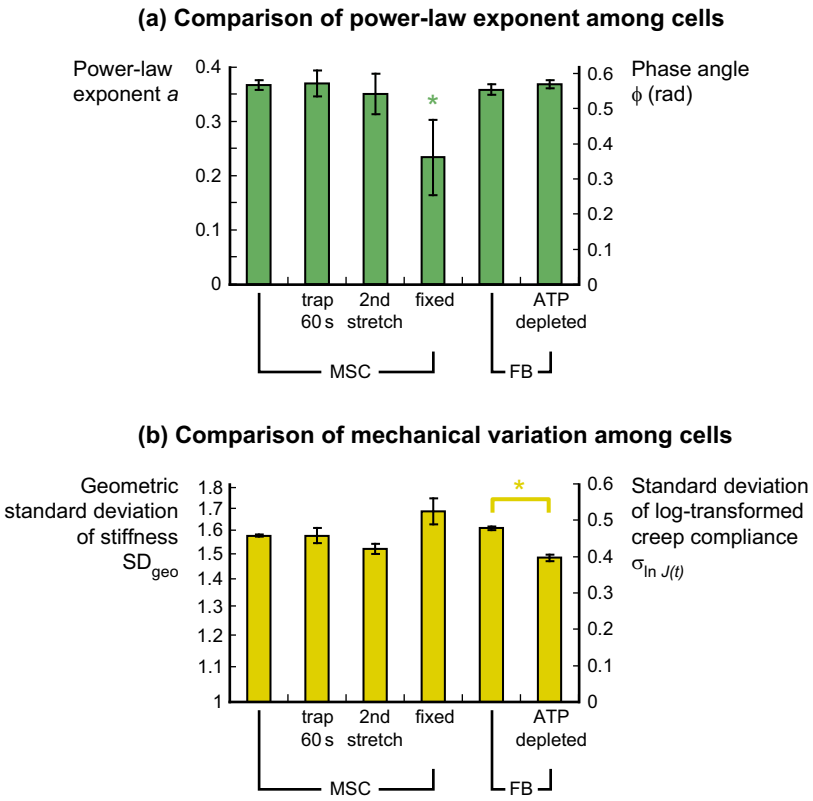

Figure 4-4: **Statistically significant alterations of power-law exponent and geometric standard deviation in two cell lines in response to chemomechanical cues.** (a) Cytoskeletal crosslinking decreases power-law exponent ($p = 0.033$ by ANOVA). (b) ATP depletion reduces mechanical heterogeneity across single whole fibroblasts ($p = 2 \times 10^{-5}$ by ANOVA).

loss modulus $G''(\omega)$, where Y_0 is a constant frequency (in the SGR model, an attempt frequency or maximum possible yielding rate [91]).

Let us now compare these predictions to experimental findings from other groups, represented in Figs. 4-1 and 4-6. Four predictions follow: First, a log-log plot of SD_{geo} vs. measurement period $1/\omega$ will have a slope σ_a for any group of measurements. Second, extrapolation to $SD_{geo} = 1$ on this plot for G' will occur at time $1/Y_0$. Third,

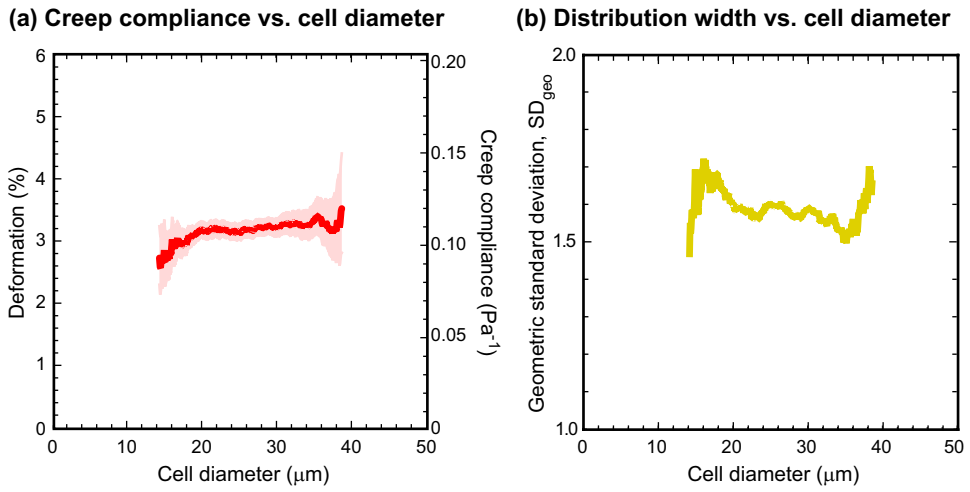

Figure 4-5: **(a) Deformability and (b) geometric standard deviation are not detectably correlated with changes in cell diameter, suggesting that the cell cycle is not the sole source of mechanical variation among cells.**

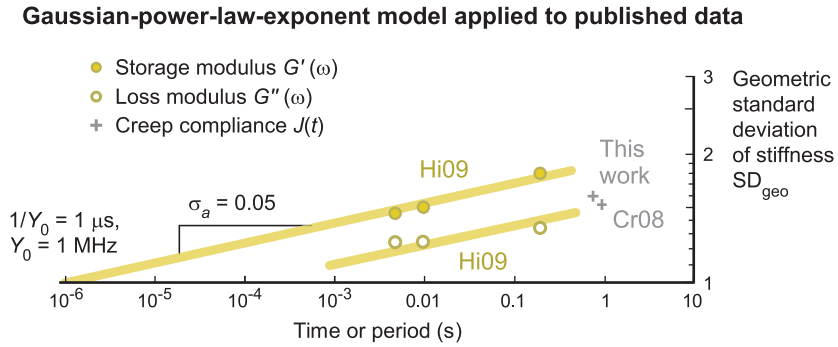

Figure 4-6: **Estimates of uncertainty lead to predictive models as shown by interpretation of Hiratsuka et al.'s experimental findings through a model of cell-to-cell mechanical variation.** Fig. 4-1(a) is replotted to include only techniques not requiring deep anchoring of probes to the cytoskeleton. The outcome from the present study (control conditions) is also shown. Hiratsuka et al. provided estimates of SD_{geo} for storage and loss moduli at multiple time scales, allowing fitting of the predictive model described in §4.3.3 and App. A.2. Solid lines show predictions relating SD_{geo} to frequency for storage (upper) and loss (lower) moduli, where the slopes correspond to $\sigma_a = 0.05$ (best fit). Extracted values of $\sigma_a = 0.05$ and $Y_0 = 1\,\text{MHz}$ are in good agreement with Fig. 4-1(a) and previous estimates of these values in the literature. Data referenced by study author and year [51, 215].

based on the multiplicative correction factor (approximately 1 for G' and approximately $e^{-\sigma_a/\bar{a}}$ for G''), it is predicted that the SD_{geo} for G'' will be approximately 20% less than for G' for $\bar{a} \approx 0.20$ and $\sigma_a \approx 0.05$. (The lower variation of G'' relative to G' can be understood by considering the hysteresivity $G''/G' = \tan(\pi a/2)$ in the structural damping model. Larger values of a reduce stiffness, but increase G'' relative to G', as shown in Fig. A-5. Therefore, fluctuations in a are naturally suppressed in G''.) Fourth, SD_{geo} will generally increase with increasing period $1/\omega$; conversely, the distribution of mechanical measurements will become more narrow with increasing measurement frequency.

All four of these predictions are confirmed by results and trends previously reported in the literature but unexplained up to this point (Fig. 4-1, Fig. 4-6). Values of σ_a and SD_{geo} have been extracted from multiple cell rheology reports, including a set of oscillatory indentation measurements of G' and G'' by Hiratsuka et al. [51]. Figure 4-6 shows a plot of SD_{geo} values of G' and G'' extracted from Hiratsuka et al.'s presentation of distributions at different frequencies, along with other groups' values. By fitting

Table 4.3: **Comparison of postulated origins of cell mechanical heterogeneity (simulation details, Balland et al. and this work).**

Factor	Balland et al. [29]	This work
Small-signal equivalent configuration	Infinite number of parallel-spring-dashpot models in series (uniform stress)	Infinite number of series-spring-dashpot models in parallel (uniform strain)
Rheological response	$G^\star(\omega) \propto \omega^a$; $J(t) \propto t^a$	$G^\star(\omega) \propto \omega^a$; $J(t) \propto t^a$
Source of variation	Varying selection of elements	Varying a
Component j stiffness	$\propto (i\omega\tau_j + 1)/\tau_j$	$\propto i\omega\tau_j/(i\omega\tau_j + 1)$
Distribution of time constants	$P(\tau) \propto \tau^{a-2}$	$P(\tau) \propto \tau^{-(a+1)}$
Creep compliance configuration	Set maximum available time constant τ_0 (constraint: simulation time $t \ll \tau_0$ or response will transition from power law to exponential)	Replace dashpot with element yield at $t = \tau_j$ and new element selection from $P(\tau)$ (constraint: simulation time $t < \max(\tau_i)$ or viscous flow will occur)
Time scale	Maximum time constant τ_0	Reciprocal attempt frequency $1/Y_0$
Simulation process	Select percentage of j from 1 to ∞ and let $\tau_j = j^{-1/(1-a)}$	Select lifetimes from $U^{-1/a}$ (where U is uniform distribution on [0,1]) and execute Gillespie algorithm; a is drawn randomly from a Gaussian distribution

the model, the following slope and unity intercept estimates are obtained: $\sigma_a \approx 0.05$ and $1/Y_0 \approx 1\,\mu s$. The first fitted parameter is in good agreement with the estimate for intrinsic exponent variation described above, with σ_a slightly less than the standard deviation (0.064, see Fig. 4-1(b)) of that group's reported a values. This finding supports the first prediction above. Second, the estimate of $Y_0 \approx 1\,MHz$ is in fairly good agreement with previous reports [26,42,43,48,150,164]. (Y_0 has previously been difficult to measure experimentally; Fabry et al.'s measurements on multiple cell lines range from $<10^3$ Hz to $>10^8$ Hz. For the cell type tested under the most conditions, human airway smooth muscle cells, the 95% confidence interval for Y_0 was [1.5, 7.8] MHz [48].) Third, Hiratsuka et al. found SD_{geo} for G'' to be 14–25% less than that for G'(Fig. 4-6), also in agreement with the prediction of how SD_{geo} should vary between the real and imaginary components of the complex modulus $G^\star$. Fourth, the reported or extracted SD_{geo} generally does increase with period for SD_{geo} values reported in the literature (Fig. 4-1).

Comparison with alternative existing model

It appears that the only other quantitative model applied to the right-skewed distribution of cell stiffness or compliance was presented by Balland et al., who modeled the cytoskeleton as a random collection of Kelvin-Voigt (i.e, parallel-spring-dashpot) units drawn from the time constant distribution $P(\tau) \propto \tau^{a-2}$ ($\tau \geq 1$) and connected in series (Table 4.3) [29].

Balland et al.'s arrangement predicts Gaussian power-law exponent and log-normal fitted creep compliance when these parameters are fitted to certain parts of the simulated creep rate curve. However, there are some advantages of the model presented here as compared with Balland et al.'s model. First, it is possible to analytically connect SD_{geo} with the noise temperature variation σ_a and make predictions about the dependence of this parameter on time or frequency. Second, the simulated creep curves are closer in appearance to experimental measurements, as shown in Fig. 4-7. Third, Balland et al.'s demonstration of a log-normal creep compliance distribution depends on

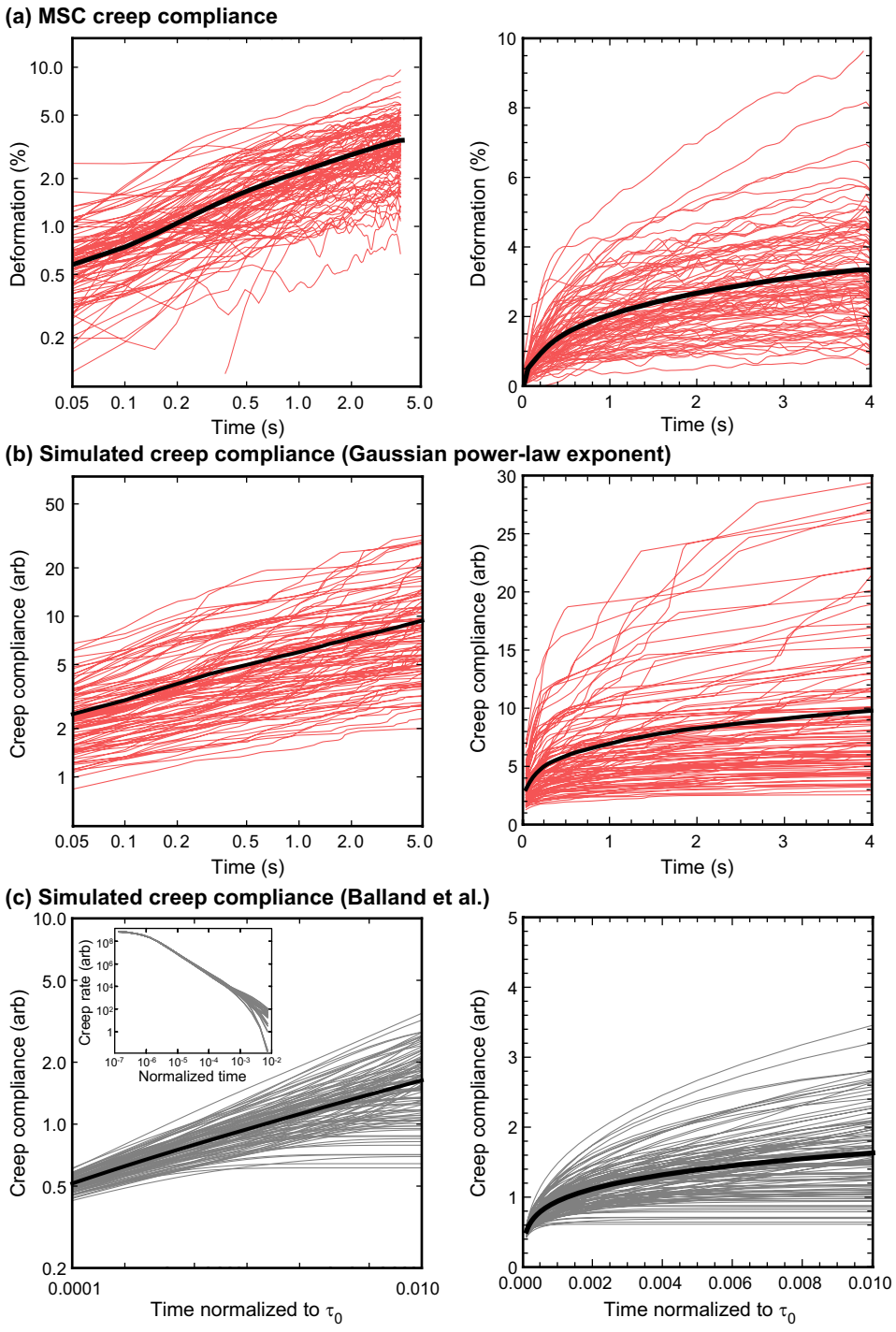

Figure 4-7: **Over two decades of time and for 100 samples each, comparison of experimental and simulated data.** (a) MSC creep compliance data obtained by optical stretching. (b) Simulated creep compliance with Gaussian a ($\sigma_a = 0.05$, $Y_0 = 10^6$ Hz). (c) Balland et al.'s simulation adjusted to give SD_{geo}=1.6 (inset, of creep rate to compare with Balland et al.'s report [29]). Experimentally observed, and predicted by simulation, is a generally increasing deformation for all cells during creep compliance experiments, through the slope on a log-log plot (corresponding to a) varies slightly based on inherent cell variation, as assumed by the model. Balland et al.'s model can be adjusted to give a similar standard deviation, but this model relies on a very small number of active elements, and also predicts that many cells cease to deform during creep compliance experiments, which is not observed experimentally.

the number of active viscoelastic elements being consistently very small. To illustrate this, let us calculate the number of elements still active, where "active" is defined as less than a fraction f extended, where f might be 90%, for example. For parallel-spring-dashpot elements connected in series, the time constants $\tau \geq -t/\ln(1-f)$ are considered. Balland et al. selected a fraction p of the population $P(\tau) \propto \tau^{a-2}$. It follows that at time t, $p[-\ln(1-f)/t]^{1-a}$ elements are still in play; for the typical value of $t = 10^{-3}$ (in dimensionless units relative to the largest time constant) and $a = 0.2$, fewer than 10 elements are active if f is taken to be 90% (and only three elements on average have extended <50%). This model therefore predicts that the pronounced right-skewed distribution of cell stiffness or compliance, measured on scales from tens of nanometers to tens of microns, rests on only a handful of effective viscoelastic units participating in deformation. The implication is that at any length scale, amplitude, or cell type, fewer than ten cytoskeletal elements remain at the end of each creep compliance test, which is implausible.

As mentioned in §3.4.3, the SGR model predicts increasing stiffness with decreasing fluidity, but previous experiments using attached beads show the opposite correlation, attributed to variation in bead anchoring depth [43, 48, 95]. Balland et al.'s model of log-normal distribution origin, which employs randomly selected groups of viscoelastic components, replicates this opposite correlation (i.e., increasing G with increasing a) [29]. In contrast, the focus in this work is intrinsic cell-to-cell mechanical variation alone, without conflation of bead attachment variation; in this context, the trend shown in Fig. 3-10 and developed in App. A.2 is internally consistent and is also compatible with the SGR framework.

A further advantage of the simulation approach developed in App. B.2 and illustrated in Fig. B-2 is that it offers an interpretation to partial recovery. Although outside the scope of the present study, it can be seen that upon load removal, the original (never-yielded) elements will relax, pulling the newer elements into oppositional tension. As recovery continues, each new element will also be drawn into tension. The equilibrium point will therefore be at a larger strain relative to the original point. This capability for interpreting partial recovery is not available with Balland et al.'s model, which always returns to its original position after load removal.

4.4 Discussion

4.4.1 Cell-to-cell mechanical variation is detectably dependent on ATP alone

The elimination of probe-cell contact, accomplished by obtaining mechanical parameters via optical stretching, did not eliminate the broad distribution ($SD_{geo} \approx 1.6$) of cell stiffness values (Fig. 4-2(a)), which corroborates the earlier conclusion drawn from Table 4.1: experimental technique is not the sole reason that measured stiffness values of cells are widely distributed.

Remarkably, the spread or distribution width of mechanical stiffness measurements, quantified as the geometric standard deviation SD_{geo} of the log-normal fit, was not detectably altered by cell lineage, mechanical cues, or cell diameter (Figs. 4-2, 4-3, 4-5). It is thus concluded that cell population heterogeneity does not depend solely on subpopulations of primary cells, perturbations in single-cell mechanical history, or cell cycle position, respectively.

It is not entirely clear why ATP depletion reduces mechanical heterogeneity among cells, but a plausible reason can be identified. Continuing the discussion from §3.4.2, recall that ATP drives the contractile process that modulates internal cell tension and the power-law exponent, and in turn the whole-cell stiffness. (Coupling between these

last two parameters is addressed in the next section.) Actomyosin binding and unbinding during ATP hydrolysis may result in considerable variation in this internal tension as the number of active motors at any moment varies stochastically. Under this view, extreme values of a and $|G^\star|$, which arise from coincidentally large or small fractions of myosin motors undergoing their power stroke, would no longer be seen when ATP depletion causes actin and myosin to remain tightly connected. This topic is further discussed at the end of §4.4.5, where several speculations are grouped that attempt to unify existing literature reports of mechanical heterogeneity and power-law rheology with the findings of this and the previous chapters.

4.4.2 Fluctuations in noise temperature could explain mechanical heterogeneity

Considerable evidence indicates that endogenous or chemomechanically cued variations in the power-law exponent a or SGR noise temperature $x = a + 1$ among cells are predominantly the source of variation in mechanical parameters.[3] First, the present studies show that a and stiffness $|G^\star|$ are correlated, as shown through repeated stretching (Fig. 3-10), and furthermore that a reduction in a distribution width is correlated to a reduction in creep compliance $J(t)$ distribution width (Fig. 3-9, Fig. 4-4). Equivalently, heterogeneity of a is coupled to the heterogeneity of $J(t)$. These findings motivate the analytical work, described in App. A.2, that successfully connects the distribution of a with the distribution of mechanical parameters such as complex modulus $G^\star = G' + iG''$, creep compliance $J(t)$, and relaxation modulus $G(t)$.

The analytical framework is applicable to animate and inanimate soft glassy regions that exhibit PLR, as long as the standard deviation of the power-law exponent quantifies the dominant source of mechanical variation. These requirements are concluded herein to be met by living cells that are measured individually and reported as a population distribution that is consequently log-normal. The present model focuses on endogenous variation and its manifestation as measured by low-contact or no-contact techniques (such as oscillatory probe indentation [51] and optical stretching, respectively), in which probe-cytoskeleton linkages are not required, thus reducing or eliminating measurement variation caused by ligand-receptor engagement of the cytoskeleton. Most valuable are high-throughput cell measurement techniques that allow robust estimates of distribution width as a function of time or oscillation frequency, as well as estimated errors in these widths. These quantities will inform models such as the one presented here that can then connect microscopic structural and energetic barriers within cells to emergent changes in mechanical distributions among cells.

4.4.3 Could mechanical anisotropy influence heterogeneity?

Earlier in this chapter, an analogy of heterogeneity in polycrystals was described. As the total length scale (the length scale that includes all measurements) increases from subgrain to grain to multigrain, collections of stiffness measurements at different points are expected to transform from a relatively homogeneous to a relatively heterogeneous collection and back again. During these transitions, orientation-dependent stiffness variation from grain to grain becomes apparent and then is "smeared out" into a Gaussian distribution via the central limit theorem when many grains are measured at once.

Could cells act analogously to grains? Can the hypothesis be tested that cell-to-cell mechanical variation results specifically from orientation-dependent stiffness? Unfortunately, the optical stretcher does not, at present, have the capability to rotate cells around an arbitrary axis. Rather, cells—which are approximately ellipsoidal with an

[3] Under this proposal, cells can be thought of as each exhibiting an average effective temperature that varies among cells, and possibly over time for any single cell, thought that correlation is not investigated here.

eccentricity close to one—typically rotate upon the application of trapping power so that the longest diameter is aligned with the laser (i.e., optical fiber) axis. Fortunately, the literature contains reports of cell anisotropy in the attached state that can inform speculations about orientation-dependent mechanical heterogeneity in the suspended state.

Based on existing literature reports, the possibility that mechanical heterogeneity is an artifact of cell orientation is unlikely. Anisotropy is not always seen [234], and findings of anisotropy in attached cells have been attributed to strongly polarized stress fiber arrangements [235] that do not appear in the suspended state. Notably, cells in which stress fibers are disrupted chemically lose their anisotropy [236]. Even with stress fibers present, the ratio between maximum and minimum stiffness is not very large—approximately 3–5× [235]. This ratio is not enough to explain tenfold differences in stiffness measurements from one cell to another, as found by optical stretching and the other studies listed in Table 4.1. Thus, the hypothesis that mechanical variation can be attributed solely, or even predominantly, to random cell orientation is not supported by available data.

4.4.4 Cancer cells: an exception to the log-normal rule?

The conclusion by Cross et al. [214] that cancer cell stiffness varies normally (rather than log-normally) draws attention; could the rheological behavior of cancer cells be fundamentally different? Furthermore, how do the best-fit parameters of these distributions compare? To examine these questions, Cross et al.'s elastic modulus data were extracted from their original and follow-up papers [215] (to the nearest 1 kPa) and the distributions of cancer and normal cells were compared on quantile-quantile charts (data not shown). The normal distribution was a slightly better fit for cancer cells, with a correlation coefficient of 0.98 vs. 0.96 for log-normal. To examine whether this better fit could be caused by chance, bootstrapping was performed to obtain a measure of the variation in these data. After repeated bootstrapping runs, the log-normal distribution was a better fit 7.4% of the time. Although this fraction is low (in contrast, the non-cancer cell stiffness data were better fit by a log-normal distribution 100% of the time), it still seems plausible that the null hypothesis of log-normal distribution (assigned based on to the prevalence of this distribution in other studies) could hold for these cancer cells and that the better fit to the normal distribution could be caused by chance.

The data from Cross et al.'s follow-up paper [215] were more equivocal; out of 100 bootstrapping runs, the cancer cells were better fit by a log-normal distribution 91% of the time (the non-cancer cells were better fit by a log-normal distribution 97% of the time). That paper did not discuss any parameterized fit for the distribution. It is concluded, therefore, that the better fit of the normal distribution to the first group of cancer cells ($n = 40$) was very plausibly caused by chance.

To examine whether there was a detectable change in distribution parameters between normal and cancer cells, log-normal distributions were fit to the data and bootstrapping performed again to determine the standard error of the distribution parameters. For the pooled data, the values were $\mathrm{SD}_{\mathrm{geo}} = 1.54 \pm 0.05$ and 1.51 ± 0.04 for the cancer and normal cells, respectively, which does not represent a statistically significant difference. Indeed, both of these values, acquired via AFM indentation on a time scale of 1 s, agree well with other reports of geometric standard deviation of cell stiffness distributions, as shown in Figs. 4-1(a) and 4-6, and indicate that cancer cells from Cross et al.'s studies do not necessarily represent an exception to the typical log-normal distribution of cell stiffness.

4.4.5 Comparison with inanimate materials

In the experimental component of the study described in this chapter, even cells killed by crosslinking exhibited the same mechanical heterogeneity as live cells, within error. Does mechanical heterogeneity require life? This question motivates a comparison of heterogeneity of cell populations vs. inanimate materials of various types to investigate the origin of cell-to-cell mechanical variation.

The metric of geometric standard deviation has generally been applied only cell populations. In contrast, Tseng and Wirtz et al. have quantified the spatial heterogeneity of complex fluids by the following metric: "... the relative contributions of the 10%, 25%, and 50% highest compliance values [obtained from the displacements of internal beads executing Brownian motion] to the mean compliance... [t]hese contributions should be exactly 10%, 25%, and 50% for a perfectly homogeneous liquid... [t]hese markers should become close to 100% in a highly heterogeneous milieu..." [237].

As an example of this metric, consider the following ten uniform measurements of a certain parameter: $\{3,3,3,3,3,3,3,3,3,3\}$. The 20% largest values are $\{3,3\}$, which contribute $(3+3)/10 = 0.6$ to the mean, or 20% of the mean of 3. Now consider the relatively heterogeneous group $\{3,3,3,3,3,3,3,3,100,100\}$. The 20% largest values, $\{100,100\}$, contribute $(100+100)/10 = 20$, which is 89% of the mean of 22.4. The distinction between the 20% and 89% contributions represents Tseng et al.'s metric of heterogeneity.

Tseng et al. do not provide a mathematical form of this metric, but the following expression is concluded to be equivalent:

$$\frac{\int_{F^{-1}(1-p)}^{\infty} x f(x)\,dx}{\int_{-\infty}^{\infty} x f(x)\,dx}, \tag{4.2}$$

where $F(x)$ and $f(x)$ are the cumulative distribution and probability distribution functions of the underlying distribution, respectively, and p is the proportion of interest (e.g., 10%).

Tseng et al.'s metric is relatively general in that it does not assume any underlying distribution of measurements. However, it might be assumed that the stiffness distribution of these complex fluids matches that of tissue cells: the log-normal distribution. (Note the implication that compliance would also be log-normal, based on the reciprocal symmetry of this distribution.) Recognizing that the numerator is the so-called partial expectation function and the denominator is the mean function, the expression can be rewritten in the case of the log-normal distribution as

$$\frac{e^{\mu+\sigma^2/2}\,\Phi\left(\frac{\mu+\sigma^2-\ln F^{-1}(1-p)}{\sigma}\right)}{e^{\mu+\sigma^2/2}}, \tag{4.3}$$

where

$$\Phi(x) = \frac{1}{2}\left[1+\operatorname{erf}\left(\frac{x}{\sqrt{2}}\right)\right] \tag{4.4}$$

is the standard cumulative normal distribution and where μ and σ are the mean and standard deviation of the log-transformed data. (Note that e^{σ} is the geometric standard deviation $\mathrm{SD}_{\mathrm{geo}}$.) With the identity

$$F^{-1}(1-p) = e^{\mu+\sigma\Phi^{-1}(1-p)} \tag{4.5}$$

for the log-normal distribution, the relationship

$$\Phi\left[\sigma-\Phi^{-1}(1-p)\right] \tag{4.6}$$

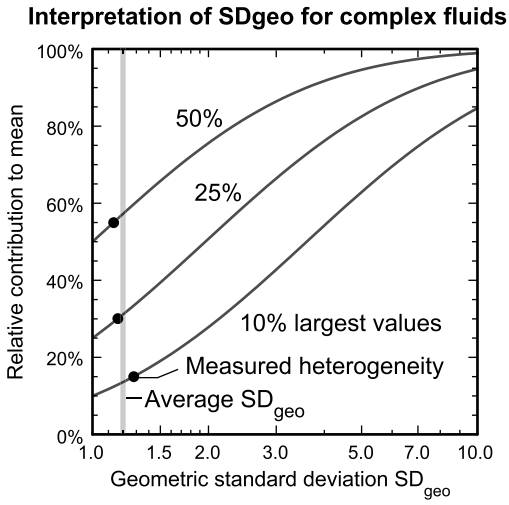

Figure 4-8: **Tseng et al.'s measurements of heterogeneity in complex fluids can be transformed into geometric standard deviation SD_{geo}, allowing data comparison of the mechanical variation of inanimate protein networks vs. that of live cells.**

is obtained.

Thus, knowing the experimentally measured value of the above expression (as a percentage that would equal p for a perfectly homogeneous material but would approach 100% for a strongly right-skewed material), the corresponding geometric standard deviation of the stiffness values can be obtained, under the reasonable assumption that stiffness is log-normally distributed.

When experimental values are given for each of the 10%, 25%, and 50% fractions proposed by Tseng et al., SD_{geo} can be calculated for each of these and the results averaged (Fig. 4-8). Consider, for example, their results for glycerin, nominally a homogeneous liquid: 15%, 30%, and 55% for the top 10%, 25%, and 50% quantiles, which corresponds to SD_{geo} values that average to 1.2. Shown in Fig. 4-8 are the corresponding SD_{geo} values as found numerically (black dots) along with the average SD_{geo}value (vertical gray line). (It should be mentioned that the metric does not describe skewness—which is essentially absent from the symmetric glycerine stiffness values—but only heterogeneity. Skewness, however, which is a function of SD_{geo} alone for the log-normal distribution, may be the more important parameter. Skewness implies heterogeneity, but the reverse is not true.)

Tseng et al. found that 3μM actin solutions evolved from an equivalent $SD_{geo} = 2.0 \rightarrow 1.0$ over 240 min; 10 μM solutions went from $SD_{geo} = 2.5 \rightarrow 1.2$, and 24 μM solutions went from $SD_{geo} = 3.0 \rightarrow 2.1$ [219]. Stiffness histograms of these samples indicate that the 24 μM solutions are the first to be prominently right-skewed. Interestingly, addition of the crosslinker Arp2/3 stiffened actin solutions considerably, and also considerably reduced both equivalent SD_{geo} and the power-law exponent [238]. These findings give support to the conjecture that large mechanical heterogeneity is associated with power-law rheology but that neither require live cells.

Shown in Fig. 4-9 is a proposed framework to inform our pursuit of the origins of mechanical heterogeneity in cells and other materials. Lipid vesicles and dilute protein gels (Fig. 4-9(a)) exhibit characteristic time constants (equivalently, can be modeled with one or several springs and dashpots), and are also found to be relatively homogeneous mechanically; that is, measurements across populations or regions are described by a Gaussian distribution [145, 217–219]. In contrast, the addition of crosslinkers or an increase in actin concentration (so that protein chains become entangled) produces a large spectrum of relaxation times, such that material rheological response resembles

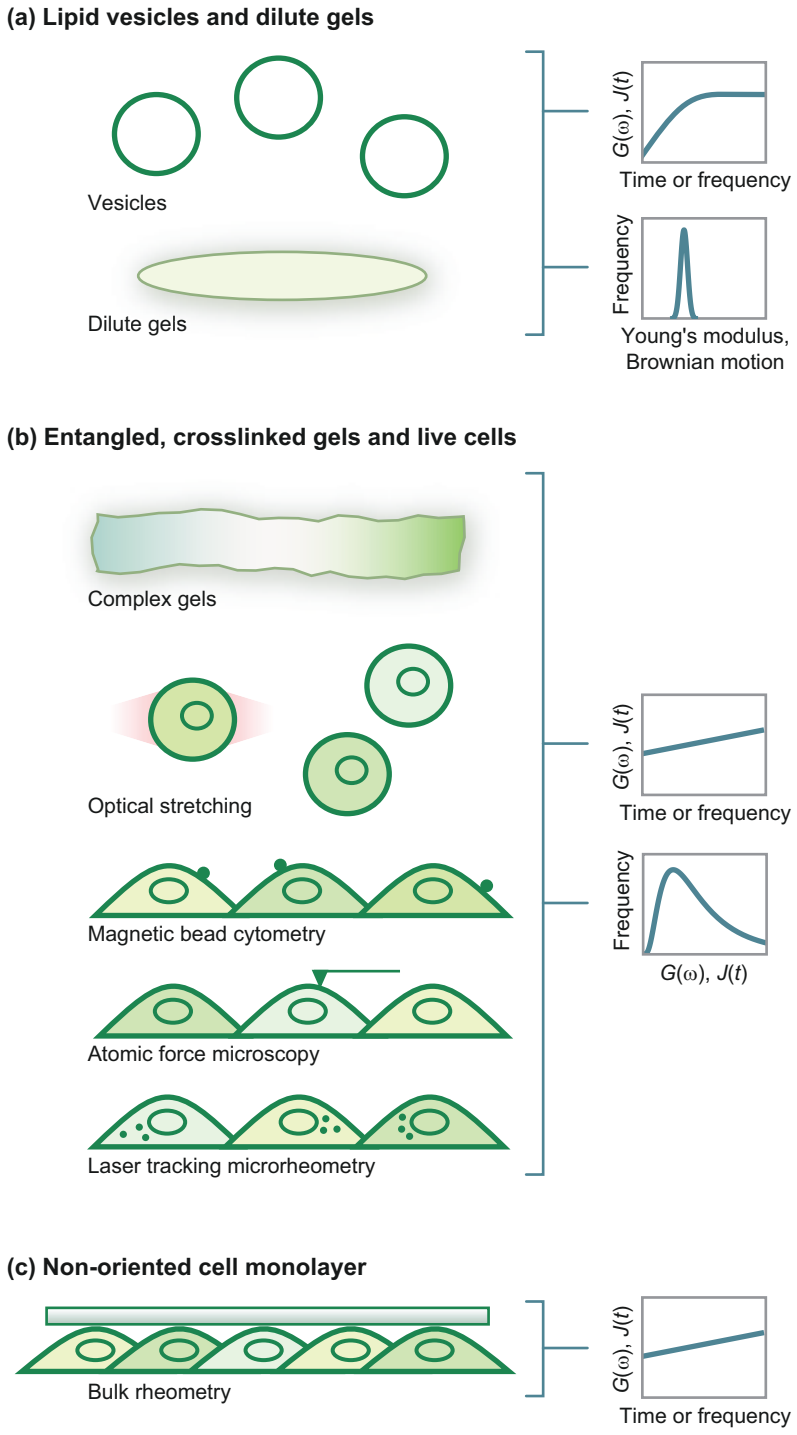

Figure 4-9: **Proposed framework for considering the origins and extents of cell-to-cell mechanical variation.** Considerable mechanical heterogeneity appears as material complexity increases from simple structures and gels to complex fluids and cells, and may decrease when cell are measured together. (a) Lipid vesicles and dilute gels exhibit one or several characteristic time scales and relative mechanical homogeneity. (b) In contrast, entangled and crosslinked gels and live cells exhibit a broad spectrum of relaxation times that appears as a power-law rheological response; these structures also exhibit considerable mechanical heterogeneity that appears as a wide, right-skewed distribution of stiffness values. (c) Cell monolayers also exhibit power-law rheology, but it is not yet clear how monolayer stiffness would be distributed when many cells' stiffnesses are averaged together.

power-law rheology (Fig. 4-9(b)). Moreover, these relatively complex fluids or gels exhibit a stiffness (as quantified by mean squared displacement of non-driven beads) that is relatively heterogeneous, as exemplified by Tseng et al.' work as discussed above. Therefore, even inanimate materials can behave, in terms of constitutive rheological behavior and heterogeneity, like a live cell. And as discussed in most of this chapter, single cells, attached and suspended, exhibit power-law rheology, with single cell stiffness distributed as a strongly right-skewed variable. Finally, monolayers of cells have been reported to deform according to power-law rheology (Fig. 4-9(c)) [228], though the variation in measured stiffness from sample to sample is not yet available and may depend on chemomechanical communication among cells.

At this point, only tentative conclusions are possible. One scenario that is compatible with general experimental findings and model guidance is that a collection of cytoskeletal proteins, suitably crosslinked like the inside of a living cell, exhibits a power-law exponent of $0.5 \lesssim a < 1$. With the existence of actomyosin contraction to tighten these chains, the power-law exponent is reduced to approximately 0.30–0.40 (0.20 for adherent cells current spread out and displaying tensioned actin stress fibers on rigid substrata). This value—for suspended cells at least—is minimally changed by mechanical perturbation, and holds for primary and immortalized cell lineages. Upon chemical crosslinking (and the death of the cell), the power-law exponent is unchanged because the tension does not change—the system is locked in place. Upon depletion of ATP, the tension also does not change, because all myosin is securely bonded to actin in the rigor configuration. However, the heterogeneity of the system does decrease because actomyosin release and binding is interrupted (and—to return to the question raised at the end of §3.4.2—these reaction events temporarily increase and decrease tension within the system that would alter a). As a result of the $a \Leftrightarrow |G^*|$ correlation described by SGR theory, a decrease in heterogeneity in a results in a decreased value of $\mathrm{SD}_{\mathrm{geo}}$. It may be that while elastic solids and viscous liquids are relatively homogeneous, evolved cells—along with synthetic polymer networks intended to reproduce their rheological behavior—lie in an intermediate position in which considerable mechanical heterogeneity arises and is somehow coupled to power-law rheology with $0 < a < 1$. However, these statements are relatively speculative. Let us turn to a more concrete subject: practical implications of unavoidable inherent cell-to-cell mechanical variation.

4.4.6 Case study I: Implications for diagnostics based on cell stiffness

This chapter has described so far evidence that mechanical variation arises naturally in the cytoskeleton, is unlikely to be caused solely by measurement techniques, and is therefore unlikely to be reduced even by optimizing measurement tools. What are the implications of a minimum mechanical variation among cells in any given population? Let us consider two possible applications: the measurement of multiple cells to search for abnormal cells indicating a disease state, and the sorting of a cell population to isolate cells from a valuable subpopulation. In the first case, the interest is in identifying mechanically abnormal cells and estimating their fraction. In the second case, the interest is likely in minimizing false negatives (equivalently, maximizing statistical power of the sorting algorithm) while consequently having to accept false positives.

In each case it is convenient to work with the log-transformed data of population stiffness so that the two subpopulations can be thought of as two Gaussian distributions (Fig. 4-10). The diagnostic case requires us to distinguish abnormal cells from the variation in the normal population caused by chance alone. Let us assume that the means μ_{A} and μ_{B} of the log-transformed data of the two populations are known and that the standard deviation σ of the log-transformed data is known and the same for both populations (i.e., $\sigma_{\mathrm{A}} = \sigma_{\mathrm{B}} = \sigma$). It is possible to fit measured creep compliance

data to the cumulative distribution function

$$\frac{P(A)}{2}\left[1+\operatorname{erf}\left(\frac{x-\mu_{\mathrm{A}}}{\sigma\sqrt{2}}\right)\right]+\frac{P(B)}{2}\left[1+\operatorname{erf}\left(\frac{x-\mu_{\mathrm{B}}}{\sigma\sqrt{2}}\right)\right] \tag{4.7}$$

to acquire a value of $P(B)$, which is the percentage of abnormal cells. But this still leaves us with the question of the uncertainty of B; how certain is the conclusion? Bootstrapping offers a way to quantify this uncertainty (App. B.1). The data can be resampled with replacement and a value of B fit each time, and the resulting distribution of $P(B)$ values tells us about the degree of confidence in the conclusion.

The value of within-population variation σ has critical implications for certainty of diagnoses. For a given distance between μ_{A} and μ_{B} (equivalently, a given ratio between the geometric means of the subpopulation stiffnesses), a larger value of σ implies a larger overlap between the histograms and a higher chance that a finite subpopulation of B cells will be hidden within the the natural variation of the histogram of A cells. As a concrete example, consider a test for oral cancer as described by Guck et al. [35], and assume that the cancerous cells are twice as compliant on average (i.e., the means of the log-transformed creep compliances differ by $\mu_{\mathrm{B}}-\mu_{\mathrm{A}}=\ln 2$). Also assume that the geometric standard deviation $\mathrm{SD}_{\mathrm{geo}}=1.6$ (so that $\sigma=\ln 1.6$) for both the cancerous and normal cells and that 5% of the cells are cancerous. Shown in Fig. 4-10(a) are simulated histograms corresponding to this scenario. When the bootstrapping technique is applied, the 95% confidence interval contains zero. Consequently, the possibility cannot be ruled out that zero cancerous cells exist based on analyzing the simulated data; in other words, natural variation in the distribution of normal cells has hidden the presence of the cancerous cells.

Figs. 4-10(b-d) show variations on this scenario. In Fig. 4-10(b), a higher number of sampled cells does allow the cancerous fraction to be detected; though uncertainty of the cancerous fraction still remains, the interpretation is that it would be very unlikely to observe this particular histogram if the fraction were zero. Alternatively, Figs. 4-10(c-d) show that a higher ratio of creep compliances or a larger fraction of cancerous cells also make it easier to identify these subpopulations. Of course, it is not always the case that Nature provides a favorable arrangement of large stiffness ratio and small variation. (For example, Guck et al. observed a stiffness ratio of $<2\times$ in their optical stretching study of oral cancer cells vs. normal cells [35].) When the parameters are unfavorable, the only solution may be to measure more cells per test, as shown in Fig. 4-10(b).

The next section describes another case study of the implications of minimum mechanical heterogeneity, one in which individual cells are sorted based on mechanical characteristics.

4.4.7 Case study II: Implications for cell sorting based on stiffness

The previous section addressed the challenge of estimating the prevalence of a subpopulation based on measurements of mechanical properties of a sample of multiple cells. An alternative application is the classification of single cells one at a time. The details of this test and the implications of a minimum intrinsic cell-to-cell mechanical variation are discussed in this section.

Consider a collection of A- and B-type cells, in which the B cells are more valuable. It is desired to isolate the B-type cells one by one in a process similar to fluorescence activated cell sorting (FACS), but based on mechanical properties. (A suitable example is mesenchymal stem cells as a rare subpopulation within the total number of cells occupying stroma such as bone marrow.) The decision process is schematized in Fig. 4-11(a). In the log-transformed domain, both populations are Gaussian distributed with some degree of overlap—perhaps negligible, perhaps considerable—that is a function

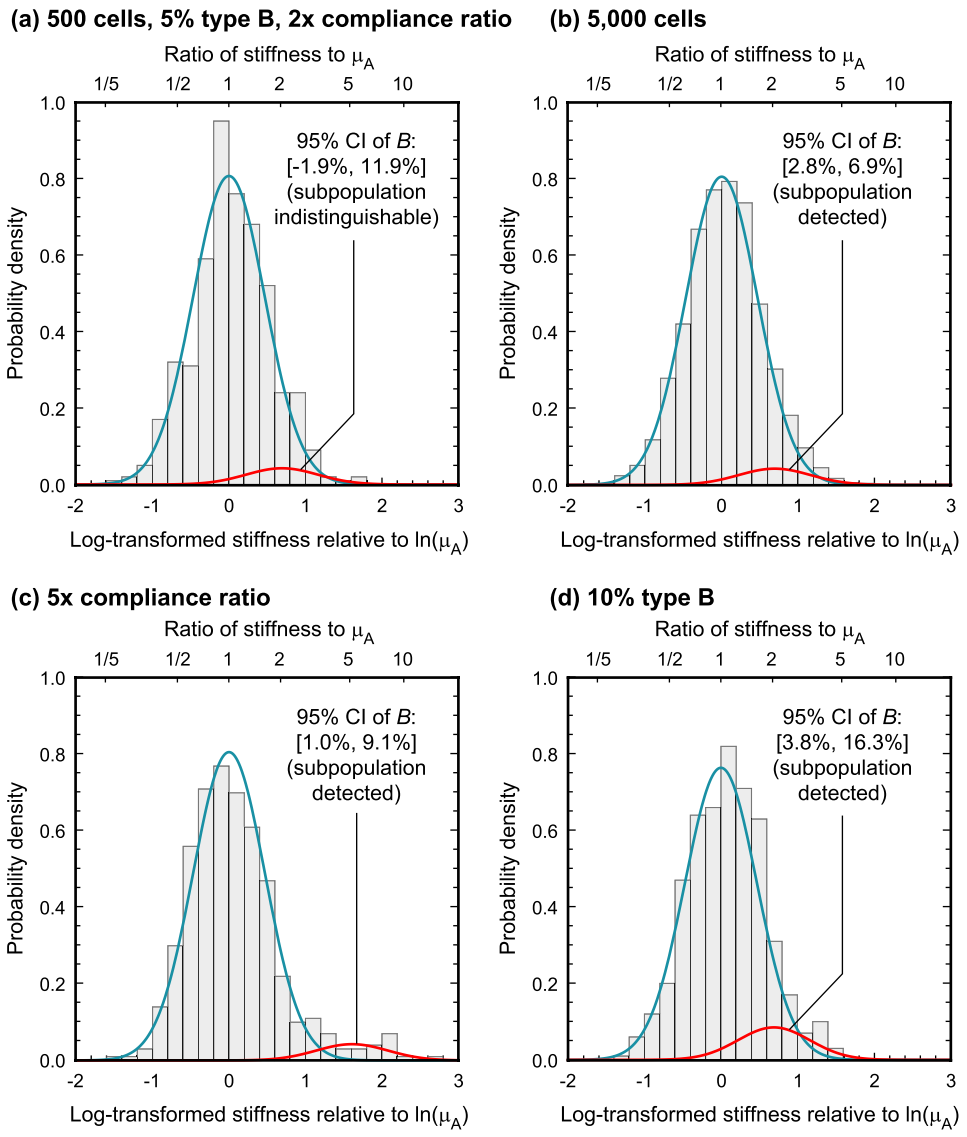

Figure 4-10: **Large mechanical variation among cells can hinder attempts to distinguish subpopulations in diagnostic applications.** Simulated distributions and deconvolutions of Gaussian parameters (representing log-transformed creep compliance measurements) demonstrating identifiability of an important subpopulation. Deconvolution provides an estimated fraction of B-type cells; bootstrapping allows simulation of repeated tests, providing a confidence interval of the expected range of results. (a) 95% confidence interval includes zero fraction of B-type cells, meaning that it cannot be ruled out that B-type cells are not present. (b) An increase in measured cells reduces the effect of random chance and makes it possible to distinguish the presence of B-type cells. (c-d) Diagnostic tests are predicted to fare better with a larger ratio of stiffness or a larger subpopulation fraction.

of intrinsic mechanical variation (and in practice, extrinsic variation such as experimental error as well). At any assigned threshold for diverting putative B-type cells, there will be some non-zero possibility of type I error (false positives, or errors of excess credulity, or probability α that an A-type cell will exceed the threshold) and some non-zero possibility of type II error (false negatives, or errors of excess skepticism, or probability β that a B-type cell will fail to exceed the threshold). Here the test designer may wish to choose the threshold to limit β, as this proportion corresponds to valuable B-type cells that are not collected. A test to distinguish B-type cells has a so-called power of $1-\beta$; this is the fraction of B-type cells that are identified. However, it can be

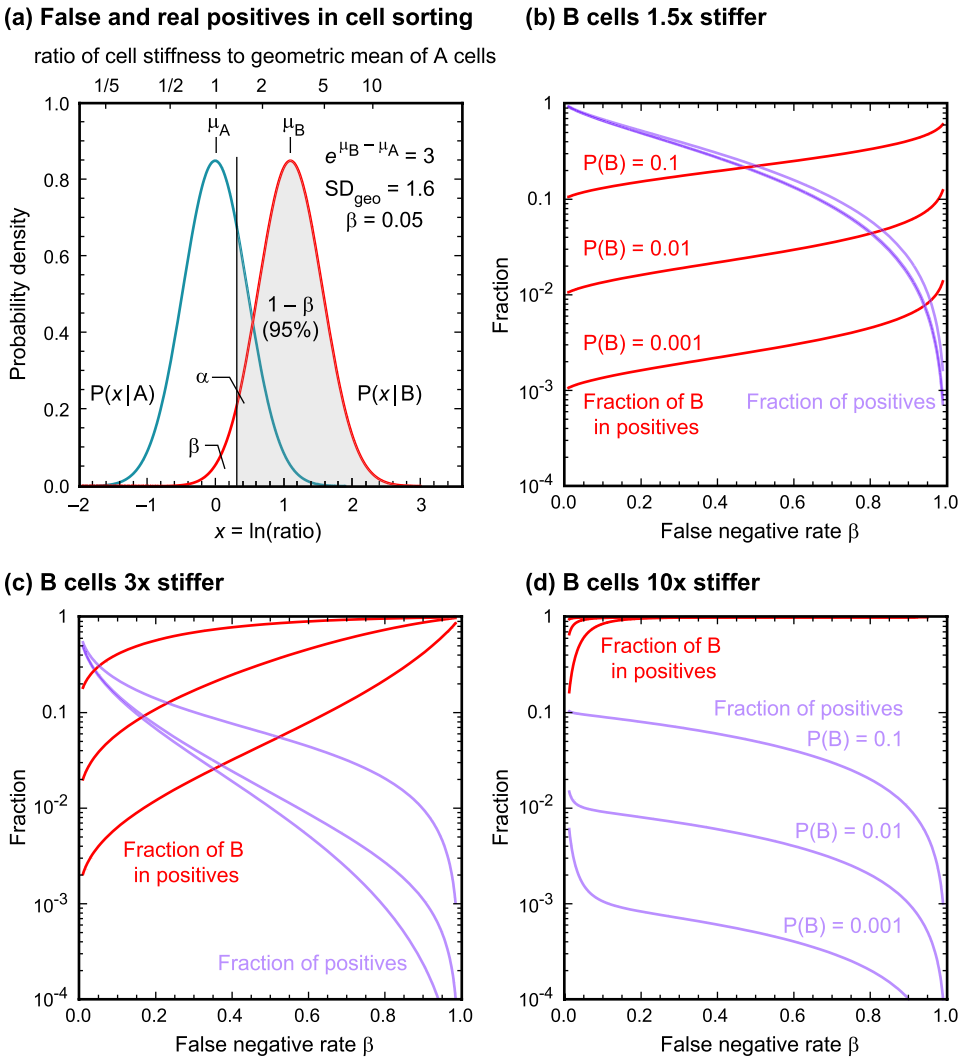

Figure 4-11: **Large mechanical variation among cells can hinder attempts to sort cells to enrich fractions of a subpopulation.** (a) Probability distributions of cell types A and B, log-transformed data, where each Gaussian shows the distribution of values assuming that type of cell is present. In this schematic, B-type cells are assumed to be 3× stiffer than A-type cells; a geometric standard deviation of 1.6, as has been measured in the present study, is also assumed. The type I error rate α of excess credulity occurs when an A-type cell is collected that happens to have extreme mechanical properties (e.g., it is relatively stiff for an A-type cell) that cause it to be misidentified as B-type. The type II error rate β of excess skepticism occurs when a B-type cell fails to be collected because its mechanical properties are not extreme enough (e.g., it is relatively compliant for a B-type cell). The number of diverted cells is therefore $\alpha P(A) + (1-\beta)P(B)$. (b-d) Examinations of predicted enrichment (fraction of B-type cells in positives) and predicted output (fraction of positives) for different ratios of mechanical properties between the two populations and also different original fractions of valuable B-type cells (in all curves, $P(B)$ is $\{0.001, 0.01, 0.1\}$ moving from bottom to top). The threshold value, here quantified by the false negative rate β can always be increased to improve enrichment at the cost of total output; the optimal threshold value depends on the particular application.

seen from Fig. 4-11(a)if the geometric means of the distributions of A and B stiffness are close, relative to the variation in these parameters, then a relatively large number of A-type cells—false positives—will be collected also.

Let us assume that μ_A, μ_B, and $\sigma_A = \sigma_B = \sigma$ are known. Then the log-transformed stiffness threshold is $\Phi_B^{-1}(\beta)$ and the proportion of false positives is $1 - \Phi_A[\Phi_B^{-1}(\beta)]$.

The fraction of correctly identified B-type cells is

$$f(B) = \frac{P(B)(1-\beta)}{P(B)(1-\beta) + [1-P(B)]\left\{1 - \Phi_A[\Phi_B^{-1}(\beta)]\right\}}. \tag{4.8}$$

Shown in Fig. 4-11(b-d) are the values of the success fraction $f(B)$ and the output fraction, defined as

$$P(B)(1-\beta) + [1-P(B)]\left\{1 - \Phi_A[\Phi_B^{-1}(\beta)]\right\}, \tag{4.9}$$

for difference in stiffness between A- and B-type cells, the true fraction of B-type cells, and threshold values (quantified here as the false negative rate β).

Let us consider as an example the relatively unfavorable circumstance in which $P(B) = 0.001$ and $e^{\mu_B - \mu_A} = 1.5$; that is, only one in one thousand eukaryotic cells is a mesenchymal stem cell, and the geometric mean of MSCs is 1.5× the geometric mean of all non-MSCs (Fig. 4-11(b)). Then it is only possible to exceed 1% B-type cells in the diverted output (an enrichment ratio of 10:1) if the threshold is set to provide $\beta > 0.97$. Thus, the consequence of this ratio of enrichment is the loss of the vast majority of the more valuable B-type cells.

4.5 Outcome

Conclusions

The results support the study's hypothesis. The approach of characterizing cell populations under different chemomechanical cues, along with an analytical model of mechanical variation, clarifies partially the origin and extent of mechanical variation among cells. It concluded from analysis of stiffness distributions acquired by optical stretching that single-cell mechanical heterogeneity cannot result solely from subpopulations within a primary cell type, recent mechanical perturbation (or lack thereof), cell-probe or cell-substratum chemomechanical influence, or cell cycle. ATP depletion, which inhibited actomyosin contraction and thus hindered the ability of cells to structurally remodel after substratum detachment, did significantly reduce the variation both in fluidity (power-law exponent or hysteresivity) and stiffness measurements. However, considerable heterogeneity persisted after all treatments that could not be reduced to negligible levels even by killing the cell by chemical crosslinking. Furthermore, re-examination of a report of Gaussian-distributed stiffness in cancer cells suggests that that rejection of a log-normal distribution was plausibly caused by chance variation in the data alone. Thus, the wide and right-skewed distribution of mechanical measurements in single cells is concluded to be a universal phenomenon.

The correlation between fluidity and stiffness that is predicted by a theory of soft glassy materials, and confirmed in multiple experiments here, is explored analytically to show how variations in these parameters are coupled. It is found that an assumed distribution of power-law exponent a—together with prefactors calculated from phenomenological and theoretical models of cell rheology—allows calculation of the distribution of rheological parameters. In fact, a Gaussian distribution of a leads immediately to a log-normal distribution of stiffness (and of compliance, because of the reciprocal nature of this distribution). Also, the minimum measurable geometric standard deviation SD_{geo} for experiments conducted in the frequency regime is found to be $\propto (Y_0/\omega)^{\sigma_a}$. The prefactor here depends upon the experimental regime, mechanical parameter of interest, and cell state, as listed in Table A.1. Presented here is a new way to estimate the standard deviation σ_a and attempt frequency Y_0 from the log-log slope and unity intercept of SD_{geo} as a function of experiment frequency. (Note that fuller interpretation of these estimates is enabled when SD_{geo} is reported over a

range of frequencies in a given study, as exemplified by Hiratsuka et al.'s report [51]). Additionally, an unexpected relationship is predicted and confirmed between the distribution widths of G' and G'' measurements for a given cell population. Finally, given that the parameter a has been linked to average activation energy or barrier height in the energy landscapes of so-called soft glassy materials, it is concluded that intrinsic fluctuations in a (among cells and/or over time in individual cells) could plausibly produce the cell-to-cell mechanical variation that is universally observed. The analytical model differs from previous investigations [29] that reproduce distribution shapes via phenomenological viscoelastic models, as testable predictions are now provided that relate physical mechanisms (e.g., attempt frequency) to measured distributions.

It is still not known, however, exactly how fluctuations in the parameter a might arise through molecular mechanisms. A look at the stiffness distributions of simpler structures such as lipid vesicles and protein gels indicates that extreme compliance does not necessarily imply a broad distribution of stiffness, as stiffness measurements among vesicles and dilute gels are found to be relatively homogeneous, as are measurements in fluids. Mechanical heterogeneity may appear once a protein network is sufficiently entangled or crosslinked to present a broad spectrum of relaxation times that is also the hallmark of power-law rheology. The coupling between these topics (the subjects of this chapter and the previous one) is conjectured only, though, and awaits further investigation or confirmation in the study of protein solutions synthesized to replicate key behaviors of live cells.

Possibilities for future work

There are at several outstanding opportunities to extend the results obtained with the present study. The first three are relatively straightforward extensions to the techniques of this chapter. The last is a relatively broad aim that continues the search for the point of origin of mechanical heterogeneity, now moving outside of the scope of this thesis by examining inanimate networks and other examples of soft or compliant matter.

First, suspended cells could be treated with histamine or serotonin to determine how values of stiffness $|G^*|$ and fluidity a, and the relationship between these parameters, are altered. The results could be interpreted in light of the present conclusion that actomyosin contraction in the cortex provides some internal tension in this structure (though relatively small compared to the tension of actin stress fibers in attached cells, resulting in higher a values vs. those in attached cells) and that this cortical tension can be detectably modulated via pharmacological intervention.

Second, the Monte Carlo simulations of cell deformation kinetics could be extended to include creep recovery, which has not been previously investigated analytically or by simulation. Substantial insight into the nature and extent of deformation recovery in cells may be provided by such simulations.

Third, cell monolayer stiffness could be measured, using the bulk rheometry method employed by Fernandez et al. [228], at different points or on different monolayers to determine whether stiffness is Gaussian distributed (which the central limit theorem would imply for the average of many independent cell stiffness values) or not (which would raise interesting questions on chemomechanical communication between cells that might cause fluidity and stiffness to be correlated over distances *in vitro* or *in vivo*.)

Fourth, further investigation of the origin of mechanical variation could focus on the appearance of variation and its correlation with power-law rheology protein solutions of increasing complexity. Even more broadly, do these correlations hold for non-polymeric soft matter independent of biological molecules or structures, such as foams, emulsions, or pastes, that exhibit power-law rheology? Such studies would support the development of a general theory of mechanical heterogeneity in soft or compliant matter.

Acknowledgments

Prof. Jochen Guck and Franziska Lautenschläger (Cavendish Laboratory, University of Cambridge) provided manufacturing design documents, customized software, and guidance for performing and interpreting optical stretching experiments. Eric Lehnhardt (Arizona State University & MIT REU program) cultured fibroblasts, performed optical stretching on them in normal and ATP-depleted states, assayed them for successful ATP depletion, and contributed interpretations of experimental results. Emer Clarke (StemCell Technologies and ReachBio) provided guidance in techniques for MSC isolation, culture, and differentiation.

Chapter 5

Mesenchymal stem cell metabolism, proliferation, and differentiation

Synopsis

The considerable stiffening of mesenchymal stem cells (MSCs) during proliferation—as measured in the attached state by atomic force microscopy (Fig. 1-5)—is interpreted in light of literature reports of subpopulations that exchange predominance over almost 20 population doublings *in vitro*. Increasing attention by the research community to the multiple mechanical parameters of live cells, along with optical stretching as a relatively high-throughput way to mechanically interrogate suspended cells, is applied to the challenge of finding characteristic mechanical markers of MSCs with greater differentiation capability, and ostensibly greater therapeutic usefulness. However, the mechanical transformation observed in the attached state is concluded to involve actin stress fiber presentation predominantly, as this transformation cannot be detected in the suspended state, which lacks stress fibers. Nevertheless, a statistically significant transformation is observed, albeit on the time scale of minutes rather than weeks: the effective stiffening of suspended MSCs soon after detachment from the substratum. The nature of this stiffening likely involves resorbed membrane area and/or improved attachment between the actin cortex and the plasma membrane, as blebs become less prevalent over the same time period. The chapter is concluded with a look back at the use of optical stretching in this thesis and the tool's advantages and disadvantages in individually characterizing thousands of single suspended cells.

5.1 Study background, hypothesis, and design

The fourth study in this thesis involves an understanding of mechanical transitions in single mesenchymal stem cells (MSCs) as they are expanded for therapeutic purposes *in vitro*. As introduced in §1.1.1, MSCs are multipotent eukaryotic cells that can be chemically differentiated *in vitro* into various terminal lineages corresponding to connective tissue (e.g., bone and cartilage). A degree of control over such terminal lineages *in vitro* has inspired strategies in which MSCs are expanded (i.e., allowed to proliferate via *in vitro* culturing), possibly exposed to chemomechanical cues, and re-injected *in vivo* in the hope of (re)growing connective tissue [247].

Unfortunately, multipotent cells cannot be produced indefinitely from an initial explanted and purified culture. The first limitation is shared by most physiological eukaryotic cells: division halts after a limited number of cell divisions (the so-called Hayflick

Table 5.1: **Reports of mechanical markers of mesenchymal stem cells and other cells.** (Techniques: AFM = atomic force microscope-enabled indentation; MPA = micropipette aspiration; OS = optical stretching; PDs = population doublings.)

Comparisons including human mesenchymal stem cells

Cell type and number	Technique	Comparison	Time scale	Group	Notes
MSC	Fluorescent staining	Osteodifferentiation	10 days	Rodriguez et al. (2004) [239]	Stress fibers spanning the cell transitioned thick bundles at the cell periphery.
MSC	AFM and fluorescent staining	Osteodifferentiation	10 days	Titushkin et al. (2007) [240]	"As osteogenic differentiation of [MSCs] progresses, more and more stress fibers are replaced with a thinner actin network that is characteristic of mature osteoblasts."
MSC	AFM	Osteodifferentiation	2 weeks	Yourek et al. (2007) [241]	Thinner parallel stress fibers were replaced with a thicker "crisscross" pattern.
MSC, osteoblast, chondrocyte, adipocyte	AFM	Stem cells vs. terminally differentiated lineages representing their progeny	N/A	Darling et al. (2008) [242]	Discussed in text.
MSC, osteoblast, osteosarcoma	AFM	Stem cells vs. terminally differentiated lineages representing their progeny	N/A	Docheva et al. (2008) [13]	Discussed in text.
MSC	MPA	Osteodifferentiation	3 weeks	Yu et al. (2010) [243]	2× increase in Young's modulus.
MSC	OS	Passaging and osteodifferentiation	18 PDs	**This work**	5× stiffening in the attached state during passaging is not detected in the suspended state, nor is a deformability change after 2 weeks osteodifferentiation.

Comparisons including other cells

Cell type and number	Technique	Comparison	Time scale	Group	Notes
Human epithelial	Passaging	AFM	≈30 PDs	Berdyyeva et al. (2005) [244]	Older cells were 2.4–3.9× stiffer.
Human fibroblast	OS	Donor age	27–80 yr	Schulze et al. (2010) [245]	Stiffening with donor age was attributed to an increase in F-actin content.
Bovine chondrocyte	AFM	*In vitro* passaging	6 passages	Wozniak et al. (2010) [246]	Increase in compliance was attributed to dedifferentiation.
Human fibroblast	AFM	Donor age	10–54 yr	Zahn et al. (2011) [244]	

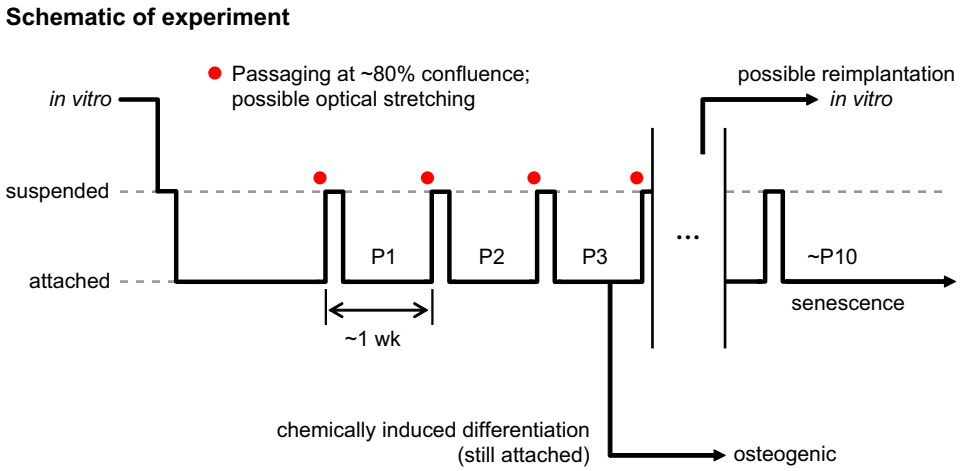

Figure 5-1: **Characterization of a population of suspended human mesenchymal stem cells during *in vitro* expansion by optical stretching.**

limit), after which the cells are senescent and nonproliferative. The second limitation is a loss in "functional plasticity"—differentiation potential—over multiple population doublings of an MSC culture. Adipogenic and chrondrogenic lineages become unavailable first, eventually leaving only the osteogenic lineage as a downstream lineage option.

Notably, previous AFM-enabled indentation experiments have shown that considerable stiffening accompanies this loss in differentiation propensity (Fig. 1-5) while chemical surface markers are minimally affected [4]. What should we interpret these mechanical alterations? And could they be used to separate useful (i.e., more plastic, or differentiable) MSCs from MSCs that have lost multipotency? Mechanical and structural differences have previously been correlated with differentiation in MSCs and with culture or donor age in other cell types (Table 5.1). As discussed in §1.2.5, it is plausible that such mechanical differences could be leveraged in high-throughput techniques (analogous to cell sorting in suspension by fluorescence detection of cell surface markers) that can isolate the MSCs with the most favorable properties. An investigation of these questions constitutes the primary aim of this study.

The study is designed as shown in Fig. 5-1. The hypothesis is:

> Stem cells have useful mechanical markers, and human mesenchymal stem cells can be distinguished and characterized by their mechanical properties as evaluated by optical stretching, as a practical demonstration of improved understanding of cell chemomechanics during and after the attached-to-suspended transition.

The present study applies the lessons learned and details uncovered in the studies that precede it. In Chap. 2, for example, a relationship was obtained between the thickness of a compliant coating atop a rigid base (serving in total as the substratum to which adherent cells attach) and the effective stiffness detected by the mechanosensory mechanism(s) of cells. It is known that stiffer substrata promote rapid proliferation of MSCs. A case study in that chapter investigated a therapeutic device into which MSCs are seeded to be held in a quiescent state of proliferation in order to extract cytokines. It would naturally be advantageous to obtain the highest percentage of MSCs possible, and therefore to have the capability for sorting MSCs.

In Chap. 3, characteristic mechanical markers of eukaryotic cells were identified. Perhaps the most obvious marker is the deformability under load, which can be quantified in terms of the creep compliance. Other potential markers that could be leveraged

include the recovery upon load removal and the power-law exponents during both stretching and recovery. It also became clear in that study that the optical stretcher can measure cell mechanics at a relatively high throughput compared to, for example, AFM, bead cytometry, microplate rheometry, or micropipette aspiration (Table 3.2). Finally, the optical stretcher can easily measure cell size (specifically, the major diameter and one minor diameter of the ellipsoidally shaped cell), enabling the study of possible correlations between stem cell usefulness, population doubling number, and cell major diameter.

In this study, optical stretching (OS) is used to acquire data to complement and extend the AFM results shown in Fig. 1-5. The focus is not only on characterizing therapeutically useful cells for possible sorting and/or diagnostic applications, but also on continuing to investigate fundamental cellular mechanisms of cell rheology. An optical stretcher augmented with syringe rotation is used to examine >10,000 cells, and to generate creep compliance measurements in stretching and recovery of >1,200 cells. These observations of dynamic MSC mechanical markers over different time scales are intended to illuminate several previously unexplored areas involving stress fiber participation. The optical stretching technique allows detection of alterations in MSC mechanics initiated by external chemomechanical cues over multiple time scales, from structural and mechanical changes over months of in vitro passaging, to cell remodeling over tens of minutes after detachment from a rigid substratum, to characteristic deformation occurring over seconds from an applied photonic load.

5.2 Materials and methods

Cell culture and optical stretching

Primary human mesenchymal stem cells (MSCs) were obtained from the bone marrow of three adult donors (Stem Cell Technologies and ReachBio LLC) and isolated and expanded by density gradient centrifugation and plating on TCPS [58]. PD1 was considered to be the first population doubling after identification of MSC colonies. Cells were cultured at 37°C in a humidified atmosphere at 5% CO_2 in proprietary media (App. C.1). Cells from donor 1 were frozen at passages 1 and 2 (P1 and P2) and later thawed, seeded at $2 \times 10^3\,\mathrm{cm}^{-2}$, and expanded to P9 (at which point the typical observed doubling time of two days increased considerably as the cells became senescent). Cells from two additional donors (donors 2 and 3) frozen at P1 and later thawed, seeded at $2 \times 10^3\,\mathrm{cm}^{-2}$, and expanded to P3 to specifically investigate possible mechanical changes at early passage numbers. Population doublings (PDs) were determined by counting cell number at seeding with a hemacytometer; each passage corresponded to approximately two PDs.

These culture conditions are generally believed to avoid widespread differentiation of adult MSCs during long-term expansion subculture [58]. (Some groups report occasional spontaneous osteodifferentiation [248] or increased expression of osteogenetic markers such as osteocalcin in expansion cultures [61], though others see decreased osteocalcin [249] and still others see little change in osteogenic gene expression over multiple passages [250].) No visual or quantitative assay evidence were seen (from inspection of phase contrast images for lipid vacuoles or mineralization, or from standard assays of alkaline phosphastase as an early marker of osteogenesis [58]) that would suggest that a considerable fraction of the MSCs were differentiating toward terminal lineages such as adipocytes or osteoblasts in the absence of deliberate chemical induction. In this work, we refer to all originally identified MSCs that have not undergone deliberate chemical differentiation as MSCs.

Differentiation was induced chemically according to protocols given in App. C.1, Inc. MSCs were expanded to PD4 and PD14, then incubated in the presence of os-

teoinductive culture media for two weeks. Differentiation was characterized by alkaline phosphatase activity normalized to total protein content (App. C.3).

Optical stretching was performed as described in Chap. 3 by using the protocol in App. C.2. Experiments were performed by stretching as many cells as possible in 2 h. Only clumps, severely blebbing cells, and dead cells were not stretched; additionally, in most experiments, every cell (stretched and non-stretched cells) was photographed to provide a visual record consisting of >10,000 images of MSC morphology in suspension.

Additional experiments were performed to investigate the influence of different detachment agents on the resulting suspended cell morphology, as smooth surface topography is easier to analyze by machine vision than blebbing topography. These chemical agents included 0.25% trypsin alone, 0.02% EDTA (Versene, Sigma) alone, and the proprietary cell detachment medium Accutase (Sigma), along with the standard treatment, 0.05% trypsin and 1 mM EDTA.

Data analysis

Blebbing cell proportions were compared between populations by using Pearson's chi-square test. Because no trend was observed in the overall power-law exponent a or the recovery parameter C with experiment time (§5.3.2) these parameters are calculated from all experiment times. The comparisons of cell maximum deformation between passages as measured by OS, however, consider only the cells stretched during the second hour of the 2 h experiment, when the cell deformability was insensitive to time, as discussed in §5.3.2. The standard error of fitted constitutive law parameters was determined by using the bootstrapping technique (App. B.1).

5.3 Results

5.3.1 Optical stretching fails to identify mechanical markers of passaging or osteodifferentiation

In contrast to the mechanical changes discovered by AFM on attached MSCs (Fig. 1-5), no passage-dependent trend in mechanical stiffness (maximum deformation at the end of the stretching period and recovery magnitude C), fluidity (stretching and recovery power-law exponents a_S and a_R), distribution width (geometric standard deviation SD_{geo}), or cell diameter was observed for suspended MSCs from three donors, as measured by OS and shown in Fig. 5-2.

Proliferation *in vitro* was accompanied by a reduction in osteogenic differentiation potential following chemical induction (Fig. 5-3(a)), as consistent with previous studies of reduced differentiation potential upon extended passaging [58, 61–63]. However, osteogenesis did not alter MSC creep compliance as measured in the suspended state by optical stretching (Fig. 5-3(b)).

5.3.2 MSCs effectively stiffen over first hour in suspension in response to detachment

Across all passages, the whole-cell compliance of suspended MSCs decreased during the first hour of the experiment (starting 30 min after the cells were detached from the TCPS substratum) before reaching an equilibrium value (Fig. 5-4). The rate of stiffening during the first hour was calculated by linear regression to be $-1.0 \pm 0.3\%$ deformation per hour. Other mechanical parameters such as the stretching and recovery power-law exponents a_S and a_R, geometric standard deviation SD_{geo}, and cell diameter did not change observably during this time frame, however. This contrast is also

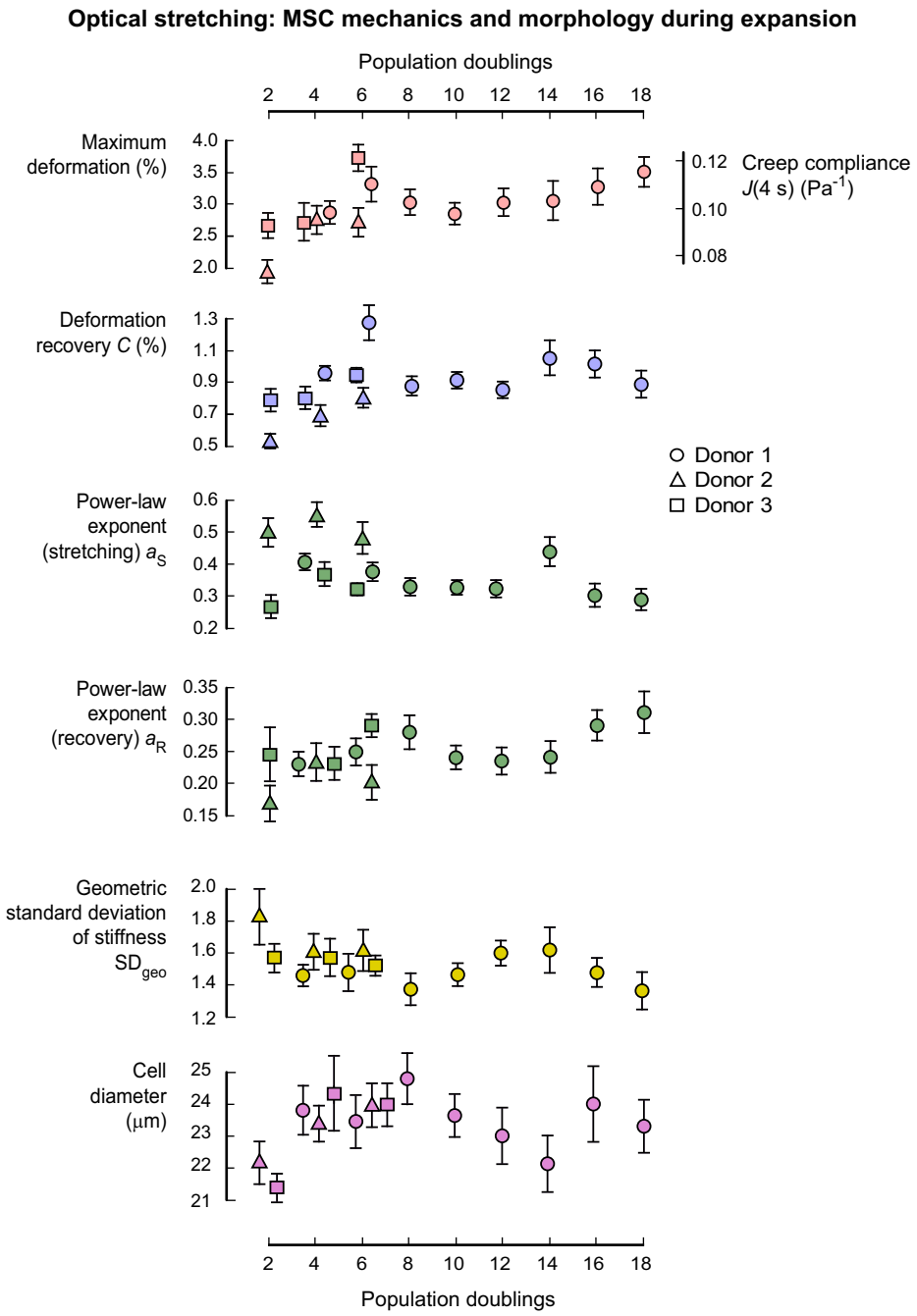

Figure 5-2: **Characterization of MSC whole-cell mechanics and size over multiple PDs *in vitro*.** No detectable change is measured in suspended MSC mechanical and morphological parameters as measured by OS (maximum deformation, recovery magnitude C, stretching and recovery power-law exponents a_S and a_R, stiffness distribution width SD_{geo}, and cell major diameter, $n = 39$ to 204 cells per PD). (All data shown as mean ± standard error.)

shown in the time frame of the stretching event, where the difference is seen to accumulate during the 4 s stretching period but is unaffected by the laser power reduction to trapping level during the 2 s recovery period (Fig. 5-4(inset)).

An experiment was performed to decouple the loss of temperature and pH control from substratum detachment, to see if one or the other was necessary to cause whole-cell stiffening (Fig. 5-5). Cells were either (1) removed from the incubator, kept at

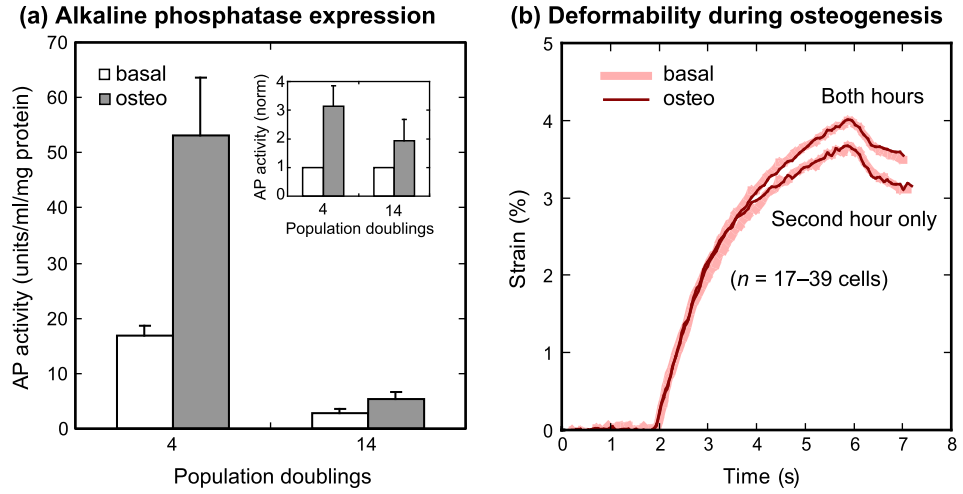

Figure 5-3: **Optical stretching does not detect a mechanical marker of decreased differentiation propensity of MSCs during extended passaging.** (a) Osteogenic differentiation propensity decreased during extended passaging, as shown by decreased alkaline phosphatase activity (an indicator of osteogenic differentiation). (Inset, alkaline phosphatase activity of osteo-induced cultures relative to basal cultures.) (b) Cell deformation is not detectably altered after osteogenic induction.

room temperature and atmosphere for 1 h, detached, and stretched; or (2) detached, stored in suspension in an incubator for 1 h with the container periodically inverted to counteract cell sinking, and stretched. Whole-cell stiffening was still observed in the population that was kept at room temperature before detachment ($p = 0.02$ for different population deformability), but was not observed in the cells that were stored after detachment ($p = 0.79$ for different population deformability); this population had already equilibrated at a higher average stiffness (i.e., lower maximum deformation). The combination of detachment and subsequent suspension was therefore found to be a necessary stimulus for stiffening of suspended MSCs over tens of minutes.

The frequency of cells with visible blebs decreased significantly during the 2 h experiment ($p = 1.3 \times 10^{-5}$): of cells from donor 3 (P1–3), 166/194 cells (i.e., 86% of cells) observed during the first 15 min had visible blebs, compared to 261/474 cells (i.e., 55% of cells) observed during the second hour. Of the cells observed over time without irradiation, blebs did not lead to cell disintegration, which would signal apoptosis (controlled cell death); instead, blebs dynamically formed and retracted at different membrane locations for many minutes (Fig. 5-6). The fraction of blebbing cells was not observably influenced by the chemical detachment mechanism (trypsin, EDTA, Accutase, or trypsin plus EDTA; data not shown), indicating that blebbing was not caused by a particular chemical agent but was instead a hallmark of recently suspended MSCs.

5.3.3 Cell availability, morphology, and deformation during optical stretching experiments

Optical stretching is a recently developed technique [34] in which single cells are serially advanced through a microfluidic assembly, irradiated to apply a photonic mechanical load, and characterized by quantifying deformation with machine vision. Presented here are experiences with cell availability and morphology, as these factors have considerable influence in throughput and image analysis, respectively.

Much variety was observed in the morphology of suspended MSCs (Fig. 5-7), which exhibited folds, blebs, and/or filopodia and were sometimes undergoing cytokinesis when detached from TCPS. Dead cells, which were identified by the lack of a white ring shown by phase contrast microscopy of an intact plasma membrane, and clumps

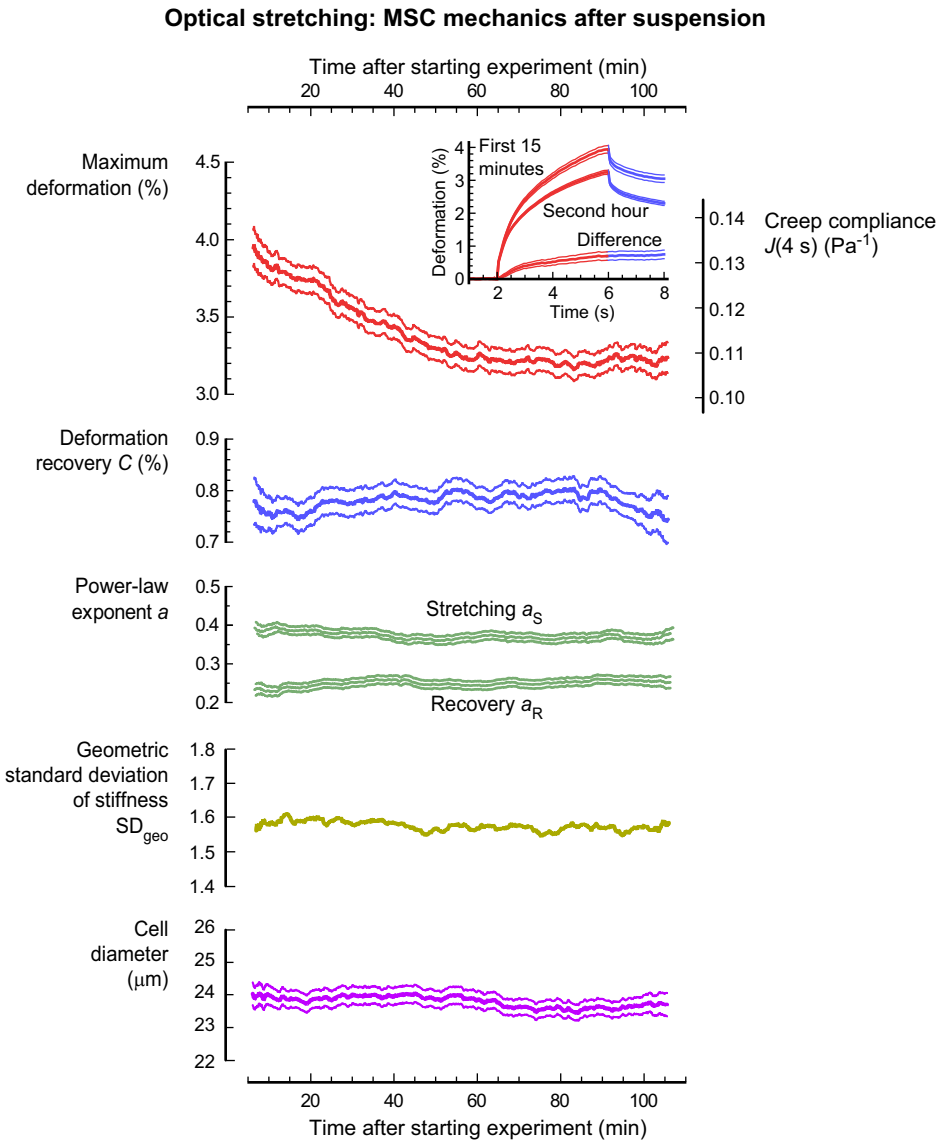

Figure 5-4: **Recently suspended cells stiffen after detachment.** MSC compliance, quantified as the average deformation at the end of the stretching period, decreases during the first hour of the stretching experiment (i.e., the time period 30–90 min after detachment) before reaching equilibrium in the second hour (400-cell moving average). Inset, accumulated difference in deformation between cells stretched in the first 15 min of the experiment ($n = 232$ cells) and cells stretched in the second hour ($n = 581$ cells) over the stretching and recovery periods. Other mechanical parameters are relatively unaffected during the same time period. (All data shown as mean ± standard error.)

of multiple cells were also observed. Single-cell appearance was divided approximately evenly between smooth and folded cells and blebbing cells, with the other morphologies observed only occasionally. Not surprisingly, more clumps of cells were observed when a higher suspension density was used.

Several hundred cells could be accessed in the capillary during a 2 h experiment, which represented approximately 1% of the total number of detached and suspended cells from a T-25 TCPS flask at 50% confluency. Through the process of stretching and analysis, this number was reduced by roughly an order of magnitude by the following constraints: first, clumps and severely blebbing cells were ruled out, and stretching was attempted on single smooth and folded cells only. Second, cells that rotated perceptibly

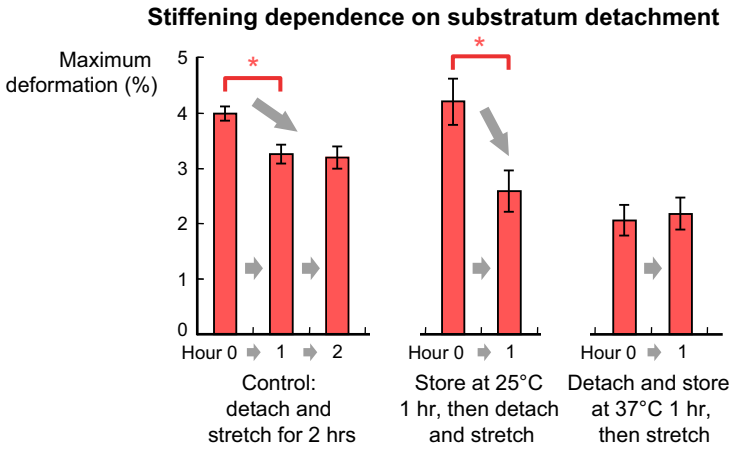

Figure 5-5: **Substratum detachment and suspension, but not exposure to room temperature and uncontrolled pH, is necessary for stiffening to occur.** Cells that were stored in the suspended state at 37°C for 1 h have already equilibrated at higher stiffness when the stretching experiment begins (labeled as Hour 0 for all conditions). (All data shown as mean ± standard error; $p = 0.0009$, 0.02, and 0.79 for first-hour stiffening for the three conditions, respectively.)

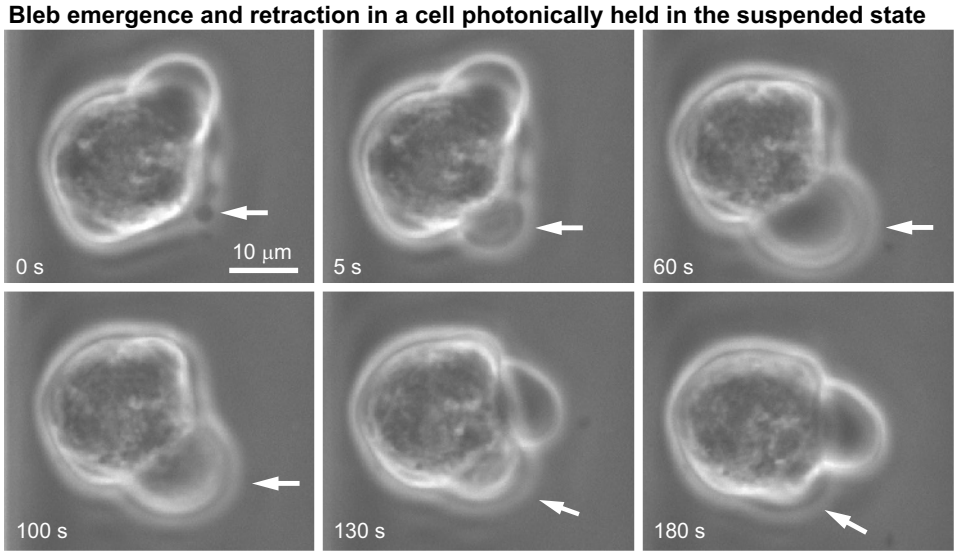

Figure 5-6: **OS at a relatively low (trapping) laser power enables observation of dynamic blebbing in a suspended adherent cell.** Repeatedly and at different locations on the cell surface, membrane detachment from the cortex is followed by cytosol streaming into a newly formed bleb, followed by actin polymerization and new cortex formation inside the membrane and bleb retraction driven by actomyosin contraction. Arrow denotes a single bleb's appearance, expansion, and contraction over 180 s; note that contraction of one bleb in these images is always correlated with the expansion of another at a different location.

during stretching were also ruled out, as the changing periphery of a rotating cell can be mischaracterized as axial elongation during automated image analysis [174]. Third, cells for which the periphery could not be accurately fit by edge detection during analysis were ruled out. Approximately 10% of all observed cells satisfied all of these conditions to make up the final data set, which typically contained several tens of cells per flask.

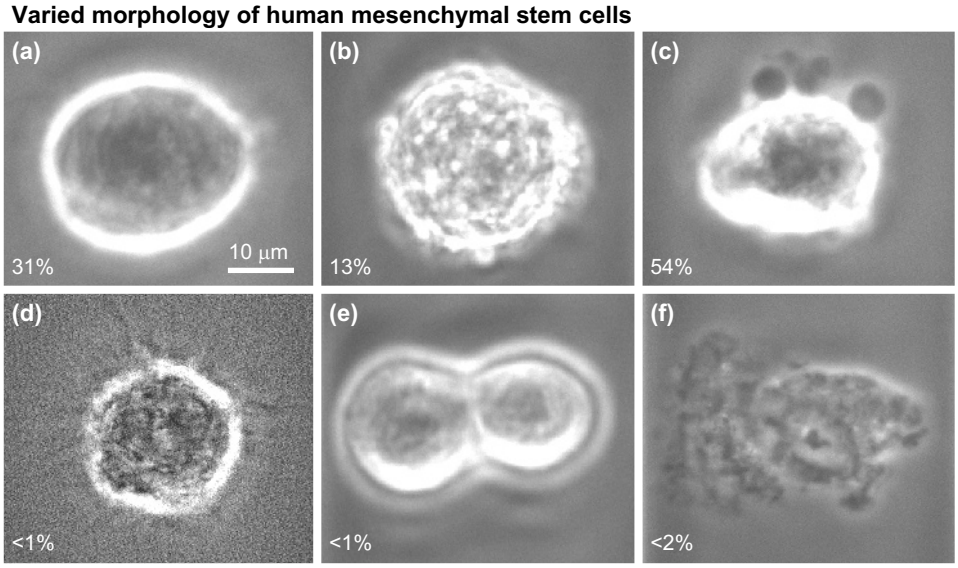

Figure 5-7: **Suspended MSCs exhibit a variety of surface morphology.** Observations include (a) smooth cells and cells with (b) folds/ruffles, (c) blebs, and (d) filopodia (image sharpness enhanced to show features more clearly); also occasionally observed are (e) cells undergoing cytokinesis and (f) dead cells, along with clumps of cells. Smooth, ruffled, and blebbing cells are most frequently observed (frequencies shown), and smooth and ruffled cells and cells with filopodia are most amenable to automated edge detection during analysis.

5.4 Discussion

5.4.1 Mechanical and structural markers of extended passaging exist for MSCs in the attached state only

Why would MSCs populations be expected to mechanically and/or structurally change over *in vitro* culture time, as shown in Fig. 1-5? Multiple MSC subpopulations have long been known to exist [58,222,223], the two most prominent of which are rapidly proliferating spindle-shaped cells and slowly proliferating round or cuboidal cells [13,251]. The more rapidly dividing cells exhaust their proliferative capacity relatively early, resulting in an increased proportion of cuboidal cells over time [222]. Docheva et al. previously found no distinctive mechanical differences in the (peri)nuclear region of spindle-shaped and cuboidal cells [13]; however, it is not this region but rather in the expression of stress fibers away from the nucleus that morphologically distinguishes these cells: spindle-shaped cells feature a more diffuse, unaligned collection of stress fibers, while cuboidal cells feature abundant pronounced fibers [13,222]. AFM images of cytoskeletal structure in living MSCs in Fig. 1-5 correlate well with these differences in observed subpopulation morphology.

It is concluded, therefore, that measurements of increasing average stress fiber radius and stiffness across all MSCs with extended passaging represent the mechanical component of a transition from cultures of predominantly spindle-shaped cells to predominantly cuboidal cells. Both subpopulations express surface markers essentially equally under optimal conditions [63,252]; however, the cuboidal cells are less likely to differentiate down any lineage other than osteoblastic [248], and thus the entire population exhibits reduced adipogenic and chondrogenic capability with extended passaging.

The finding of mechanical alterations in the attached state (by AFM scanning and indentation, Fig. 1-5) contrasts with the absence of detectable changes in the suspended state (by optical stretching, Fig. 5-2), even when the suspended cells were

attached to TCPS only some tens of minutes before beginning each OS experiment. It is important to note that cell detachment does not erase the passaging-dependent mechanical stiffening trend found with AFM, as all MSCs were detached every other PD for passaging. Evidently, no correlation is seen with OS because the predominant cytoskeletal changes are manifested only in the attached state. It is concluded that MSC population aging is structurally characterized by considerable changes in stress fiber organization but minimal changes in cortical actin organization. The conclusion is compatible with Darling et al.'s finding that mechanical differences lessened between MSCs and cells representing their downstream lineages when the cells were barely attached [242]. Additionally, the observed reduction in MSC differentiation potential and eventual loss of proliferative ability is in agreement with previous reports of *in vitro* culture [58,61–63]. Structural contrasts between different lineages/passages that arise with attachment and spreading (and disappear with detachment) are expected if stress fiber organization is readily altered by differentiation/passaging while total actin content and cortical thickness and organization is not readily altered. It is not suggested that all measurable mechanical differences vanish when adherent cells are suspended; differences in cancer cells and chemically differentiated cells have in fact been found in the suspended state [35, 39]. However, differences that manifest themselves primarily in altered morphology and mechanical properties of stress fibers, which appear only in attached cells, may be difficult or impossible to detect while the cells are suspended.

5.4.2 Effective stiffening of recently suspended MSCs correlates with cortex-membrane remodeling and stabilization

The stiffening observed 30–90 min after MSC detachment (subsequent to a presumed reduction in stiffness when stress fibers depolymerized during trypsinization) could conceivably originate from the detachment process or from extended time at room temperature and pH uncontrolled by the CO_2-bicarbonate buffer system during OS experiments. It is found from decoupling these two conditions that prolonged suspension for tens of minutes triggers MSC stiffening over this timescale. It is possible that actin made available from stress fiber depolymerization is incorporated into the actin cortex, but one would expect to observe stiffening both in stretching and recovery if this mechanism were dominant. Instead, the cells effectively stiffen only in stretching, suggesting that an asymmetric process such as molecular unbinding occurs. Furthermore, the power-law exponent does not detectably change during the tens of minutes after suspension. This exponent is linked to the stiffness and internal tension of the cytoskeleton, as explored in Chaps. 3–4 of this thesis. The fact that the exponent is unchanged while the whole-cell deformability changes is further evidence that the transition occurs at the membrane-cortex connection only.

Over the same timescale a significant reduction in blebbing occurs, in agreement with literature reports of surface remodeling and blebbing reduction in multiple cell lines over tens of minutes following detachment [78–80, 253]. As mentioned earlier, the actin cortex is actively contractile, and the results are seen prominently in the form of blebs, local surface herniations or blisters where the plasma membrane detaches from the cortex [81, 165, 254, 255]. Blebs initially appear as growing hemispheres consisting of cytosol squeezed out of the cell by contraction-driven internal pressure. Blebs were long thought to represent only cell damage, and it is true that apoptosis involves blebbing (in a different form that leads to to cell disintegration). However, the blebbing of interest here (particularly blebbing after cell detachment) is now recognized to be a normal part of cell behavior [254], possibly a migration mechanism in attached cells [82], and a signal of mechanical remodeling in recently suspended cells [253]. The cell even has its own bleb recovery system; polymerization of actin on the inside of the bleb surface enables actomyosin contraction that withdraws the bleb [165].

It is known that the plasma membrane provides a reservoir of surface area that

adapts to the changing needs of the cell during suspension and attachment [256]; in general, cells that are initially more spread out upon substrata exhibit more blebs in suspension after detachment [257] as the cells assume a spherical shape. It has recently been reaffirmed that cell rounding induces cortex-membrane destabilization [82]. Norman et al. have described a model that predicts bleb density reduction in the hour following detachment as membrane surface tension increases because of membrane resorption [253].

Optical and scanning electron microscopy (SEM) studies of recently suspended adherent cells show considerable blebbing after detachment, decreasing over several tens of minutes [78–80]. Current understanding is that blebbing arises as the relatively large membrane area during attachment is collected, reattached, and resorbed as the cell transitions into a relatively taut sphere [256]. The same time scale happens to be relevant in the context of injection and extravasation of mesenchymal stem cells for therapeutic purposes. Blebbing thus serves as a reporter system for morphological, and possibly mechanical, alterations that could be relevant during stem cell implantation; however, these alterations have apparently been unexplored to this point because of the inability to probe cell mechanics without contacting the cell and perturbing the phenomenon.

It is concluded that these two correlated temporal processes (stiffening and blebbing reduction) are connected, and that the remodeling process (predominantly, the reattachment and strengthening of cytoskeletal-membrane links, along with absorption of excess plasma membrane) stiffens the suspended cell. It would follow first that a certain amount of bond detachment occurs between the membrane and actin cortex during stretching (but not recovery, because of minimal or absent driving force), and second that bond strength and/or density increases with increasing time since cell detachment from the substratum. This explanation is compatible with the significantly lower percentage of blebbing cells observed after some time in suspension, and with the previous literature reports on cell remodeling, heretofore unquantified in terms of resulting mechanical stiffness changes. Interestingly, Norman et al. found that blebbing does not occur when detachment is slow, and they predict that blebbing would be lessened if the initial attachment is poor [253], suggesting that blebbing would be reduced after detachment from a relatively compliant substratum. Their finding, along with the near-constant value of the power-law exponent over time (Fig. 5-4, argues against an alternate explanation of myosin overactivation upon detachment (which would be expected to increase internal pressure and promote blebbing). Their investigations and models also inspire approaches to modulate blebbing, which could be of use in modulating the deformability of MSCs as they are injected into the bloodstream.

5.4.3 Optical stretching presents advantages and limitations for characterizing MSC mechanics

In collecting a large data set describing MSC deformability, numerous observations have been recorded that are relevant to the OS technique; in this section are summarized briefly its advantages and disadvantages as identified in this study. There are certainly favorable aspects of investigating MSCs with a tool that accepts these adherent cells in suspension rather than in the attached state. For example, suspended cells can be examined with a higher throughput, made possible by the combination of microfluidic delivery with automated trapping and positioning of cells as they approach the trapping area. Mechanics studies by OS could be useful in collecting data to inform the design of other high-throughput cell mechanics testing tools such as microfabricated deformability-based cell sorters [176]. Nevertheless, this technique, at least at the laser power and time scale explored in the current study, does not appear to identify characteristic mechanical markers of MSCs that are correlated with extended passaging. If no identifiable markers exist in the suspended state, it could be consider-

ably more difficult to separate cells via microfluidic parallel sorting, in addition to the limitations caused by minimum intrinsic mechanical variation between cells (§4.4.7).

Nevertheless, OS does allow cell mechanics to be quantified without the complicating effects of physical contact and stress concentrators. Other single-cell rheological techniques such as atomic force microscopy, bead cytometry, and microplate rheometry all involve cell attachment to a physical surface. This attachment cues cell activity such as focal adhesion and stress fiber formation that may complicate interpretation [48]. Even the use of relatively inert coatings involves cell-substratum contact, albeit minimal. OS, in contrast, is a fully noncontact technique capable of applying a mechanical load photonically, thus avoiding these complications.

It is noted that the current analysis approach is sensitive to blebbing cells, the edges of which are difficult to detect by machine vision. As discussed earlier, blebs form when the membrane detaches from the cortex; these characteristics have been seen in other cell lines for approximately an hour after the cell is detached from its substratum, but subside as the cell reinforces membrane-cortex links. Such blebbing can successfully reduced by storing the cells in suspension for one hour or more at 37°C and 5% CO_2 before beginning the stretching process, in order to avoid stretching during the "blebby" transition period. In the present study, the goal was to stretch the adherent cells as soon as possible after detachment to obtain measurements during the time period that MSCs might be re-implanted by injection. The propensity of MSCs to bleb did hinder certain experiments. For example, one arm of the present study involved pharmacological cytoskeletal inhibitors applied to modulate the stiffness of the MSC actin cortex. However, chemicals such as cytochalasin D, blebbistatin, and ML-7 that inhibit actin (de)polymerization and actomyosin contraction produced suspended MSCs with blebs that could not be retracted (data not shown), as bleb retraction requires actin polymerization followed by actomyosin contraction [81]. The resulting "blebby" surface topography made image analysis difficult and consequently has prevented efforts to measure suspended MSC deformability immediately after detachment while chemically modulating cytoskeletal behavior. Fortunately, fibroblast morphology is relatively smooth when observed in the suspended state, avoiding the variety seen in Fig. 5-7(a-c) and enabling sufficient throughput to provide data set sizes of many tens of cells from each two-hour stretching period.

5.5 Outcome

Conclusions

The results support the study's hypothesis, in part.

One can view a newly explanted MSC population as a heterogeneous mixture of cells that proliferate rapidly on stiff substrata. As subpopulations enter senescence at different time points, population profile changes are observable partly through cytoskeletal coarsening and stiffening. The present contribution has been to quantify the mechanics of this transition and show its dependence on stress fiber presentation: five-fold stiffening of attached MSCs is observed in the typical conditions for *in vitro* expansion and subsequent study. Such mechanical changes provide further evidence of altered MSC characteristics during extended passaging on stiff substrata, and may compete with the effects of other stimuli (e.g., cytoskeletal alteration during chemically induced differentiation). Ultimately, the duration and mechanical environment of MSC expansion should be balanced against these structural, mechanical, and functional adaptations of culture-expanded MSC populations; furthermore, these findings motivate the development of culture conditions that will control or minimize such changes. The absence of corresponding stiffness differences in the suspended state unfortunately hinders efforts to sort MSC subpopulations by stiffness in a high-throughput tool. How-

ever, an optimistic finding is the capability of AFM in complement with OS to decouple the mechanical contributions of stress fibers without the need of cytoskeletal inhibitors.

It is exciting and illuminating to uncover, by a noncontact technique, mechanical stiffening of an adherent cell over tens of minutes after the cell is released from substratum contact. Correlations with changing cell surface topography (specifically, the reduction of blebbing as membrane-cortex connections develop and strengthen) suggest that a previously unquantified mechanical component of cell remodeling can now be measured. Observations of blebbing indicate that contractility continues in the suspended state. Existing evidence from the literature that the power-law exponent, internal stress, and material stiffness are coupled can be applied to posit that stress and bulk stiffness are essentially constant in the recently suspended cell. Nevertheless, dynamic behavior can still be concluded to exist at molecular connections between the membrane and the cortex. The transition to a spherical morphology is known to require membrane reattachment and resorption of excess membrane. The practical implication of this stiffening, and a strong motivator for continued research, is that MSCs implanted intravenously may extravasate at a different rate depending on how long they have been detached from the *in vitro* culture surface. Further study is needed, however, to determine which cytoskeletal components and connections dominate in this transition, and whether effective stiffening, putatively cortex-membrane reconnection, of recently suspended cells has any influence on therapeutic applications involving injection of suspended MSCs and their subsequent extravasation and migration in vivo.

Possibilities for future work

An open question concerns the nature of the increase in cortex-membrane bond density and/or strength that was concluded to occur during the first hour after detachment. Additionally, how could the resulting mechanical transition affect MSC implantation in therapeutic applications? It is not currently clear what triggers blebbing or what is the precise mechanism(s) of bleb expansion (some candidates are membrane-cortex interface tearing, lipid flow, and membrane unwrinkling) [258]. The proteins filamin, ezrin, radixin, and moesin are known to play a role in membrane-cortex attachment in the context of blebbing [165, 258], and it could be fruitful to consider ways to distinguish bonds involving these molecules. An investigation of changes in membrane area after detachment, possibly employing hypo- and hyper-osmotic stresses, may illuminate the nature of internal stresses and excess membrane area on whole-cell mechanical properties [259–261]. Finally, the literature of MSC extravasation and homing [262–266] could be examined, and recently suspended MSCs allowed to infiltrate synthetic endothelial models, to predict whether the increase in effective stiffness is likely to correspond affect migration of MSCs delivered *in vivo*.

Online material

A video of MSC blebbing in the suspended state (sped up 30×) can be accessed at the following location:

`http://www.sciencedirect.com/science/article/pii/S0006349510010489`

as part of the supplementary content for a published version of this chapter [4].

Acknowledgments

Prof. Jochen Guck and Franziska Lautenschläger (Cavendish Laboratory, University of Cambridge) provided manufacturing design documents, customized software, and guidance for performing and interpreting optical stretching experiments. Emer Clarke

(StemCell Technologies and ReachBio) provided guidance in techniques for MSC isolation, culture, and differentiation. Kyle Bryson (Pennsylvania State University & MIT REU program) performed optical stretching on MSCs treated with cytoskeletal relaxing agents. Portions of this chapter and associated appendices have been previously published [4], and are reprinted with the permission of Elsevier.

Chapter 6

Conclusions

6.1 Summary of results

Let us now look back at the results of the four studies described in Chap. 2–5, and the four hypotheses tested in the course of this work.

The driving hypotheses for three of the studies were confirmed. A combination of analytical, simulation, and experimental techniques were successfully developed and brought to bear on a set of crucial questions in the context of attached and suspended cell chemomechanics (Chap. 2–4). Table 6.1 summarizes these results in the form of answers to the leading questions of attached and suspended cell chemomechanics raised in Chap. 1.

The fourth study's hypothesis was partially confirmed. As described in Chap. 5, attached stem cells lose characteristic mechanical markers when they are detached from a substratum for relatively high-throughput mechanical measurements; as a result, mechanical sorting of stem cells for putative usefulness—differentiation propensity, for example—was not possible, at least with the optical stretching configuration and settings used here. However, another (previously unquantified) mechanical transition was observed by the same technique over the time scale of tens of minutes, and this transition may be generalizable across all adherent cells.

With this summary in mind, it is now possible to review the major contributions of this work.

6.2 Contributions

The major contributions of this thesis—resolved questions along with demonstrated capabilities and limitations—are as follows:

Reconciliation of the depth that attached cells can detect a rigid underlying base. New equations describe cell-induced surface deformation atop compliant film of finite thickness. The effective stiffness of a finite-thickness, finite stiffness coating is usefully determined by the dividing bulk stiffness by a nondimensional term that is analytically identified here and also approximated by closed-form equations for convenient use. The model connects surface deformation to coating thickness and provides a tool for researchers to estimate an effective stiffness in cases where semi-infinite geometry is not attainable because of considerations such as processing, optical clarity, or cost. These tools could also be used to investigate the possibility of *in vivo* morphogenetic signaling by environmental stiffness-thickness cues. The model has been validated through observations of cell behavior on compliant coatings with various thicknesses and by considering the existing literature describing cell behavior on substrata with a range

Table 6.1: **Thesis summary: answers to leading questions that arise when describing the cell as a chemomechanical material.**

Unique cell attribute(s)	Attached state	Suspended state
Contractility, mechanosensing	**How deep do cells "feel"? (§1.2.1, §2.3.2)** Cells feel a distance into their surrounding environment in relation to the size of their focal adhesions, as predicted by an analytical extension of existing elasticity theory and experimental confirmation of cell behavior on compliant substrata of varying thickness.	**What is the role of actomyosin contraction in recently suspended cells? (§1.2.2, §3.4.2 and §5.3.2)** Optical stretching experiments reveal whole-cell stiffening, concurrent with bleb reduction, over tens of minutes following cell suspension; blebbing confirms continued active contraction as the suspended cell seeks to engage a substratum. ATP-driven actomyosin contraction is crucial for remodeling into a spherical shape after substratum detachment.
Compliant, heterogeneous cytoskeletal network	**What are the origins and extent of cell-to-cell mechanical variation? (§1.2.4, §4.3.3)** Energy barriers and/or agitation energy in soft networks vary intrinsically within cells, and this variation explains the universal log-normal distribution of measured cell stiffness. Mechanical heterogeneity is inherently exhibited by cells, but can be modulated somewhat by ATP availability.	**Do suspended cells exhibit power-law rheology (PLR) despite lacking stress fibers? (§1.2.3, §3.3.2)** Suspended cells unequivocally exhibit weak power-law rheology, based on time- and frequency-domain measurements of thousands of cells; stress fibers are not a necessary component for PLR.
Metabolism, proliferation, differentiation	**Do stem cells have useful mechanical markers? (§1.2.5, §5.4.1)** Yes; measured cytoskeletal coarsening and stiffening of attached mesenchymal stem cells (MSCs) during long-term (weeks to months) of *in vitro* proliferation represents a shift in predominance between at least two subpopulations with different differentiation propensity.	**Can we leverage putative mechanical markers for high-throughput suspended stem cell sorting? (§1.2.5, §5.4.1)** Not as yet. Mechanical markers of MSCs are predominantly or solely expressed in the form of actin stress fiber presentation; because these stress fibers are absent in suspended cells, mechanical markers are not distinguishable in this state, at least by optical stretching in the present configuration.

of stiffnesses and thicknesses. Though a central question—the precise mechanism of mechanosensitivity—remains unanswered, the tools developed here are intended to inform studies to investigate this question.

Implications of stress fiber presentation in cells. A new understanding is established of when stress fibers are important and when they are not. As described in Chap. 2, stress fibers are crucial to the mechanosensitive mechanism that pulls at the surrounding environment (through transmembrane connections) and integrates the resulting deformation signal to determine the stiffness of the adjacent material. As mesenchymal stem cells proliferate on rigid substrata, a subpopulation dominates in which stress fibers are strongly presented as coarse bundles that exhibit relatively high stiffness by AFM-enabled indentation. Nevertheless, efforts to detect these dynamic cytoskeletal changes fail when cells are interrogated in the suspended state, as stress fibers disappear when cells are detached from the substratum. The phenotype returns, however, when suspended cells are given the opportunity to attach and spread on stiff substrata again. Importantly, stress fibers are not necessary for a cell to exhibit power-law rheology, in contrast to previous reports. It is demonstrated here that the cell can be assigned an effective stiffness for a particular loading time and deformation scale that is independent of cell size, in the manner of composite materials. These finding are expected to be valuable in the development of theories describing soft matter, or complex fluids, here providing insight into what qualities are necessary for materials (animate and inanimate) to exist in an intermediate position between solid and liquid.

Profile of mechanical heterogeneity in cells in response to chemomechanical cues. By chemical and mechanical perturbation, and by studying different cell types and applying different testing methods, evidence is accumulated that mechanical variation is intrinsic and does not depend on any animate process, at least during O(1 s) deformation periods. Multiple possible origins for this intrinsic variation were examined and compared to existing data; the best explanation is a relationship between stiffness and "noise temperature" that is explored here experimentally and analytically. A derivation is provided here for the cell-to-cell mechanical variation (quantified by the geometric standard deviation of measured stiffness), based on plausible assumptions of the variation of an effective temperature of the material that manifests itself as the power-law exponent of cell rheology. This tool is applicable not just to complex modulus (storage and loss moduli) but also to other rheological parameters such as creep compliance and stress relaxation modulus. This thesis also introduces the practice of reporting the standard error in estimated distribution width to allow comparisons between different populations and experimental conditions. Just as existing literature was "mined" to extract empirical reports of geometric standard deviation from the literature (Chap. 4, for example), the presentation of ample data concerning heterogeneity here is hoped to be useful as other groups explore this area.

Characterization of the recently suspended state. The measurements of a mechanical transformation in suspended cells over the hours following substratum detachment should not be ignored, though these findings are presented at the end of this thesis (§5.3.2). Reported immediately after a conclusion that optical stretching cannot detect structural changes in cells that are manifested primarily by stress fibers (because these are depolymerized when cells are detached from a substratum), these findings nevertheless demonstrate an outstanding application for the noncontact optical stretcher: mechanical interrogation of a process predicated on a lack of cell-detected physical contact. New quantifications of cell stiffening in suspension can join compatible—but qualitative—reports of blebbing reduction over the last several decades for various cell types.

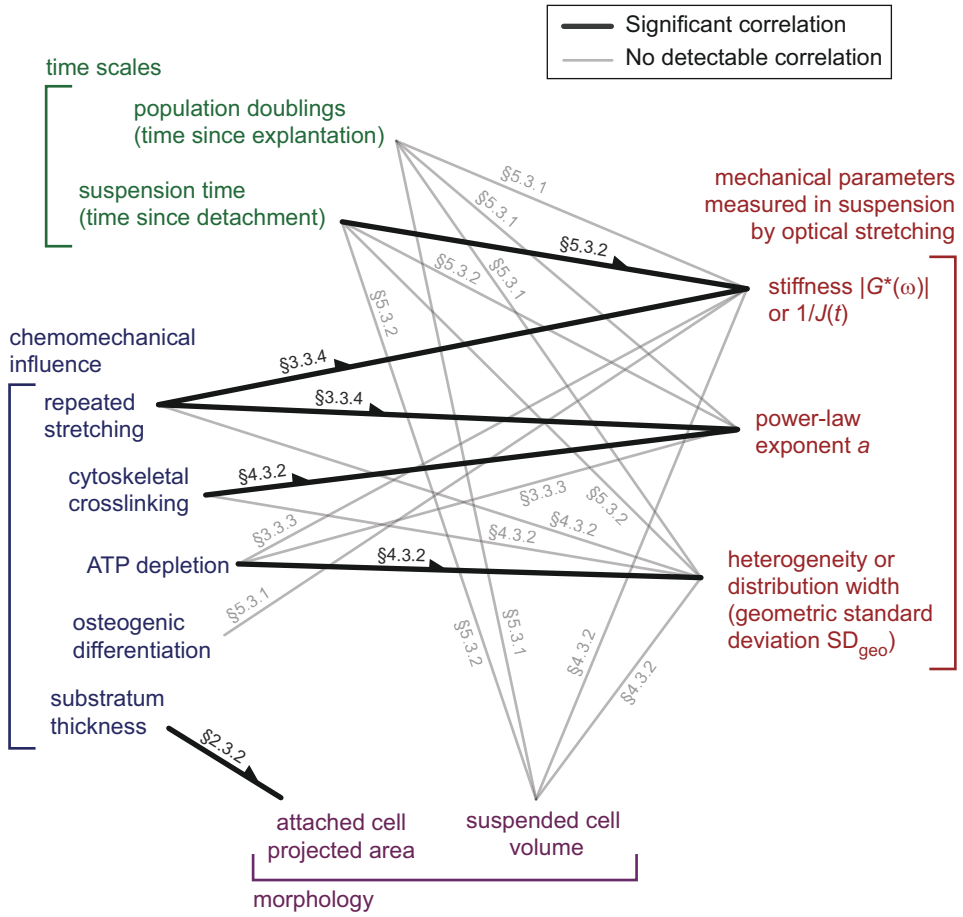

Figure 6-1: **Correlations (detected and undetected) examined in the course of this thesis.** Examination over different time scales or in response to different chemomechanical cues can reveal changes in mechanical markers and morphology in the attached and suspended states. Links are annotated with section numbers of text discussion and, for detected correlations, causative direction. ($|G^*|$ = complex modulus magnitude, $J(t)$ = creep compliance.)

Mapping of correlations. As shown in Fig. 6-1, multiple chemomechanical influences on cell mechanics and morphology were quantitatively explored; the majority have never before been examined in the literature. Fig. 6-1 illustrates eighteen possible correlations that were investigated in Chaps. 2–5 (section number are given for precise location of findings); a third of these were found to be present to a magnitude unlikely to be due to chance. Such a map has multiple uses. First, it displays which cues prominently modulate which mechanical parameters, and is therefore expected to be of use in developing and confirming theories in the active field of cell rheology. Second, and conversely, this information reports where relationships do *not* detectably exist, and is therefore useful as justification for pooling data together, as deformability data from different MSC passages were in Chaps. 2–4 based on the findings of passage independence in Chap. 5. Third, it shows where further studies could fill in missing knowledge. For example, are the power-law exponents of a single cell correlated in the attached and the suspended state? What is the correlation time of the exponent a—does a more fluidic cell remain that way permanently, or does the value vary over time? Knowledge in this area would help bridge the gap between polymer and soft glassy rheology theories originally developed for inanimate material and the undeniably animate nature of the cell.

Multiple new analytical, experimental, and analytical techniques. Chaps. 2–4 each contain sections of "Novel methods," techniques that were developed in the course of this work and were indispensable in gathering data and drawing conclusions. These include, for example, a solution of surface deformation caused by finite-area traction atop a compliant elastic layer, a solution of stiffness distribution shape and width based on the fluctuation of a "noise temperature" postulated to enable mechanical relaxation in soft glassy materials, and syringe rotation to maintain cell suspension and thus increase total throughput in optical stretching studies of single-cell deformability.

6.3 Perspectives

This thesis began by asking:

"How should we think of the cell as a material? With its complex animate nature—internal molecular motors, dynamic and heterogeneous physical structure, and near-fluidic behavior—the living eukaryotic animal cell differs considerably from the idealized elastic solid featured in introductory Mechanics of Materials texts."

Have these challenges been successfully negotiated?

The cell as a chemomechanical material and the utility of existing models

Based on the findings of this thesis, it is concluded that the cell can indeed be usefully described as a chemomechanical material. It is argued here that material class generally known as "soft matter" now belongs with the existing prominent classes of metals, ceramics, and polymers in materials science and engineering (MSE) research, development, and education. This view is based on the idea that the preeminent material to be studied is the single live cell, as asserted in the introduction, and that the cell is increasingly associated with physical theories of soft matter. Broadly, we might associate the deformation nature of soft matter to be reorganization of disorganized material, just as we associate the deformation of ductile metal polycrystals with dislocation motion, brittle ceramics with crack propagation, and elastomers with polymer chain uncoiling and sliding.[1] Of course, other soft matter joins the cell in the classification discussed here: foams, emulsions, slurries, and pastes are all complex fluids, all essential in commercial products, and all being studied actively in physics today. However, the cell is maintained here to be the flagship example, not only in its importance to our existence, but also in the contrast between carbon-based life and other ceramic and polymer carbon compounds. One of the most remarkable facts of the variability in matter is that diamond, graphite, rubber, and cells are all filled with carbon atoms, yet their stiffness values range across eleven orders of magnitude. (Such is the benefit of achieving compliance through mesoscale rearrangement of protein chains in the cell vs. stretching carbon-carbon bonds in diamond.)

The cell is an incredibly complex material, exhibiting complex and emergent behavior to a degree not seen in other substances. When can existing models be applied, and when can they not? Recall the experimental finding of stiffening with repeated loading (§3.3.4) and the possible mechanisms: actin recruitment (an active cell response), increased tension that reduces the fluidity (a characteristic of soft glassy materials), or the nonlinear response of polymers in stretching (a polymeric effect). Only the last mechanism is also seen with individual constituent molecules; the other two are emergent properties less well understood. Note that Sollich et al.'s SGR theory, proposed to apply to cells by Fabry and Fredberg, rates well as a model in predicting weak power law rheology and frequency-independent phase angle (both shown this thesis) as well as fluidization and resolidification (shown by the Fredberg Group), and is also generic

[1] Some overlap exists between soft matter and polymers under these definitions.

enough to describe foams and emulsions. As a result, however, it cannot predict strain stiffening caused by the nonlinear elastic response of polymers. It is says nothing about the precise role of ATP in biopolymer network construction, maintenance, and agitation. These shortcomings provide an example of the difficulty of describing cell chemomechanics with any single existing model.

Coda

> *"If we were compelled to suggest a model [of cell mechanics] we would propose Mother's Work Basket—a jumble of beads and buttons of all shapes and sizes, with pins and threads for good measure, all jostling about and held together by colloidal forces."* Francis Crick and Arthur Hughes, "The physical properties of cytoplasm," (1950) [267]

In one sense, Crick and Hughes' whimsical comment is remarkably prescient.[2] One could imagine the beads and threads as globular and filamentous proteins, the pins as molecular crosslinks, and the jostling as a foreshadowing of the agitation that enables fluidity in cells. In their actual paper, tantalizing hints are found of many of the topics of this thesis: intracellular rheology, viscoelasticity, creep and partial recovery, active (non-Brownian) motion, anisotropy.

In another sense, though, these hints are just that—hints of an understanding that could not possibly be fully developed at the time, sixty years ago. Experimentally, Crick and Hughes recorded the driven motion of phagocytosed magnetic particles with a film camera. The invention of the laser was a decade away, the development of digital imaging and the associated necessary computer power even further. In terms of a theoretical foundation, the science of polymers was in its infancy. Knowledge of the cell interior was essentially limited to the nucleus, cytoplasm, and some specialized organelles such as mitochondria. It would be over fifty years more until an understanding of the "glassy state" was declared not only relevant to cell mechanics [90], but also one of the crucial problems to be solved over the next hundred years [89].

Nevertheless, by 1950 the existence of ATP was known, and even its reaction with myosin (already labeled an ATPase due to its enzymatic properties) was understood to a degree. The p-value was in use. Interestingly, hypotheses about a cytoskeleton—a "mosaic" of filamentous proteins—had existed since the 1930s [269]. An understanding of the entropic contributions to polymer elasticity, too, had existed for about the same time.

The situation today is in some ways similar, despite the obvious scientific and technological advances since Crick and Hughes' work. Once again, researchers in the field have accumulated substantial quantitative data on cell deformability, and they have drawn conclusions that range in confidence from tentative to relatively certain. Once again, we confront experimental limitations. To give an example from the present work, it is not currently possible to rotate the suspended cell around axes orthogonal to the fiber axis in order to investigate a cell's mechanical anisotropy, and this limitation hinders investigation of why one cell is measured to be stiffer or more compliant than another (§4.4.3). We also face limitations in theory and mechanistic understanding; again, one relevant example is the lack of clarity in exactly how the cell transduces attenuated adhesion site deformation into a chemical signal that represents strong attachment to a stiff substratum (§2.4.1). Another is the current debate on how animate processes such as actomyosin contraction in the cell modulate emergent mechanical parameters such as the noise temperature (§3.4.2). These questions will remain for a little while longer.

[2] Compare Thomson's "The active cell is a whirlpool of colloidal substances," (1932) [268] which, while also evocative, is less illuminating in retrospect.

The goal of this thesis has been to advance meaningful hypotheses, develop and apply new techniques as appropriate to test these hypotheses, and to interpret the results and their implications. When we consider the conclusions that these investigations have enabled—with some limitations identified as well—it seems impossible not to feel simultaneously humble and optimistic about our understanding of the cell as a chemomechanical material.

Appendix A

Analytical protocols

A.1 Substratum surface deformation from constant tangential loading over a circular area

As described in Chap. 2, it is desired to calculate how the cell-induced surface deformation of a compliant film is attenuated by the presence of an underlying rigid base. Therefore, let us consider two geometries, as shown in Fig. 2-1, where the coordinate system is defined so that z points downward into the substratum and x corresponds to the direction of tangential loading. In the case of a semi-infinite region, shear stress is applied to a finite region on the surface of a substratum consisting of a semi-infinite region—or half space—occupying $0 \leq z < \infty$. In the case of a finite-thickness-film, shear stress is applied to a finite region on the surface of a coating that occupies $0 \leq z \leq h$ and is perfectly bonded to a perfectly rigid base occupying $h < z < \infty$. If both cases appear similar, the presence of the rigid base is essentially undetectable; if not, the influence of the base can be quantified by the reduction of deformation.

All materials are assumed to be isotropic, homogeneous, and linearly elastic. Additionally, let us consider only a single area of traction, as it is initially assumed that the traction-related deformation due to other adhesion sites is negligible compared to the response due to the site of interest.

Case I: Semi-infinite substratum

The first step in these calculations is to determine deformation for the first case described above, to provide a basis of comparison for the second case. The program is to integrate infinitesimal displacements around finite areas to avoid the divergence that would otherwise occur at the idealized adhesion site. Two modes of deformation (displacement and distortion, as illustrated in Fig. 2-3) are quantified to emphasize that there are multiple ways to describe surface deformation. A reminder: the subscript "B" is used for results of the first case, as these correspond to the (B)oussenesq solution.

Displacement

A point force is coupled to the resulting displacement field by Green's tensor. For a half space with a surface point force acting at (x_0, y_0), the surface Green's tensor

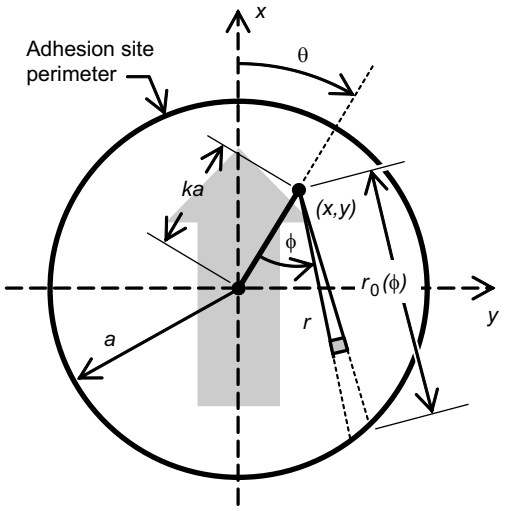

Figure A-1: Schematic for integrating the displacement due to a tangential point force in the x direction around an arbitrary interior point (x, y), to obtain the displacement due to a finite area of tangential traction centered on the origin.

$\mathbf{G}_{\mathrm{B}}(x, y, x_0, y_0)$ is [68, 71, 106, 270]

$$\mathbf{G}_{\mathrm{B}} = \frac{1}{2\pi\mu}\begin{pmatrix} \dfrac{2-\nu}{2r} + \dfrac{\nu(\hat{x}^2-\hat{y}^2)}{2r^3} & \dfrac{\nu\hat{x}\hat{y}}{r^3} & -\dfrac{(1-2\nu)\hat{x}}{2r^2} \\ \dfrac{\nu\hat{x}\hat{y}}{r^3} & \dfrac{2-\nu}{2r} - \dfrac{\nu(\hat{x}^2-\hat{y}^2)}{2r^3} & -\dfrac{(1-2\nu)\hat{y}}{2r^2} \\ \dfrac{(1-2\nu)\hat{x}}{2r^2} & \dfrac{(1-2\nu)\hat{y}}{2r^2} & \dfrac{1-\nu}{r} \end{pmatrix}, \quad \text{(A.1)}$$

where ν is Poisson's ratio, $\mu = E/2(1+\nu)$ is the shear modulus and E is Young's elastic modulus, and

$$\hat{x} = x - x_0 \qquad \hat{y} = y - y_0 \qquad r = \sqrt{\hat{x}^2 + \hat{y}^2}. \quad \text{(A.2)}$$

Because Equation A.1 diverges at the location of the applied point force ($r \to 0$) [73, 112], and we are interested in the deflections specifically at an adhesion site centered on this location, let us build on this result by integrating over a finite area S:

$$\mathbf{u}_{\mathrm{B}}(x, y) = \iint_S \mathbf{G}_{\mathrm{B}}(\hat{x}, \hat{y})\mathbf{T}\, dS_0, \quad \text{(A.3)}$$

where $\mathbf{u}_{\mathrm{B}} = (u_{\mathrm{B}}\ v_{\mathrm{B}}\ w_{\mathrm{B}})^{\mathsf{T}}$ and $\mathbf{T}$ is the traction at the adhesion site.

From the assumption of tangential loading and the definition of the coordinate system, we have $\mathbf{T} = (T\ 0\ 0)^{\mathsf{T}}$. Let us assume that S is a circular region, centered at the origin, with radius a. The displacement at any arbitrary point inside the circle is found by integrating as shown in Figure A-1 and adapted from Saada's treatment of circular normal loading [271]:

$$\mathbf{u}_{\mathrm{B}}(k, \theta) = \frac{T}{2\pi\mu}\int_0^{2\pi}\int_0^{r_0(\phi)} \begin{pmatrix} \dfrac{1-\nu+\nu\cos^2(\theta-\phi)}{r} \\ \dfrac{\nu\sin(\theta-\phi)\cos(\theta-\phi)}{r} \\ \dfrac{(1-2\nu)\sin(\theta-\phi)}{2r} \end{pmatrix} r\, dr\, d\phi, \quad \text{(A.4)}$$

where

$$r_0(\phi) = a\left(k\cos\phi + \sqrt{1-k^2\sin^2\phi}\right), \tag{A.5}$$

and we have used

$$\hat{x} = x - x_0 = r\cos(\theta-\phi) \qquad \hat{y} = y - y_0 = r\sin(\theta-\phi). \tag{A.6}$$

After evaluating the integrals, the displacement field $\mathbf{u}_B(k,\theta)$ is

$$\mathbf{u}_B = \frac{Ta}{\mu}\begin{pmatrix} \frac{2-\nu}{\pi}\mathscr{E}(k) + \frac{\nu\cos 2\theta}{3\pi k^2}\left[(2-k^2)\mathscr{E}(k) - 2(1-k^2)\mathscr{K}(k)\right] \\ \frac{\nu\sin 2\theta}{3\pi k^2}\left[(2-k^2)\mathscr{E}(k) - 2(1-k^2)\mathscr{K}(k)\right] \\ \frac{k(1-2\nu)\cos\theta}{4} \end{pmatrix}, \tag{A.7}$$

where k represents the normalized radial distance and $\mathscr{K}(k)$ and $\mathscr{E}(k)$ are the complete elliptic integrals of the first and second kind, respectively. (Figure 2-3, which shows the surface deformation of the circular area for different values of T/μ and T/E, was constructed by plotting this displacement field, and these values are also shown in Fig. A-2 for $\theta = 0$ and three values of ν.)

A key result is the x-direction displacement at the center of the circular adhesion site:

$$u_B(0,0) = \frac{Ta(2-\nu)}{2\mu}. \tag{A.8}$$

The y and z displacements v_B and w_B, respectively, are zero at the center of the circle and average to zero over the area circumscribed by the circle.

The average u_B displacement within the circular area is

$$u_{B,ave} = \frac{1}{\pi}\int_0^{2\pi}\int_0^1 u_B\, k\, dk\, d\theta = \frac{4Ta(2-\nu)}{3\pi\mu}, \tag{A.9}$$

which is roughly 85% of the center displacement. From this value we can determine the strain energy stored in the substratum by a force-distance calculation to be $4T^2a^3(2-\nu)/3\mu$. Finally, an effective spring constant for substratum surface displacement can be defined as

$$k_{eff} = \frac{F}{u_B(0,0)} = \frac{T\pi a^2}{u_B(0,0)} = \frac{2\pi\mu a}{2-\nu} = \frac{\pi E a}{(1+\nu)(2-\nu)}. \tag{A.10}$$

Distortion

Note that the circular area of traction does not displace uniformly; in fact, the center moves the most (Fig. A-2(a)), resulting in distortion: a contraction at the leading edge and an elongation at the trailing edge (Fig. 2-3). This type of deformation is recognized to be the normal strain, but this strain is zero at the center of the circle (Fig. A-2(b)); instead, let us use the first derivative of the strain to characterize the distortion.

The normal strain characterizes the amount of contraction on the side of positive x, the side corresponding to the direction of applied tangential traction, and elongation of the side of negative x (see Figure 2-3). The normal strain in the x direction ($\theta = 0$) within the circle can be calculated from Equation A.4 as

$$\varepsilon_{xx,B} = \frac{1}{a}\left(\frac{\partial u_B}{\partial k}\right) = \frac{T}{2\pi\mu a}\int_0^{2\pi}\frac{\partial r_0(\phi)}{\partial k}(1-\nu+\nu\cos^2\phi)\, d\phi. \tag{A.11}$$

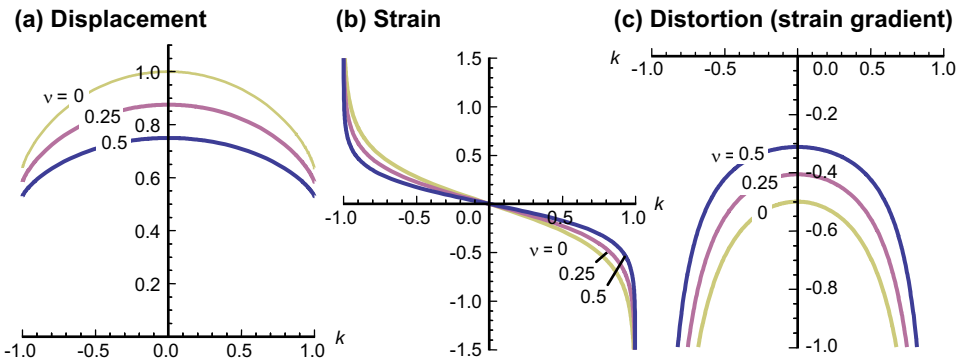

Figure A-2: Normalized (a) surface displacement $u_B\mu/Ta$, (b) normal strain $\varepsilon_{xx}\mu/T$, and (c) distortion, or normal strain gradient, $(\mu/T)(d\varepsilon_{xx}/dk)$ are plotted as a function of k, the normalized radial distance to the adhesion site center, for three values of substratum Poisson's ratio ν (0, 0.25, 0.5) along the x axis ($\theta = 0$). A discontinuity in displacement exists at $k = 1$ (or $r = a$); the focus is therefore on quantifying effects at the center of the circle.

This normal strain is zero at the center of the circle, which is the most convenient point to use (see Figure A-2). Let us therefore differentiate again to quantify the rate of transition from contraction at positive x to elongation at negative x. This parameter is used to quantify distortion:

$$\frac{\partial \varepsilon_{xx,\mathrm{B}}}{\partial k} = \frac{T}{2\pi\mu a}\int_0^{2\pi} \frac{\partial^2 r_0(\phi)}{\partial k^2}(1-\nu+\nu\cos^2\phi)\,d\phi. \tag{A.12}$$

At the center of the circular area of traction, the distortion is

$$\frac{\partial \varepsilon_{xx,\mathrm{B}}(0,0)}{\partial k} = -\frac{T(4-3\nu)}{8\mu}, \tag{A.13}$$

another key result; the minus sign indicates that the normal strain ε_{xx} at the surface changes from positive to negative in the direction of positive x, as shown in Figure A-2. This evaluation uses the identities

$$\lim_{k\to 0} r_0(\phi) = a, \qquad \lim_{k\to 0}\frac{\partial r_0(\phi)}{\partial k} = a\cos\phi, \qquad \lim_{k\to 0}\frac{\partial^2 r_0(\phi)}{\partial k^2} = -a\sin^2\phi. \tag{A.14}$$

To summarize, available now are the center displacement and distortion values $u_B(0,0) = Ta(2-\nu)/2\mu$ and $\partial\varepsilon_{xx,\mathrm{B}}(0,0)/\partial k = -T(4-3\nu)/8\mu$, respectively, as baselines for comparison with the finite-thickness coating results derived in the following section.

Case II: Finite-thickness coating

Assume now that a perfectly bonded, rigid base exists under a compliant coating at a depth h. The C (coating) subscript is used for the parameters derived under this condition, illustrated in Fig. 2-1(b). Note that an additional boundary condition $\mathbf{u}_C = 0$ at $z = h$ now applies.

There are at least two existing analytical methods for incorporating the effect of an underlying base, and two methods—those of Yue [110] and Fabrikant [111]—are described here. Yue's method utilizes Fourier integral transforms in a backward transfer matrix approach to calculate the stresses and displacements in a multilayered isotropic half space subject to surface traction. Merkel et al. have presented experimental support for Yue's solution [68]. Fabrikant's method involves image forces that produce an infinite sum of reciprocals and solves a single transversely isotropic coating atop a

rigid base. Here, Yue's approach is used; Fabrikant's approach will later be shown to be equivalent.

Displacement

In Yue's approach, the Green's tensor relating deformation and traction is [110]:

$$\mathbf{G}_{\mathrm{C}}(x,y,x_0,y_0) = \frac{1}{2\pi}\int_0^\infty \begin{pmatrix} -\Phi_1 J_0 + \dfrac{\hat{x}^2-\hat{y}^2}{r^2}\Phi_2 J_2 & \dfrac{2\hat{x}\hat{y}}{r^2}\Phi_2 J_2 & \dfrac{\hat{x}}{r}\Phi_{13} J_1 \\ \dfrac{2\hat{x}\hat{y}}{r^2}\Phi_2 J_2 & -\Phi_1 J_0 - \dfrac{\hat{x}^2-\hat{y}^2}{r^2}\Phi_2 J_2 & \dfrac{\hat{y}}{r}\Phi_{13} J_1 \\ -\dfrac{\hat{x}}{r}\Phi_{31} J_1 & -\dfrac{\hat{y}}{r}\Phi_{31} J_1 & -\Phi_{33} J_0 \end{pmatrix} d\rho, \tag{A.15}$$

where

$$\Phi_1 = \frac{1}{2}\left[\Phi_{11}(\rho h) + \Phi_{22}(\rho h)\right], \qquad \Phi_2 = \frac{1}{2}\left[\Phi_{11}(\rho h) - \Phi_{22}(\rho h)\right], \tag{A.16}$$

where Φ represents a collection of characteristic terms to be defined below, and where $J_m = J_m(\rho r)$ is the Bessel function of order m. The dummy variable ρ used in integration corresponds to the conjugate of distance in the Fourier-transformed domain.

The relevant terms in the portion of the Green's tensor $\mathbf{G}_{i1}$ relating displacements to a tangential point force $\mathbf{T} = (T\ 0\ 0)^{\mathsf{T}}$ are calculated by Yue's method to be

$$\Phi_{11}(\rho h) = \frac{1}{\mu}\left(\frac{(1-\nu)\left[3-4\nu-4\rho h e^{2\rho h} - (3-4\nu)e^{4\rho h}\right]}{(3-4\nu)(1+e^{4\rho h}) - 4\nu + 2(5+2\rho^2 h^2 - 12\nu + 8\nu^2)e^{2\rho h}}\right), \tag{A.17}$$

$$\Phi_{22}(\rho h) = \frac{1}{\mu}\left(\frac{1-e^{2\rho h}}{1+e^{2\rho h}}\right), \tag{A.18}$$

$$\Phi_{31}(\rho h) = \frac{1}{\mu}\left(\frac{2e^{2\rho h}\left(2\rho^2 h^2 + 8\nu^2 - 10\nu + 3\right) - (8\nu^2 - 10\nu + 3)(1+e^{4\rho h})}{2\left[(3-4\nu)(1+e^{4\rho h}) + 2e^{2\rho h}\left(2\rho^2 h^2 + 8\nu^2 - 12\nu + 5\right) - 3\right]}\right), \tag{A.19}$$

where μ is the shear modulus, ν is Poisson's ratio, and h is the coating thickness.

It can be verified that

$$\Phi_1(0) = \Phi_2(0) = \Phi_{31}(0) = 0, \tag{A.20}$$

which satisfies the condition of zero displacement when the coating thickness h is zero, and that

$$\lim_{h\to\infty}\Phi_1 = -\frac{2-\nu}{2\mu}, \qquad \lim_{h\to\infty}\Phi_2 = \frac{\nu}{2\mu}, \qquad \lim_{h\to\infty}\Phi_{31} = -\frac{1-2\nu}{2\mu}, \tag{A.21}$$

which, considering that the Bessel function integrals are normalized, recovers the half-space solution for an infinitely thick coating. The Φ terms are related to those given by Merkel et al. for pointlike adhesion sites for the analysis of cell traction microscopy and are presented here for clarity. (Note that in Merkel et al.'s notation, though, Φ_1 and Φ_2 are equivalent to $\mu\Phi_1 + (2-\nu)/2$ and $\mu\Phi_2 - \nu/2$, respectively, in Yue's and my notation.)

Let us first calculate x-direction displacement due to uniform traction applied over

a finite area S for the case with an underlying rigid base, as part of the program of comparing deformation in both configurations shown in Fig. 2-1. This displacement $u_C(x,y)$ is

$$u_C = T \iint_S G_{11,C}\, dS_0 \tag{A.22a}$$

$$= \frac{T}{2\pi} \iint_S \int_0^\infty \left(-\Phi_1 J_0 + \frac{\hat{x}^2 - \hat{y}^2}{r^2} \Phi_2 J_2 \right) d\rho\, dS_0. \tag{A.22b}$$

When integrating over a circular area around the center, the second term in the integrand is zero:

$$u_C(0,0) = -\frac{T}{2\pi} \int_0^{2\pi} \int_0^a \int_0^\infty \Phi_1(\rho h) J_0(\rho r)\, d\rho\, r\, dr\, d\phi \tag{A.23a}$$

$$= -Ta \int_0^\infty \frac{1}{\rho} \Phi_1\left(\frac{\rho h}{a}\right) J_1(\rho)\, d\rho. \tag{A.23b}$$

The dimensionless ratio h/a connects the two length scales used so far (coating thickness and adhesion size). (The goal, however, is not to rely on a scaling argument to assert that the critical thickness $h_{\text{crit}} \approx a$, but rather to derive a quantitative prediction to be tested.)

It is useful to define a dimensionless factor U_1 that represents the normalized x-direction displacement at the center of the circle when an underlying rigid base is present:

$$u_C(0,0) = U_1(h/a) u_B(0,0). \tag{A.24}$$

By combining Eqs. A.8 and A.23b, the normalized displacement $U_1(h/a)$ can be written as

$$U_1 = -\frac{2\mu}{2-\nu} \int_0^\infty \frac{1}{\rho} \Phi_1 \left(\frac{\rho h}{a}\right) J_1(\rho)\, d\rho \tag{A.25a}$$

$$= 1 - \frac{2}{2-\nu} \int_0^\infty \frac{1}{\rho} \left[\mu \Phi_1 \left(\frac{\rho h}{a}\right) + \frac{2-\nu}{2} \right] J_1(\rho)\, d\rho, \tag{A.25b}$$

where the second expression in Equation A.25 is more amenable to numerical evaluation. (Merkel et al. have noted that convergence of these types of integrals is improved if the semi-infinite region solution is taken outside the integral, leaving the integrand to represent the difference between this solution and the finite-thickness coating solution [68].) This expression, plotted in Fig. 2-4(a), accomplishes a primary goal of this Appendix—to derive a factor for calculating an effective cell-sensed stiffness via Eq. 2.3—for the *displacement* of the adhesion site. A derivation for the *distortion* factor follows.

Distortion

Let us now consider the attenuation in distortion due to the presence of an underlying rigid base. (The equations are more intricate than the displacement case, but the strategy is identical.) In Equation A.22b, let $F(\rho h, \rho r) = -\Phi_1 J_0 + \Phi_2 J_2 \cos 2\phi$. Then

$$u_C = \frac{T}{2\pi} \int_0^{2\pi} \int_0^{r_0(\phi)} \int_0^\infty F(\rho h, \rho r)\, d\rho\, r\, dr\, d\phi, \tag{A.26}$$

$$\varepsilon_{xx,\mathrm{C}} = \frac{1}{a}\left(\frac{\partial u_{\mathrm{C}}}{\partial k}\right) = \frac{T}{2\pi a}\int_0^{2\pi}\frac{\partial r_0(\phi)}{\partial k} r_0(\phi)\int_0^{\infty} F(\rho h, \rho r_0(\phi))\, d\rho\, d\phi, \tag{A.27}$$

$$\begin{aligned}\frac{\partial \varepsilon_{xx,\mathrm{C}}}{\partial k} &= \frac{1}{a}\left(\frac{\partial^2 u_{\mathrm{C}}}{\partial k^2}\right)\\ &= \frac{T}{2\pi a}\int_0^{\infty}\int_0^{2\pi}\left\{\left[\frac{\partial^2 r_0}{\partial k^2} r_0 + \left(\frac{\partial r_0}{\partial k}\right)^2\right] F(\rho h, \rho r_0(\phi))\right.\\ &\qquad \left. + r_0\left(\frac{\partial r_0}{\partial k}\right)\frac{\partial}{\partial k}[F(\rho h, \rho r_0(\phi))]\right\} d\phi\, d\rho.\end{aligned} \tag{A.28}$$

Again, let the normalized radius k approach zero and apply the limits in Equation A.14 to give

$$\begin{aligned}\frac{\partial \varepsilon_{xx,\mathrm{C}}(0,0)}{\partial k} = \frac{Ta}{2}\int_0^{\infty}&\left\{\Phi_2(\rho h) J_2(\rho a) + a\rho\, \Phi_1(\rho h) J_1(\rho a)\right.\\ &\left. + \frac{a\rho}{4}\Phi_2(\rho h)\left[J_1(\rho a) - J_3(\rho a)\right]\right\} d\rho,\end{aligned} \tag{A.29}$$

which can be rewritten as

$$\frac{\partial \varepsilon_{xx,\mathrm{C}}(0,0)}{\partial k} = \frac{T}{2}\int_0^{\infty}\rho\, \Phi_1\left(\frac{\rho h}{a}\right) J_1(\rho) + \Phi_2\left(\frac{\rho h}{a}\right) J_{\mathrm{A}}(\rho)\, d\rho, \tag{A.30}$$

where $J_{\mathrm{A}} = (\rho/4)J_1(\rho) + J_2(\rho) - (\rho/4)J_3(\rho)$.

This equation can be shown to reduce to the half-space solution by letting $h \to \infty$ and by using the identities

$$\int_0^{\infty} J_n\, d\rho = 1, \qquad \int_0^{\infty}\rho J_n\, d\rho = n, \tag{A.31}$$

for $n = 1, 2, 3$.

As before, a normalized coefficient is defined by

$$\frac{\partial \varepsilon_{xx,\mathrm{C}}(0,0)}{\partial k} = U_2(h/a)\frac{\partial \varepsilon_{xx,\mathrm{B}}(0,0)}{\partial k}. \tag{A.32}$$

The parameter U_2 represents the normalized distortion (the gradient of x-direction normal strain) when an underlying rigid base is present. By using Eqs. A.13 and A.30, it is found that

$$U_2(h/a) = -\frac{4\mu}{4-3\nu}\int_0^{\infty}\rho\, \Phi_1\left(\frac{\rho h}{a}\right) J_1(\rho) + \Phi_2\left(\frac{\rho h}{a}\right) J_{\mathrm{A}}(\rho)\, d\rho, \tag{A.33}$$

which is plotted in Fig. 2-4(b). As in the case of U_1, this equation can be written as

$$\begin{aligned}U_2(h/a) = 1 - \frac{4}{4-3\nu}\int_0^{\infty}&\left\{\rho\left[\mu\Phi_1\left(\frac{\rho h}{a}\right) + \frac{2-\nu}{2}\right] J_1(\rho)\right.\\ &\left. + \left[\mu\Phi_2\left(\frac{\rho h}{a}\right) - \frac{\nu}{2}\right] J_{\mathrm{A}}(\rho)\right\} d\rho\end{aligned} \tag{A.34}$$

to be more amenable to numerical evaluation. This completes the derivation, for two modes of deformation, of the percent displacement (U_1) or distortion (U_2) remaining

when a rigid base is now assumed to exist under a compliant film (Fig. 2-1), resulting in the new constraint $u_C = 0$ at $z = h$.

Equivalence of Fabrikant's formulation

Let us now address Fabrikant's solution [111], which relies upon the method of images. Fabrikant writes $G_{11,C}(x, y, x_0, y_0)$ in a form equivalent to

$$G_{11,C} = G_{11,B} + \frac{1}{2\pi\mu}\sum_{m=1}^{\infty}\left[\frac{1-\nu}{2}Q_m + (-1)^m\left(\frac{1}{\hat{r}(2m)} + \frac{\hat{x}^2-\hat{y}^2}{\hat{r}(2m)[\hat{r}(2m)+2mh]^2}\right)\right], \quad \text{(A.35)}$$

where $\hat{r}(\beta) = \sqrt{r^2+(\beta h)^2}$, and where Q_m is calculated by considering the boundary conditions in a calculation-intensive process [111]. For example, the first three terms in the case of $\nu = 0.5$ are

$$Q_1 = -2f(2) - 4f'(2) - 4f''(2), \quad \text{(A.36)}$$

$$Q_2 = 2f(4) + 8f'(4) + 16f''(4) + 16f'''(4) + 16f''''(4), \quad \text{(A.37)}$$

$$Q_3 = -2f(6) - 12f'(6) - 36f''(6) - 64f'''(6) - 96f''''(6) - 64f^{(5)}(6) - 64f^{(6)}(6), \quad \text{(A.38)}$$

where

$$f(\beta) = \frac{1}{\hat{r}(\beta)} - \frac{\hat{x}^2-\hat{y}^2}{\hat{r}(\beta)[\hat{r}(\beta)+\beta h]^2}, \quad \text{(A.39)}$$

and where the derivatives indicated by f', f'', etc. are taken with respect to β.

By using an approach outlined by Fabrikant, it is possible to show the equivalence of Yue's and Fabrikant's equations. Begin with Equation A.19 and rewrite Yue's Φ_{11} and Φ_{22} as

$$\Phi_{11} = \frac{1-\nu}{\mu}\left(e^{-4\rho h} - 1 - \frac{4\rho h e^{-2\rho h}}{3-4\nu}\right) \times \sum_{n=0}^{\infty}\left(-e^{-4\rho h} - \frac{1+4\rho^2h^2+(3-4\nu)^2}{3-4\nu}e^{-2\rho h}\right)^n, \quad \text{(A.40)}$$

$$\Phi_{22} = \frac{1}{\mu}\left(e^{-2\rho h}-1\right)\sum_{n=0}^{\infty}(-e^{-2\rho h})^n. \quad \text{(A.41)}$$

These expressions can be evaluated term by term with the identities

$$\int_0^{\infty}(\rho h)^{\alpha}e^{-\beta\rho h}J_0(\rho r)\,d\rho = \left(-\frac{\partial}{\partial\beta}\right)^{\alpha}\frac{1}{\hat{r}(\beta)}, \quad \text{(A.42)}$$

$$\int_0^{\infty}(\rho h)^{\alpha}e^{-\beta\rho h}J_2(\rho r)\,d\rho = \left(-\frac{\partial}{\partial\beta}\right)^{\alpha}\left(\frac{r^2}{\hat{r}(\beta)[\hat{r}(\beta)+\beta h]^2}\right), \quad \text{(A.43)}$$

and are found to be equivalent to Equation A.35.

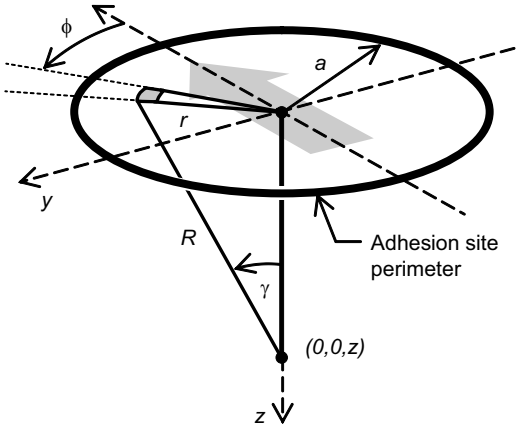

Figure A-3: Schematic for integrating the deflection at an arbitrary depth under the center of a circular area of tangential traction in the x direction.

Expressions of U_i for finite-thickness substrata

It is desirable to have simple analytical expressions or approximations for the normalized deformation functions U_1 and U_2. The relationship $U_1(h/a)$ when $\nu = 0.5$ is found through software detection [272] to be well fitted by the approximate equation

$$U_1(h/a) \approx \left[1 + 0.443(a/h)^{1.15}\right]^{-1} \tag{A.44}$$

with an error of less than 4% for $h/a > 0.1$. Although this empirical equation fits well, it has no physical basis.

A closed-form approximation with physical basis can be developed by the following reasoning: by comparing the deflection beneath the center of the adhesion site in both configurations shown in Figure 2-1, it can be seen that the displacements u_C and u_B, which have been calculated analytically, are similar in the range $0 \le z \le h$ except for a constant offset. Therefore, an approximation to u_C is pursued by subtracting the deflection u_B at $z = h$ from the deflection u_B at the surface, giving the following closed-form approximation to U_1:

$$U_1^\star(z/a) = 1 - \frac{u_B(0,0,z)}{u_B(0,0,0)}. \tag{A.45}$$

To make this approximation, we must calculate the deflection within the substratum directly underneath the center of the circular area, which can be found from the more general expression of $G_{B,11}(x,y,x_0,y_0,z)$ for arbitrary z [109]:

$$G_{B,11} = \frac{1}{4\pi\mu}\left[\frac{1}{R} + \frac{\hat{x}^2}{R^3} + (1-2\nu)\left(\frac{1}{R+z} - \frac{\hat{x}^2}{r(R+z)^2}\right)\right], \tag{A.46}$$

where $R = \sqrt{r^2+z^2}$ and positive z is again measured downward into the substratum.

Let us restrict the focus to the deformation under the center so that $\hat{x} = x$ and $\hat{y} = y$. The deflection at arbitrary depth under the center of the circle is (see Figure A-3)

$$u_B(0,0,z) = T\int_0^{2\pi}\int_0^a G_{B,11}\, r\, dr\, d\gamma. \tag{A.47}$$

Make the variable substitutions $r = R\sin\phi$ and $R = z\sec\phi$ so that $x = -R\cos\gamma\sin\phi$

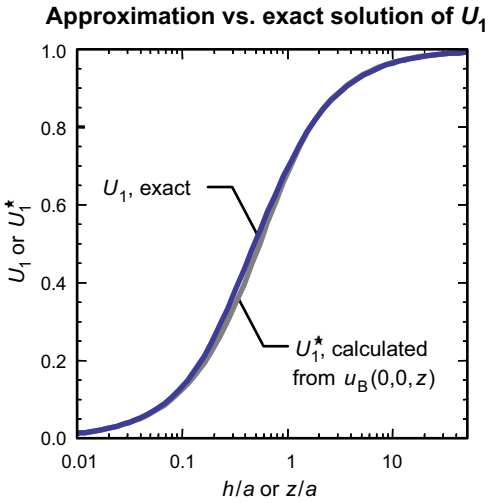

Figure A-4: Exact numerical evaluation of $U_1(h/a)$ in Equation A.25 compared to approximation $U_1^\star(z/a)$ in Equation A.51; substratum Poisson's ratio $\nu = 0.5$ for both calculations.

and $dr = z\sec^2\phi\, d\phi$:

$$u_B(0,0,z) = \frac{Tz}{4\pi\mu}\int_0^{2\pi}\int_0^{\tan^{-1}(a/z)}\left[\left(\frac{1}{\sec\gamma}+\frac{1-2\nu}{1+\sec\gamma}\right)\right.$$
$$\left.+\cos^2\gamma\left(\frac{\sin^2\phi}{\sec\phi}-(1-2\nu)\frac{\sin^2\phi\sec\phi}{(1+\sec^2\phi)^2}\right)\right]\tan\phi\sec^2\phi\, d\phi\, d\gamma. \quad \text{(A.48)}$$

From this we obtain

$$u_B(0,0,z) = \frac{T}{4\mu}\left(\frac{z^2}{\sqrt{a^2+z^2}}+(4-2\nu)\sqrt{a^2+z^2}-(5-2\nu)z\right). \quad \text{(A.49)}$$

It can be verified by using the approximations

$$\sqrt{a^2+z^2} \approx \begin{cases} a+z^2/2a & \text{if } z \ll a, \\ z+a^2/2z & \text{if } z \gg a. \end{cases} \quad \text{(A.50)}$$

that this equation simplifies to the point force case $Ta^2(3-2\nu)/8\mu z$ when a is small and to the surface displacement solution $Ta(2-\nu)/2\mu$ as $z \to 0$.

Equation A.45 and Equation A.49 are combined as

$$U_1^\star(z/a) = 1 - \frac{1}{2a(2-\nu)}\left[\frac{z^2}{\sqrt{a^2+z^2}}+(4-2\nu)\sqrt{a^2+z^2}-(5-2\nu)z\right]. \quad \text{(A.51)}$$

Subtracting the at-depth deflection $u_B(0,0,0)$ from the surface deflection $u_B(0,0,z)$ in this manner produces an exact answer only in the case of $a \to \infty$, which is equivalent to a shear stress applied over the entire coating surface. For a finite a, this estimate leaves the boundary condition $\mathbf{u}_C = (u_C\ v_C\ w_C)^T = 0$ at $z = h$ unsatisfied except at (0,0,h). However, this discrepancy appears to have only minor consequences, as shown in Figure A-4. The approximation has the benefit of deviating by less than 10% from the exact solution when $\nu = 0.5$. Additionally, both the exact solution and the approximation converge to $4h/3a$ for small h/a when $\nu = 0.5$, so that the relative error converges to zero for these conditions.

The relationship $U_2(h/a)$ when $\nu = 0.5$ is found through software detection [272] to be well fitted by the approximate equation

$$U_2(h/a) \approx 0.83^{(a/h)^{1.36}} \tag{A.52}$$

with an error of less than 12% for $h/a > 0.1$ and by

$$U_2(h/a) \approx \frac{1}{\exp\left[-1.2h/a - 0.4(\log h/a)^3\right]} \tag{A.53}$$

with an error of less than 5% for $h/a > 0.2$. No physically motivated expression for U_2 has been found in this work, however, and thus consideration of distortion effects requires numerical evaluation of Equation A.34 or one of these approximations.

As described in Chap. 2, it is desired to calculate how the cell-induced surface deformation of a compliant film is attenuated by the presence of an underlying rigid base. Therefore, let us consider two geometries, as shown in Fig. 2-1, where the coordinate system is defined so that z points downward into the substratum and x corresponds to the direction of tangential loading. In the case of a semi-infinite region, shear stress is applied to a finite region on the surface of a substratum consisting of a semi-infinite region—or half space—occupying $0 \leq z < \infty$. In the case of a finite-thickness-film, shear stress is applied to a finite region on the surface of a coating that occupies $0 \leq z \leq h$ and is perfectly bonded to a perfectly rigid base occupying $h < z < \infty$. If both cases appear similar, the presence of the rigid base is essentially undetectable; if not, the influence of the base can be quantified by the reduction of deformation.

A.2 Probability distribution transformation from noise temperature to mechanical parameter

Let us consider the the soft glassy rheology (SGR) noise temperature $x = a + 1$ (where a now represents the power-law exponent rather than the focal adhesion radius of the previous section) and its relationship to mechanical parameters such as the complex modulus $G^*(\omega) = G'(\omega) + iG''(\omega)$, creep compliance $J(t)$, and stress relaxation modulus $G(t)$.

It is postulated here that the power-law exponent a varies *intrinsically* in cells as a Gaussian distributed variable. This assumption is based on the following evidence: First, experimental measurements of the exponent a have actually been found to exhibit a Gaussian distribution [29, 44, 50, 51]. Moreover, literature reports on the variation of a (quantified as standard deviation σ_a), as shown in Fig. 4-1(a), suggest an intrinsic variation that lies in the approximate range 0.02–0.10 and is sustained even when hundreds of individual cells are sampled. Second, SGR relates a to an energy representing the sum of many agitation events from neighboring regions [91,92]; from the central limit theorem, therefore, a is expected to be approximately Gaussian regardless of the distributions of its constitutive components. Thus, the assumption of intrinsic Gaussian exponent appears plausible in both experimental and theoretical contexts. It is further assumed that endogenous variation in a dominates over other sources of variation such as direct engagement of the cytoskeleton via adhesion complexes [43].

Sollich's expression for complex modulus for a linear soft glassy material above its

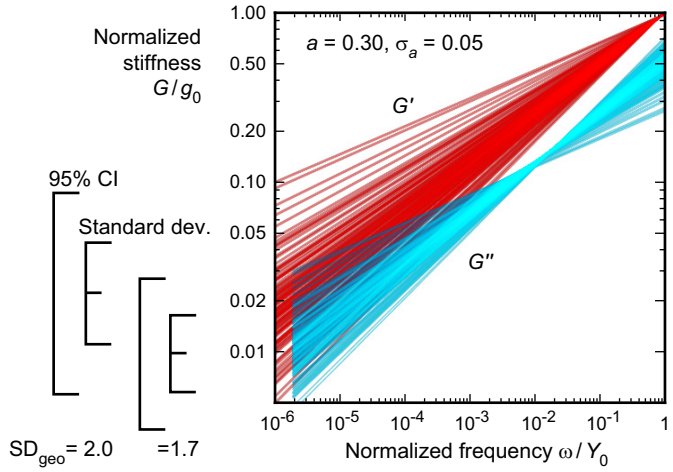

Figure A-5: Schematic of variation in storage modulus G' and loss modulus G'' as a function of variation in power-law exponent a. A Gaussian distribution of a implies an approximate log-normal distribution of G' and G''; furthermore, variations in G'' are naturally suppressed—resulting in a small SD_{geo} value—because this parameter is itself an increasing function of a. G' can be thought to pivot around an invariant point at Y_0 (B. Fabry, personal communication).

glass transition temperature, as reviewed in App. B.2, is [92]:

$$G^*(\omega) = g_0\Gamma(1+a)\Gamma(1-a)\left(\frac{i\omega}{Y_0}\right)^a = g_0\Gamma(1+a)\Gamma(1-a)\left[\cos\left(\frac{\pi a}{2}\right)+i\sin\left(\frac{\pi a}{2}\right)\right]\left(\frac{\omega}{Y_0}\right)^a, \quad \text{(A.54)}$$

where g_0 is a constant with units of stiffness (we no longer scale stiffness by element stiffness k, as in App. B.2), Γ is the gamma function, and Y_0 is the attempt frequency representing the maximum yielding frequency in the material.

(Fabry et al., following Hildebrandt [47], begin with a postulated stress relaxation modulus form of $G(t) = g_0(t/t_0)^{-a} + \text{const.}$ and use Laplace transforms to obtain $G^*(\omega) = g_0\Gamma(1-a)(i\omega/Y_0)^a$ [48]. The difference by a factor of $\Gamma(1+a)$ between this and the above equation is negligible for the purposes of this discussion and cancels out when considering the phase angle $\phi = \tan^{-1}(G''/G')$ and power-law exponent $a = 2\phi/\pi$.)

Postulated fluctuations in the power-law exponent a can now be related to quantitative predictions of variation in mechanical parameters. G' and G'' can be expressed as $\propto f(a)(\omega/Y_0)^a$, where $f(a)$ is a characteristic prefactor for that component (namely, $\Gamma(1+a)\Gamma(1-a)\cos[\pi(a/2]$ for G' and $\Gamma(1+a)\Gamma(1-a)\sin[\pi a/2]$ for G''). Assuming that a is Gaussian with average $\overline{a}$ and standard deviation σ_a for a given study (Fig. 4-1(b)) the change-of-variables equation $P[G(\omega)] = |da/dG(\omega)|P(a)$ is used to obtain

$$P[G(\omega)] = \frac{1}{G(\omega)\sqrt{2\pi}}\frac{1}{\left|\sigma_a\left(\ln\frac{Y_0}{\omega} - \frac{d\ln f(a)}{da}\right)\right|} \times \exp\left(-\frac{\left[\ln G(\omega)/f(a) - \overline{\ln G(\omega)/f(a)}\right]^2}{2\left(\sigma_a \ln\frac{Y_0}{\omega}\right)^2}\right), \quad \text{(A.55)}$$

which appears similar to the exact log-normal distribution

$$P[G(\omega)] = \frac{1}{G(\omega)\sqrt{2\pi}} \frac{1}{\left|\sigma_a \left(\ln \frac{Y_0}{\omega} - \frac{d \ln f(a)}{da}\right)\right|} \exp\left(-\frac{\left[\ln G(\omega) - \overline{\ln G(\omega)}\right]^2}{2\sigma_a^2 \left(\ln \frac{Y_0}{\omega} - \frac{d \ln f(a)}{da}\right)^2} \right), \tag{A.56}$$

where the place of the standard deviation is taken by the absolute value term. Under what conditions are these two expressions equal? Setting them equal and canceling common terms, we obtain

$$\left|\ln G - \ln f(a) - \overline{\ln G} + \overline{\ln f(a)}\right| \left(\ln \frac{Y_0}{\omega} - \frac{d \ln f(a)}{da}\right) = \ln \frac{Y_0}{\omega} \left|\ln G - \overline{\ln G}\right|, \tag{A.57}$$

where it is assumed that $d \ln f(a)/da < \ln(Y_0/\omega)$, which applies for typical experimental condition $\omega \ll Y_0$. It can be verified by plotting that $f(a)$ increases monotonically with a for G' and G'', and therefore

$$\frac{d \ln f(a)}{da} = \frac{\ln f - \overline{\ln G}}{a - \overline{a}}; \tag{A.58a}$$

$$\ln f - \overline{f(a)} \propto a - \overline{a}. \tag{A.58b}$$

It can further be verified graphically that $\overline{\ln f(a)} \approx \ln f(\overline{a})$ for small σ_a and that $\ln f(a)$ is approximately linear with a. Consequently, the equality above is at least approximately equal; to verify this, simulated storage and loss moduli are calculated for Gaussian a, and the resulting fitted $\mathrm{SD}_{\mathrm{geo}}$ compared to predicted values (Fig. A-5). The match is indeed reasonably accurate for $\sigma_a < \overline{a}$, which has been the case for cells (Fig. 4-1(b)).

When $f(a)$ is only weakly dependent on a, as is the case for the storage modulus (Table A.1), then

$$\frac{d \ln f(a)}{da} = \frac{\pi}{2} \cot\left(\frac{\pi(a+1)}{2}\right) - \psi(1-a) + \psi(1+a)$$
$$= 0 + \frac{\pi^2 a}{12} + \frac{\pi^4 a^3}{720} + \cdots \approx 0, \tag{A.59}$$

where ψ is the polygamma function. The standard deviation is thus approximately $\sigma_a \ln(Y_0/\omega)$. This standard deviation corresponds to a geometric standard deviation $\mathrm{SD}_{\mathrm{geo}} \approx (Y_0/\omega)^{\sigma_a}$ for the storage modulus. When this approximation is not valid (specifically, for the loss modulus), then

$$\frac{d \ln f(a)}{da} = \psi(1+a) - \psi(1-a) - \frac{\pi}{2} \tan\left(\frac{\pi(a+1)}{2}\right)$$
$$= \frac{1}{a} + \frac{\pi^2 a}{4} + \frac{\pi^4 a^3}{48} + \cdots \approx \frac{1}{a}, \tag{A.60}$$

and the base term $(Y_0/\omega)^{\sigma_a}$ is multiplied by a sub-unity correction factor $e^{\sigma_a/\overline{a}}$. The resulting complete $\mathrm{SD}_{\mathrm{geo}}$ terms and first-order, Taylor-series-expanded approximations for $a > 0$ are listed in Table A.1.

The distribution widths for creep compliance $J(t)$ and relaxation modulus $G(t)$ are readily calculated in the same way as the complex modulus. Different prefactors are possible for each of $J(t)$ and $G(t)$ depending on whether $t \ll t_w$ or $t \gg t_w$, where t_w is the time between a fluidizing large-strain event and the start of the experiment, as modeled by Fielding et al. [160] and experimentally explored in live-cell studies

Table A.1: Predicted geometric standard deviation $\mathrm{SD}_{\mathrm{geo}}$ of log-normal distributions for a collection of rheological parameters in the context of cell power-law rheology, where complex modulus increases with frequency as ω^a and creep compliance and reciprocal relaxation modulus increase with time as t^a, where the power-law exponent $a > 0$.

Mechanical parameter	Form	Prefactor $f(a)$ [26, 91, 160]	Geometric standard deviation $\mathrm{SD}_{\mathrm{geo}}$
Storage modulus $G'(\omega)$	$\propto f(a)\left(\frac{\omega}{Y_0}\right)^a$	$\Gamma(1+a)\Gamma(1-a)\cos\left(\frac{\pi a}{2}\right)$	$\exp\left(-\sigma_a \frac{d\ln f(a)}{da}\right)\left(\frac{Y_0}{\omega}\right)^{\sigma_a} \approx \left(\frac{Y_0}{\omega}\right)^{\sigma_a}$
Loss modulus $G''(\omega)$	$\propto f(a)\left(\frac{\omega}{Y_0}\right)^a$	$\Gamma(1+a)\Gamma(1-a)\sin\left(\frac{\pi a}{2}\right)$	$\exp\left(-\sigma_a \frac{d\ln f(a)}{da}\right)\left(\frac{Y_0}{\omega}\right)^{\sigma_a} \approx \left[e^{-1/\bar{a}}\left(\frac{Y_0}{\omega}\right)\right]^{\sigma_a}$
Creep compliance $J(t)$ $(t \ll t_w)$	$\propto f(a)(Y_0 t)^a$	$\frac{1}{\Gamma(1+a)^2\Gamma(1-a)}$	$\exp\left(\sigma_a \frac{d\ln f(a)}{da}\right)(Y_0 t)^{\sigma_a} \approx (Y_0 t)^{\sigma_a}$
Creep compliance $J(t)$ $(t \gg t_w)$	$\propto f(a)(Y_0 t)^a$	$\frac{1}{\Gamma(1+a)^2\Gamma(1-a)-\Gamma(1+a)}$	$\exp\left(\sigma_a \frac{d\ln f(a)}{da}\right)(Y_0 t)^{\sigma_a} \approx \left(e^{-2/\bar{a}} Y_0 t\right)^{\sigma_a}$
$\frac{1}{\text{Relaxation modulus } G(t)}$ $(t \ll t_w)$	$\propto f(a)(Y_0 t)^a$	$\frac{1}{\Gamma(1+a)}$	$\exp\left(\sigma_a \frac{d\ln f(a)}{da}\right)(Y_0 t)^{\sigma_a} \approx (Y_0 t)^{\sigma_a}$

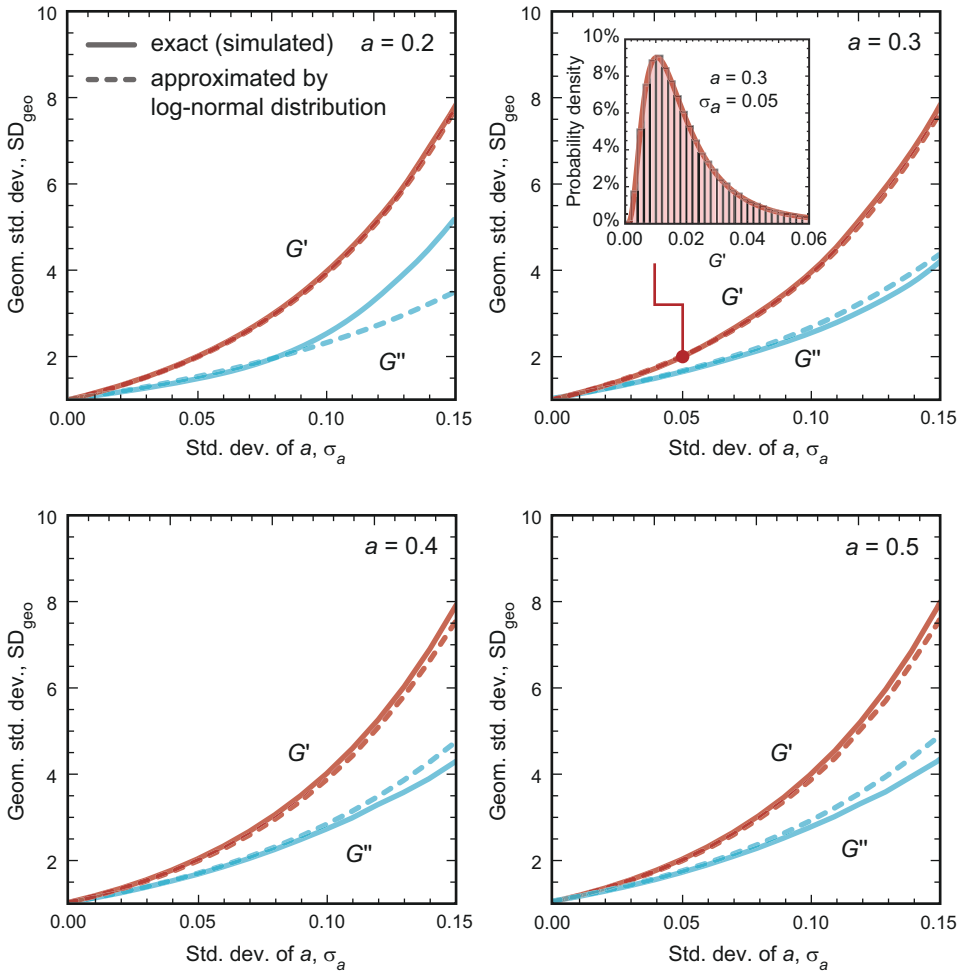

Figure A-6: Exact (as simulated) and approximated geometric standard deviation $\mathrm{SD}_{\mathrm{geo}}$ of storage and loss moduli G' and G'' as a function of standard deviation σ_a of the power-law exponent a, for different values of a. The log-normal approximation is generally good except for values of σ_a exceeding $a/2$ (which does not occur in any literature reports). Inset for $a = 0.3$, $\sigma_a = 0.05$ shows excellent agreement between histogram of simulated storage modulus and a probability distribution function plotted from the predicted $\mathrm{SD}_{\mathrm{geo}} = 2.0$.

conducted by Bursac et al. and Trepat et al. [151, 157]. Despite these additional scenarios, the determination of $\mathrm{SD}_{\mathrm{geo}}$ parallels the treatment of the complex modulus. The resulting $\mathrm{SD}_{\mathrm{geo}}$ terms of $G(t)$ and $J(t)$ and first-order, Taylor-series-expanded approximations for $a > 0$ are listed in Table A.1 as predictions to be verified. (It is assumed that $d \ln f(a)/da < \ln(Y_0 t)$, which applies for typical experimental condition $t \gg 1/Y_0$. Shown here is only the more experimentally relevant case of $t \ll t_w$ for the relaxation modulus $G(t)$; at long times, $G(t) \to 0$.)

An assumed distribution of power-law exponent a—together with prefactors calculated from phenomenological and theoretical models of cell rheology—thus allows calculation of the distribution of dynamic stiffness, creep compliance, and stress relaxation modulus. In particular, a Gaussian distribution of a leads immediately to a log-normal distribution of stiffness. We find the minimum measurable geometric standard deviation $\mathrm{SD}_{\mathrm{geo}}$ for experiments conducted in the frequency regime to be $\propto (Y_0/\omega)^{\sigma_a}$, where the prefactor depends upon the experimental regime, modulus of interest, and cell state, as listed in Table A.1. These predictions are compared to experimental results in §4.3.3.

Appendix B

Simulation protocols

B.1 Bootstrapping: a non-parametric resampling tool for data inference

Motivation

We often use collected data to estimate the true value of some parameter, and it is desirable—not to say obligatory—to identify and report the uncertainty in such estimates. For example, we may wish to estimate the true mean of a population; in this case, it is known that the best estimator for this value is simply the average of the sample values. Mathematically, we would say that the sample average $\overline{x} = \sum x_i/n$ is an estimator for the population mean μ. Further, this estimator is unbiased in that its expected value equals the true value.[1] We know from the central limit theorem that $\overline{x}$ is approximately a Gaussian-distributed variable for sufficiently large data set size n, and that an estimator of the standard deviation of this distribution is

$$s_{\overline{x}} = \sqrt{\frac{1}{n(n-1)} \sum_{i=1}^{n} (x_i - \overline{x})^2}, \tag{B.1}$$

also known as the standard error of the mean.

So far, so good; we have assured unbiasedness and an analytically expressed uncertainty of the parameter of interest. Tools such as the latter are called parametric, as they are analytically derived based on an assumed distribution. But what if the underlying distribution is unknown? Or what if our parameter of interest is sufficiently unusual that parametric tools do not exist to calculate its uncertainty?

Our ultimate goal remains: we desire to report unbiased estimates along with the uncertainty, or variation, in these estimates. Without knowing this uncertainty, it is impossible to compare one measurement with another (possibly obtained under different conditions) to conclude whether or not the difference arose by chance. Put another way, we cannot determine—with statistical confidence—whether *any* adjustment or

[1] Examples of unbiased and biased estimators are the average ($\overline{x} = \sum x_i/n$) and nonreduced standard deviation ($\sqrt{\sum (x_i - \overline{x})^2/n}$) of a sample set x_i as estimators of the true mean μ and true standard deviation σ of the population. The nonreduced standard deviation is biased in that it generally underestimates σ, which can be understood as follows: typically somewhere out in the population, not included in our sample, are large positive and negative values. These extreme values tend to cancel each other out when calculating averages, and so they do not cause much of a difference between the sample and population means (over the long run, they cause no difference at all). However, extreme values, positive or negative, always increase standard deviation calculations because of the squared term. Our sample estimator is therefore too small as a result of missing them. We can reduce the bias by using $(n-1)$ in the denominator instead of n, thus increasing slightly the value of our estimator.

treatment applied in science or engineering is influential or useful. Obviously, this is an unacceptable situation.

Consider the following example: the creep compliance of single suspended cells under a photonic load is well described by the constitutive relation $\overline{\varepsilon}(t) = At^a$ (§3.3.2). The use of the mean or geometric mean $\overline{\varepsilon}$ of multiple cells reduces noise in the data and promotes convergence of nonlinear regression algorithms. However, once a parameter has been fit ($a = 0.35$, say), what is the expected uncertainty? Is it 0.1? 0.000001? If another batch of cells exhibited a power-law exponent of $a = 0.36$, would this different be likely caused by chance, or would it signal a meaningful difference between the two groups of cells?

One solution is to perform the experiments over and over, perhaps hundreds of times. This repetition would provide the distribution of a in the example above, along with an indication of how much a tends to vary between cells. If we obtained all types of values from $a = 0.30$ to $a = 0.40$ for each condition, for example, then a difference of $\Delta a = 0.01$ in a single comparison could have arisen by chance and would not be particularly meaningful. If, however, we obtained $a_1 = 0.35$, $a_2 = 0.36$ consistently one hundred times, we would be quite sure that the difference is not simply attributable to chance, and we could use this confidence to draw a well-supported conclusion about the increased fluidity of the second group of cells.

Unfortunately, this degree of repetition (hundreds of repetitions of every experiment) may not be practical with the resources available to us. Is there another solution? There is.

Bootstrapping overview

Bootstrapping is a Monte Carlo (i.e., randomized simulation) technique in which we create, from an original data set, a new data set of the same size n by resampling *with replacement* [181]. Equivalently, the probability that any one value will be selected is always $1/n$ regardless of whether is has been selected before. The new data set is somewhat different from the original data set; some values have probably been repeated, others omitted. We estimate the parameter of interest again with this new set, and then repeat the process many (e.g., hundreds or thousands of) times. At the end, we have a distribution of parameter values. Remarkably, the distribution's width is a measure of the uncertainty of the original parameter, and its mean contains information about whether the original estimate was biased or not.

The central idea of bootstrapping is: *Lacking additional data, we* simulate *additional data by resampling existing data.* We metaphorically "pull ourselves up by our own bootstraps" by extracting additional useful data from an existing data set without performing more experiments. The calculations involved in performing the iterations could never have been performed before substantial computing power became available. Because this technique still is rarely covered in statistics classes, an overview is given here. Several applications of this idea, all used in this thesis, will be reviewed, based on original exposition of the theory and subsequent texts containing interpretation and examples [181–186].

Parameter variance

Let us denote the original estimated parameter by $\hat{\theta}$ and the B bootstrapped parameters by θ_i. Then an estimate of the uncertainty of $\hat{\theta}$ is

$$s_{\hat{\theta}} = s_\theta \sqrt{\frac{n}{n-1}} = \sqrt{\frac{n}{(n-1)(B-1)} \sum_{i=1}^{B} (\theta_i - \overline{\theta})^2} \tag{B.2}$$

where $\overline{\theta} = \sum \theta_i / B$. That is, the uncertainty in the standard error of the parameter value is approximately the standard deviation of the distribution of bootstrapped parameter estimates. For large data sets, the correspondence approaches equality.

Parameter bias

An unbiased estimate of the parameter $\hat{\theta}$ is

$$\hat{\theta}' = 2\hat{\theta} - \overline{\theta}. \tag{B.3}$$

The interpretation here is that if sampling from the true population (during the experiment) induced some amount of bias, then the resampling process will accentuate this bias, and the difference can be corrected for.

Confidence intervals

A Monte Carlo confidence interval can be defined from the collection of bootstrapped parameters θ_i. In the simplest example, known as the percentile or Efram's method, we obtain the $(1-\alpha)$% confidence interface by dropping the fraction α of the most extreme θ_i values. If we denote the f th percentile of the sorted bootstrapped values by $\theta_{f\%}$, then the 95% confidence interval, for example, is $[\theta_{2.5\%}, \theta_{97.5\%}]$. Note the intuitive nature of this operation; under the key idea that the bootstrapped distribution simulations repeated experiments, we would expect the parameter of interest to lie within this interval 95% of the time.

A slightly more complex method, known as the basic or Hall's method, corrects for bias with the technique used in Eq. B.3: the $(1-\alpha)$% interval is $[2\hat{\theta} - \theta_{(1-\alpha)/2\%}, 2\hat{\theta} - \theta_{\alpha/2\%}]$. The 95% confidence interval is therefore $[2\hat{\theta} - \theta_{97.5\%}, 2\hat{\theta} - \theta_{2.5\%}]$. For the data sets examined in this thesis, there was no substantial difference between these results and results from the percentile method, as the accumulated bootstrapped distributions were essentially symmetric and therefore non-biased.

More complex techniques such as the bias corrected and accelerated (BCa) bootstrap are available [273], but these tools generally lack the intuitive nature of the calculations described above. These more advanced techniques were not required for this work.

Hypothesis testing

Parametric tools exist for comparing whether the means of two Gaussian-distributed populations are equal. When the data sets are large, for example, the z test asks whether the difference in the means, normalized to a pooled standard deviation, is large enough to not likely occur by chance. The answer is quantified in terms of a p-value, the likelihood of at least such an extreme result arising if the true means are actually identical. When the data sets are not so large, Student's t test revises the z threshold somewhat, but the question is the same, and this test also provides a p-value. If the p-value is sufficiently low (0.05, say), than we might conclude that chance alone does not explain the difference in the means of the two sampled populations.

However, what if the populations are not Gaussian distributed, or if the distributions are skewed, if the parameter is less common than the mean, or if the standard deviations of the parameter are not available? Bootstrapping provides an intuitive approach that matches the strategy of the classic hypothesis test (and provides the practitioner with a better understanding of what hypothesis tests p-values are actually reporting). We simply pool the two data sets together, shuffle them, and divide them into the same original sizes, and then recalculate the parameter of interest for each group. If the difference between the bootstrapped groups is more extreme than the difference between

the original groups, the test is scored "1"; if not, "0." Repetition of this test many times (thousands of times, perhaps) provides an effective p-value in the form of the fraction of "1" scores. By pooling and shuffling the data, we are simulating the null hypothesis, and the repeated tests are determining how likely it is, over the long run, for such a condition to produce as extreme (or more extreme) a comparison as we saw with the original data set.

ANOVA based on bootstrapped results

Analysis of variance (ANOVA) is a parametric technique for comparing multiple parameters simultaneously.[2] However, the process of performing ANOVA based on bootstrapped results is not a well-known result, and thus is derived here. The test statistic F is

$$F = \frac{\text{variance between groups}}{\text{variance within groups}} = \frac{\sum_{i=1}^{K} n_i(\overline{X_i} - \overline{X})^2/(K-1)}{\sum_{i=1}^{K}(n_i-1)s_i^2/(N-K)}, \tag{B.4}$$

where n_i is the number of samples in group i, $\overline{X_i}$ is the mean of group i, $\overline{X}$ is the total mean, K is the number of groups, n is the total number of samples, and s_i is the sample standard deviation of group i. Assume that we actually have estimates of means $\hat{\mu}_i$ and population standard deviations $\hat{\sigma}_i$ from bootstrapping, and that the distributions are Gaussian. Now we might assume that group sizes are equal and very large so that $(n_i-1)s_i^2 = n_i\hat{\sigma}_i^2$ and $N = n_iK$:

$$F = \frac{K\sum_{i=1}^{K}(\hat{\mu}_i - \hat{\mu})^2}{(K-1)\sum_{i=1}^{K}\hat{\sigma}_i^2}. \tag{B.5}$$

This statistic follows the F-distribution with degrees of freedom $\{K-1,\ K(n_i-1)\}$. Moreover, as $n_i \to \infty$, the distribution asymptotically approaches the χ^2 distribution of $K\sum_i(\hat{\mu}_i - \overline{\hat{\mu}})^2/\sum\hat{\sigma}_i^2$ with $K-1$ degrees of freedom. The p-value is thus

$$p = 1 - \chi^2_{K-1}\left(\frac{K\sum_{i=1}^{K}(\hat{\mu}_i - \overline{\hat{\mu}})^2}{\sum_{i=1}^{K}\hat{\sigma}_i^2}\right) = 1 - \chi^2_{K-1}\left(\frac{\sum_{i=1}^{K}(\hat{\mu}_i - \overline{\hat{\mu}})^2}{\overline{\hat{\sigma}_i^2}}\right). \tag{B.6}$$

Details and limitations

How many bootstrapping iterations should be performed? If computation is cheap, we should iterate until the results have suitably settled. For example, one can calculate the estimated standard error based on all iterations performed so far and track this value until the desired convergence is achieved. An example of this convergence is shown in Fig. 3-7.

It should be clear that bootstrapping will not explore the data space sufficiently if the data space is too small. How small is too small? The general consensus is that the data set size should not be lower than $n \sim \mathrm{O}(10)$. This requirement is satisfied by all the data sets examined in this thesis.

[2] It is not appropriate to perform multiple z or t tests because each test has a false positive rate of α when the null hypothesis holds. These errors would accumulate, almost guaranteeing one or more false positives somewhere in our results, were those tests simply repeated over many pairs without adjusting α. ANOVA adjusts the test statistic to avoid this problem.

B.2 Soft glassy rheology: overview and simulation of a coarse-grained trap model

Overview

Soft glassy rheology (SGR) theory is a phenomenological model developed by Sollich et al. [91, 92, 160] and applied generically to so-called soft glassy materials (e.g., foams, pastes, emulsions, slurries), which are defined to be materials with a disordered and metastable structure. SGR abstracts physical material deformation as the motion of many particles within an energy landscape, and each physical parameter or concept corresponds to a component of this abstraction (Table B.1). Physically, SGR theory treats a material in a coarse-grained way as containing many mesoscopic regions. Each region is caged or trapped in its current configuration with thermal energy insufficient to induce deformation. However, stochastic yielding occurs occasionally as a result of considerable jostling from neighboring regions and from applied stress. Jostling or agitation is treated as a uniform "noise temperature" x that is analogous to actual temperature, but with far greater effective magnitude.

Each element/well has an associated energy E corresponding to yielding; in the absence of noise, $E = kl_y^2/2$ where l_y is the yield strain. E is the height of the barrier and is a property of the element. Strain in a region is treated as an increase in particle height of magnitude $kl^2/2$, where k is the region's stiffness and l is its strain. For the work described in this thesis, however, this strain energy is always assumed to be negligible compared to x and E; that is, yielding is always noise-induced and independent of strain. This assumption yields a linear constitutive equation of power-law rheology, as we will see. "Fluidization," as investigated elsewhere in the cell mechanics *milieu* [40], is a consequence of the strain energy $kl^2/2$ becoming significant compared to E, and results in nonlinear deformation that may include a complete transition to viscous flow.

As shown in Fig. B-1(a), the yielding process is viewed as a particle's escape from its existing well and reappearance in a new well and in an unstrained condition. Bauchaud previously found that if new wells are selected from the distribution $\rho(E) = e^{-E}$, then a glass transition can occur in the material; a yield stress exists below but not above this threshold [274]. The noise temperature x is scaled to this glass transition energy, so that $x > 1$ corresponds to a viscoelastic material assuming small strains. (We will consider only $x > 1$.) The yield rate $Y(E)$ of a region (equivalently, hop rate out of

Table B.1: Abstractions of the soft glassy rheology (SGR) model.

Physical region or event	SGR abstraction
Mesoscopic material region	Element
Metastability	Confinement to well with depth $\gg kT$
Strain	Rise to height $kl^2/2$ in well
Jostling from adjacent connected regions	Noise temperature x
Glass transition	$x = 1$; at $x > 1$, no yield stress exists (deformation occurs upon any loading) and the material transitions toward the equilibrium distribution $P_0(E)$
Yield: rearrange into new configuration with zero strain	Hop at rate $\propto e^{(E-kl^2/2)/x}$ into bottom of a new well selected from $\rho(E) = e^{-E}$
Shear thinning, fluidization	Sufficiently large strain that $kl^2/2$ is no longer negligible; widespread yielding means that average well depth is temporarily shallower and the average yield rate is temporarily larger
Resolidification	Element relaxation into deeper wells (on average) over time

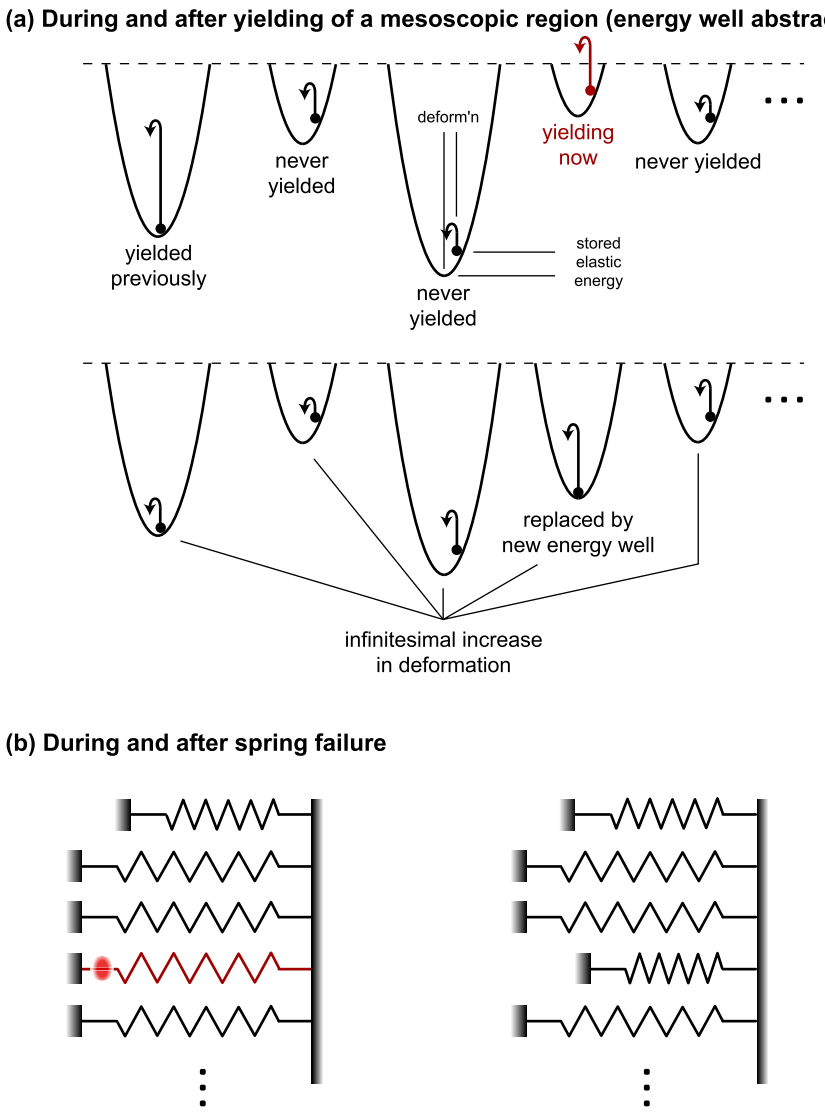

Figure B-1: Energy well schematic representing region rearrangement in the soft glassy rheology theory, and schematic of an equivalent spring configuration used in simulation. (a) Yielding of mesoscopic regions is abstracted as particles hopping out of energy wells as a result of non-thermal agitation (and strain, in the general case). The first well has yielded previously and thus has smaller accumulated strain. The fourth well is currently yielding. (b) Equivalently, the well could be viewed as a collection of springs, each with their own yielding rate. Again, the first region yielded a short time ago and now stores less strain energy. The yielding of the fourth region is shown as a failure of the existing spring and replacement with a new spring.

a trap) with energy E is the Arrhenius factor $Y_0 e^{-E/x}$, where Y_0 denotes an attempt frequency and where x replaces the usual kT. Equivalently, the lifetime of a region before yielding is $\tau(E) = e^{E/x}/Y_0$.

Parameters

In the SGR model, the strain rate $\dot{\gamma}$, noise temperature x, and element stiffness k are all uniform throughout the material. The element-specific values are energy E, strain γ, yield rate $Y(E)$, expected trap lifetime $\tau(E) = 1/Y(E)$, length l, and stress kl. The model scales all energy values E and the noise temperature x in terms of the glass transition energy x_g, and scales the stress σ in terms of k and l.

A key parameter in the theory is the distribution $P(E,t)$ of traps or well of depth E at time t, because knowledge of this distribution allows calculation of bulk values [92]. The time-dependent master equation for the probability of occurrence $P(E)$ of an element with yield energy E is

$$\begin{aligned}\text{change in } P(E) = &-(\text{prob. of being at } E) \times (\text{rate of leaving } E) \\ &+ \sum_{\text{all } E} (\text{rate of leaving}) \times (\text{prob. of landing at } E)\end{aligned} \tag{B.7a}$$

$$\frac{\partial}{\partial t} P(E,t) = -P(E,t) Y_0 e^{-E/x} + \left[\int_0^\infty P(E,t) Y_0 e^{-E/x} \, dE \right] e^{-E} \tag{B.7b}$$

which has normalized stationary solution

$$P_0(E) = \left(\frac{x-1}{x} \right) e^{-E} e^{E/x}, \tag{B.8}$$

which is the equilibrium distribution for the linear regime with $x > 1$.

The average (bulk) value of any term $y(E,l,t)$ is

$$\langle y(t) \rangle = \int_0^\infty \int_0^\infty y(E,l,t) P(E,l,t) \, dE \, dl. \tag{B.9}$$

Thus, the average yielding rate at equilibrium across all elements is

$$Y_{\text{eq}} = \langle Y_0 e^{-E/x} \rangle = \int_0^\infty Y_0 e^{-E/x} P_0(E,t) \, dE = Y_0 \left(\frac{x-1}{x} \right). \tag{B.10}$$

We will generally assume that the distribution at the start of any experiment is the equilibrium distribution, or equivalently that fluidization has not occurred recently. It is an important but perhaps not easily seen detail that in the regime of noise-induced yielding, the equilibrium distribution $P_0(E)$ persists over time even though new wells are selected from $\rho(E) = e^{-E}$, because the shallower wells are also the generally the first to yield again.

Constitutive equations

Two constitutive equations form the foundation of SGR. The first equation effectively states that all elements at time t either remain from the original distribution at the beginning of the experiment and have not yielded yet, or have yielded at least once (most recently, at time t') and are now in a new trap selected from the distribution $\rho(E) = e^{-E}$:

$$\begin{aligned}\text{all elements} = &\sum_{\text{all } E} (\text{original distribution}) \times (\text{prob. of remaining}) \\ &+ \sum_{\text{all } E,\ t'} (\text{yielding rate at t}') \times (\text{chance of landing in } E) \times (\text{prob. of remaining})\end{aligned} \tag{B.11a}$$

$$1 = \int_0^\infty P_0(E) e^{-t/\tau(E)} \, dE + \int_0^\infty \int_0^t \langle Y(t') \rangle \rho(E) e^{-(t-t')/\tau(E)} \, dt' \, dE. \tag{B.11b}$$

(This and the following equation are written in a slightly different form compared to Sollich et al.'s presentation in order to emphasize the average time to yield $\tau(E)$.) The second equation divides the stress in the material between the elements still in their

original wells and the elements that have yielded at least once:

$$\sigma(t) = \int_0^\infty \gamma(t) P_0(E) e^{-t/\tau(E)}\, dE + \int_0^\infty \int_0^t [\gamma(t) - \gamma(t')] \langle Y(t') \rangle \rho(E) e^{-(t-t')/\tau(E)}\, dt'\, dE. \quad \text{(B.12)}$$

These equations can be combined and interpreted in another way: that the stress in the material is linearly coupled with a term representing the strain, offset by yielding events that enable relaxation:

$$\sigma(t) = \gamma(t) - \int_0^\infty \int_0^t \gamma(t') \langle Y(t') \rangle \rho(E) e^{-(t-t')/\tau(E)}\, dt'\, dE. \quad \text{(B.13)}$$

This equation can be shown by integration by parts to be equal to

$$\sigma(t) = \int_0^t \dot{\gamma}\,(t') \int_0^\infty P_0(E) e^{-(t-t')/\tau(E)}\, dE\, dt', \quad \text{(B.14)}$$

the Fourier transform of which gives the complex modulus:

$$G^\star(\omega) = i\omega \int_0^\infty e^{i\omega t} \int_0^\infty P_0(E) e^{-(t-t')/\tau(E)}\, dE\, dt = \int_0^\infty P_0(E) \frac{i\omega\tau(E)}{i\omega\tau(E)+1}\, dE = \left\langle \frac{i\omega\tau(E)}{i\omega\tau(E)+1} \right\rangle, \quad \text{(B.15)}$$

which is the sum of an infinite number of Maxwell elements with relaxation times chosen from $P(\tau)$ [92]. Integration of this expression gives (for $\omega \ll Y_0$, which applies for all experimental conditions of interest here)

$$G^*(\omega) = \Gamma(1+a)\Gamma(1-a) \left(\frac{i\omega}{Y_0} \right)^{x-1}, \quad \text{(B.16)}$$

which displays the power-law dependence on frequency for the complex modulus. A power-law dependence on time for the creep compliance $J(t)$ and reciprocal relaxation modulus $1/G(t)$ follows from standard methods [29, 47, 48].

Simulation

Let us now extend this work by developing a procedure to simulate creep compliance. Assume that the cell starts at the equilibrium distribution $P_0(E)$. (Note that it is essentially equivalent for a fluidizing event to have taken place longer ago that the creep compliance experiment will last [160].) The material can be viewed as a parallel arrangement of springs with stiffness k that occasionally fail and are replaced with unstrained springs (Figs. B-1, B-2).

It is frequently the case in the Gillespie algorithm (and Monte Carlo simulations in general) that we need to sample from a particular distribution. For example, the expected waiting time τ for any random element to yield is selected from $P(\tau) \propto \tau^{-x}$. If we have at hand a way to generate random numbers uniformly distributed between 0 and 1 (let us denote this by $U = U[0,1]$), we can simulate such a distribution by using the inverse transformation method, where we calculate the cumulative distribution

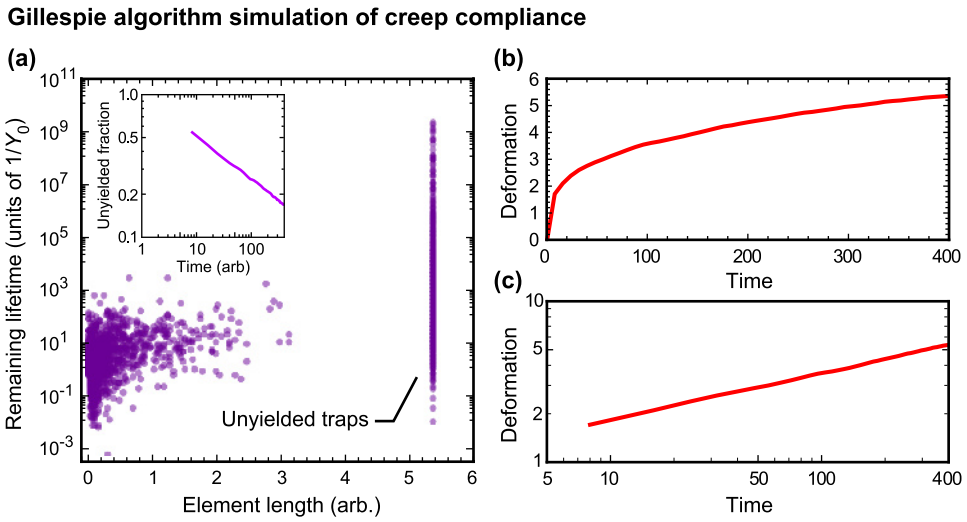

Figure B-2: **Monte Carlo kinetic simulation of creep compliance of the soft glassy rheology model, as calculated by the Gillespie algorithm.** (a) At a simulation time of $t = 400$ (normalized by the reciprocal attempt frequency $1/Y_0$), 83% of the 200 simulated traps have yielded and been replaced with unyielded traps; 17% have not yielded, bear a nondimensional strain of just under 5.4, and hold the vast majority of the strain energy (inset, fraction of unyielded traps over time). (b,c) Linear and log-log plots of nondimensional creep compliance suitable resemble average creep compliance of real cells (cf. Figs. 3-6, 3-8).

function

$$C(\tau) \equiv \int_0^{\tau} (\tau')^{-x}\, d\tau' = (1 - \tau^{1-x}). \tag{B.17}$$

We take the inverse function C^{-1} and set this equal to U to see that we need to sample from $(1-U)^{1/(1-x)} = U^{1/(1-x)}$.

Interestingly, the simulation can be simplified (and thus sped up) by considering that the strain energy in the system is divided between elements that have never yielded and elements that have yielded at least once. The first integral in Eq. B.11b above can be integrated to get (for $t \gg 1/Y_0$)

$$1 = \Gamma(x)(Y_0 t)^{1-x} + \int_0^{\infty} \int_0^{t} \left(\frac{x-1}{x}\right) e^{-E} e^{-(t-t')/\tau(E)}\, dt'\, dE \tag{B.18}$$

where Γ is the gamma function. Fielding et al. have found the creep compliance of the system to be

$$J(t) = (Y_0 t)^{x-1} / [\Gamma^2(x)\Gamma(2-x)]. \tag{B.19}$$

Therefore, the total amount of stress supported by these original elements is simply $1/[\Gamma(x)\Gamma(2-x)]$, or a constant 86% for $x = 1.3$. (By numerical integration, the strain energy in these original elements is found to be 96% of the strain energy.) These calculations suggest the possibility of simulating the original elements only (which would result in the simulation speeding up with time) and correcting the applied stress (or the resulting simulated creep compliance) by the sub-unity factor $1/[\Gamma(x)\Gamma(2-x)]$.

Appendix C

Experimental protocols[1]

C.1 Cell culture[2]

Thawing, passaging, and freezing

Materials:

1. (Fibroblasts only) NIH-3T3 fibroblasts (ATCC #CRL-1658), Dulbecco's Modified Eagle's Medium (as basal media) (Gibco #11885), bovine calf serum (HyClone #SH30070.01)
2. (Mesenchymal stem cells only) Primary mesenchymal stem cells (Stem Cell Technologies, ReachBio, or isolated in-house), Mesencult Basal Media (Stem Cell Technologies #5401), Mesencult Supplements (Stem Cell Technologies #5402)
3. L-glutamine (200 mM) (Gibco #25030)
4. Ca^{2+}- and Mg^{2+}-free phosphate-buffered saline (PBS, Gibco #10010)
5. Trypsin (0.05%) / EDTA (1 mM) (Gibco #25300)
6. Dimethylsulfoxide (DMSO, Sigma #276855)
7. Fetal bovine serum (FBS, Atlanta Biologicals #S11550)

Methods (thawing):

1. Prepare complete media: 94% basal media, 5% serum/supplements, 1% glutamine (to replenish degraded glutamine in basal media; if basal media is less than several months old, skip glutamine and replace with basal media).
2. Warm media to 37°C.
3. Retrieve frozen cryovial of cells and thaw in 37°C water bath until ice is almost gone.
4. Spray vial thoroughly with 70% ethanol and transfer to sterile hood.
5. Gently transfer cells into a 15 mL centrifuge tube, and add 15 mL warm media drop by drop, swirling to mix.
6. Centrifuge at 300 g (1200 rpm) for 8 min.
7. Aspirate supernatent, resuspend pellet in approximately 1 mL warm complete media, and transfer to a tissue culture polystyrene flask or dish.

[1] It is assumed in all protocols that common cell biology laboratory supplies such as sterile water, 70% ethanol, and centrifuge tubes are available.

[2] Adapted from Stem Cell Technologies Catalog #28453, "Technical Report: Enumeration, Expansion, and Differentiation of Human Mesenchymal Stem Cells Using Mesencult."

8. The next day, exchange media.

Methods (passaging):[3]

1. Check cells under a phase contrast microscope to ensure that the cells are at an adequate stage for passaging (80% confluence).
2. Aspirate media and wash the cells with 5 mL PBS to remove residual serum-containing media.
3. Add 1 mL Trypsin/EDTA to cover cells and incubate at 37°C for 5–10 min.
4. Check under microscope to ensure that the cells have detached. Add 1 mL complete media to neutralize the action of trypsin.
5. Collect trypsinized cells into a centrifuge tube and centrifuge the cells at 300 g (1200 rpm) for 8 min.
6. Aspirate supernatant and resuspend pelleted cells in complete media.
7. The cells can now be divided into new tissue culture polystyrene flasks or dishes. The recommended dilution is 1:4 (mesenchymal stem cells) or 1:10 (fibroblasts).

Methods (freezing):

1. Before beginning, have all reagents cold (2–8°C) and label sterile cryovials with an indelible marker.
2. Make up 20% DMSO in FBS and filter sterilize with a 0.2 μm filter. Keep on ice.
3. Harvest cells from the tissue culture surface by using the passaging protocol described above. Centrifuge cells and resuspend in FBS at a concentration of 2×10^6 cells mL^{-1}. Place this cell suspension on ice.
4. Mix cells gently with 20% DMSO in FBS at a ratio of 1:1 (the final cell suspension will be 90% FBS/10% DMSO). Transfer 1 mL of cells in freezing media to each cryovial. The final cell concentration will be 10^6 cells per vial.
5. Place cryovials immediately into thawed 70% isopropanol freezing container ("Mr. Frosty"). Place container in −80°C freezer overnight. (Do not let cells sit in freezing media at room temperature. Keep on ice and transfer within 5 min to the freezing container.)
6. On the next day, remove frozen vials from the freezing container and store in liquid nitrogen.

ATP depletion

Materials:

1. Glucose-free DMEM (Invitrogen #11966-025)
2. 2-Deoxyglucose (Sigma #D8375-1G)
3. Sodium azide (Sigma #S2003-500G)
4. Ca^{2+}- and Mg^{2+}-free phosphate-buffered saline (PBS, Gibco #10010)

Methods:

1. Make 0.25% solution of sodium azide, use as diluent to make 250 mM solution of 2-deoxyglucose. This serves as a 5× depletion solution that can be refrigerated for at least one month.

[3]Reagent quantities are specified to treat a T-25 (25 cm^2 surface area) flask. For other culture vessels, scale quantities with surface area.

2. Dilute this solution 1:5 in glucose-free DMEM to make ATP depletion media.
3. Cells can be exposed to ATP depletion media either before or after substratum detachment. If before, wash cells with 5 mL PBS to remove residual complete media. Cells will assume a rounded appearance after several hours. If after, quench trypsin with complete media, centrifuge, and resuspend the pellet in ATP depletion media. Incubate for 30 min before performing optical stretching as described in App. C.2.

Light fixation for rheology measurements

Materials:

1. Complete media (App. C.1)
2. Ca^{2+}- and Mg^{2+}-free phosphate-buffered saline (PBS, Gibco #10010)
3. Trypsin (0.05%) / EDTA (1 mM) (Gibco #25300)
4. 25% glutaraldehyde (JT Baker #M752-07)

Methods:

1. Dilute glutaraldehyde to 0.2% in PBS.
2. Aspirate media and wash the cells with 5 mL PBS to remove residual complete media.
3. Add 1 mL Trypsin/EDTA to cover cells and incubate at 37°C for 5–10 min.
4. Check under microscope to ensure that the cells have detached. Add 4.75 mL complete media, transfer to a centrifuge tube, and incubate 1 hour to allow cells to remodel and adopt a spherical shape with reduced blebbing.
5. Add 0.25 mL of 0.2% glutaraldehyde (to achieve a concentration of 0.01%) and incubate for 10 min.
6. Dilute solution with at least 25 mL complete media and centrifuge the cells at 300 g (1200 rpm) for 8 min.
7. Resuspend in <1 mL complete media and perform optical stretching as described in App. C.2.

MSC osteogenic differentiation

Materials:

1. Mesencult Basal Medium (Stem Cell Technologies #05401, 450 mL).
2. Osteogenic Stimulatory Supplements (Stem Cell Technologies #05405, 80 mL) used at 15% final volume. Aliquot into 10×8 mL and store at −20°C.
3. β-glycerophosphate (Stem Cell Technologies #05406, 10 mL, 1 M), used at a final concentration of 3.5 mM. Aliquot into 10 × 1 mL vials and store at −20°C.
4. Dexamethasone (Stem Cell Technologies #05407, 1 mg), used at a final concentration of 10^{-8} M. Dissolve the powder in a small volume of absolute ethanol and then add ethanol to a final volume of 25.5 mL to make a stock concentration of 10^{-4} M. Aliquot into multiple 500 µL vials and store at −20°C.
5. Ascorbic acid (Stem Cell Technologies #07157, 100 mg), used at a final concentration of 50 $\mu g\,mL^{-1}$ (dissolve the powder in 10 mL of Mesencult MSC Basal Medium (Human) to obtain a stock solution of 10 $mg\,mL^{-1}$. Aliquot into 10 × 1 mL vials and store at −20°C.

Methods:

1. To prepare Complete Mesencult Osteogenic Medium, pipette 42.5 mL of Mesencult MSC Basal Medium into a 50 mL conical tube and add the following:
   (a) 7.5 mL Osteogenic Stimulatory Supplements
   (b) 5 μL dexamethasone (10^{-4} M stock solution)
   (c) 250 μL ascorbic acid (10 mg mL^{-1} stock solution)
   (d) 175 μL β-glycerophosphate (stock solution at 1.0 M) (Note: this component is not added to the complete media at initiation of the assay. Typically glycerophosphate is added only after there is evidence, by phase microscopy, of cell multilayering.)
2. Seed mesenchymal stem cells in tissue culture-treated flasks or plates at a concentration of $1–2\times10^5$ cells cm^{-2}.
3. Replenish the culture media after 5 days by removing the media (and non-adherent cells). These cells and the media can be discarded. Replenish cultures with fresh Complete Mesencult Osteogenic Medium, again without glycerophosphate unless cell multilayering has been noted. Multilayering is the layering of cells on top of each other, forming a matrix as opposed to growing in a planar manner. Multilayering is indicative of the beginning of bone generation.
4. Once multilayering has been observed, add glycerophosphate to Complete Mesencult Osteogenic Medium. Continue to replenish cultures with this complete media every 2–3 days.

C.2 Tools

Polyacrylamide (PAAm) gel fabrication[4]

Materials:

1. 40% acrylamide solution and 2% bis solution (Bio-Rad Labs #161-0140 and #161-0142)
2. 4-(2-hydroxyethyl)-1-piperazineethanesulfonic acid (HEPES, Sigma #H3537)
3. Ammonium persulfate (Bio-Rad Labs #161-0700)
4. Tetramethylethylenediamine (TEMED, Sigma #T22500)
5. Gluteraldehyde (JT Baker #M752-07)
6. Sodium hydroxide (Sigma #319511)
7. 3-aminopropyltriethoxysilane (APTES, Sigma #440140)
8. Glass slide
9. Polystyrene beads (Sigma #84135)
10. 1-ethyl-3-(3-dimethylaminopropyl)carbodiimide methiodide (EDC, Sigma #E6383)
11. Gelatin (Becton Dickinson #214340)

Methods (polymerization of >5 μm films):

1. Dispense 0.1 M NaOH on slide and let dry.
2. Dispense APTES on slide and incubate at room temperature for 5 min.
3. Wash with distilled water on shaker until surfaces are clear.
4. Remove from water, pipette 0.5% gluteraldehyde to cover, and incubate 30 min.

[4] Adapted from Wang et al. [119]

5. Wash with distilled water on shaker until surfaces are clear.
6. Mix acrylamide, bis, HEPES, and water in the following ratio: 625/325/50/4000 to produces a 1–10 kPa film.
7. Degas the solution for 20 min in dessicator attached to vacuum line.
8. Add 30 μL ammonium persulfate and 20 μL TEMED. Swirl.
9. Pipette acrylamide mixture onto activated glass surface (use 15 μL for a 75 μm thick gel); place a circular cover slip onto the droplet.
10. Allow acrylamide to polymerize for 30 min.
11. Cover the surface with ≈2 mL of 50 mM HEPES and remove cover slip.
12. Rinse the substrate with 50 mM HEPES.

Methods (polymerization of <5 μm films):

After adding TEMED and ammonium persulfate to activate the polymerization of the PAAm:

1. Have an activated cover slip ready with 2 μL of bead solution pipetted on the center of the surface (the bead solution should be ∼O(0.1%) solids in water).
2. Quickly pipette 2 μL of activated PAAm solution onto the cover slip and mix with the water bead solution using pipette tip (be sure to make the PAAm solution accounting for the dilution that will take place during this step).
3. Place another cover slip on top of the activated cover slip with PAAm solution.
4. Take this cover slip/liquid/cover slip sandwich and place onto a glass slide on the edge of the counter; place another glass slide on top of this.
5. Using a C-clamp, clamp the sandwich of glass slides down onto the counter and make sure that the PAAm solution is spreading across the cover slip (be sure not to clamp down hard enough to break the glass, and also attempt to keep the glass slides and cover slips from rotating relative to each other).
6. Let polymerize for 30 min, then unclamp and remove excess slides and cover slips very carefully.

Methods (gelatin adsorption):

1. Remove EDC from −20°C fridge and let warm to room temp to avoid condensation upon opening.
2. Make solution of 1 mg mL^{-1} gelatin in PBS, warming PBS in microwave to assist gelatin dissolution if necessary.
3. When ready to functionalize gel, add EDC to the solution at a concentration of 52 mM. Mix well and cover gel surface within 20 min of adding EDC to the PBS-gelatin solution.
4. Incubate for 2 hours.
5. Rinse gently with distilled water several times.
6. Store in 50 mM HEPES in 4°C fridge.

As shown in Fig. C-1, gelatin adsorption results in an undetectable thickness increase as measured by atomic force microscopy (AFM) profiling over fresh scratches in polyacrylamide gels of nominal 3 μm thickness and similar formulation (8% acrylamide) to that used in cell culture experiments (5% acrylamide). Store gels in 50 mM HEPES buffer at 4°C.

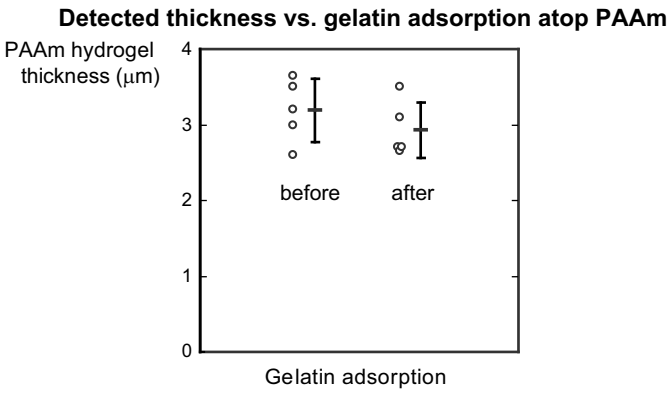

Figure C-1: Gelatin adsorption atop controlled-thickness polyacrylamide results in no detectable thickness change, as measured by AFM profiling (mean ± standard deviation).

Optical stretching[5]

Materials:

1. Complete media
2. Trypsin (0.05%) / EDTA (1 mM) (Gibco #25300)
3. Phosphate-buffered saline (PBS, Gibco #10010)
4. Two 1 mL syringes (A and B)
5. Three 1 mL cryovials (C, D, and E)
6. At least 10K cells in culture, ideally >50K

Methods (preparation):

1. Warm the trypsin/EDTA and complete media in 37°C heat bath.
2. Open "Stretcher" LabView program and configure flask settings: file directory for saved data, round and flask number, cell and media type, passage number, and cell count.
3. Aspirate the media from the cells, and wash gently with 5 mL PBS. Aspirate PBS.
4. Trypsinize the cells as described earlier. While the cells are detaching, draw 1 mL of complete media into each of the 1 mL syringes (A and B). Carefully remove all air bubbles in each syringe by flicking each syringe sharply.
5. Attach the Luer tip (syringe socket) to the tubing of the optical stretcher and flush the tubing with complete media from syringe A, taking care to ensure that air bubbles are not left in the tubing. Use the red valve to change flush directions, and be certain that both the reservoir and syringe terminals are flushed thoroughly.
6. Place 200–500 μL of complete media each in cryovials C and D and replace caps with perforated caps; these cryovials will serve as reservoirs.
7. Remove cells from incubation and inspect under microscope to ensure that cells have detached. Deactivate trypsin with 1 mL of warmed complete media, transfer the solution to a centrifuge tube, and centrifuge at 1200 rpm for 8 min.
8. While the centrifuge is running, check that syringe B has no air bubbles, and expel all of the excess media until only the tip of the syringe contains fluid only.
9. Aspirate the supernatent and resuspend the cells with complete media such that the final concentration is between 100K–300K cells mL^{-1}.

[5] Protocol developed with Franziska Lautenschläger, Kyle Bryson, and Eric Lehnhardt.

10. Use the micropipettor to slowly agitate the solution (by pipetting and expelling solution) to break apart cellular clumps, taking care not to introduce air bubbles into the suspension.
11. Transfer the cells to cryovial E, taking care not to introduce any air bubbles. Draw up the solution from the cryovial into syringe B.
12. Attach syringe B to the interface socket on the rotator, and inject 20 μL of the suspension into the tubing. Begin rotation of the syringe to keep cells from settling.

Methods (stretching):

1. By raising and lowering the downstream reservoir, isolate a single cell in the area of the laser axis.
2. Trap the cell, and, carefully noting the boundaries for capturing frames, stretch the cell. Record the cell number and note any rotations or other errant behaviors that might skew edge detection data.
3. Continue to isolate and stretch individual cells. Inject additional 10–20 μL of cell suspension as needed when cell density is depleted.
4. After completing a stretching experiment, flush the tubing with 10% bleach by using the rinsing steps outlined above. Leave the tubing filled with 10% bleach and terminated by the 10% bleach syringe and fresh reservoirs filled with 10% bleach

Methods (edge detection):

1. Use edge detection software to quantify the displacement of the edges of the cell. Adjust contrast, brightness, filter, etc. settings to ensure a good fit.
2. Watch the processing of each individual cell, making note of rotations, blebbing, or other interference that would invalidate the data.
3. Record the cells that pass edge detection analysis, and separate out those that do not from further data analysis.
4. Run the ellipse to data program, or equivalent, to convert the fitted edge data to quantified waveform data.
5. If the data collected included cyclical waveforms, analysis of signal to noise ratio may be performed to determine the precision of data.

Methods (subsequent data analysis):

Log-normal parameters can be fit by several approaches, including the method of moments [275]

$$\hat{\mu} = 2\ln\left(\frac{1}{n}\sum_i^n x_i\right) - \frac{1}{2}\ln\left(\frac{1}{n}\sum_i^n x_i^2\right) \tag{C.1a}$$

$$\hat{\sigma} = \sqrt{\ln\left(\frac{1}{n}\sum_i^n x_i^2\right) - 2\ln\left(\frac{1}{n}\sum_i^n x_i\right)}, \tag{C.1b}$$

the maximum likelihood estimators

$$\hat{\mu} = \frac{1}{n}\sum_i^n \ln x_i \qquad \hat{\sigma} = \sqrt{\frac{1}{n}\sum_i^n \left[\ln(x_i) - \hat{\mu}\right]^2}, \tag{C.2}$$

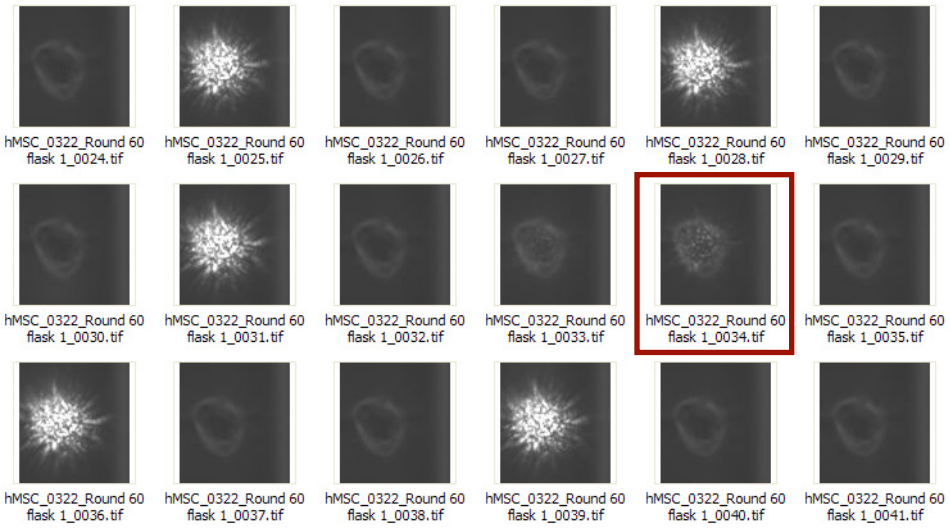

Figure C-2: Images recorded (without an infrared filter) during brief infrared laser illumination of a suspended cell enable precise timing of laser control and photography. A dimmer image of an irradiated cell indicates that the 5 ms laser pulse is synchronized with a brief pause separating frames.

and nonlinear regression fitting of the log-normal cumulative distribution function to the actual cumulative distribution, where the uniform statistic medians are calculated by by Filliben's method [276]:

$$m_i = \begin{cases} 1 - m_n & (i = 1) \\ (i - 0.3175)/(n + 0.365) & (i = 2, 3, \ldots, n-1) \\ 2^{-1/n} & (i = n). \end{cases} \tag{C.3}$$

The estimation methods are compared in Fig. C-4.

When extracting a phase lag from the signal acquired from edge detection of phase contrast images, it is essential to account for systematic delays caused by communication between the LabView operating software and the data acquisition (DAQ) card, the DAQ card and the laser; and the camera and the Firewire port. The characteristic time delay of the system can be determined by using the method shown in Fig. C-2, which shows brief (<5 μs) laser pulses being acquired in successive camera frames. (The infrared-blocking filter normally attached to the camera has been removed for this procedure.) Synchronization with camera pulses is indicated by the splitting of pulses between two frames or by part of the pulse occurring the interval between frame collection. The system delay was found to be 41 ms by this method.

Interpolation was used to apply uniform time measurements to deformability data that was originally time-stamped with values returned when the frame recorded. For example, the (time, deformability) data (2.87, 2.01), (2.95, 2.07), (3.03, 2.14) was transformed into (2.90, 2.019), (2.95, 2.06), (3.00, 2.09), (3.05, 2.13). A comparison of the average deformability of 704 cells before and after transformation is shown in Fig. C-5.

Photonic stress σ_0 on the cell was calculated as [170, 180]

$$\sigma_0 = \frac{4P(n_{\text{cell}} - n_{\text{med}})}{c\pi w_{\text{beam}}^2 n_{\text{med}}}, \tag{C.4a}$$

$$w_{\text{beam}} = w_{\text{core}} \sqrt{1 + \frac{B^2}{z_0^2}}, \tag{C.4b}$$

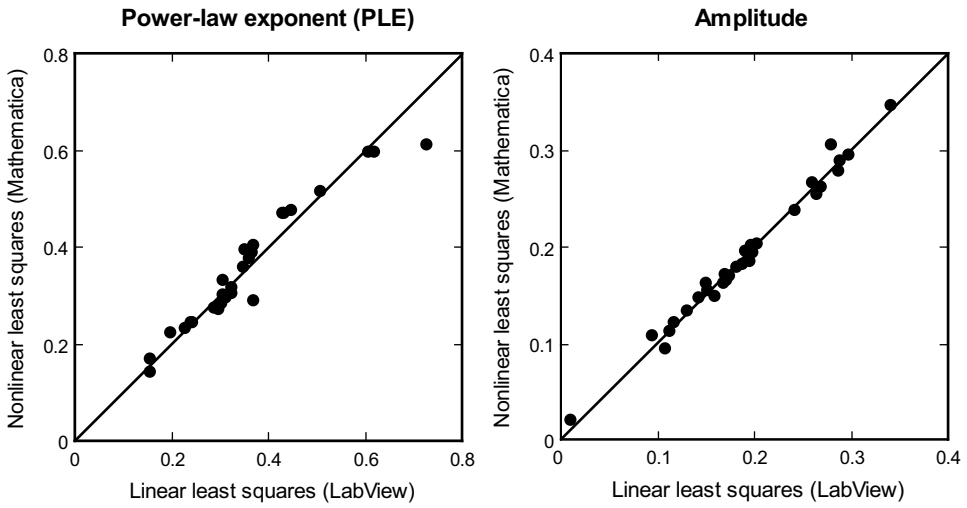

Figure C-3: There is good agreement between nonlinear and linear regression approaches for extracting the phase angle of oscillatory cell deformation. Subroutines programmed into the software packages Mathematica and Labview gave comparable results.

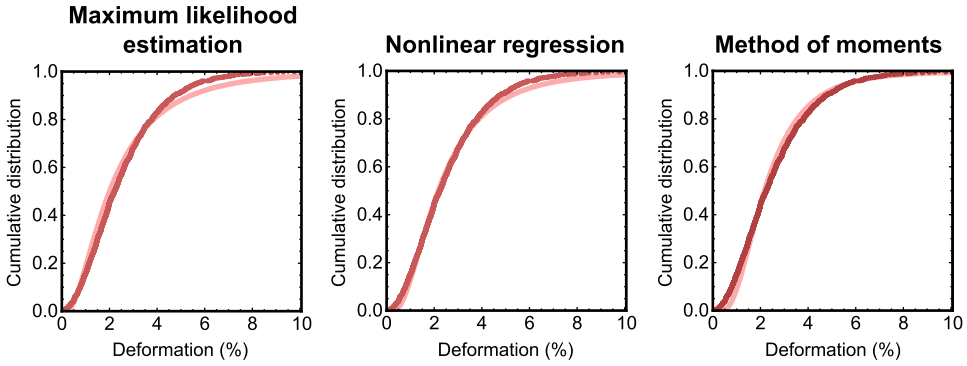

Figure C-4: There is good agreement between multiple techniques for estimating parameters of a log-normal distribution.

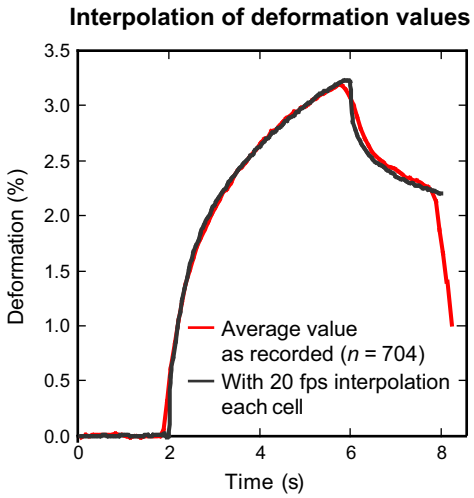

Figure C-5: Interpolation of deformability values for individual cells to 20 fps (from original ≈12–15 fps recordings) reduces undesirable smoothing of the average deformability near sudden changes and enables better comparisons of data sets.

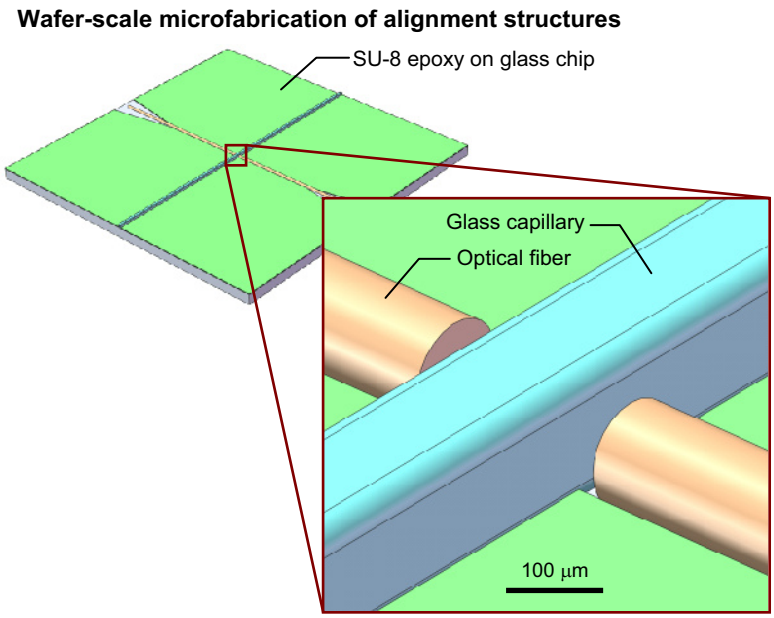

Figure C-6: Microfabricated SU-8 epoxy patterns produced at a wafer level provide multiple chips for orthogonal alignment of optical fibers and a glass capillary in the optical stretcher.

$$B = n_{\text{gel}} \left(\frac{z_{\text{med}}}{n_{\text{med}}} + \frac{z_{\text{glass}}}{n_{\text{glass}}} \right) + z_{\text{gel}}, \tag{C.4c}$$

$$z_0 = \frac{w_{\text{core}}^2 \pi n_{\text{gel}}}{\lambda}, \tag{C.4d}$$

where P is the total applied power; $n_{\text{cell}} = 1.372$, $n_{\text{med}} = 1.335$, and $n_{\text{gel}} = 1.449$ are the cell, medium, and gel refractive indices, respectively; w_{core} is 3.1 μm for the fibers used here; c is the speed of light, and $\lambda = 1064$ nm is the laser wavelength.

Wafer-scale microfabrication of alignment structures

Materials:

1. 4-inch Pyrex wafers
2. Piranha solution (a 3:1 mixture of concentrated sulfuric acid and 30% hydrogen peroxide)
3. SU-8 2035 (Microchem)

Methods:[6]

1. Clean wafers in piranha solution; rinse, spin dry, and dehydrate on a 200°C hot plate for at least 5 min.
2. Spin SU-8 on wafer at 3000 rpm to achieve 35 μm thickness. (Ramp to 500 rpm at an acceleration of 100 rpm s^{-1} and hold at this speed for 5–10 s to allow the resist to cover the entire surface; then ramp to final spin speed at an acceleration of 300 rpm s^{-1} and hold for a total of 30 s.)
3. Soft bake for 2 min on a 65°C hot plate followed by 5 min on a 95°C hot plate.
4. Expose to at least 0.4 J cm^{-2} (e.g., >40 s at 10 mW cm^{-2}) on an i-line (365 nm) aligner.

[6] Adapted from the Microchem SU-8 2000 series protocol.

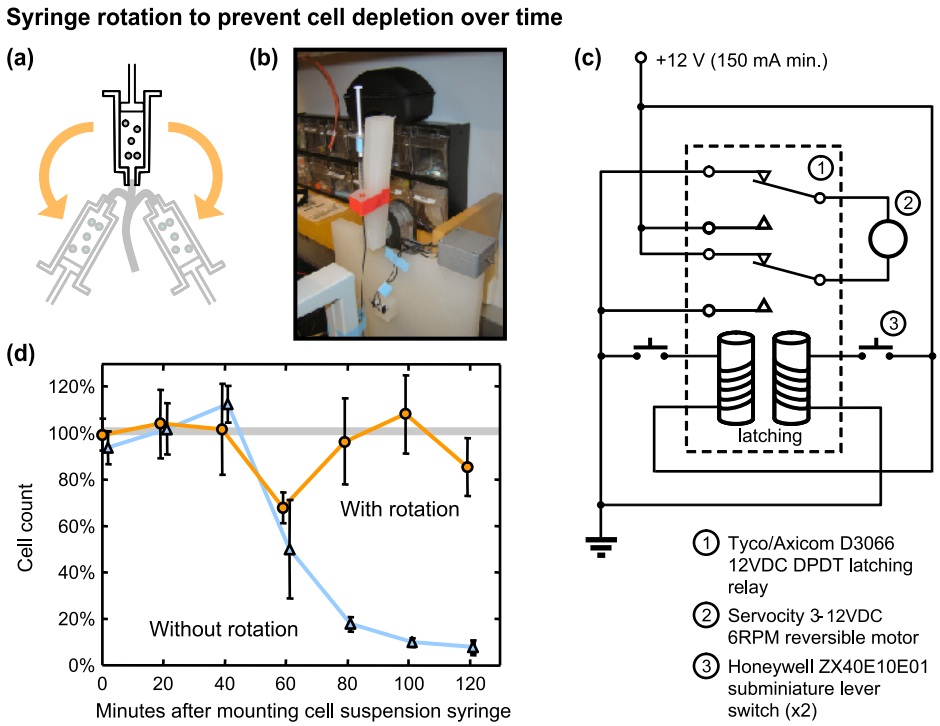

Figure C-7: Syringe rotation prevents settling of relatively heavy adherent cells during multi-hour optical stretching experiments. A syringe containing the cell suspension is attached to a customized 6 rpm syringe rotator ((a) schematic and (b) photograph) to prevent cell settling. (c) Circuit diagram. (d) Syringe rotation ensures cell availability during 2 h stretching experiments; without rotation, the syringe becomes depleted of suspended cells within approximately 1 h.

5. Post-exposure bake for 1 min on a 65°C hot plate followed by 3 min on a 95°C hot plate, and allow wafer to cool slowly to 65°C or less to avoid cracking.
6. Develop for at least 5 min in propylene glycol monomethyl ether acetate (PGMEA) and rinse with isopropyl alcohol.
7. Dice at 15 mm pitch and mount fibers and capillary (Fig. C-6).

Syringe rotation

A circuit was designed and constructed to rotate a syringe at 6 rpm via a motor triggered to reverse direction by limit switches (Fig. C-7). Motorized syringe rotation counteracted cell sinking in the input syringe over time and enabled experiments to proceed for longer times and with an increased number of cells analyzed per experiment. Portions of the cell suspension are typically injected from the syringe multiple times per hour to resupply cells into the capillary. Without syringe rotation, cell sinking (at a terminal speed estimated to be 10 μm s for hMSCs) resulted in few to no cells available after several tens of minutes due to syringe depletion. When using syringe rotation, however, the density of cells available for injection through the capillary to the trap was relatively unaffected over a 2 h experiment.

C.3 Assays

Fluorescent staining[7]

Materials:

1. Chemicon/Millipore FAK100 focal adhesion staining kit (vinculin monoclonal antibody, TRITC-conjugated phalloidin, DAPI)
2. 16% paraformaldehyde (Alfa Aesar #43368)
3. 0.1% Triton X-100 (Fluka #93443)
4. Blocking solution (1% BSA in 1× PBS) (Sigma #A7906)
5. Fluorescent-labeled anti-mouse secondary antibody (e.g., CHEMICONR #AP124F)
6. 1× wash buffer (e.g. 1× PBS containing 0.05% Tween-20) (Teknova #P1176)
7. Antifade mounting solution (e.g., Prolong Gold)
8. Glass slides and coverslips

Methods:

1. Passage cells and culture in suitable media until approximately 50–60% confluent.
2. Fix cultured cells with 4% paraformaldehyde in PBS for 15–20 min at room temperature.
3. Wash twice with 1× wash buffer.
4. Permeabilize cells with 0.1% Triton X-100 in 1× PBS for 1–5 min at room temperature.
5. Wash twice with 1× wash buffer.
6. Apply blocking solution for 30 min at room temperature.
7. Dilute primary antibody (anti-vinculin) to a working concentration in blocking solution, and incubate for 1 hour at room temperature.
8. Wash three times (5–10 min each) with 1× wash buffer.
9. Dilute secondary antibody (Gt × Ms, FITC-conjugated, for example CHEMICONR Cat. No. AP124F) in 1x PBS just before use and incubate for 30–60 min at room temperature. For double labeling 1:2,000 TRITC-conjugated Phalloidin can be incubated simultaneously with the secondary antibody for 30–60 min at room temperature.
10. Wash three times (5–10 min each) with 1× wash buffer.
11. Following this washing step, nuclei counterstaining can be performed by incubating cells with 1:5,000 DAPI for 1–5 min at room temperature, followed by washing cells three times (5–10 min each) with 1× wash buffer.
12. If immunocytochemistry was performed on a 24-well plate, cells should be covered with 1× PBS prior to visualization to prevent cells from drying out. However, if cells are stained on a coverslip it can be mounted on a slide by using Universal Mount (Gibco) or ProLong Gold.
13. Fluorescence images can be visualized with a fluorescence microscope (IX-81, Olympus).

[7] Adapted from the Chemicon/Millipore FAK100 Staining Kit manual.

Luciferase assay for quantifying ATP depletion[8]

Materials:

1. Glucose-free DMEM (Invitrogen #11966-025)
2. Complete media (App. C.1)
3. 2-deoxyglucose (Sigma #D8375-1G)
4. Sodium azide (Sigma #S2003-500G)
5. Trypsin (0.05%) / EDTA (1 mM) (Gibco #25300)
6. Phosphate-buffered saline (PBS) (Gibco #10010)
7. Xylenol blue (Santa Cruz Biotechnology #E3111)
8. Tris-acetate / EDTA (Sigma #93296)
9. Trichloroacetic acid (Sigma #T0199)
10. Two 1 mL cryovials
11. Two 1 mL syringes
12. 96-well, clear-bottomed, white plastic luminescence plate
13. Cellular sample of interest (e.g. two flasks of 80% confluent cells)
14. Enliten Assay System (Promega #FF2000):
    (a) rL/L reagant
    (b) Reconstitution buffer
    (c) ATP standard (10^{-7} M)
    (d) ATP-free water

Methods (solution preparation):

1. Prepare 1.0% (weight-by-volume) of trichloroacetic acid in sterile, ATP-free, Millipore water. One mL will be needed for each sample ($\approx$ 10 mL per run). Add a minimal amount of xylenol blue dye such that the solution is visibly pink in color. Store in sterile environment until needed.
2. Prepare pH 7.75 buffer or tris-acetate/EDTA in sterile, ATP-free, Millipore water. Using a calibrated pH probe, add tris-acetate/EDTA with stirring until pH increases to 7.75. For 50 mL, less than 1 g should be necessary. Store in sterile environment until needed.
3. Prepare ATP depletion "cocktail" from serum- and glucose-free DMEM, with 0.05% sodium azide and 50 mM deoxyglucose.
4. Prepare ATP standards from standard solution and buffer/acid extractant solution. Dilution solution should be at pH 7.75, made from approximately 1 mL trichloracetic acid solution and 9.5 mL tris-acetate/EDTA buffer. By serial dilution, prepare standards that range from 10^{-11} M to 10^{-16} M.
5. Reconstitute the rL/L luminescent reagant from the reagant and reconstitution buffer provided in the Enliten Assay system: In light-free conditions, add the buffer to the lyophilized reagent, and swirl to mix. Freeze 1 mL aliquots of the reconstituted buffer at $-20°$C; aliquots may be used for up to two weeks.

Methods (sample preparation):

1. Wash two T-25 flasks of same-passage NIH 3T3 fibroblasts (or other desired cell type) with 5 mL of PBS, and aspirate the PBS.

[8] Courtesy of Eric Lehnhardt, adapted from Promega Enliten ATP assay kit instructions.

2. Trypsinize the cells for 5–8 min at 37°C in 5% CO_2 with 1 mL each of trypsin/EDTA solution.
3. Prepare two 1 mL syringes, one with ATP depletion media, and the other with 3T3 complete media, as described in the optical stretching methods.
4. Neutralize trypsin action with 1 mL each of complete 3T3 media, and centrifuge each sample for 8 min at 1200 rpm in 15 mL falcon tubes.
5. Aspirate the solution and resuspend the cell pellets in either 500 μL of warmed 3T3 complete media, or 500 μL of ATP depletion media. The complete media sample is now the control; label appropriately.
6. Transfer the ATP depletion and control samples to their respective syringes (by way of cryovial, as described in the optical stretching protocols). Incubate 60 min at room temperature while using the rotator to ensure that cells remain in the suspended state.
7. Thaw, to room temperature, three aliquots of the reconstituted rL/L reagent in light-free conditions. Allow to sit at room temp for an hour to incubate.
8. Transfer control and depletion cells to falcon tubes, and centrifuge 8 min at 1200 rpm.
9. Aspirate media from control and depletion tubes, and then resuspend both samples in 1 mL of trichloroacetic acid lysis buffer, and mix using the micropipettor. Rock gently for 10 min at room temperature.
10. Titrate the control and depletion samples to pH 7.75, using approximately 9.5 mL of the tris-acetate buffer. The xylenol blue dye should be yellow in the solution; check with pH probe as needed.

Methods (plating and analysis):

1. In light-free conditions, plate the ATP standards (thaw to room temperature) in triplicate. Use 10 μL per well. Include one standard that is just the extractant/buffer.
2. Plate the samples (control and depletion) in triplicate each (six wells total) with 10 μL of sample.
3. Add 100 μL of reconstituted and thawed (to room temp) rL/L agent to each well (110 μL total volume per well).
4. Read plate with luminometer, using a 10-second integration time, bottom-read, and checking for all wavelengths.
5. To remove the noise baseline, average together the values from all the blank wells, and subtract that value from each well that contained sample or standard. Adjust for background ATP noise using the extractant/buffer wells as needed.
6. Establish a calibration curve from the standards, and determine the total amount of ATP in each sample, as well as the percent depletion.

Alkaline phosphatase expression assay for quantifying osteogenesis[9]

Materials:

1. Lysis buffer (0.2% NP-40 in 1 mM $MgCl_2$):
   (a) 0.10165 g $MgCl_2$ (Sigma #208337)
   (b) 1 mL NP-40 (Fluka #56741)
   (c) 500 mL water

[9] Courtesy of Manu Platt.

2. Phosphatase substrate:
   (a) 100 mg capsule (p-nitrophenyl phosphate, disodium) (Sigma #P5744, contents only)
   (b) 25 mL water
3. Sodium hydroxide solutions:
   (a) Beaker 1 (1 M): 1 mL of 10 M into 9 mL of water
   (b) Beaker 2 (0.02 M): 2 mL of 1 M into 98 mL of water
4. Diluted p-nitrophenol standard solution (50 μM):
   (a) 0.5 mL of 10 mM p-nitrophenol (Sigma #N7660)
   (b) 100 mL of 0.02 M sodium hydroxide solution (beaker 2)
5. 221 alkaline buffer solution (Sigma #A9226) (2-amino-2-methyl-1-propanol, 1.5 M, pH 10.3 at 25°C)

Methods:

1. Prepare the following standards:

Tube #	Diluted p-nitrophenol solution (mL)	0.02 M NaOH (mL)	Alkaline phosphatase activity (Sigma units mL^{-1})
0 (Blank)	0.0	1.1	0
1	0.1	1.0	1
2	0.2	0.9	2
3	0.4	0.7	4
4	0.6	0.5	6
5	0.8	0.3	8
6	1.0	0.1	10

2. Cells are to be rinsed twice with PBS and scraped into lysis buffer with a rubber policeman and sonicate for 10 s (with probe sonicator or about one minute with water bath sonicator): 24-well, 200 μL of lysis buffer; T-25 flask, 2.63 mL of lysis buffer; T-75 plate, 7.90 mL of lysis buffer.
3. Dilute samples 1:10 (5 μL in 45 μL lysis buffer).
4. Take 10–20 μL of the lysate for each sample, add into 1.5 mL tubes, and q.s. to 200 μL with lysis buffer.
5. Make BLANK by adding 200 μL of lysis buffer to BLANK 1.5 mL tube.
6. Add 1 mL of 221 alkaline buffer solution and stock substrate solution (1:1) (500 μL of 221 alkaline buffer solution, 500 μL of stock substrate solution).
7. Incubate for 30 min at 37°C. The yellow color is indicative of alkaline phosphatase activity.
8. Add 12 μL of 1 M NaOH (beaker 1) to each sample and the BLANK to stop the reaction.
9. Measure absorbance at 405 nm (calibrate to BLANK).

Normalize the results to total protein content, measured as described in the next section.

BCA assay for quantifying total protein content[10]

Materials:

1. BCA Protein Assay Kit, including albumin standard (Pierce #23225)

Methods:

1. Make 1 mL diluted lysis buffer (DLB, 1:10 dilution)
2. Make diluted albumin standard (diluted BSA, 50 $\mu g\,mL^{-1}$):
   (a) 13 µL albumin stock
   (b) 507 µL water
3. Set up standards in 96-well plate:

Well	$\mu g\,mL^{-1}$	Water (µL)	Diluted BSA (µL)	DLB (µL)
1	BLANK	90	0	10
2	2	86	4	10
3	4	82	8	10
4	8	74	16	10
5	12	66	24	10
6	16	58	32	10
7	20	50	40	10
8	25	40	50	10
9	30	30	60	10

4. Prepare dilution of unknowns in separate 96-well plate or in tubes:

	Diluent (µL)	Sample (µL)	Final dilution
#1	45 water	5 of lysate	100
#2	40 DLB	10 of #1	500
#3	45 DLB	5 of #1	1000

   Dilution #1 can be made at the time of lysis and frozen or made from a small aliquot of lysate at time of BCA assay.
5. Add 90 µL of water to wells for samples.
6. Transfer 10 µL of each sample dilution to corresponding well on measurement plate.
7. Add BCA Cocktail. Make 6 mL for each 1/2 plate to measure. (3 mL A, 2.88 mL B, 120 µL C). Add 100 µL to each well.
8. Cover and incubate for 1 hour at 37°C.
9. Measure absorbance at 562 nm.

[10] Courtesy of Pam Kreeger and Manu Platt, adapted from BCA Protein Assay Kit protocol. Designed for lysates with protein concentration >2 $mg\,mL^{-1}$.

Bibliography

[1] J. Maloney, E. Walton, C. Bruce, and K. Van Vliet, "Influence of finite thickness and stiffness on cellular adhesion-induced deformation of compliant substrata," *Physical Review E*, vol. 78, no. 4, p. 41923, 2008.

[2] R. Krishnan, B. Oommen, E. Walton, J. Maloney, and K. Van Vliet, "Modeling and simulation of chemomechanics at the cell-matrix interface," *Cell Adhesion & Migration*, vol. 2, no. 2, pp. 13–24, 2008.

[3] S. Lee, A. Zeiger, J. Maloney, M. Kotecki, K. Vliet, and I. Herman, "Pericyte actomyosin-mediated contraction at the cell–material interface can modulate the microvascular niche," *Journal of Physics: Condensed Matter*, vol. 22, p. 194115, 2010.

[4] J. Maloney, D. Nikova, F. Lautenschläger, R. Langer, J. Guck, and K. Van Vliet, "Mesenchymal stem cell mechanics from the attached to the suspended state," *Biophysical Journal*, vol. 99, no. 8, pp. 2479–2487, 2010.

[5] K. Van Vliet, "Chemomechanics of complex materials: challenges and opportunities in predictive kinetic timescales," *Scientific Modeling and Simulations*, vol. 15, no. 1–3, pp. 67–80, 2009.

[6] S. Lee, J. Mandic, and K. Van Vliet, "Chemomechanical mapping of ligand–receptor binding kinetics on cells," *Proceedings of the National Academy of Sciences*, vol. 104, no. 23, pp. 9609–9614, 2007.

[7] I. Chen, O. Kuksenok, V. Yashin, R. Moslin, A. Balazs, and K. Van Vliet, "Shape-and size-dependent patterns in self-oscillating polymer gels," *Soft Matter*, 2011.

[8] C. Izzard and L. Lochner, "Cell-to-substrate contacts in living fibroblasts: an interference reflexion study with an evaluation of the technique," *Journal of Cell Science*, vol. 21, no. 1, pp. 129–59, 1976.

[9] K. Burridge, K. Fath, T. Kelly, G. Nuckolls, and C. Turner, "Focal adhesions: transmembrane junctions between the extracellular matrix and the cytoskeleton," *Annual Reviews in Cell Biology*, vol. 4, no. 1, pp. 487–525, 1988.

[10] P. Kanchanawong, G. Shtengel, A. Pasapera, E. Ramko, M. Davidson, H. Hess, and C. Waterman, "Nanoscale architecture of integrin-based cell adhesions," *Nature*, vol. 468, no. 7323, pp. 580–584, 2010.

[11] S. Mitra, D. Hanson, and D. Schlaepfer, "Focal adhesion kinase: in command and control of cell motility," *Nature Reviews Molecular Cell Biology*, vol. 6, no. 1, pp. 56–68, 2005.

[12] L. Moran, K. Scrimgeour, H. Horton, R. Ochs, and J. Rawn, *Biochemistry*. Neil Patterson Publishers-Prentice Hall: Englewood Cliffs, NJ, 1994.

[13] D. Docheva, D. Padula, C. Popov, W. Mutschler, H. Clausen-Schaumann, and M. Schieker, "Researching into the cellular shape, volume and elasticity of mesenchymal stem cells, osteoblasts and osteosarcoma cells by atomic force microscopy," *Journal of Cellular and Molecular Medicine*, vol. 12, no. 2, pp. 537–552, 2008.

[14] B. Geiger and A. Bershadsky, "Assembly and mechanosensory function of focal contacts," *Current Opinion in Cell Biology*, vol. 13, no. 5, pp. 584–592, 2001.

[15] N. Balaban, U. Schwarz, D. Riveline, P. Goichberg, G. Tzur, I. Sabanay, D. Mahalu, S. Safran, A. Bershadsky, L. Addadi, and B. Geiger, "Force and focal adhesion assembly: a close relationship studied using elastic micropatterned substrates," *Nature Cell Biology*, vol. 3, no. 5, pp. 466–472, 2001.

[16] D. Choquet, D. Felsenfeld, and M. Sheetz, "Extracellular matrix rigidity causes strengthening of integrin-cytoskeleton linkages," *Cell*, vol. 88, no. 1, pp. 39–48, 1997.

[17] R. Pelham Jr and Y. Wang, "Cell locomotion and focal adhesions are regulated by substrate flexibility," *Proceedings of the National Academy of Sciences*, vol. 94, no. 25, pp. 13661–13665, 1997.

[18] D. Discher, P. Janmey, and Y. Wang, "Tissue cells feel and respond to the stiffness of their substrate," *Science*, vol. 310, no. 5751, pp. 1139–1143, 2005.

[19] S. Peyton, C. Ghajar, C. Khatiwala, and A. Putnam, "The emergence of ECM mechanics and cytoskeletal tension as important regulators of cell function," *Cell Biochemistry and Biophysics*, vol. 47, no. 2, pp. 300–320, 2007.

[20] A. Engler, L. Bacakova, C. Newman, A. Hategan, M. Griffin, and D. Discher, "Substrate compliance versus ligand density in cell on gel responses," *Biophysical Journal*, vol. 86, no. 1, pp. 617–628, 2004.

[21] S. Peyton, C. Raub, V. Keschrumrus, and A. Putnam, "The use of poly(ethylene glycol) hydrogels to investigate the impact of ECM chemistry and mechanics on smooth muscle cells," *Biomaterials*, vol. 27, no. 28, pp. 4881–4893, 2006.

[22] A. Engler, S. Sen, H. Sweeney, and D. Discher, "Matrix elasticity directs stem cell lineage specification," *Cell*, vol. 126, no. 4, pp. 677–689, 2006.

[23] J. Goffin, P. Pittet, G. Csucs, J. Lussi, J. Meister, and B. Hinz, "Focal adhesion size controls tension-dependent recruitment of α-smooth muscle actin to stress fibers," *The Journal of Cell Biology*, vol. 172, no. 2, pp. 259–268, 2006.

[24] J. Winer, P. Janmey, M. McCormick, and M. Funaki, "Bone marrow-derived human mesenchymal stem cells become quiescent on soft substrates but remain responsive to chemical or mechanical stimuli," *Tissue Engineering Part A*, vol. 15, no. 1, pp. 147–154, 2008.

[25] J. Meredith Jr, B. Fazeli, and M. Schwartz, "The extracellular matrix as a cell survival factor," *Molecular Biology of the Cell*, vol. 4, no. 9, pp. 953–961, 1993.

[26] B. Fabry, G. Maksym, J. Butler, M. Glogauer, D. Navajas, and J. Fredberg, "Scaling the microrheology of living cells," *Physical Review Letters*, vol. 87, no. 14, p. 148102, 2001.

[27] E. Koay, A. Shieh, and K. Athanasiou, "Creep indentation of single cells," *Journal of Biomechanical Engineering*, vol. 125, no. 3, pp. 334–341, 2003.

[28] D. Stamenović, B. Suki, B. Fabry, N. Wang, J. Fredberg, and J. Buy, "Rheology of airway smooth muscle cells is associated with cytoskeletal contractile stress," *Journal of Applied Physiology*, vol. 96, no. 5, pp. 1600–1605, 2004.

[29] M. Balland, N. Desprat, D. Icard, S. Féréol, A. Asnacios, J. Browaeys, S. Hénon, and F. Gallet, "Power laws in microrheology experiments on living cells: Comparative analysis and modeling," *Physical Review E*, vol. 74, no. 2, p. 21911, 2006.

[30] S. Tan, W. Pan, G. Ma, N. Cai, K. Leong, and K. Liao, "Viscoelastic behaviour of human mesenchymal stem cells," *BMC Cell Biology*, vol. 9, no. 1, p. 40, 2008.

[31] K. Kasza, A. Rowat, J. Liu, T. Angelini, C. Brangwynne, G. Koenderink, and D. Weitz, "The cell as a material," *Current Opinion in Cell Biology*, vol. 19, no. 1, pp. 101–107, 2007.

[32] N. Petersen, W. McConnaughey, and E. Elson, "Dependence of locally measured cellular deformability on position on the cell, temperature, and cytochalasin B," *Proceedings of the National Academy of Sciences*, vol. 79, no. 17, pp. 5327–5331, 1982.

[33] C. Rotsch and M. Radmacher, "Drug-induced changes of cytoskeletal structure and mechanics in fibroblasts: an atomic force microscopy study," *Biophysical Journal*, vol. 78, no. 1, pp. 520–535, 2000.

[34] J. Guck, R. Ananthakrishnan, H. Mahmood, T. Moon, C. Cunningham, and J. Käs, "The optical stretcher: a novel laser tool to micromanipulate cells," *Biophysical Journal*, vol. 81, no. 2, pp. 767–784, 2001.

[35] J. Guck, S. Schinkinger, B. Lincoln, F. Wottawah, S. Ebert, M. Romeyke, D. Lenz, H. Erickson, R. Ananthakrishnan, D. Mitchell, *et al.*, "Optical deformability as an inherent cell marker for testing malignant transformation and metastatic competence," *Biophysical Journal*, vol. 88, no. 5, pp. 3689–3698, 2005.

[36] M. Tsai, R. Waugh, and P. Keng, "Passive mechanical behavior of human neutrophils: effects of colchicine and paclitaxel," *Biophysical Journal*, vol. 74, no. 6, pp. 3282–3291, 1998.

[37] N. Wang and D. Stamenović, "Contribution of intermediate filaments to cell stiffness, stiffening, and growth," *American Journal of Physiology - Cell Physiology*, vol. 279, no. 1, pp. C188–C194, 2000.

[38] F. Wottawah, S. Schinkinger, B. Lincoln, R. Ananthakrishnan, M. Romeyke, J. Guck, and J. Käs, "Optical rheology of biological cells," *Physical Review Letters*, vol. 94, no. 9, p. 98103, 2005.

[39] F. Lautenschläger, S. Paschke, S. Schinkinger, A. Bruel, M. Beil, and J. Guck, "The regulatory role of cell mechanics for migration of differentiating myeloid cells," *Proceedings of the National Academy of Sciences*, vol. 106, no. 37, p. 15696, 2009.

[40] X. Trepat, G. Lenormand, and J. Fredberg, "Universality in cell mechanics," *Soft Matter*, vol. 4, no. 9, pp. 1750–1759, 2008.

[41] B. Hoffman and J. Crocker, "Cell mechanics: dissecting the physical responses of cells to force," *Annual Review of Biomedical Engineering*, vol. 11, pp. 259–288, 2009.

[42] G. Lenormand, E. Millet, B. Fabry, J. Butler, and J. Fredberg, "Linearity and time-scale invariance of the creep function in living cells," *Journal of The Royal Society Interface*, vol. 1, no. 1, pp. 91–97, 2004.

[43] M. Puig-de Morales, E. Millet, B. Fabry, D. Navajas, N. Wang, J. Butler, and J. Fredberg, "Cytoskeletal mechanics in the adherent human airway smooth muscle cell: probe specificity and scaling

of protein-protein dynamics," *American Journal of Physiology - Cell Physiology*, vol. 287, no. 3, pp. C643–C654, 2004.

[44] G. Massiera, K. Van Citters, P. Biancaniello, and J. Crocker, "Mechanics of single cells: rheology, time dependence, and fluctuations," *Biophysical Journal*, vol. 93, no. 10, pp. 3703–3713, 2007.

[45] J. Hemmer, J. Nagatomi, S. Wood, A. Vertegel, D. Dean, and M. LaBerge, "Role of cytoskeletal components in stress-relaxation behavior of adherent vascular smooth muscle cells," *Journal of Biomechanical Engineering*, vol. 131, no. 4, p. 041001, 2009.

[46] S. Hiratsuka, Y. Mizutani, A. Toda, N. Fukushima, K. Kawahara, H. Tokumoto, and T. Okajima, "Power-law stress and creep relaxations of single cells measured by colloidal probe atomic force microscopy," *Japanese Journal of Applied Physics*, vol. 48, no. 8, p. 08JB17, 2009.

[47] J. Hildebrandt, "Comparison of mathematical models for cat lung and viscoelastic balloon derived by Laplace transform methods from pressure–volume data," *Bulletin of Mathematical Biology*, vol. 31, no. 4, pp. 651–667, 1969.

[48] B. Fabry, G. Maksym, J. Butler, M. Glogauer, D. Navajas, N. Taback, E. Millet, and J. Fredberg, "Time scale and other invariants of integrative mechanical behavior in living cells," *Physical Review E*, vol. 68, no. 4, p. 41914, 2003.

[49] J. Fredberg and B. Fabry, "The cytoskeleton as a soft glassy material," in *Models and Measurements in Cell Mechanics* (M. Mofrad and R. Kamm, eds.), ch. 3, pp. 50–70, Cambridge University Press: Cambridge, UK, 2006.

[50] N. Desprat, A. Richert, J. Simeon, and A. Asnacios, "Creep function of a single living cell," *Biophysical Journal*, vol. 88, no. 3, pp. 2224–2233, 2005.

[51] S. Hiratsuka, Y. Mizutani, M. Tsuchiya, K. Kawahara, H. Tokumoto, and T. Okajima, "The number distribution of complex shear modulus of single cells measured by atomic force microscopy," *Ultramicroscopy*, vol. 109, no. 8, pp. 937–941, 2009.

[52] B. Hoffman, G. Massiera, K. Van Citters, and J. Crocker, "The consensus mechanics of cultured mammalian cells," *Proceedings of the National Academy of Sciences*, vol. 103, no. 27, p. 10259, 2006.

[53] P. Kollmannsberger and B. Fabry, "Active soft glassy rheology of adherent cells," *Soft Matter*, vol. 5, no. 9, pp. 1771–1774, 2009.

[54] M. Pittenger, A. Mackay, S. Beck, R. Jaiswal, R. Douglas, J. Mosca, M. Moorman, D. Simonetti, S. Craig, and D. Marshak, "Multilineage potential of adult human mesenchymal stem cells," *Science*, vol. 284, no. 5411, pp. 143–147, 1999.

[55] E. Horwitz, D. Prockop, L. Fitzpatrick, W. Koo, P. Gordon, M. Neel, M. Sussman, P. Orchard, J. Marx, R. Pyeritz, and M. Brenner, "Transplantability and therapeutic effects of bone marrow-derived mesenchymal cells in children with osteogenesis imperfecta," *Nature Medicine*, vol. 5, no. 3, pp. 309–313, 1999.

[56] S. Chen, W. Fang, F. Ye, Y. Liu, J. Qian, S. Shan, J. Zhang, R. Chunhua, L. Liao, S. Lin, and J. Sun, "Effect on left ventricular function of intracoronary transplantation of autologous bone marrow mesenchymal stem cell in patients with acute myocardial infarction," *The American Journal of Cardiology*, vol. 94, no. 1, pp. 92–95, 2004.

[57] C. Westminster, C. Westminister, C. Vail, and D. Busse, "Increased knee cartilage volume in degenerative joint disease using percutaneously implanted, autologous mesenchymal stem cells," *Pain Physician*, vol. 11, no. 3, pp. 343–353, 2008.

[58] S. Bruder, N. Jaiswal, and S. Haynesworth, "Growth kinetics, self-renewal, and the osteogenic potential of purified human mesenchymal stem cells during extensive subcultivation and following cryopreservation," *Journal of Cellular Biochemistry*, vol. 64, no. 2, pp. 278–294, 1997.

[59] M. Dominici, K. Le Blanc, I. Mueller, I. Slaper-Cortenbach, F. Marini, D. Krause, R. Deans, A. Keating, D. Prockop, and E. Horwitz, "Minimal criteria for defining multipotent mesenchymal stromal cells. The International Society for Cellular Therapy position statement," *Cytotherapy*, vol. 8, no. 4, pp. 315–317, 2006.

[60] F. Chowdhury, S. Na, D. Li, Y. Poh, T. Tanaka, F. Wang, and N. Wang, "Material properties of the cell dictate stress-induced spreading and differentiation in embryonic stem cells," *Nature Materials*, vol. 9, no. 1, pp. 82–88, 2009.

[61] A. Banfi, A. Muraglia, B. Dozin, M. Mastrogiacomo, R. Cancedda, and R. Quarto, "Proliferation kinetics and differentiation potential of *ex vivo* expanded human bone marrow stromal cells: implications for their use in cell therapy," *Experimental Hematology*, vol. 28, no. 6, pp. 707–715, 2000.

[62] M. Bonab, K. Alimoghaddam, F. Talebian, S. Ghaffari, A. Ghavamzadeh, and B. Nikbin, "Aging of mesenchymal stem cell *in vitro*," *BMC Cell Biology*, vol. 7, no. 1, p. 14, 2006.

[63] J. Kim, J. Kang, J. Park, Y. Choi, K. Choi, K. Park, D. Baek, S. Seong, H. Min, and H. Kim, "Biological characterization of long-term cultured human mesenchymal stem cells," *Archives of Pharmacal Research*, vol. 32, no. 1, pp. 117–126, 2009.

[64] K. Ghosh, Z. Pan, E. Guan, S. Ge, Y. Liu, T. Nakamura, X. Ren, M. Rafailovich, and R. Clark, "Cell

adaptation to a physiologically relevant ECM mimic with different viscoelastic properties," *Biomaterials*, vol. 28, no. 4, pp. 671–679, 2007.

[65] J. Solon, I. Levental, K. Sengupta, P. Georges, and P. Janmey, "Fibroblast adaptation and stiffness matching to soft elastic substrates," *Biophysical Journal*, vol. 93, no. 12, pp. 4453–4461, 2007.

[66] D. Discher, D. Mooney, and P. Zandstra, "Growth factors, matrices, and forces combine and control stem cells," *Science*, vol. 324, no. 5935, pp. 1673–1677, 2009.

[67] J. Casella, M. Flanagan, and S. Lin, "Cytochalasin D inhibits actin polymerization and induces depolymerization of actin filaments formed during platelet shape change," *Nature*, vol. 293, no. 5830, pp. 302–305, 1981.

[68] R. Merkel, N. Kirchgessner, C. Cesa, and B. Hoffmann, "Cell force microscopy on elastic layers of finite thickness," *Biophysical Journal*, vol. 93, no. 9, pp. 3314–3323, 2007.

[69] J. Mendelsohn, S. Yang, J. Hiller, A. Hochbaum, and M. Rubner, "Rational design of cytophilic and cytophobic polyelectrolyte multilayer thin films," *Biomacromolecules*, vol. 4, no. 1, pp. 96–106, 2003.

[70] M. Thompson, M. Berg, I. Tobias, M. Rubner, and K. Van Vliet, "Tuning compliance of nanoscale polyelectrolyte multilayers to modulate cell adhesion," *Biomaterials*, vol. 26, no. 34, pp. 6836–6845, 2005.

[71] M. Dembo and Y. Wang, "Stresses at the cell-to-substrate interface during locomotion of fibroblasts," *Biophysical Journal*, vol. 76, no. 4, pp. 2307–2316, 1999.

[72] K. Beningo and Y. Wang, "Flexible substrata for the detection of cellular traction forces," *Trends in Cell Biology*, vol. 12, no. 2, pp. 79–84, 2002.

[73] U. Schwarz, N. Balaban, D. Riveline, A. Bershadsky, B. Geiger, and S. Safran, "Calculation of forces at focal adhesions from elastic substrate data: The effect of localized force and the need for regularization," *Biophysical Journal*, vol. 83, no. 3, pp. 1380–1394, 2002.

[74] J. Butler, I. Tolic-Norrelykke, B. Fabry, and J. Fredberg, "Traction fields, moments, and strain energy that cells exert on their surroundings," *American Journal of Physiology - Cell Physiology*, vol. 282, no. 3, pp. 595–605, 2002.

[75] A. Engler, L. Richert, J. Wong, C. Picart, and D. Discher, "Surface probe measurements of the elasticity of sectioned tissue, thin gels and polyelectrolyte multilayer films: correlations between substrate stiffness and cell adhesion," *Surface Science*, vol. 570, no. 1-2, pp. 142–154, 2004.

[76] B. Oommen and K. Van Vliet, "Effects of nanoscale thickness and elastic nonlinearity on measured mechanical properties of polymeric films," *Thin Solid Films*, vol. 513, no. 1-2, pp. 235–242, 2006.

[77] K. Yamada and E. Cukierman, "Modeling tissue morphogenesis and cancer in 3D," *Cell*, vol. 130, no. 4, pp. 601–610, 2007.

[78] C. Harrison and T. Allen, "Cell surface morphology after trypsinisation depends on initial cell shape," *Differentiation*, vol. 15, no. 1-3, pp. 61–66, 1979.

[79] H. Garnett, "A scanning electron microscope study of the sequential changes in morphology occuring in human fibroblasts placed in suspension culture.," *Cytobios*, vol. 27, no. 105, pp. 7–18, 1980.

[80] S. Kinn and T. Allen, "Conversion of blebs to microvilli: cell surface reorganisation after trypsin," *Differentiation*, vol. 20, no. 1-3, pp. 168–173, 1981.

[81] G. Charras, M. Coughlin, T. Mitchison, and L. Mahadevan, "Life and times of a cellular bleb," *Biophysical Journal*, vol. 94, no. 5, pp. 1836–1853, 2008.

[82] O. Fackler and R. Grosse, "Cell motility through plasma membrane blebbing," *Journal of Cell Biology*, vol. 181, no. 6, pp. 879–884, 2008.

[83] E. Zhou, S. Quek, and C. Lim, "Power-law rheology analysis of cells undergoing micropipette aspiration," *Biomechanics and Modeling in Mechanobiology*, vol. 9, no. 5, pp. 1–10, 2010.

[84] P. Roca-Cusachs, I. Almendros, R. Sunyer, N. Gavara, R. Farré, and D. Navajas, "Rheology of passive and adhesion-activated neutrophils probed by atomic force microscopy," *Biophysical Journal*, vol. 91, no. 9, pp. 3508–3518, 2006.

[85] E. McDowell, A. Ellerbee, M. Choma, B. Applegate, and J. Izatt, "Spectral domain phase microscopy for local measurements of cytoskeletal rheology in single cells," *Journal of Biomedical Optics*, vol. 12, no. 4, p. 044008, 2007.

[86] F. Wottawah, S. Schinkinger, B. Lincoln, S. Ebert, K. Müller, F. Sauer, K. Travis, and J. Guck, "Characterizing single suspended cells by optorheology," *Acta Biomaterialia*, vol. 1, no. 3, pp. 263–271, 2005.

[87] L. MacQueen, M. Buschmann, and M. Wertheimer, "Mechanical properties of mammalian cells in suspension measured by electro-deformation," *Journal of Micromechanics and Microengineering*, vol. 20, no. 6, p. 065007, 2010.

[88] P. Pullarkat, P. Fernández, and A. Ott, "Rheological properties of the eukaryotic cell cytoskeleton," *Physics Reports*, vol. 449, no. 1-3, pp. 29–53, 2007.

[89] D. Kennedy and C. Norman, "What don't we know?," *Science*, vol. 309, no. 5731, p. 75, 2005.

[90] B. Fabry and J. Fredberg, "Remodeling of the airway smooth muscle cell: are we built of glass?," *Respiratory Physiology & Neurobiology*, vol. 137, no. 2-3, pp. 109–124, 2003.

[91] P. Sollich, F. Lequeux, P. Hébraud, and M. Cates, "Rheology of soft glassy materials," *Physical Review Letters*, vol. 78, no. 10, pp. 2020–2023, 1997.

[92] P. Sollich, "Rheological constitutive equation for a model of soft glassy materials," *Physical Review E*, vol. 58, no. 1, pp. 738–759, 1998.

[93] K. Kroy and J. Glaser, "The glassy wormlike chain," *New Journal of Physics*, vol. 9, p. 416, 2007.

[94] C. Semmrich, T. Storz, J. Glaser, R. Merkel, A. Bausch, and K. Kroy, "Glass transition and rheological redundancy in F-actin solutions," *Proceedings of the National Academy of Sciences*, vol. 104, no. 51, p. 20199, 2007.

[95] B. Fabry, G. Maksym, S. Shore, P. Moore, R. Panettieri Jr, J. Butler, and J. Fredberg, "Time course and heterogeneity of contractile responses in cultured human airway smooth muscle cells," *Journal of Applied Physiology*, vol. 91, no. 2, pp. 986–994, 2001.

[96] K. Van Citters, B. Hoffman, G. Massiera, and J. Crocker, "The role of F-actin and myosin in epithelial cell rheology," *Biophysical Journal*, vol. 91, no. 10, pp. 3946–3956, 2006.

[97] Z. Yang, J. Lin, J. Chen, and J. Wang, "Determining substrate displacement and cell traction fields—a new approach," *Journal of Theoretical Biology*, vol. 242, no. 3, pp. 607–616, 2006.

[98] J. del Álamo, R. Meili, B. Alonso-Latorre, J. Rodriguez-Rodriguez, A. Aliseda, R. Firtel, and J. Lasheras, "Spatio-temporal analysis of eukaryotic cell motility by improved force cytometry," *Proceedings of the National Academy of Sciences*, vol. 104, no. 33, p. 13343, 2007.

[99] A. Buxboim, K. Rajagopal, A. Brown, and D. Discher, "How deeply cells feel: methods for thin gels," *Journal of Physics: Condensed Matter*, vol. 22, no. 19, p. 194116, 2010.

[100] Y. Lin, D. Tambe, C. Park, M. Wasserman, X. Trepat, R. Krishnan, G. Lenormand, J. Fredberg, and J. Butler, "Mechanosensing of substrate thickness," *Physical Review E*, vol. 82, no. 4, p. 41918, 2010.

[101] W. Leong, C. Tay, H. Yu, A. Li, S. Wu, D. Duc, C. Lim, and L. Tan, "Thickness sensing of hMSCs on collagen gel directs stem cell fate.," *Biochemical and Biophysical Research Communications*, vol. 401, no. 2, pp. 287–292, 2010.

[102] C. Lo, H. Wang, M. Dembo, and Y. Wang, "Cell movement is guided by the rigidity of the substrate," *Biophysical Journal*, vol. 79, no. 1, pp. 144–152, 2000.

[103] K. Beningo, M. Dembo, I. Kaverina, J. Small, and Y. Wang, "Nascent focal adhesions are responsible for the generation of strong propulsive forces in migrating fibroblasts," *The Journal of Cell Biology*, vol. 153, no. 4, pp. 881–888, 2001.

[104] T. Yeung, P. Georges, L. Flanagan, B. Marg, M. Ortiz, M. Funaki, N. Zahir, W. Ming, V. Weaver, and P. Janmey, "Effects of substrate stiffness on cell morphology, cytoskeletal structure, and adhesion," *Cell Motility and the Cytoskeleton*, vol. 60, no. 1, pp. 24–34, 2005.

[105] S. Peyton and A. Putnam, "Extracellular matrix rigidity governs smooth muscle cell motility in a biphasic fashion," *Journal of Cellular Physiology*, vol. 204, no. 1, pp. 198–209, 2005.

[106] J. Boussinesq, *Applications des Potentiels à l'Étude de l'Équilibre et du Mouvement des Solides Élastiques*. Gauthier-Villars: Paris, France, 1885.

[107] V. Cerruti, "Sulla deformazione di un corpo elastico isotropo per alsune speciali condizioni ai limiti," *Roma. Acc. Linc. Rend.*, vol. 4, p. 785, 1888.

[108] A. Love, *A Treatise on the Mathematical Theory of Elasticity*. University Press, 1920.

[109] K. Johnson, *Contact Mechanics*. Cambridge University Press, 1987.

[110] Z. Yue, "On elastostatics of multilayered solids subjected to general surface traction," *The Quarterly Journal of Mechanics and Applied Mathematics*, vol. 49, no. 3, pp. 471–499, 2003.

[111] V. Fabrikant, "Tangential contact problem for a transversely isotropic elastic layer bonded to a rigid foundation," *Mathematical Proceedings of the Cambridge Philosophical Society*, vol. 138, no. 01, pp. 173–191, 2005.

[112] B. Sabass, M. Gardel, C. Waterman, and U. Schwarz, "High resolution traction force microscopy based on experimental and computational advances," *Biophysical Journal*, vol. 94, no. 1, pp. 207–220, 2008.

[113] J. Stricker, B. Sabass, U. Schwarz, and M. Gardel, "Optimization of traction force microscopy for micron-sized focal adhesions," *Journal of Physics: Condensed Matter*, vol. 22, no. 19, p. 194104, 2010.

[114] W. Guo, M. Frey, N. Burnham, and Y. Wang, "Substrate rigidity regulates the formation and maintenance of tissues," *Biophysical Journal*, vol. 90, no. 6, pp. 2213–2220, 2006.

[115] S. Maskarinec, C. Franck, D. Tirrell, and G. Ravichandran, "Quantifying cellular traction forces in three dimensions," *Proceedings of the National Academy of Sciences*, vol. 106, no. 52, p. 22108, 2009.

[116] T. Boudou, J. Ohayon, C. Picart, and P. Tracqui, "An extended relationship for the characterization of Young's modulus and Poisson's ratio of tunable polyacrylamide gels," *Biorheology*, vol. 43, no. 6,

pp. 721–728, 2006.

[117] T. Boudou, J. Ohayon, C. Picart, R. Pettigrew, and P. Tracqui, "Nonlinear elastic properties of polyacrylamide gels: implications for quantification of cellular forces," *Biorheology*, vol. 46, no. 3, pp. 191–205, 2009.

[118] D. Holmes and N. Stellwagen, "Estimation of polyacrylamide gel pore size from Ferguson plots of linear DNA fragments. II. Comparison of gels with different crosslinker concentrations, added agarose and added linear polyacrylamide," *Electrophoresis*, vol. 12, no. 9, pp. 612–9, 1991.

[119] Y. Wang and R. Pelham Jr, "Preparation of a flexible, porous polyacrylamide substrate for mechanical studies of cultured cells," *Methods Enzymology*, vol. 298, pp. 489–96, 1998.

[120] C. Deroanne, C. Lapiere, and B. Nusgens, "*In vitro* tubulogenesis of endothelial cells by relaxation of the coupling extracellular matrix-cytoskeleton," *Cardiovascular Research*, vol. 49, no. 3, p. 647, 2001.

[121] J. Huang, X. Peng, L. Qin, T. Zhu, C. Xiong, Y. Zhang, and J. Fang, "Determination of cellular tractions on elastic substrate based on an integral Boussinesq solution," *Journal of Biomechanical Engineering*, vol. 131, no. 6, p. 061009, 2009.

[122] A. Nicolas, A. Besser, and S. Safran, "Is the mechanics of cell-matrix adhesion amenable to physical modeling?," *Journal of Adhesion Science and Technology, 24*, vol. 13, no. 14, pp. 2203–2214, 2010.

[123] S. Walcott and S. Sun, "A mechanical model of actin stress fiber formation and substrate elasticity sensing in adherent cells," *Proceedings of the National Academy of Sciences*, vol. 107, no. 17, p. 7757, 2010.

[124] I. Bischofs, "Cell organization in soft media due to active mechanosensing," *Proceedings of the National Academy of Sciences*, vol. 100, no. 16, pp. 9274–9279, 2003.

[125] U. Schwarz, T. Erdmann, and I. Bischofs, "Focal adhesions as mechanosensors: The two-spring model," *Biosystems*, vol. 83, no. 2-3, pp. 225–232, 2006.

[126] A. Nicolas, B. Geiger, and S. Safran, "Cell mechanosensitivity controls the anisotropy of focal adhesions," *Proceedings of the National Academy of Sciences*, vol. 101, no. 34, pp. 12520–12525, 2004.

[127] A. Besser and S. Safran, "Force-induced adsorption and anisotropic growth of focal adhesions," *Biophysical Journal*, vol. 90, no. 10, pp. 3469–3484, 2006.

[128] A. Nicolas and S. Safran, "Limitation of cell adhesion by the elasticity of the extracellular matrix," *Biophysical Journal*, vol. 91, no. 1, p. 61, 2006.

[129] E. Dimitriadis, F. Horkay, J. Maresca, B. Kachar, and R. Chadwick, "Determination of elastic moduli of thin layers of soft material using the atomic force microscope," *Biophysical Journal*, vol. 82, no. 5, pp. 2798–2810, 2002.

[130] J. Tan, J. Tien, D. Pirone, D. Gray, K. Bhadriraju, and C. Chen, "Cells lying on a bed of microneedles: an approach to isolate mechanical force," *Proceedings of the National Academy of Sciences*, vol. 100, no. 4, pp. 1484–1489, 2003.

[131] O. du Roure, A. Saez, A. Buguin, R. Austin, P. Chavrier, P. Silberzan, and B. Ladoux, "Force mapping in epithelial cell migration," *Proceedings of the National Academy of Sciences*, vol. 102, no. 7, p. 2390, 2005.

[132] A. Saez, A. Buguin, P. Silberzan, and B. Ladoux, "Is the mechanical activity of epithelial cells controlled by deformations or forces?," *Biophysical Journal*, vol. 89, no. 6, pp. 52–54, 2005.

[133] B. Parekkadan, D. Van Poll, K. Suganuma, E. Carter, F. Berthiaume, A. Tilles, and M. Yarmush, "Mesenchymal stem cell-derived molecules reverse fulminant hepatic failure," *PLoS One*, vol. 2, no. 9, p. e941, 2007.

[134] D. van Poll, B. Parekkadan, C. Cho, F. Berthiaume, Y. Nahmias, A. Tilles, and M. Yarmush, "Mesenchymal stem cell-derived molecules directly modulate hepatocellular death and regeneration *in vitro* and *in vivo*," *Hepatology*, vol. 47, no. 5, pp. 1634–1643, 2008.

[135] W. Hörl, *Replacement of Renal Function by Dialysis*. Springer Netherlands, 2004.

[136] S. Hur, Y. Zhao, Y. Li, E. Botvinick, and S. Chien, "Live cells exert 3-dimensional traction forces on their substrata," *Cellular and Molecular Bioengineering*, vol. 2, no. 3, pp. 425–436, 2009.

[137] H. Delanoë-Ayari, J. Rieu, and M. Sano, "4D traction force microscopy reveals asymmetric cortical forces in migrating dictyostelium cells," *Physical Review Letters*, vol. 105, no. 24, p. 248103, 2010.

[138] W. Legant, J. Miller, B. Blakely, D. Cohen, G. Genin, and C. Chen, "Measurement of mechanical tractions exerted by cells in three-dimensional matrices," *Nature Methods*, vol. 7, no. 12, pp. 969–971, 2010.

[139] K. Ko and C. McCulloch, "Intercellular mechanotransduction: cellular circuits that coordinate tissue responses to mechanical loading," *Biochemical and Biophysical Research Communications*, vol. 285, no. 5, pp. 1077–1083, 2001.

[140] C. Reinhart-King, M. Dembo, and D. Hammer, "Cell-cell mechanical communication through compliant substrates," *Biophysical Journal*, vol. 95, no. 12, pp. 6044–6051, 2008.

[141] J. Winer, S. Oake, and P. Janmey, "Non-linear elasticity of extracellular matrices enables contractile cells to communicate local position and orientation," *PLoS One*, vol. 4, no. 7, p. e6382, 2009.

[142] P. Yurchenco, "Basement membrane structure in situ: evidence for lateral associations in the type IV collagen network," *The Journal of Cell Biology*, vol. 105, no. 6, pp. 2559–2568, 1987.

[143] A. Shukla, A. Dunn, M. Moses, and K. Van Vliet, "Endothelial cells as mechanical transducers: enzymatic activity and network formation under cyclic strain," *Mechanics and Chemistry of Biosystems*, vol. 1, no. 4, pp. 279–290, 2004.

[144] C. Bruce, "Experimental Determination of Cell Adhesion and Proliferation Response to Substrata Thickness," tech. rep., Massachusetts Institute of Technology, 2008.

[145] H. Zhou, B. Gabilondo, W. Losert, and W. van de Water, "Stretching and relaxation of vesicles," *Physical Review E*, vol. 83, no. 1, p. 11905, 2011.

[146] M. Gardel, F. Nakamura, J. Hartwig, J. Crocker, T. Stossel, and D. Weitz, "Prestressed F-actin networks cross-linked by hinged filamins replicate mechanical properties of cells," *Proceedings of the National Academy of Sciences*, vol. 103, no. 6, pp. 1762–1767, 2006.

[147] M. Puig-de Morales-Marinkovic, K. Turner, J. Butler, J. Fredberg, and S. Suresh, "Viscoelasticity of the human red blood cell," *American Journal of Physiology - Cell Physiology*, vol. 293, no. 2, pp. C597–C605, 2007.

[148] K. Dahl, A. Engler, J. Pajerowski, and D. Discher, "Power-law rheology of isolated nuclei with deformation mapping of nuclear substructures," *Biophysical Journal*, vol. 89, no. 4, pp. 2855–2864, 2005.

[149] J. Alcaraz, L. Buscemi, M. Grabulosa, X. Trepat, B. Fabry, R. Farré, and D. Navajas, "Microrheology of human lung epithelial cells measured by atomic force microscopy," *Biophysical Journal*, vol. 84, no. 3, pp. 2071–2079, 2003.

[150] B. Smith, B. Tolloczko, J. Martin, and P. Grütter, "Probing the viscoelastic behavior of cultured airway smooth muscle cells with atomic force microscopy: stiffening induced by contractile agonist," *Biophysical Journal*, vol. 88, no. 4, pp. 2994–3007, 2005.

[151] X. Trepat, L. Deng, S. An, D. Navajas, D. Tschumperlin, W. Gerthoffer, J. Butler, and J. Fredberg, "Universal physical responses to stretch in the living cell," *Nature*, vol. 447, no. 7144, pp. 592–595, 2007.

[152] G. Schmid-Schönbein, K. Sung, H. Tözeren, R. Skalak, and S. Chien, "Passive mechanical properties of human leukocytes," *Biophysical Journal*, vol. 36, no. 1, pp. 243–256, 1981.

[153] K. Sung, C. Dong, G. Schmid-Schönbein, S. Chien, and R. Skalak, "Leukocyte relaxation properties," *Biophysical Journal*, vol. 54, no. 2, pp. 331–336, 1988.

[154] A. Bausch, W. Möller, and E. Sackmann, "Measurement of local viscoelasticity and forces in living cells by magnetic tweezers," *Biophysical Journal*, vol. 76, no. 1, pp. 573–579, 1999.

[155] W. Trickey, T. Vail, and F. Guilak, "The role of the cytoskeleton in the viscoelastic properties of human articular chondrocytes," *Journal of Orthopaedic Research*, vol. 22, no. 1, pp. 131–139, 2004.

[156] S. Teo, A. Goryachev, K. Parker, and K. Chiam, "Cellular deformation and intracellular stress propagation during optical stretching," *Physical Review E*, vol. 81, p. 051924, 2010.

[157] P. Bursac, G. Lenormand, B. Fabry, M. Oliver, D. Weitz, V. Viasnoff, J. Butler, and J. Fredberg, "Cytoskeletal remodelling and slow dynamics in the living cell," *Nature Materials*, vol. 4, no. 7, pp. 557–561, 2005.

[158] L. Deng, X. Trepat, J. Butler, E. Millet, K. Morgan, D. Weitz, and J. Fredberg, "Fast and slow dynamics of the cytoskeleton," *Nature Materials*, vol. 5, no. 8, pp. 636–640, 2006.

[159] G. Lenormand, A. Alencar, X. Trepat, E. Zhou, B. Fabry, J. Butler, and J. Fredberg, "The cytoskeleton of the living cell as an out-of-equilibrium system," *Phase Transitions in Cell Biology*, pp. 111–141, 2008.

[160] S. Fielding, P. Sollich, and M. Cates, "Aging and rheology in soft materials," *Journal of Rheology*, vol. 44, no. 2, pp. 323–369, 2000.

[161] M. Gardel, F. Nakamura, J. Hartwig, J. Crocker, T. Stossel, and D. Weitz, "Stress-dependent elasticity of composite actin networks as a model for cell behavior," *Physical Review Letters*, vol. 96, no. 8, p. 88102, 2006.

[162] P. Janmey, S. Hvidt, J. Lamb, and T. Stossel, "Resemblance of actin-binding protein/actin gels to covalently crosslinked networks," *Nature*, vol. 345, no. 6270, pp. 89–92, 1990.

[163] D. Stamenović, "Effects of cytoskeletal prestress on cell rheological behavior," *Acta Biomaterialia*, vol. 1, no. 3, pp. 255–262, 2005.

[164] R. Laudadio, E. Millet, B. Fabry, S. An, J. Butler, and J. Fredberg, "Rat airway smooth muscle cell during actin modulation: rheology and glassy dynamics," *American Journal of Physiology - Cell Physiology*, vol. 289, no. 6, pp. C1388–C1395, 2005.

[165] G. Charras, C. Hu, M. Coughlin, and T. Mitchison, "Reassembly of contractile actin cortex in cell

blebs," *The Journal of Cell Biology*, vol. 175, no. 3, pp. 477–490, 2006.

[166] J. Fredberg and R. Kamm, "Stress transmission in the lung: pathways from organ to molecule," *Annual Review of Physiology*, vol. 68, pp. 507–541, 2006.

[167] T. Nguyen and J. Fredberg, "Strange dynamics of a dynamic cytoskeleton," in *Proceedings of the American Thoraic Society*, vol. 5, pp. 58–61, 2008.

[168] P. Kollmannsberger and B. Fabry, "Linear and nonlinear rheology of living cells," *Annual Review of Materials Research*, vol. 41, no. 1, pp. 75–97, 2011.

[169] F. Chowdhury, S. Na, O. Collin, B. Tay, F. Li, T. Tanaka, D. Leckband, and N. Wang, "Is cell rheology governed by nonequilibrium-to-equilibrium transition of noncovalent bonds?," *Biophysical Journal*, vol. 95, no. 12, pp. 5719–5727, 2008.

[170] J. Guck, *Optical Deformability: Micromechanics from Cell Research to Biomedicine*. PhD thesis, University of Texas at Austin, 2001.

[171] Y. Mizutani, M. Tsuchiya, S. Hiratsuka, K. Kawahara, H. Tokumoto, and T. Okajima, "Elasticity of living cells on a microarray during the early stages of adhesion measured by atomic force microscopy," *Japanese Journal of Applied Physics*, vol. 47, no. 7, pp. 6177–6180, 2008.

[172] P. Kollmannsberger, C. Mierke, and B. Fabry, "Nonlinear viscoelasticity of adherent cells is controlled by cytoskeletal tension," *Soft Matter*, vol. 7, no. 7, pp. 3127–3132, 2011.

[173] A. Friedenstein, R. Chailakhyan, and U. Gerasimov, "Bone marrow osteogenic stem cells: *in vitro* cultivation and transplantation in diffusion chambers," *Cell Proliferation*, vol. 20, no. 3, pp. 263–272, 1987.

[174] B. Lincoln, S. Schinkinger, K. Travis, F. Wottawah, S. Ebert, F. Sauer, and J. Guck, "Reconfigurable microfluidic integration of a dual-beam laser trap with biomedical applications," *Biomedical Microdevices*, vol. 9, no. 5, pp. 703–710, 2007.

[175] G. Lenormand, P. Bursac, J. Butler, and J. Fredberg, "Out-of-equilibrium dynamics in the cytoskeleton of the living cell," *Physical Review E*, vol. 76, no. 4, p. 41901, 2007.

[176] H. Bow, I. Pivkin, M. Diez-Silva, S. Goldfless, M. Dao, J. Niles, S. Suresh, and J. Han, "A microfabricated deformability-based flow cytometer with application to malaria," *Lab on a Chip*, vol. 11, no. 6, pp. 1065–1073, 2011.

[177] D. Humphrey, C. Duggan, D. Saha, D. Smith, and J. Kas, "Active fluidization of polymer networks through molecular motors," *Nature*, vol. 416, no. 6879, pp. 413–416, 2002.

[178] K. Burnham and D. Anderson, *Model Selection and Multimodel Inference*. ASA, 2002.

[179] H. Motulsky and A. Christopoulos, *Fitting Models to Biological Data Using Linear and Nonlinear Regression: A Practical Guide to Curve Fitting*. Oxford University Press, 2004.

[180] B. Lincoln, *The Microfluidic Optical Stretcher*. PhD thesis, University of Leipzig, 2006.

[181] B. Efron, "Bootstrap methods: another look at the jackknife," *The Annals of Statistics*, vol. 7, no. 1, pp. 1–26, 1979.

[182] B. Efron and R. Tibshirani, *An Introduction to the Bootstrap*, vol. 57. Chapman & Hall/CRC, 1993.

[183] M. Chernick, *Bootstrap Methods: A Practitioner's Guide*. Wiley: New York, NY, 1999.

[184] T. Hesterberg, *The Practice of Business Statistics: Companion Chapter 18, Bootstrap Methods and Permutation Tests*. WH Freeman, 2003.

[185] B. Manly, *Randomization, Bootstrap and Monte Carlo Methods in Biology*. Chapman & Hall/CRC, 2007.

[186] C. Shalizi, "The bootstrap," *American Scientist*, vol. 98, no. 3, pp. 186–190, 2010.

[187] E. Peterman, F. Gittes, and C. Schmidt, "Laser-induced heating in optical traps," *Biophysical Journal*, vol. 84, no. 2, pp. 1308–1316, 2003.

[188] S. Ebert, K. Travis, B. Lincoln, and J. Guck, "Fluorescence ratio thermometry in a microfluidic dual-beam laser trap," *Optics express*, vol. 15, no. 23, pp. 15493–15499, 2007.

[189] F. Wetzel, S. Rönicke, K. Müller, M. Gyger, D. Rose, M. Zink, and J. Käs, "Single cell viability and impact of heating by laser absorption," *European Biophysics Journal*, vol. 40, no. 9, pp. 1109–1114, 2011.

[190] R. Barer and S. Joseph, "Refractometry of living cells," *Quarterly Journal of Microscopical Science*, vol. 3, no. 32, p. 399, 1954.

[191] R. Barer and S. Tkaczyk, "Refractive index of concentrated protein solutions," *Nature*, vol. 173, no. 4409, pp. 821–822, 1954.

[192] G. Berry and D. Plazek, "On the use of stretched-exponential functions for both linear viscoelastic creep and stress relaxation," *Rheologica Acta*, vol. 36, no. 3, pp. 320–329, 1997.

[193] M. Keller, J. Schilling, and E. Sackmann, "Oscillatory magnetic bead rheometer for complex fluid microrheometry," *Review of Scientific Instruments*, vol. 72, no. 9, p. 3626, 2001.

[194] C. Wilhelm, "Out-of-equilibrium microrheology inside living cells," *Physical Review Letters*, vol. 101,

no. 2, p. 28101, 2008.

[195] D. Mizuno, C. Tardin, C. Schmidt, and F. MacKintosh, "Nonequilibrium mechanics of active cytoskeletal networks," *Science*, vol. 315, no. 5810, pp. 370–373, 2007.

[196] P. Bareil, Y. Sheng, and A. Chiou, "Local stress distribution on the surface of a spherical cell in an optical stretcher," *Optics Express*, vol. 14, no. 25, pp. 12503–12509, 2006.

[197] A. Ekpenyong, C. Posey, J. Chaput, A. Burkart, M. Marquardt, T. Smith, and M. Nichols, "Determination of cell elasticity through hybrid ray optics and continuum mechanics modeling of cell deformation in the optical stretcher," *Applied Optics*, vol. 48, no. 32, pp. 6344–6354, 2009.

[198] D. Chen, Q. Wen, P. Janmey, J. Crocker, and A. Yodh, "Rheology of soft materials," *Condensed Matter Physics*, vol. 1, pp. 301–322, 2010.

[199] L. Le Goff, F. Amblard, and E. Furst, "Motor-driven dynamics in actin-myosin networks," *Physical Review Letters*, vol. 88, no. 1, p. 18101, 2001.

[200] D. Stamenović, "Cytoskeletal mechanics in airway smooth muscle cells," *Respiratory physiology & neurobiology*, vol. 163, no. 1-3, pp. 25–32, 2008.

[201] M. e Silva, M. Depken, B. Stuhrmann, M. Korsten, F. MacKintosh, and G. Koenderink, "Active multistage coarsening of actin networks driven by myosin motors," *Proceedings of the National Academy of Sciences*, vol. 108, no. 23, pp. 9408–9413, 2011.

[202] C. Chen, R. Krishnan, E. Zhou, A. Ramachandran, D. Tambe, K. Rajendran, R. Adam, L. Deng, and J. Fredberg, "Fluidization and resolidification of the human bladder smooth muscle cell in response to transient stretch," *PLoS One*, vol. 5, no. 8, p. e12035, 2010.

[203] P. Onck, T. Koeman, T. Van Dillen, and E. Van der Giessen, "Alternative explanation of stiffening in cross-linked semiflexible networks," *Physical Review Letters*, vol. 95, no. 17, p. 178102, 2005.

[204] P. Fernández, P. Pullarkat, and A. Ott, "A master relation defines the nonlinear viscoelasticity of single fibroblasts," *Biophysical Journal*, vol. 90, no. 10, pp. 3796–3805, 2006.

[205] P. Fernández and A. Ott, "Single cell mechanics: stress stiffening and kinematic hardening," *Physical Review Letters*, vol. 100, no. 23, p. 238102, 2008.

[206] X. Trepat, M. Grabulosa, F. Puig, G. Maksym, D. Navajas, and R. Farré, "Viscoelasticity of human alveolar epithelial cells subjected to stretch," *American Journal of Physiology - Lung Cellular and Molecular Physiology*, vol. 287, no. 5, p. L1025, 2004.

[207] C. Mierke, P. Kollmannsberger, D. Paranhos Zitterbart, J. Smith, B. Fabry, and W. Goldmann, "Mechano-coupling and regulation of contractility by the vinculin tail domain," *Biophysical Journal*, vol. 94, no. 2, pp. 661–670, 2008.

[208] O. Thoumine and A. Ott, "Time scale dependent viscoelastic and contractile regimes in fibroblasts probed by microplate manipulation," *Journal of Cell Science*, vol. 110, no. 17, pp. 2109–2116, 1997.

[209] D. Icard-Arcizet, O. Cardoso, A. Richert, and S. Hénon, "Cell stiffening in response to external stress is correlated to actin recruitment," *Biophysical Journal*, vol. 94, no. 7, pp. 2906–2913, 2008.

[210] J. Xu, Y. Tseng, and D. Wirtz, "Strain hardening of actin filament networks," *Journal of Biological Chemistry*, vol. 275, no. 46, pp. 35886–35892, 2000.

[211] V. Lulevich, Y. Shih, S. Lo, and G. Liu, "Cell tracing dyes significantly change single cell mechanics," *The Journal of Physical Chemistry B*, vol. 113, no. 18, pp. 6511–6519, 2009.

[212] W. Choi, C. Fang-Yen, K. Badizadegan, S. Oh, N. Lue, R. Dasari, and M. Feld, "Tomographic phase microscopy," *Nature Methods*, vol. 4, no. 9, pp. 717–719, 2007.

[213] F. Alenghat, B. Fabry, K. Tsai, W. Goldmann, and D. Ingber, "Analysis of cell mechanics in single vinculin-deficient cells using a magnetic tweezer," *Biochemical and Biophysical Research Communications*, vol. 277, no. 1, pp. 93–99, 2000.

[214] S. Cross, Y. Jin, J. Rao, and J. Gimzewski, "Nanomechanical analysis of cells from cancer patients," *Nature Nanotechnology*, vol. 2, no. 12, pp. 780–783, 2007.

[215] S. Cross, Y. Jin, J. Tondre, R. Wong, J. Rao, and J. Gimzewski, "AFM-based analysis of human metastatic cancer cells," *Nanotechnology*, vol. 19, no. 38, p. 384003, 2008.

[216] P. Kollmannsberger, *Nonlinear Microrheology of Living Cells*. PhD thesis, University of Erlangen-Nuremberg, Germany, 2009.

[217] P. Girard, J. Pécréaux, G. Lenoir, P. Falson, J. Rigaud, and P. Bassereau, "A new method for the reconstitution of membrane proteins into giant unilamellar vesicles," *Biophysical Journal*, vol. 87, no. 1, pp. 419–429, 2004.

[218] J. Apgar, Y. Tseng, E. Fedorov, M. Herwig, S. Almo, and D. Wirtz, "Multiple-particle tracking measurements of heterogeneities in solutions of actin filaments and actin bundles," *Biophysical Journal*, vol. 79, no. 2, pp. 1095–1106, 2000.

[219] Y. Tseng, K. An, and D. Wirtz, "Microheterogeneity controls the rate of gelation of actin filament networks," *Journal of Biological Chemistry*, vol. 277, no. 20, pp. 18143–18150, 2002.

[220] M. Stolz, R. Raiteri, A. Daniels, M. VanLandingham, W. Baschong, and U. Aebi, "Dynamic elastic

modulus of porcine articular cartilage determined at two different levels of tissue organization by indentation-type atomic force microscopy," *Biophysical Journal*, vol. 86, no. 5, pp. 3269–3283, 2004.

[221] R. Hertzberg, *Deformation and Fracture of Engineering Materials*. John Wiley & Sons, New York, NY, 1996.

[222] T. Mets and G. Verdonk, "*In vitro* aging of human bone marrow derived stromal cells," *Mechanisms of Ageing and Development*, vol. 16, no. 1, pp. 81–89, 1981.

[223] D. Colter, I. Sekiya, and D. Prockop, "Identification of a subpopulation of rapidly self-renewing and multipotential adult stem cells in colonies of human marrow stromal cells," *Proceedings of the National Academy of Sciences*, vol. 98, no. 14, pp. 7841–7845, 2001.

[224] B. Alberts, D. Bray, J. Lewis, M. Raff, K. Roberts, and J. Watson, *Molecular Biology of the Cell*. Garland Science: New York, 1989.

[225] D. Morgan, *The Cell Cycle: Principles of Control*. New Science Press, 2007.

[226] M. Carter and J. Shieh, *Guide to Research Techniques in Neuroscience*. Academic Press, 2009.

[227] J. Hutter, J. Chen, W. Wan, S. Uniyal, M. Leabu, and B. Chan, "Atomic force microscopy investigation of the dependence of cellular elastic moduli on glutaraldehyde fixation," *Journal of Microscopy*, vol. 219, no. 2, pp. 61–68, 2005.

[228] P. Fernández, L. Heymann, A. Ott, N. Aksel, and P. Pullarkat, "Shear rheology of a cell monolayer," *New Journal of Physics*, vol. 9, p. 419, 2007.

[229] G. Lenormand, E. Millet, C. Park, C. Hardin, J. Butler, N. Moldovan, and J. Fredberg, "Dynamics of the cytoskeleton: How much does water matter?," *Physical Review E*, vol. 83, no. 6, p. 061918, 2011.

[230] D. Gillespie, "A general method for numerically simulating the stochastic time evolution of coupled chemical reactions," *Journal of Computational Physics*, vol. 22, no. 4, pp. 403–434, 1976.

[231] D. Gillespie, "Exact stochastic simulation of coupled chemical reactions," *The Journal of Physical Chemistry*, vol. 81, no. 25, pp. 2340–2361, 1977.

[232] D. Wilkinson, "Stochastic modelling for quantitative description of heterogeneous biological systems," *Nature Reviews Genetics*, vol. 10, no. 2, pp. 122–133, 2009.

[233] S. Andrews, T. Dinh, A. Arkin, and R. Meyers, "Stochastic models of biological processes," in *Encyclopedia of Complexity and System Science* (R. A. Meyers, ed.), pp. 8730–8749, New York: Springer, 2009.

[234] C. Picard and A. Donald, "The impact of environmental changes upon the microrheological response of adherent cells," *The European Physical Journal E: Soft Matter and Biological Physics*, vol. 30, no. 2, pp. 127–134, 2009.

[235] J. del Álamo, G. Norwich, Y. Li, J. Lasheras, and S. Chien, "Anisotropic rheology and directional mechanotransduction in vascular endothelial cells," *Proceedings of the National Academy of Sciences*, vol. 105, no. 40, pp. 15411–15416, 2008.

[236] K. Nagayama and T. Matsumoto, "Mechanical anisotropy of rat aortic smooth muscle cells decreases with their contraction," *JSME International Journal Series C*, vol. 47, no. 4, pp. 985–991, 2004.

[237] Y. Tseng, T. Kole, and D. Wirtz, "Micromechanical mapping of live cells by multiple-particle-tracking microrheology," *Biophysical Journal*, vol. 83, no. 6, pp. 3162–3176, 2002.

[238] Y. Tseng and D. Wirtz, "Dendritic branching and homogenization of actin networks mediated by Arp2/3 complex," *Physical Review Letters*, vol. 93, no. 25, p. 258104, 2004.

[239] J. Pablo Rodríguez, M. González, S. Ríos, and V. Cambiazo, "Cytoskeletal organization of human mesenchymal stem cells (MSC) changes during their osteogenic differentiation," *Journal of Cellular Biochemistry*, vol. 93, no. 4, pp. 721–731, 2004.

[240] I. Titushkin and M. Cho, "Modulation of cellular mechanics during osteogenic differentiation of human mesenchymal stem cells," *Biophysical Journal*, vol. 93, no. 10, pp. 3693–3702, 2007.

[241] G. Yourek, M. Hussain, and J. Mao, "Cytoskeletal changes of mesenchymal stem cells during differentiation," *ASAIO Journal*, vol. 53, no. 2, pp. 219–228, 2007.

[242] E. Darling, M. Topel, S. Zauscher, T. Vail, and F. Guilak, "Viscoelastic properties of human mesenchymally-derived stem cells and primary osteoblasts, chondrocytes, and adipocytes," *Journal of Biomechanics*, vol. 41, no. 2, pp. 454–464, 2008.

[243] H. Yu, C. Tay, W. Leong, S. Tan, K. Liao, and L. Tan, "Mechanical behavior of human mesenchymal stem cells during adipogenic and osteogenic differentiation," *Biochemical and Biophysical Research Communications*, vol. 393, no. 1, pp. 150–155, 2010.

[244] T. Berdyyeva, C. Woodworth, and I. Sokolov, "Human epithelial cells increase their rigidity with ageing *in vitro*: direct measurements," *Physics in Medicine and Biology*, vol. 50, no. 1, pp. 81–92, 2005.

[245] C. Schulze, F. Wetzel, T. Kueper, A. Malsen, G. Muhr, S. Jaspers, T. Blatt, K. Wittern, H. Wenck, and J. Käs, "Stiffening of human skin fibroblasts with age," *Biophysical Journal*, vol. 99, no. 8, pp. 2434–

2442, 2010.

[246] M. Wozniak, N. Kawazoe, T. Tateishi, and G. Chen, "Change of the mechanical properties of chondrocytes during expansion culture," *Soft Matter*, vol. 6, no. 11, pp. 2462–2469, 2010.

[247] A. Caplan and D. Correa, "The MSC: An injury drugstore," *Cell Stem Cell*, vol. 9, no. 1, pp. 11–15, 2011.

[248] C. DiGirolamo, D. Stokes, D. Colter, D. Phinney, R. Class, and D. Prockop, "Propagation and senescence of human marrow stromal cells in culture: a simple colony-forming assay identifies samples with the greatest potential to propagate and differentiate," *British Journal of Haematology*, vol. 107, no. 2, pp. 275–281, 2001.

[249] M. Kozhevnikova, A. Mikaelyan, O. Payushina, and V. Starostin, "Comparative characterization of mesenchymal bone marrow stromal cells at early and late stages of culturing," *Biology Bulletin*, vol. 35, no. 2, pp. 132–138, 2008.

[250] P. Guillot, C. De Bari, F. Dell'Accio, H. Kurata, J. Polak, and N. Fisk, "Comparative osteogenic transcription profiling of various fetal and adult mesenchymal stem cell sources," *Differentiation*, vol. 76, no. 9, pp. 946–957, 2008.

[251] I. Sekiya, B. Larson, J. Smith, R. Pochampally, J. Cui, and D. Prockop, "Expansion of human adult stem cells from bone marrow stroma: conditions that maximize the yields of early progenitors and evaluate their quality," *Stem Cells*, vol. 20, no. 6, pp. 530–541, 2002.

[252] R. Pal, M. Hanwate, M. Jan, and S. Totey, "Phenotypic and functional comparison of optimum culture conditions for upscaling of bone marrow-derived mesenchymal stem cells," *Journal of Tissue Engineering and Regenerative Medicine*, vol. 3, no. 3, pp. 163–174, 2009.

[253] L. Norman, J. Brugés, K. Sengupta, P. Sens, and H. Aranda-Espinoza, "Cell blebbing and membrane area homeostasis in spreading and retracting cells," *Biophysical Journal*, vol. 99, no. 6, pp. 1726–1733, 2010.

[254] C. Cunningham, "Actin polymerization and intracellular solvent flow in cell surface blebbing," *The Journal of Cell Biology*, vol. 129, no. 6, pp. 1589–1599, 1995.

[255] G. Charras, J. Yarrow, M. Horton, L. Mahadevan, and T. Mitchison, "Non-equilibration of hydrostatic pressure in blebbing cells," *Nature*, vol. 435, no. 7040, pp. 365–369, 2005.

[256] C. Erickson and J. Trinkaus, "Microvilli and blebs as sources of reserve surface membrane during cell spreading," *Experimental Cell Research*, vol. 99, no. 2, pp. 375–384, 1976.

[257] Y. Rovensky and J. Vasiliev, "Surface topography of suspended tissue cells," *International Review of Cytology*, vol. 90, pp. 273–307, 1984.

[258] G. Charras, "A short history of blebbing," *Journal of Microscopy*, vol. 231, no. 3, pp. 466–478, 2008.

[259] J. Dai and M. Sheetz, "Membrane tether formation from blebbing cells," *Biophysical Journal*, vol. 77, no. 6, pp. 3363–3370, 1999.

[260] J. Tinevez, U. Schulze, G. Salbreux, J. Roensch, J. Joanny, and E. Paluch, "Role of cortical tension in bleb growth," *Proceedings of the National Academy of Sciences*, vol. 106, no. 44, pp. 18581–18586, 2009.

[261] V. Ragoonanan, A. Hubel, and A. Aksan, "Response of the cell membrane-cytoskeleton complex to osmotic and freeze/thaw stresses," *Cryobiology*, vol. 61, no. 3, pp. 335–344, 2010.

[262] G. Chamberlain, J. Fox, B. Ashton, and J. Middleton, "Concise review: mesenchymal stem cells: their phenotype, differentiation capacity, immunological features, and potential for homing," *Stem Cells*, vol. 25, no. 11, pp. 2739–2749, 2007.

[263] R. Henschler, E. Deak, and E. Seifried, "Homing of mesenchymal stem cells," *Transfusion Medicine and Hemotherapy*, vol. 35, no. 4, pp. 306–312, 2008.

[264] J. Karp and G. Leng Teo, "Mesenchymal stem cell homing: the devil is in the details," *Cell Stem Cell*, vol. 4, no. 3, pp. 206–216, 2009.

[265] C. Toma, W. Wagner, S. Bowry, A. Schwartz, and F. Villanueva, "Fate of culture-expanded mesenchymal stem cells in the microvasculature: *in vivo* observations of cell kinetics," *Circulation Research*, vol. 104, no. 3, p. 398, 2009.

[266] H. Salem and C. Thiemermann, "Mesenchymal stromal cells: current understanding and clinical status," *Stem Cells*, vol. 28, no. 3, pp. 585–596, 2010.

[267] F. Crick and A. Hughes, "The physical properties of cytoplasm: a study by means of the magnetic particle method," *Experimental Cell Research*, vol. 1, no. 1, pp. 37–80, 1950.

[268] J. Thomson, *The Great Biologists*. Ayer Company Publishers, 1932.

[269] A. Clark, W. Straub, R. Peters, J. Quastel, H. Ing, J. Gaddum, W. Yorke, and J. Danielli, "Discussion on the chemical and physical basis of pharmacological action," *Proceedings of the Royal Society of London. Series B, Biological Sciences*, vol. 121, no. 825, pp. 580–609, 1937.

[270] L. Landau and E. Lifshitz, *Theory of Elasticity*. Pergammon: Oxford, UK, 1986.

[271] A. Saada, *Elasticity Theory and Applications*. Krieger Publishing Company, 1993.

[272] M. Schmidt and H. Lipson, "Distilling free-form natural laws from experimental data," *Science*, vol. 324, no. 5923, pp. 81–85, 2009.

[273] B. Efron, "Better bootstrap confidence intervals," *Journal of the American Statistical Association*, vol. 82, no. 397, pp. 171–185, 1987.

[274] J. Bouchaud, "Weak ergodicity breaking and aging in disordered systems," *J. Phys. I (France)*, vol. 2, no. 9, pp. 1705–1713, 1992.

[275] P. Cizek, R. Weron, and W. Härdle, *Statistical Tools for Finance and Insurance*. Springer-Verlag Berlin Heidelberg, 2005.

[276] J. Gentle, *Computational Statistics*. Springer Verlag, 2009.